

**AN INVESTIGATION OF THE MAGNETIC PROPERTIES OF SPIN-
VALVES USING TRANSMISSION ELECTRON MICROSCOPY**

by Murray Fulton Gillies

Submitted for the degree of Ph.D. at the University of Glasgow

November 1995

© 1995 Murray F. Gillies

ProQuest Number: 13833435

All rights reserved

INFORMATION TO ALL USERS

The quality of this reproduction is dependent upon the quality of the copy submitted.

In the unlikely event that the author did not send a complete manuscript and there are missing pages, these will be noted. Also, if material had to be removed, a note will indicate the deletion.



ProQuest 13833435

Published by ProQuest LLC (2019). Copyright of the Dissertation is held by the Author.

All rights reserved.

This work is protected against unauthorized copying under Title 17, United States Code
Microform Edition © ProQuest LLC.

ProQuest LLC.
789 East Eisenhower Parkway
P.O. Box 1346
Ann Arbor, MI 48106 – 1346

Heris
10321
C 71

GLASGOW
UNIVERSITY
LIBRARY

CONTENTS

ACKNOWLEDGEMENTS

DECLARATION

SUMMARY

CHAPTER 1: FERROMAGNETISM AND MAGNETIC RECORDING 1-21

1.1 INTRODUCTION	1
1.2 BASIC FERROMAGNETISM	1
1.3 ENERGY CONSIDERATIONS	2
1.3.1 Exchange Energy	2
1.3.2 Anisotropy Energy	3
1.3.3 Magnetostatic Energy	4
1.3.4 Magnetic Domains and Wall Energy	5
1.3.5 Total Energy	7
1.4 MAGNETORESISTANCE	7
1.4.1 Anisotropic Magnetoresistance	8
1.4.2 Giant Magnetoresistance	8
1.4.3 Spin-valves	10
1.5 MAGNETIC RECORDING	14
1.5.1 Hysteresis	14
1.5.2 Inductive Heads	15
1.5.3 Reading with Magnetoresistive Heads	17
1.5.4 Comparison of Inductive and Magnetoresistive Heads	18
1.6 HEAD ASSEMBLY IN THE PHILIPS DIGITAL COMPACT CASSETTE	18

CHAPTER 2: TECHNIQUES AND IMAGING MODES	22-45
2.1 INTRODUCTION	22
2.2 ELECTRON MICROSCOPY	23
2.2.1 The Electron Gun	23
2.2.2 The Electron Microscope Column	24
2.2.3 The Recording of Images	26
2.2.4 Aberrations in a CTEM	27
2.3 OBSERVATION OF MAGNETIC DOMAINS BY ELECTRON MICROSCOPY	28
2.3.1 Electron Beam and Specimen Interaction	29
2.4 CTEM MODES	31
2.4.1 The Fresnel Mode	31
2.4.2 The Foucault Mode	32
2.4.3 Low Angle Diffraction	32
2.5 STEM MODES	33
2.5.1 Scanning Transmission Electron Microscopy	34
2.5.2 Image Formation in a STEM	37
2.5.3 Modified Differential Phase Contrast (MDPC) Imaging	39
2.6 KERR MICROSCOPY	40
2.6.1 The Magneto-optical Rotation	40
2.6.2 Implementation of Kerr Microscopy	42
2.6.3 Choosing Which Kerr Effect to Use	43
2.7 SUMMARY	45

**CHAPTER 3: CHARACTERISTICS OF SINGLE PERMALLOY LAYERS 46-64
IN THE NANOMETRE RANGE**

3.1 INTRODUCTION	46
3.2 ALLOYS OF NICKEL AND IRON	46
3.3 SPECIMEN PREPARATION	47
3.4 MAGNETISATION RIPPLE AS A FUNCTION OF FILM THICKNESS	49
3.5 IN-SITU MAGNETISING EXPERIMENTS	53
3.5.1 Easy Axis Reversal Mechanism	54
3.5.2 Hard Axis Reversal Mechanism	57
3.6 INCLUSIONS WHICH PERTURB THE MAGNETIC CHARACTERISTICS	59
3.7 THE CRYSTALLINE STRUCTURE OF PERMALLOY	62
3.8 SUMMARY	64

**CHAPTER 4: FREE LAYER REVERSALS IN SPIN-VALVES WITH 65-92
CO-LINEAR EASY AXIS AND BIASING DIRECTIONS**

4.1 INTRODUCTION	65
4.2 REVIEW OF SPIN-VALVES	65
4.3 MAGNETISATION DISTRIBUTIONS IN THE ABSENCE OF AN APPLIED FIELD	67

4.4 FREE LAYER REVERSAL MECHANISMS FOR FIELDS PARALLEL TO THE BIASING DIRECTION	69
4.4.1 Type (i) Spin-valve	69
4.4.2 Type (ii) Spin-valve	74
4.4.3 Type (iii) Spin-valve	76
4.5 DISCUSSION AND COMPARISON OF SPIN-VALVE PROPERTIES	80
4.6 THE APPLICATION OF FIELDS ORTHOGONAL TO THE BIASING DIRECTION	88
4.6.1 Rotation of Magnetisation Ripple	88
4.7 SUMMARY	92
CHAPTER 5: THE OPTIMISATION OF FREE LAYER REVERSAL MECHANISMS FOR USE IN GMR SPIN-VALVE HEADS	93-124
5.1 INTRODUCTION	93
5.2 UTILISING THE DEMAGNETISING FIELD	93
5.3 CHANGING THE BIASING DIRECTION	95
5.4 ZERO FIELD STATES	96
5.5 FRESNEL STUDIES OF FREE LAYER REVERSAL MECHANISMS FOR FIELDS PARALLEL TO THE BIASING DIRECTION	98
5.5.1 Spin-valves with Weakly Coupled Ferromagnetic Layers	98
5.5.2 Spin-valves with Moderately Coupled Ferromagnetic Layers	100
5.5.3 Spin-Valves with Strongly Coupled Ferromagnetic Layers	102

5.6 THE APPLICATION OF FIELDS AT SMALL ANGLES TO THE BIASING DIRECTION	104
5.7 THE COHERENT ROTATION OF FREE LAYER MAGNETISATION	107
5.8 DOMAIN WALL PROFILES OF 180° WALLS IN SPIN-VALVES	113
5.9 HIGH RESOLUTION MDPC STUDIES OF 360° WALLS	115
5.10 CHANGES IN MAGNETIC STRUCTURE OF A STRONGLY PINNED 360° WALL AS M_{free} COHERENTLY ROTATES	120
5.11 SUMMARY AND CONCLUSIONS	124
CHAPTER 6: BIASING MECHANISMS IN SPIN-VALVE STRUCTURES	125-156
6.1 INTRODUCTION	125
6.2 BIASING MECHANISMS	125
6.3 FeMn BIASED SPIN-VALVES	128
6.4 TbCo BIASED SPIN-VALVES	131
6.4.1 Biased Layer Reversal of a Uniaxial Biased TbCo Spin-valve	132
6.4.2 Detailed Study of Magnetisation Creep	135
6.5 PROBING THE TbCo BIASING MECHANISM USING VERTICAL FIELDS	140
6.6 PROBING THE TbCo BIASING MECHANISM USING FIELDS AT SMALL ANGLES TO THE VERTICAL	148

6.7 VARYING THE DIRECTION OF THE INITIALISING FIELD	153
6.8 SUMMARY AND CONCLUSIONS	155
CHAPTER 7: THE STABILISATION OF A MAGNETIC VORTEX USING A VERTICAL FIELD	157-165
7.1 INTRODUCTION	157
7.2 CREATION OF THE VORTEX AND INITIAL OBSERVATIONS	158
7.3 REDUCTION OF A VERTICAL FIELD AFTER NUCLEATION	159
7.4 THE RESPONSE OF A VORTEX TO SLIGHT CHANGES IN THE ORIENTATION OF THE APPLIED FIELD	161
7.5 THE VORTEX CORE	163
7.6 DISCUSSION AND CONCLUSIONS	165
CHAPTER 8: DOMAIN STRUCTURES IN FeNbSiN FLUXGUIDES FOR USE IN THIN FILM HEADS	166-193
8.1 INTRODUCTION	166
8.2 FeNbSiN	168
8.3 IMAGING MAGNETIC CONTRAST USING THE KERR ROTATION	170
8.4 SAMPLES FOR OBSERVATION	172

8.5 ZERO FIELD STATES	173
8.5.1 Si Substrate	173
8.5.2 Ceramic Substrate	175
8.5.3 Ferrite Substrate	178
8.6 THEORY OF DOMAIN STRUCTURES IN FLUXGUIDES	182
8.7 IN-SITU MAGNETISING EXPERIMENTS	185
8.7.1 Remanent States	185
8.7.2 Response of Fluxguides on a non-magnetic Substrate to an External Field	186
8.7.3 Response of Fluxguides on a-magnetic Substrate to an External Field	190
8.8 SUMMARY	193
CHAPTER 9: CONCLUSIONS AND FUTURE WORK	194-205
9.1 INTRODUCTION	194
9.2 CONCLUSIONS	194
9.3 FUTURE WORK ON CONTINUOUS FILMS	196
9.3.1 Reasons for the existence of Weak Ferromagnetic coupling across the Spacer Layer	196
9.3.2 Further Investigations of Reversal Mechanisms in Spin-valves	197
9.3.3 Further studies of 360° Wall Structures	198
9.3.4 Further studies of Magnetisation Creep	199
9.3.5 Other biasing mechanisms	199
9.3.6 Calculations for Vortex	200

9.4 PATTERNED SPIN-VALVES	200
9.4.1 Picture Frame Structures	200
9.4.2 Small Elements	202

ACKNOWLEDGEMENTS

There are many people who made my life over the past 3 years a lot easier than it could have been. Primarily I must thank Prof. John Chapman who in my opinion was a most excellent supervisor. I am deeply indebted to Dr. Jacques Kools who not only supplied the majority of samples but also contributed greatly to my understanding of the resulting data. On a similar footing I would like to thank Prof. Paulo Freitas for depositing the TbCo biased spin-valves and making constructive comments about the results. Special mention should also be given to Dr. Stephen McVitie who gave up many hours for informal discussions even though he was not directly involved with my research.

I am grateful to Prof. Robert Ferrier for his continual encouragement and the provision of electron microscopes in the Solid State Physics group at the University of Glasgow. I would also like to thank Dr. Laura Heyderman for teaching me how to operate the CM20 microscope and similarly I would like to thank Dr Pat Nicholson for his help on the microscope side of things.

I am deeply indebted to many people at the Philips Research Laboratories in Eindhoven. In particular I would like to thank Dr. Hans van Kesteren who supervised me during the 3 month period which I spent at the Nat. Lab. I would also like to thank all those who made my stay at Philips most enjoyable. These include Prof. Reinder Coehoorn and Theo. Rijks for many informative discussions during my stay.

During the past three years there were various people who should not go unacknowledged. In particular Mr A. Howie has played an important role in maintaining the CM20 microscope and his computer wizardry has undoubtedly eased the pain of writing up. For maintenance of the JEOL- 2000 microscope facilities I would like to thank Mr S. Conner, Mr C. How, the late Mr. J. Simms and the late Miss M. Low.

Finally it remains for me to thank my friends and family for their continual support over the past three years. Special thanks should be paid to Miss Sandra Gray for her continual support during my period of study.

DECLARATION

This thesis is a record of the experiments which have been carried out by myself in the Department of Physics and Astronomy at the University of Glasgow during 1992-95. The work described herein is my own, apart from the preparation of the samples which were prepared by Dr J.C.S Kools, Prof P.P. Freitas and Dr. L. Postma. Some of the work given in this thesis can be found in the following papers;

(1) Micromagnetic characteristics of single permalloy layers in the nanometre range.

M.F. Gillies, J.N. Chapman and J.C.S. Kools *J. Magn. Magn. Mat.*, **140-144**, 721 (1995)

(2) Magnetisation reversal mechanisms in NiFe/Cu/NiFe/FeMn spin-valve structures

M.F. Gillies, J.N. Chapman and J.C.S. Kools, *J. Appl. Phys* **78(9)** Nov (1995)

(3) The magnetisation reversal process in TbCo-biased spin-valves

J.N. Chapman, M.F. Gillies and P.P. Freitas, proceedings of MMM '95 (1995)

(4) Influence of Grain Size on the Transport Properties of Ni₈₀Fe₂₀ and Cu Thin Films

Th.G.S.M. Rijks, R.L.H. Sour, J.C.S. Kools, D.G. Neerincx, M.F. Gillies, A.E.M. de Veirman, R. Coehoorn and W.J.M. de Jonge *IEEE Trans. Mag.* **in press** (1995)

(5) Magnetisation ripple in thin, sputter-deposited, permalloy films

J.C.S. Kools, Th.G.M. Rijks, R.F.O. Reneerkens, M.F. Gillies and J.N. Chapman, submitted to *J. Appl. Physics*, (1995)

SUMMARY

The work presented in this thesis is primarily a study of the reversal mechanisms of the magnetic layers within spin-valve materials. Spin-valve materials display the phenomenon of Giant Magnetoresistance (GMR) and are strong candidates for use in future generation magnetoresistive read heads where predicted areal bit densities are beyond that which is presently recoverable using existing Anisotropic Magnetoresistance technology.

Spin-valves typically consist of two ferromagnetic layers separated by a spacer layer. One of the ferromagnetic layers is exchange coupled to a layer of FeMn, TbCo or NiO which effectively shifts the hysteresis loop by a few hundred Oersted. External fields with a magnitude less than this have little effect on the magnetisation of the exchange biased layer but do switch the other ferromagnetic layer. Thus the magnetisation in the two ferromagnetic layers can be switched, by the application of a small field (≈ 10 Oe), from a parallel low resistance state, which exists at zero field, to an antiparallel high resistance state. The majority of the work presented in this thesis is concerned with the reversal mechanisms of continuous spin-valves which are imaged using the Lorentz mode of transmission electron microscopy. Domain structures within fluxguides, which are suitable for use in thin film recording heads, are also studied, but using Kerr microscopy. Since this is a secondary topic only chapter 8 is given over to these results.

The first chapter of this thesis reviews the basic concepts of ferromagnetism, magnetoresistance and magnetic recording, which are all relevant to this work. Since the dominant method of imaging used in this thesis is transmission electron microscopy chapter 2 concentrates on both the image formation theory of electron microscopy and the techniques available to reveal magnetic contrast. The theory of Kerr microscopy is also briefly reviewed with respect to FeNbSiN fluxguides.

As a prelude to investigating spin-valve structures thin permalloy films are studied in chapter 3 where typical hard and easy axis reversal mechanisms are observed upon applying an external field. Magnetisation ripple is visible in all films studied and by considering images acquired using the Differential Phase Contrast (DPC) mode of electron microscopy it is apparent that the ripple structure is dependent on the thickness of the film. The ripple is partially quantified as a function of film thickness by analysis of the Fourier Transforms of the DPC images. Interactions between domain walls and inclusions are

studied in some detail and in particular the mechanism for the creation of 360° walls, via this interaction, is looked at.

In chapter 4 spin-valve structures are studied for the first time in this thesis. The first samples discussed have co-linear easy axes and biasing directions. Magnetisation ripple is observed in both the free and biased layers of the spin-valves, though it appears to be substantially reduced. The reversal of spin-valves with a permalloy free layer differs markedly from that of an isolated permalloy layer with the most obvious difference being the large number of stable 360° walls involved. Unlike those in an isolated layer, these 360° walls are not necessarily associated with topographical contrast and often change direction several times along the length of the wall. The effect on the free layer reversal of the addition of thin GMR enhancing Co layers at the spacer layer interfaces is also studied.

In chapter 5 the free layer reversal mechanisms for spin-valves with orthogonal easy axis and biasing directions are considered. The main result from this chapter is the fact that coherent rotation of the free layer magnetisation in a spin-valve can be achieved by deliberately off-setting the applied field with the biasing direction by only a small angle. A perfect alignment however causes the rotation of adjacent regions of the free layer magnetisation in clockwise and anti-clockwise senses with the formation of 360° walls between the boundaries. High resolution profiles are made across these walls using DPC imaging.

In chapter 6 the pinning mechanism of the biased layer in a spin-valve is investigated by studying the response of the biased layer to external fields. In the case of FeMn the reversal of the biased layer proceeds by the nucleation of erratic domain structures which exist on a fine scale (typically a few microns). In the case of uniaxial TbCo the reversal is quite different and the phenomenon of magnetisation creep is prominent during the reversal process. The reversal is dominated by domain wall motion and due to there being relatively few nucleation sites the domain wall density is low. The walls which do exist are again erratic and typically change direction many times over a length scale of a few microns. Domain structures are observed in the biased layer of uniaxial TbCo spin-valves after the application of a vertical field. These structures are replicated in the free layer and double domain walls exist at the boundaries. DPC imaging is used to study the domain boundaries in fine detail and allows the in-plane component of magnetisation in the TbCo layer to be estimated. A model with two easy axes is postulated to account for domain structures in the remanent state.

Chapter 7 deals with the nucleation of a magnetic vortex which is stabilised in a buckled film by the presence of a vertical field. While the structure of the vortex is not fully understood the application of fields with an in-plane component reveals that it is confined to regions with exaggerated bend contours.

In chapter 8 the magnetic states of fluxguides, which are intended for thin film recording heads, are studied. These structures were deposited on both magnetic and non-magnetic substrates and the zero field states are studied as a function of the shape of the fluxguide. The study reveals what appears to be a transition from a multiple domain state to a single domain state, for fluxguides deposited on a ferrite substrate, at a fluxguide height of $\approx 8\mu\text{m}$. This may be responsible for an improvement in the noise characteristics which have been observed for prototype thin film heads with throatheights below $\approx 8\mu\text{m}$.

CHAPTER 1: FERROMAGNETISM AND MAGNETIC RECORDING

1.1 INTRODUCTION

This chapter describes the basic concept of ferromagnetism and discusses the various energy considerations which determine the properties and characteristics of ferromagnetic materials. The topic of magnetoresistance, in particular giant magnetoresistance (GMR), is introduced and a spin-valve structure, which displays the phenomenon of GMR, is discussed. The application of ferromagnetism in magnetic recording is also discussed and finally there is a brief overview of the head structure in the Philips Digital Compact Cassette system (DCC).

1.2 BASIC FERROMAGNETISM

A material which possesses a spontaneous non-zero net magnetic moment, in the absence of an applied field, is known as a ferromagnet. Ferromagnets can be transition metals, rare earths, alloys or oxides but they all display ferromagnetism below a critical temperature which is known as the Curie temperature (T_C). Elemental ferromagnetic materials have a magnetic dipole moment associated with each atom. This is caused by the angular momentum which, due to the quenching of orbital angular momentum, arises predominantly from the spin of unpaired electrons in the 3d or 4f shells. Unlike a paramagnet, where the magnetic dipoles are randomly oriented due to thermal agitation, the dipoles in a ferromagnet are aligned parallel to each other below the Curie temperature. In order to account for this co-operative phenomenon Weiss (1907) proposed an internal molecular field. This internal field, H_m , is proportional to M and causes the parallel alignment of the atomic dipole moments.

The molecular field was accounted for by Heisenberg (1928) who proposed a quantum mechanical interaction, known as the exchange force, acting between each atom and its nearest neighbours. Due to the Pauli exclusion principle the total wavefunction for a quantum mechanical system comprising electrons must be antisymmetric. The wavefunction can, however, be thought of as the product of spatial and spin wavefunctions and for a two electron system the electrostatic energy is dependent on the relative angle between the two spins. When the spins are parallel a minimum in electrostatic energy is

obtained when the spatial part of the wavefunction is antisymmetric. The exchange force tends to align the atomic magnetic dipoles in order to lower the energy and is therefore the phenomenon responsible for ferromagnetism.

1.3 ENERGY CONSIDERATIONS

By considering various macroscopic energy terms it is possible, in certain cases, to predict the magnetic state of a system by minimising the total energy. For many systems, however, the energies of different states are finely balanced and micromagnetic calculations are required.

1.3.1 Exchange Energy

As discussed in Section 1.2 the exchange energy is responsible for the spontaneous alignment of atomic magnetic dipoles in a ferromagnet. The interaction energy between two individual particles takes the form,

$$E_{\text{ex}} = -2J(r_{ij})\mathbf{S}_i \cdot \mathbf{S}_j \quad (1.1)$$

where $J(r_{ij})$ is the exchange integral for the two interacting particles, separated by r_{ij} , and \mathbf{S}_i and \mathbf{S}_j are the spin parts of the two wavefunctions which describe the particles. It is usually only necessary to consider nearest neighbour interactions and Fig 1.1 shows the dependence of J on the distance between nearest neighbours for transition metals.

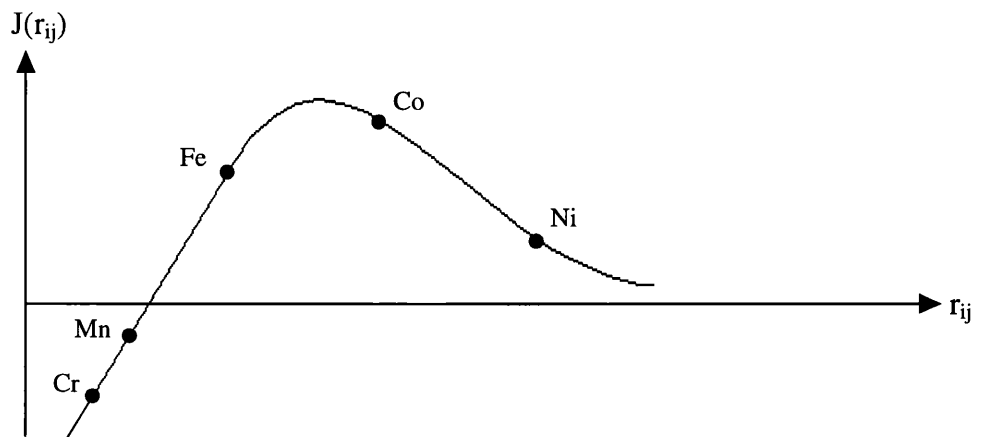


Fig 1.1: Dependence of exchange integral on distance between interacting particles

From equation (1.1) it is seen that to favour parallel alignment and thus ferromagnetism J must be positive. In terms of a finite volume of magnetic material the exchange energy is more completely described by,

$$E_{\text{ex}} = A \int_V [(\nabla\alpha)^2 + (\nabla\beta)^2 + (\nabla\gamma)^2] \quad (1.2)$$

where α , β and γ are the directional cosines of the magnetic vector and A is the exchange constant of the material as defined below,

$$A = \frac{kJS^2}{a} \quad (1.3)$$

k is a constant depending on the crystalline structure, a is the lattice constant and S the magnitude of the magnetic moment of the atom.

1.3.2 Anisotropy Energy

A magnetic material is anisotropic if in zero field the magnetisation vector has a preferred direction. This preferred direction is often referred to as the easy axis and in the case of magnetocrystalline anisotropy is related to lattice directions. Deviations of the magnetisation vector from the easy axis result in an increase in the anisotropy energy.

For a single cubic crystal the anisotropy energy is well described by the first two terms of a series expansion,

$$E_K = \int_V [K_1(\alpha^2\beta^2 + \beta^2\gamma^2 + \gamma^2\alpha^2) + K_2\alpha^2\beta^2\gamma^2] dV \quad (1.4)$$

where α , β and γ are the direction cosines and K_1 and K_2 are the first two anisotropy constants of the material. For transition metals $K_1 \gg K_2$ and the anisotropy energy can be approximated to just a single term.

For hexagonal or uniaxial crystals the anisotropy energy is described by,

$$E_K = \int_V [K_1(1 - \gamma^2) + K_2(1 - \gamma^2)] dV \quad (1.5)$$

where the c axis coincides with the symmetry axis.

When the magnetic material is micro-polycrystalline then the direction of magnetocrystalline anisotropy varies locally from crystallite to crystallite. This results in a random contribution to the local easy axis direction and causes local fluctuations in the direction of the magnetisation vector. This phenomenon is often referred to as magnetisation ripple (Fuller and Hale, 1960)

In a polycrystalline, random alloy such as permalloy ($\text{Ni}_{80}\text{Fe}_{20}$), where the stoichiometry gives near zero magnetocrystalline anisotropy, it is possible to induce a significant anisotropy, by either depositing in a magnetic field or annealing after deposition in the presence of a field. This induced anisotropy is caused by a preferential ordering of atom pairs in the otherwise random alloy (Chikazumi, 1964). During deposition an interaction between the local magnetisation and the atom pairs tends to align the "pair axis" with the magnetisation vector. This results in a "pair axis" throughout the sample and, after deposition, the induced anisotropy remains. The composition of permalloy is also such that there is near zero magnetostriction. This results in the magnetic properties of permalloy films being relatively unaffected by stress.

1.3.3 Magnetostatic Energy

The magnetostatic contribution to the energy of a magnetic system arises from the interaction between magnetic "free poles" which are either generated within the volume of the magnetic material or at its surface where there is a divergent component of magnetisation. These free poles give rise to both an external stray field and an internal field, which is in the opposite sense to the magnetisation. These can be described in terms of an integral over the volume and surface of the source. The field is often termed the demagnetising field, H_d , and is given by,

$$H_d = \frac{1}{4\pi} \int_v \frac{-\nabla \cdot \mathbf{M}}{r^2} dV + \frac{1}{4\pi} \int_s \frac{\mathbf{M} \cdot \mathbf{n}}{r^2} dS \quad (1.6)$$

where r is the position vector for the points in space where the field from the charge is evaluated (field points) and \mathbf{n} the outward pointing unit vector, normal to the surface. This integral is easily evaluated for an ellipse but for other common shapes, such as rectangles, the integral has no simple analytical form.

The energy contribution from the interaction of "free poles" takes the form,

$$E_m = -\frac{1}{2}\mu_0 \int_v \mathbf{M} \cdot \mathbf{H}_d \, dV \quad (1.7)$$

In the presence of an external applied field, H_{app} , there is also a magnetostatic contribution from the interaction between the magnetisation and the applied field. This is known as the Zeeman energy and is given by,

$$E_m = -\mu_0 \int \mathbf{M} \cdot \mathbf{H}_{app} \, dV \quad (1.8)$$

1.3.4 Magnetic Domains and Wall Energy

The net magnetisation of a ferromagnetic body is often substantially less than the saturation magnetisation of the magnetic material from which it is made. In order to explain this, Becker (1930) introduced the concept of magnetic domains. This hypothesis, which was later confirmed by Bitter (1931), assumes that there are many different areas of spontaneously aligned magnetisation within a sample, each with a different direction of magnetisation. These different directions of magnetisation result in a lowering of the overall net magnetisation of the body. The boundaries between domains are known as domain walls and the magnetisation vector smoothly rotates within a wall between the two directions of magnetisation in the adjacent domains. Depending on how the magnetisation vector rotates the wall is either referred to as a Bloch, Néel or cross-tie wall. In a Bloch wall the magnetisation rotates out of the plane of the film as shown schematically in Fig 1.2(a). A Néel wall however has an in plane rotation of magnetisation, Fig 1.2(b), while a cross-tie is an intermediate structure with sections of both Bloch and Néel walls, Fig 1.2(c).

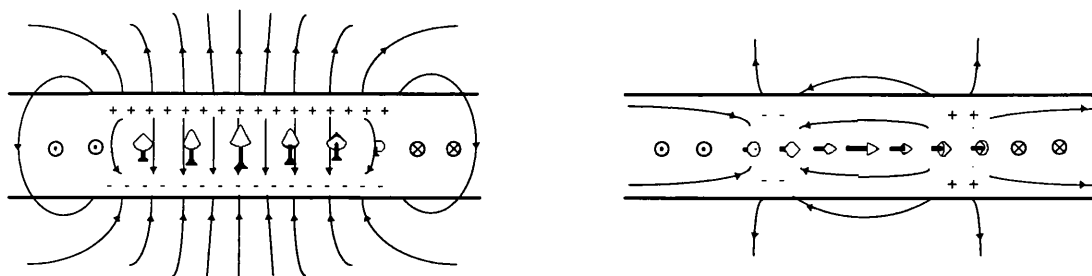
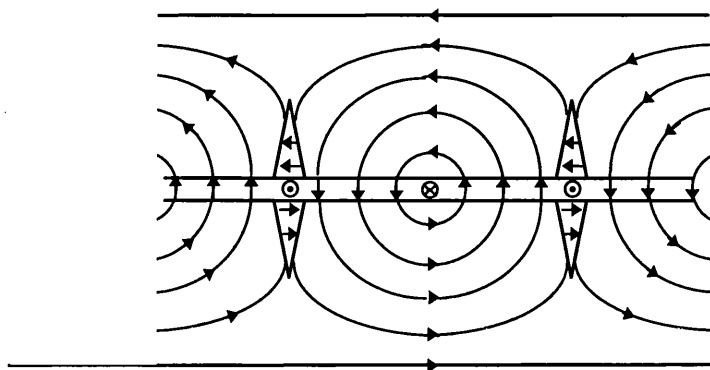


Fig 1.2:(a) Cross-section of Bloch wall

(b) Cross-section of Néel Wall



(c) Planar view of cross-tie wall

The type of domain wall is very dependent on the film thickness and Fig 1.3 shows the expected wall type in permalloy as a function of film thickness.

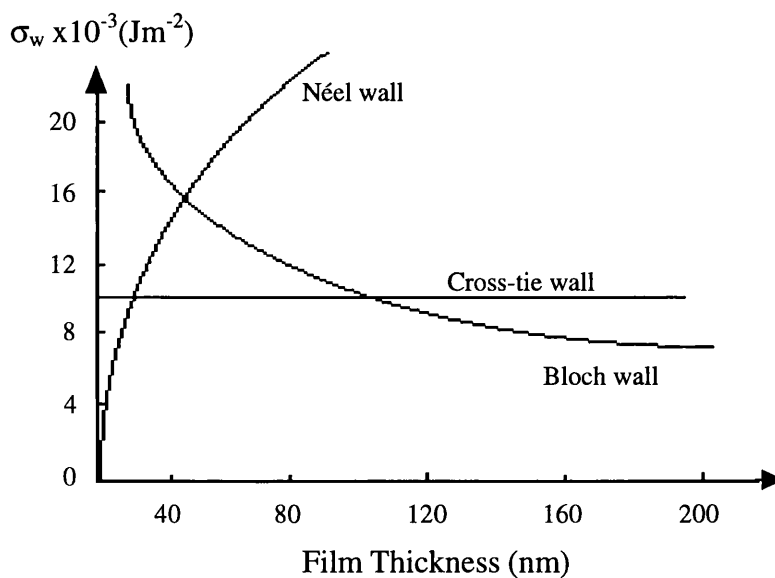


Fig 1.3: Comparison between the energy densities of Bloch, Néel and cross-tie walls as a function of film thickness (Prutton, 1964)

The rotation of magnetisation through a domain wall results in contributions to the exchange energy, the anisotropy energy and in some cases, magnetostatic energy. For a

Bloch wall in a bulk material it is possible to define the domain wall energy per unit area of the wall,

$$\sigma_{\text{wall}} = 4\sqrt{AK} \quad (1.9)$$

Although wall energy is a combination of previously introduced energies it is valid to consider it as a separate entity, E_{wall} .

1.3.5 Total Energy

The total energy of a magnetic system, E_{tot} , is given by the summation of all the energies introduced above,

$$E_{\text{tot}} = E_{\text{ex}} + E_K + E_m + E_w \quad (1.10)$$

In order to find the magnetic state of the system the total energy must be minimised. The four energy terms are inter-related and the balance between them is the factor which controls the magnetic state of the sample. For example, in many cases the magnetostatic energy may be lowered, or even nulled by the formation of closure domains. This however has the consequence of increasing other energies, E_w is increased due to the closure domain walls and E_K is increased since the closure domains are often orthogonal to the easy axis direction. In a fully demagnetised state the magnetic system will be such that there is a global minimum in the total energy. When, however, the system has not been demagnetised the remanent state is only a local minimum. Thus the energy of the system is dependent on the previously applied field. This dependence of the magnetic state on the history of the sample is known as hysteresis and will be dealt with in section 1.5.1

1.4 MAGNETORESISTANCE

Magnetoresistance (MR) is the change in electrical resistance of a material in the presence of an external magnetic field. This property can be utilised as a magnetic field sensor in various devices such as magnetic read heads or electrical compasses.

1.4.1 Anisotropic Magnetoresistance

Anisotropic magnetoresistance, AMR, was discovered by Thomson (1851) and arises from two distinct physical effects which occur upon the application of an external field to a ferromagnetic body. In the absence of an applied field the conduction electrons within a ferromagnetic body experience a Lorentz deflection which is proportional to the component of magnetisation, orthogonal to the electron motion. When the direction of current is orthogonal to the average direction of magnetisation, the Lorentz deflection is a maximum and, in the case of a thin film, this leads to strong electronic scattering from the film surfaces. Upon the application of an external field, which is non-parallel to the magnetic vector, the magnetisation rotates towards the field direction. Consequently there is a decrease in the component of magnetisation, orthogonal to the electron path, and the Lorentz deflection is lowered. This results in a cosine squared dependence for the AMR amplitude for fields applied orthogonal to the zero field direction of magnetisation.

The second physical effect, which is still referred to as AMR, occurs upon increasing the applied field beyond that required for the alignment of the magnetisation with the current direction. This results in a gradual change in magnetoresistance which can be interpreted in terms of Mott's theory of resistivity (1936). The majority of the current in transition metals is carried by either s, d or hybridised sd electrons. The resistivity of the metal is proportional to the probability of these electrons being scattered. In either zero or weak magnetic fields the upper part of the spin up level of the thermally excited states are vacant and it is to these states that the conduction electrons are predominantly scattered. In the presence of a sufficiently strong external field these states are filled, with spin up electrons. This causes a decrease in the number of vacant sites to which the conduction electrons can be scattered and thus a decrease in the resistivity of the material. (Chikazumi, 1964)

In the following discussions reference to AMR should be taken as meaning the former of the two phenomena which are described above.

1.4.2 Giant Magnetoresistance

Giant magnetoresistance, GMR, was first reported by Baibich et al (1988) for a Fe/Cr multilayer superlattice. The sample was grown by molecular beam epitaxy (MBE) and at $T=4.2\text{K}$ the resistivity was lowered by almost a factor of 2 upon the application of a 2 T

magnetic field. The origin of GMR was correctly suggested by these authors to be due to spin-dependent scattering of conduction electrons, predominantly at the interfaces of the multilayer. Upon varying the thickness of the Cr layer oscillations in the coupling constant between the adjacent layers were observed, Fig 1.4. This led to either ferromagnetic or antiferromagnetic layer coupling, depending on the Cr layer thickness.

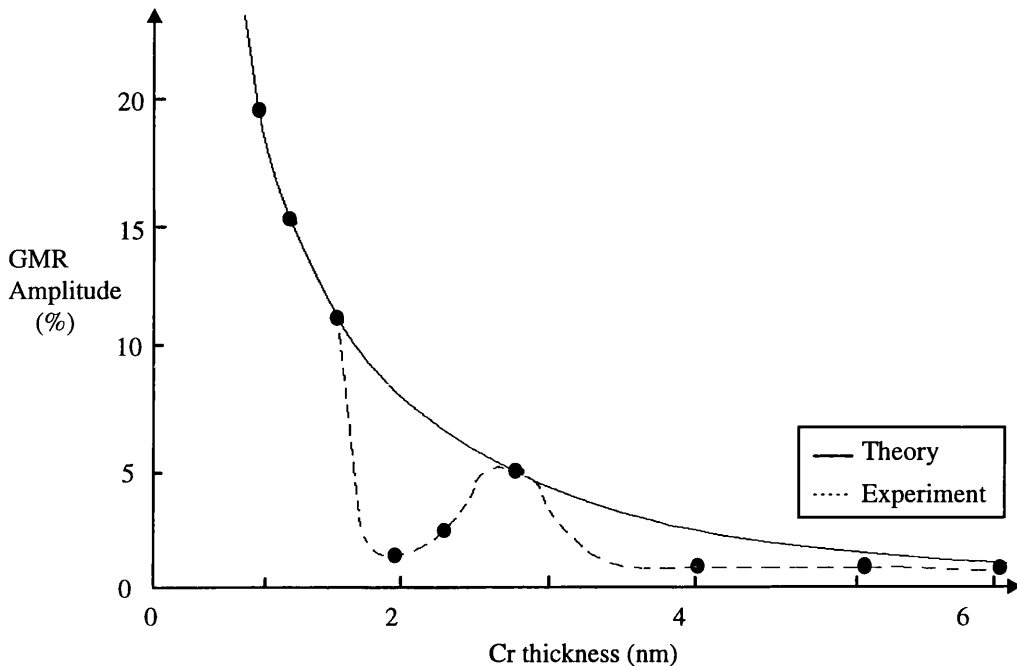


Fig 1.4: GMR amplitude in Fe 30 Å/Cr multilayers versus thickness of Cr layers. Experimental and calculated data from Gijs and Okada (1992)

To date several other transition-metal based multilayer systems have been discovered which exhibit GMR. Due to the strong influence of interfacial spin-dependent scattering the magnitude of the GMR effect is characteristic of the multilayer system as a whole rather than a summation of terms arising from individual layers. An interface which exhibits very strong spin-dependent scattering is Co/Cu. A Co/Cu multilayer system has exhibited 115%, with the sense current in the plane of the layers, but unfortunately required a 13kOe field to achieve maximum MR (Parkin et al, 1991).

When quoting magnetoresistance values for GMR multilayer materials it is always important to specify whether the sense current is in the plane of the layers (current in plane (CIP)) or perpendicular to the layers (current perpendicular to plane (CPP)). In general CPP geometries give rise to a larger change in resistance since the current is directed across the interfaces rather than along the layers. It is, however, important to note that in CPP the total

resistance of the multilayer is very low (typically $10^{-8}\Omega$ for a 1mm^2 multilayer). At present this prevents any application of the CPP geometry as the contact leads have a much higher resistance than the sensor. It is standard to measure the MR curve of a multilayer exhibiting GMR by using the four probe set-up.

1.4.3 Spin-valves

Many of the applications of GMR require a material system which exhibits a relatively large magnetoresistance at room temperature for small applied fields (<10 Oe). One such system, which is the main subject of this thesis, is the spin-valve multilayer, and is shown schematically in Fig 1.5.

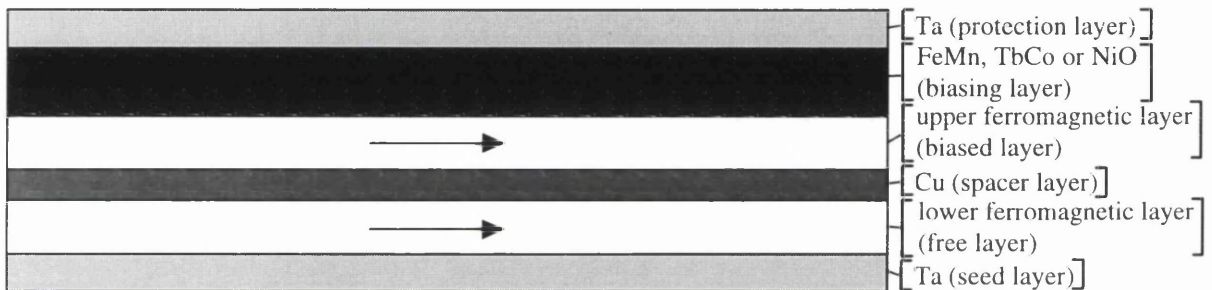


Fig 1.5: Schematic of typical spin-valve structure.

The structure, which is grown on a Ta seed layer to enhance $\langle 111 \rangle$ growth and so minimise magnetocrystalline anisotropy, consists of two ferromagnetic layers (in this thesis, permalloy or a NiFeCo alloy) which are separated by a non-magnetic Cu spacer layer. The upper ferromagnetic layer, referred to as the biased layer, is exchange coupled to either FeMn, TbCo, or NiO. In the results presented in this thesis however, the spin-valves studied are only biased by either FeMn or TbCo. The thickness of the Cu spacer is such that there is weak ferromagnetic coupling between the layers which results in their magnetisations being aligned in zero field. The magnetisation of the lower layer, known as the free layer, may be switched, in relatively low fields (<10 Oe), to lie anti-parallel to that of the biased layer. This causes an increase in the resistivity of the sample which can be interpreted by the two current model (Fert and Bruno, 1992). The resistivity of the parallel state (low resistance state) is given by,

$$\rho_p = \frac{\rho_{\uparrow} \rho_{\downarrow}}{(\rho_{\uparrow} + \rho_{\downarrow})} \quad (1.11)$$

where ρ_{\uparrow} and ρ_{\downarrow} designate the resistivity of the spin \uparrow and spin \downarrow electrons respectively. The antiparallel state (high resistance state) is given by,

$$\rho_{ap} = \frac{(\rho_{\uparrow} + \rho_{\downarrow})}{4} \quad (1.12)$$

and the MR amplitude by,

$$\frac{\Delta\rho}{\rho_{ap}} = \left(\frac{\rho_{\uparrow} - \rho_{\downarrow}}{\rho_{\uparrow} + \rho_{\downarrow}} \right)^2 = \left(\frac{\alpha - 1}{\alpha + 1} \right)^2 \quad \text{with } \alpha = \frac{\rho_{\downarrow}}{\rho_{\uparrow}} \quad (1.13)$$

A typical MR response for an FeMn biased spin-valve is shown in Fig 1.6.

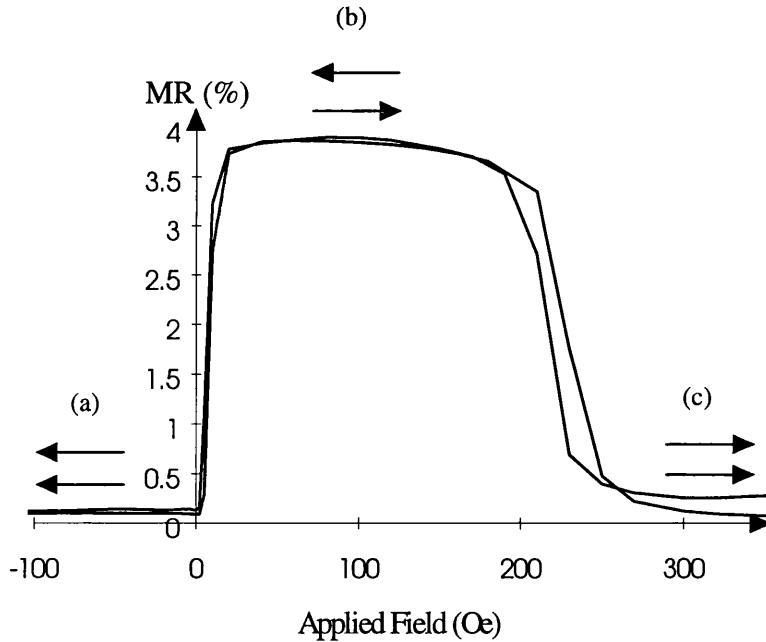


Fig 1.6: Typical MR response of a spin-valve biased by FeMn.

The relative directions of the two permalloy layers are indicated on the figure and the curve may be divided into three main regimes; (a) the 1st low resistance state ($-\infty \rightarrow \approx 10$ Oe) where there is a parallel alignment between the two ferromagnetic layers, (b) the high resistance plateau ($\approx 10 \rightarrow \approx 250$ Oe) where there is anti-parallel alignment between the two ferromagnetic layers and finally (c) the 2nd low resistance state ($\approx 250 \rightarrow +\infty$ Oe) where the biasing is overcome and there is again parallel alignment.

Spin-valve systems have generated considerable interest in the magnetic recording industry where the low field transition between parallel and antiparallel states (free layer reversal) can be used to sense the stray field from a passing tape or disk. When Parkin et al (1990) first demonstrated that GMR could be observed in sputtered samples and that the GMR amplitude was often greater than those grown by MBE, it was widely predicted that spin-valve materials would be used as magnetoresistive sensors in read heads. This prediction has been seen to be correct and at present (1995) there are several laboratories with prototype heads which utilise GMR, (Tsang et al ,1994, Folkerts et al, 1994 and Freitas et al, 1994).

When incorporating a spin-valve into a working head it is important to optimise the thicknesses of the two permalloy layers (t_{NiFe}) as well as the spacer layer thickness (t_{Cu}). The typical dependence of MR on t_{NiFe} , is shown in Fig 1.7, and has a maximum at around 8nm.

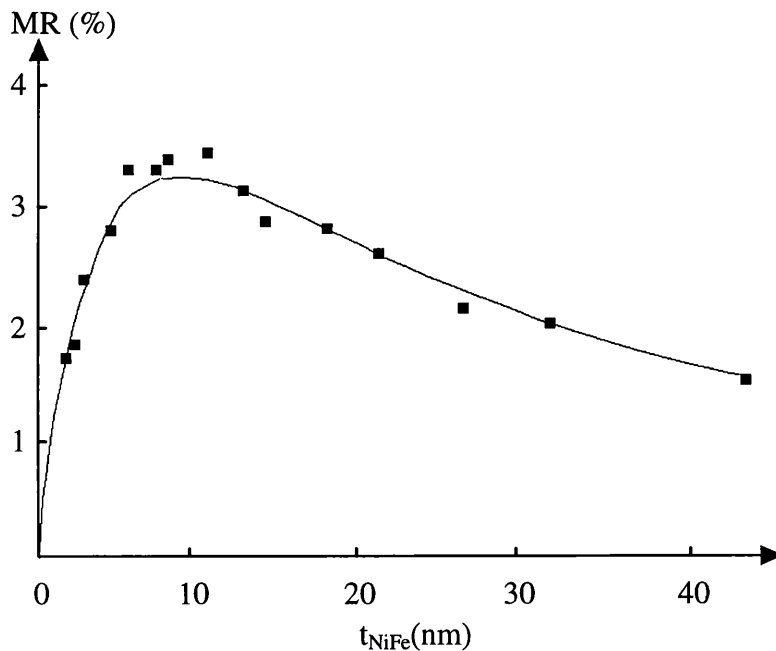


Fig 1.7: Magnetoresistance amplitude as a function of permalloy layer thickness (Dieny et al, 1991).

The decrease in MR for $t_{\text{NiFe}} > 8\text{nm}$ is due to shunting of the sense current and insufficient mixing of the current between the two permalloy layers. The decrease in MR for $t_{\text{NiFe}} < 8\text{nm}$ is caused by insufficient scattering of spin \downarrow electrons in the permalloy layers where the mean free path of spin \downarrow electrons is greater than the permalloy layer thickness (Dieny, 1994).

Fig 1.8 shows a monotonic decrease in MR for increasing t_{Cu} . This is again due to increased shunting but it is important to realise that if t_{Cu} is reduced below say $\approx 2.5\text{nm}$, in order to maximise MR, then interlayer coupling between the permalloy layers is too great for full anti-parallel alignment to be attained.

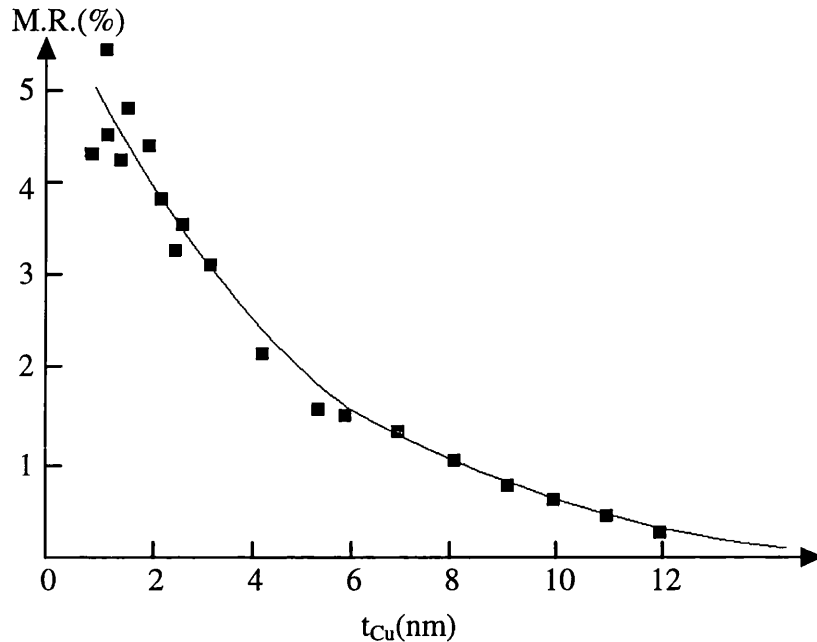


Fig 1.8: *Magnetoresistance amplitude as a function of Cu spacer layer thickness (Dieny et al, 1991).*

The magnetoresistance of the spin-valve can be increased by depositing very thin ($\approx 1.5\text{nm}$) layers of Co at the NiFe/Cu interfaces (Parkin, 1993). Although this increases the MR (from typically 5% to 8%) it also has the effect of increasing the anisotropy of the free layer and thus decreasing the sensitivity of the spin-valve. For example, without Co at the interfaces the sensitivity of a typical spin-valve is $\approx 2.5\%/Oe$ whereas when Co is present, at both interfaces, the sensitivity is only $\approx 1.6\%/Oe$ (Gurney et al, 1993).

Throughout this thesis there is a particular emphasis on the switching between different resistance states. The studying of the free layer reversal allows possible sources of noise to be identified while the reversal of the biased layer allows such things as the uniformity of the biasing field to be assessed.

1.5 MAGNETIC RECORDING

The application of magnetism to store data has been recognised for decades and during this time there has been unrelenting pressure to increase the amount of information which can be stored using magnetic media. In the case of digital recording the information is stored as a series of bits which are written by an inductive head onto a magnetic disk or tape. Stray magnetic field emanates from these bits and it is this which a magnetic recording system must be able to detect in order to retrieve the information at a later date.

1.5.1 Hysteresis

Hysteresis is fundamental to magnetic recording and describes the net magnetisation of a body as a function of applied field. A typical hysteresis loop for a ferromagnetic material is shown in Fig 1.9.

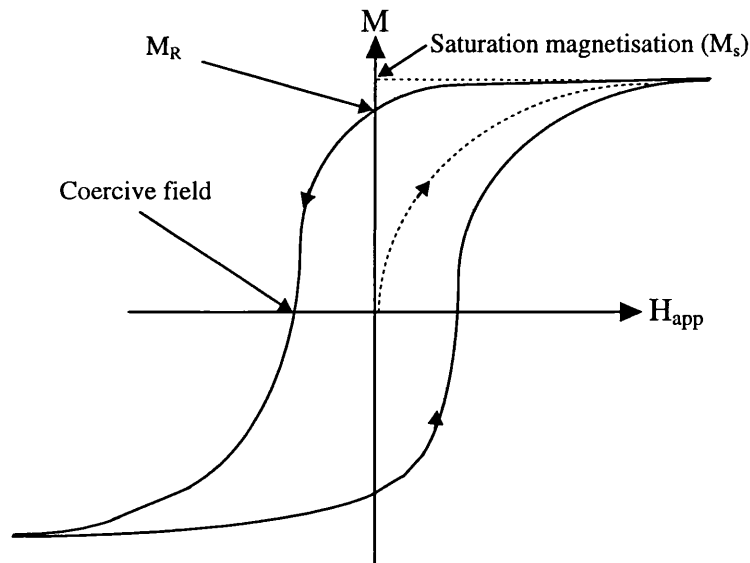


Fig 1.9: A typical hysteresis loop for a soft ferromagnetic material

In a demagnetised state and in the absence of an applied field the magnetisation within an isotropic sample is divided into domains, each with a local direction of magnetisation. In the absence of coupling between these domains the direction of magnetisation within each is orientated randomly in space with respect to the others. Upon the application of a magnetic field the magnetisation within these domains becomes aligned with the field direction, either by the rotation of magnetisation or by domain wall motion. The body therefore now possesses a net magnetic moment which increases with applied field until the saturation magnetisation of the material is reached and all magnetic dipoles, within the

body, are aligned. Upon relaxing the field to zero the body does not return to its original demagnetised state but instead possesses a remanent magnetisation, M_R . This is due to the non-random distribution of magnetisation, within the domains which continue to be partially aligned with the previously applied field. This remanent magnetisation means that the magnetic state of any sample is dependent on its history. If the field arising from the remanent magnetisation can be sensed it is then possible to distinguish whether the material has been exposed to a magnetic field or not. This is the basis of magnetic recording where information is written by locally magnetising areas of the media. At a later date the local remanent magnetisation can be sensed and the information recovered.

1.5.2 Inductive Heads

The utilisation of hysteresis for magnetic storage is easily implemented using an inductive read/write head. The most common of these heads is the “ring-head”, which is illustrated in the simplified schematic of Fig 1.10.

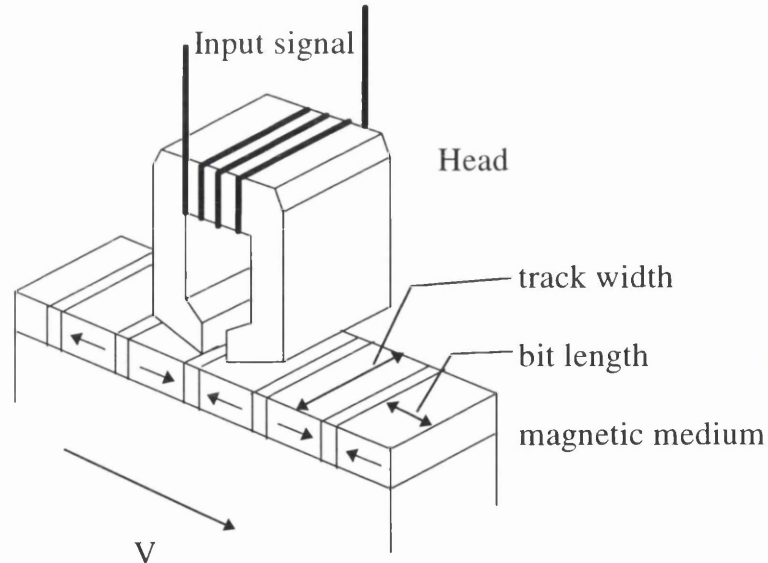


Fig1.10: Simplified schematic of a “ring-head”

The signal to be recorded is passed through the coil which is wound around a magnetic core. This has the effect of generating a magnetic field, along the axis of the coil, which magnetises the core of the head and in turn leads to the generation of a magnetic field at the gap, which is proportional to the input signal. Due to hysteresis the emanating field can be recorded on any suitable ferromagnetic material which passes in front of the gap. The stray

field which emanates from the magnetic media after recording is representative of the recorded signal and can also be detected using an inductive head. An inductive head, working in the read mode, provides a flux closure path for stray fields emanating from the media. The variation of magnetisation within the core which results from this flux closure induces an output voltage in the coil which is given by Faraday's Induction Law. This law states that the e.m.f. induced in a circuit is equal to the rate of change of flux linking the circuit,

$$V = -N \frac{d\phi}{dt} \quad (1.11)$$

where V is the induced e.m.f., N is the number of turns in the coil and ϕ the magnetic flux. This process is analogous to that of writing but with the input and output roles reversed.

The introduction of thin film technology has allowed inductive heads to be deposited layer by layer. This has resulted in smaller pole tips and consequently higher bit densities can now be written by inductive heads. Unfortunately however the present bit densities which can be written do not result in a sufficiently large stray field for inductive data recovery. This is the limiting factor preventing higher bit densities and will be returned to in section 1.5.4.

The recording media can be either in the form of a spinning disk or a passing magnetic tape and inductive recording can be used to record either analogue or digital signals. The advantage of digital recording is the vast improvement in signal to noise ratio and the ability to store a greater amount of information on a smaller area of magnetic material.

Prior to 1980 the majority of magnetic recording media was particulate in nature and at present (1995) this technology still accounts for approximately 40-50% of the overall magnetic recording media market (Grochowski and Thompson, 1994). For high density recording applications, however, continuous films are preferable as they allow a reduction in bit size well below that obtainable with particulate media.

1.5.3 Reading with Magnetoresistive Heads

A magnetoresistive (MR) sensor can only be used to recover information which has previously been written by an inductive head. Consequently a system which utilises magnetoresistive readback must either have separate read/write heads or, as is more common, a single composite structure which incorporates both an inductive write coil and an MR sensor.

The response of a typical AMR material to an external field is shown in Fig 1.11. This is a non-linear function and if the material was worked at around zero field the change in resistance would be extremely small ($\ll 1\%$). If AMR is to be used as a practical sensor it is necessary to bias an AMR head and so operate it at the point of inflection on the MR response curve. In reality this corresponds to having the sense current at 45° to the magnetisation in zero field and typically gives a sensitivity of $0.5\ \%/Oe$, with a linear response.

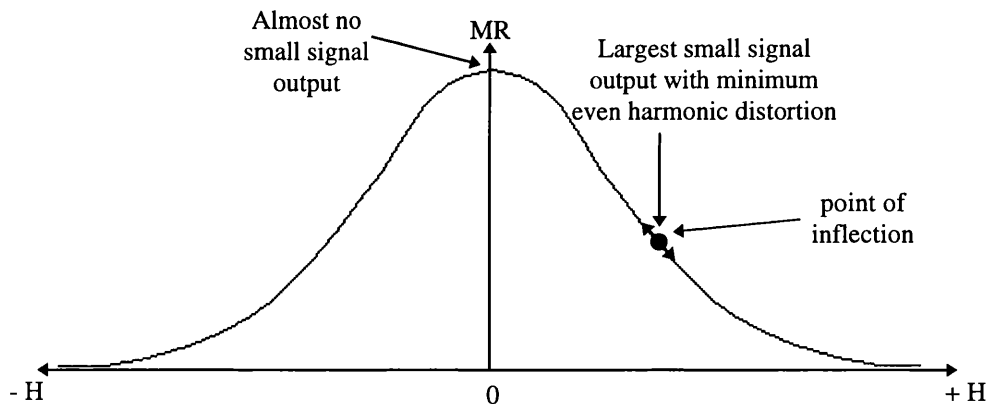


Fig 1.11: Typical response of AMR material

There are several ways of biasing AMR heads so as to work at the point of inflection. These include such things as electrical biasing, where a DC off-set current is passed through the sensor, shielding or barber poling (see Section 1.6). The utilisation of spin-valves as sensors in read heads can be achieved by using the change in resistance which arises between parallel and anti-parallel states. This switch, which corresponds to the transition between regions (a) and (b) in Fig 1.6 is, to a good approximation, linear and so well suited for data recovery.

1.5.4 Comparison of Inductive and Magnetoresistive Heads.

Although the output from AMR heads is often substantially greater than that from inductive heads their widespread use has been hampered by the often complicated biasing mechanisms which they require. They are however used in some IBM disk drives where high areal bit densities result in a weak stray field which cannot be read inductively

Recent increases in areal bit densities have led to a shift in the computer industry to smaller hard disk diameters which are capable of holding more information. This has favoured MR heads as the output of an MR sensor is independent of the head-disk velocity and is only proportional to the magnetic flux ϕ . In the case of very large disks (10'') the circumferential velocity is high and consequently so is the output signal from an inductive head. For smaller disk diameters the velocity is substantially lower and the number of turns required on an inductive head is larger than that attainable with thin film technology.

Due to the fact that GMR heads are relatively simple to bias and can recover information from disks with smaller diameters and increased areal bit densities it is likely that GMR heads will be incorporated in the next generation of computer hard disk drives. It is also probable that GMR sensors will be used in future tape applications. In the case of Quarter Inch Cassette (QIC) systems Leal et al (1995) have successfully developed a GMR head which can recover information with a trackwidth of $12\mu\text{m}$. The initial thrust for GMR tape applications from Philips Research was for use in a low power DCC (Digital Compact Cassette) system. More recently however the focus has also turned towards QIC applications.

1.6 HEAD ASSEMBLY IN THE PHILIPS DIGITAL COMPACT CASSETTE

The Philips Digital Compact Cassette system, which has been in production since 1992, uses the Precision Adaptive Subband Coding (PASC) system to store music in a digital format on a CrO_2 tape (Lokhoff, 1991). In order to be backward compatible with analogue systems the tape speed is relatively slow and the system recovers 864 kbits/second. This rate of data recovery is achieved through 9 digital channels which are each read separately, in parallel, by AMR sensors. The head is made by thin film technology and a planar view of the read layers is shown in Fig 1.12.

The right hand side of the head is used for analogue recording and the 9 digital channels can be seen on the left-hand side. Each of the digital channels are identical though it is only the first 8 which are used for music storage. The ninth holds text information about the specific recording which can be displayed during play-back.

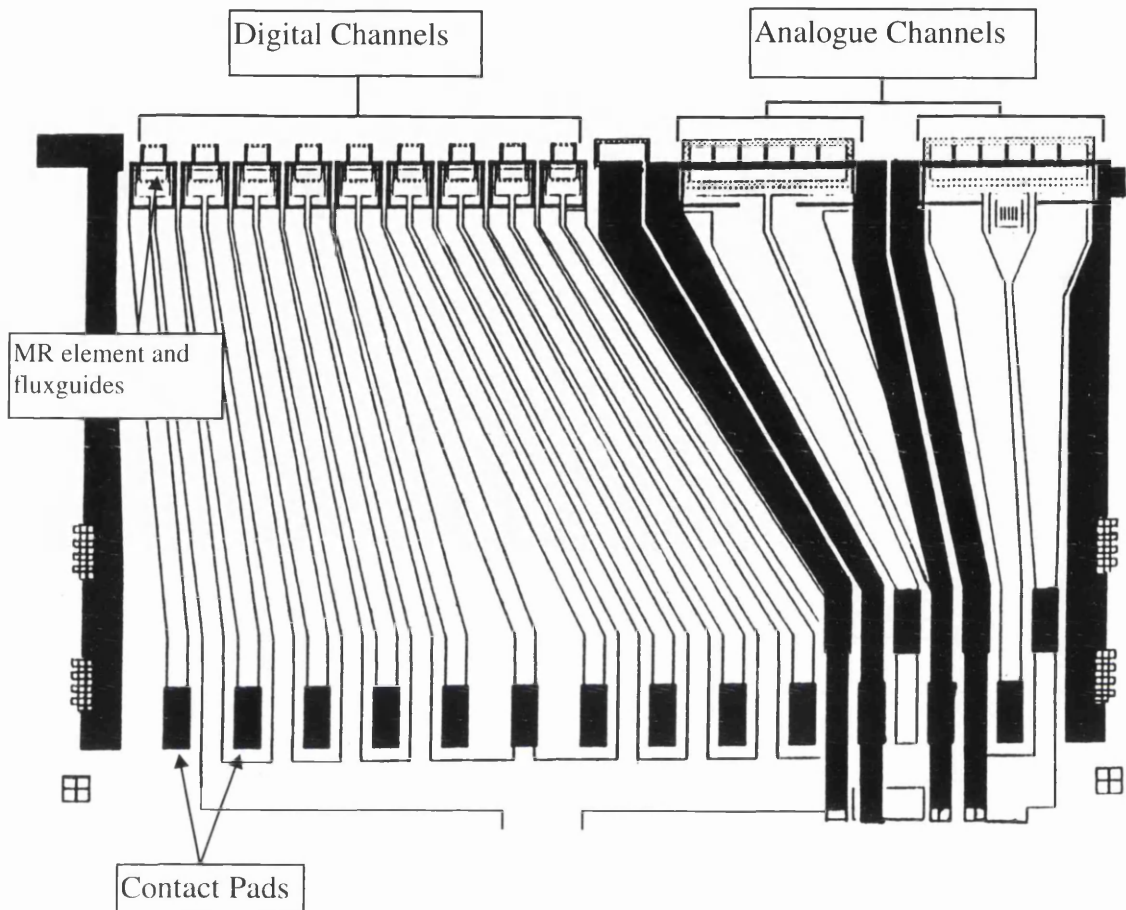


Fig 1.12: Mask used for read layers in DCC head (Zieren et al, 1993)

The write coil is part of the same structure and its position within the head can be seen in the photograph of a cross-section through a digital channel, Fig 1.13. The various fluxguides, which are presently made from permalloy, channel the magnetic flux either to or from the passing tape. The section of the fluxguides which is most critical, for readback, is the part between the CrN protective coating and the magnetoresistive element. This is known as the front fluxguide and movement of domain walls in this section will result in large Barkhausen noise in the output of the MR element. The 65nm CrN coating is needed because the DCC head is in contact with the recording media and if it were not present the tape would soon erode the fluxguide.

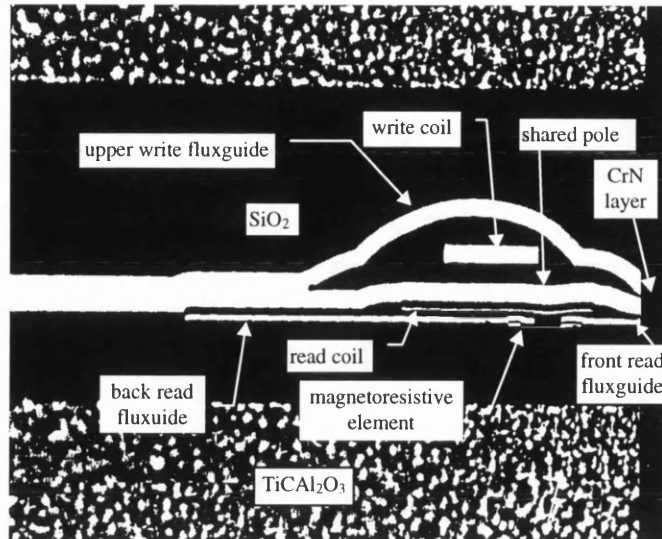


Fig 1.13: Photograph of cross-section through digital channel (Zieren et al, 1993)

The AMR sensor is biased by the barber pole method (Kuijk et al, 1975). This method consists of depositing thin strips of Cu or Au on top of a continuous layer of permalloy, Fig 1.14.

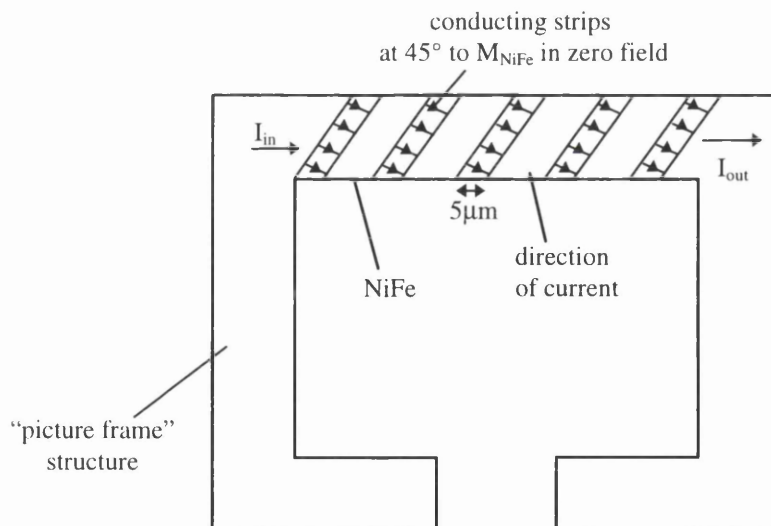


Fig 1.14: Schematic showing barber pole biasing of an AMR sensor

These strips are at a 45° angle to the length of the sensor, and since the resistivity of Cu is significantly less than permalloy (1.7×10^{-6} as opposed to 20×10^{-6} ohm cm) the sense current is channelled across the strips. When the sense current passes through the permalloy it is therefore at 45° to the direction of M_{NiFe} and the sensor is correctly biased.

A disadvantage of this biasing mechanism is that the width of the sensing area is reduced to approximately 40% of the actual physical width of the sensor. Also the optical

lithography required to define the barber pole has to be of a high resolution even for the large trackwidths used in the DCC system. For the smaller trackwidth QIC systems the small scale patterning required to define a barber pole is beyond that possible using optical lithography.

A prototype of the DCC head which utilises a spin-valve, displaying GMR, has also been fabricated by Philips (Folkerts et al 1994). Since the output of this head is significantly higher than AMR, less amplification is required. The head is easily biased by superimposing a small DC off-set on the sense current and due to the low power consumption is ideal for portable applications.

In this thesis results will be presented for spin-valve materials which are equally applicable to GMR heads whether they are incorporated in a disk drive or a tape system. In particular the switching between regions of different resistances are studied in microscopic detail via transmission electron microscopy.

CHAPTER 2: TECHNIQUES AND IMAGING MODES

2.1 INTRODUCTION

The purpose of this chapter is to describe the various techniques which can be used to image magnetic domains. Particular emphasis will be paid to Lorentz electron microscopy as this is the imaging technique used to collect the majority of results in this work. There will however, at the end of this chapter, be a brief discussion about Kerr microscopy as this technique was used to study fluxguides for use in thin film heads

The most simple technique for imaging magnetic domains was first demonstrated by Bitter(1931). This involved coating the magnetic material of interest with a colloidal suspension of fine ferromagnetic particles. Due to the stray magnetic field, which emanates from domain walls, these particles accumulated at domain boundaries and thus revealed information about the magnetic state of the sample. This technique has relatively low resolution (only a few μm) and gives no information about either the wall structures or the direction of magnetisation within the domains.

Other optical techniques include those which make use of the Kerr and Faraday effects. The Kerr effect occurs when polarised light is reflected by a magnetic material and results in the rotation of the polarisation of the light. The angle of rotation depends on the direction of magnetisation with respect to the plane of incidence of the light, and can therefore be used to generate magnetic contrast in an image. In the case of the Faraday effect the incident polarised light is transmitted through the sample and also experiences a rotation of polarisation. Studies utilising the Faraday effect are limited by the transparency of the magnetic sample while those which use the Kerr effect are only capable of imaging domain structures which exist on the surface of the bulk material. The techniques are, however, relatively simple to implement and allow a number of different specimens to be studied in a short period of time. The implementation of Kerr microscopy will be considered in detail later in this chapter.

The Lorentz deflection of an electron beam by a magnetic specimen may be utilised in an electron microscope in order to image magnetic structures. This was first achieved by Hale et al (1959) and has since led to the development of a number of imaging modes, which rely on the Lorentz deflection. In the following sections we shall review, in detail,

both the techniques required for the various modes of Lorentz microscopy and the electron microscopes on which they are implemented.

2.2 ELECTRON MICROSCOPY

The majority of experiments reported in this thesis have been performed on the PHILIPS CM20 and the JEOL 2000FX electron microscopes at The University of Glasgow. There is therefore, in the following discussions, an emphasis on aspects which are of a particular relevance to these microscopes.

2.2.1 The Electron Gun

The electron gun is the source of electrons in an electron microscope and is typically capable of producing electrons in the energy range of 40 to 3000keV. At present, however, an accelerating voltage of 200keV is sufficient for the majority of applications and is standard in most Conventional Transmission Electron Microscopes (CTEMs). Within the electron gun the source of the electrons is often referred to as the filament and is held at a high negative potential. For some applications, where a very bright source is not required, a heated tungsten wire is sufficient. For Lorentz microscopy, however, it is important that the source is not only bright and small but also that the angle subtended by it at the specimen is significantly less than the Lorentz deflection angle. This is achievable by a simple tungsten filament but often a lanthanum-hexaboride (LaB_6) crystal is the preferred option. Although a LaB_6 filament is more than adequate for the majority of CTEM applications there are some, such as coherent Foucault imaging (Chapman et al, 1994) and electron holography (Tonomora, 1987, Cowley, 1992), which require a higher level of coherence. In this case a thermal field emission gun is the preferred option and a schematic of a typical design is shown in Fig 2.1. This gun, which is used in the PHILIPS CM20 at Glasgow University, is optimised for high current and stability. The gun vacuum is pumped in such a way that it is independent from that in the column. The accelerator region is differentially pumped down to a level of 10^{-6} Pa by a 25 l/s ion pump, providing the first separation from the specimen area. The source, extraction anode and electrostatic lenses are pumped

separately by a 8 l/s ion pump which creates a vacuum of $5 \cdot 10^{-7}$ Pa. The separation of accelerator and source prevents small bursts of gas, from the accelerator, disturbing the electron emission.

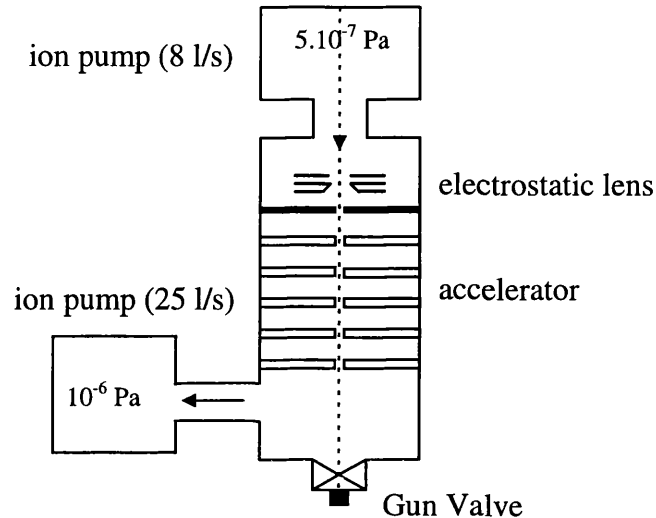


Fig 2.1: Schematic diagram of Field Emission Gun in the PHILIPS CM20

The gun lens is a 3-element electrostatic gun lens which, combined with an entrance aperture lens, provides 5-fold magnification of the source in the acceleration tube. Such a gun configuration provides very low chromatic aberration (see later) and produces a very coherent electron beam of up to $400\mu\text{A}$ from a virtual source size of 3nm. A more complete description of the FEG gun in the PHILIPS CM20 is given by Mul et al (1990)

2.2.2 The Electron Microscope Column.

The microscope column encapsulates the path of the electron beam from the gun to the viewing screen. Along the length of the column there are several magnetic lenses which focus the beam onto the specimen and then subsequently transfer the formed image to the viewing screen. The column, excluding the lens coils, is typically held at 10^{-5} Pa and is shown schematically, again for the PHILIPS CM20, in Fig 2.2

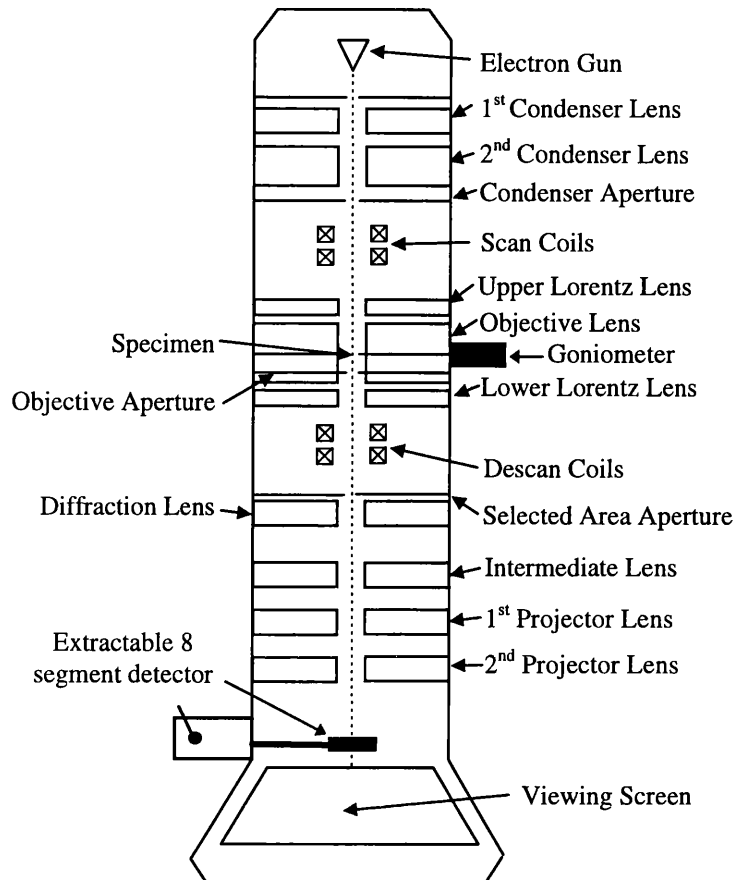


Fig 2.2: Schematic of the Philips CM20 electron microscope

Situated between the gun and the specimen are two condenser lenses which control the source size and angular convergence of the electrons at the specimen plane. In electron microscopes which are not modified for magnetic imaging the specimen is situated within the main imaging lens, which is referred to as the objective lens. This lens focuses the electron beam to produce a diffraction pattern near its back-focal plane and as in optical microscopy it is aberrations within this lens which determine the final resolution of the microscope. In the standard imaging mode of CTEM the image, which is formed by the objective lens, is then magnified and projected onto the viewing screen, or camera, by a number of intermediate and projector lenses (typically three). It is also possible, by changing the post-specimen lenses, to project the back focal plane of the objective onto the viewing screen. This corresponds to imaging the diffraction pattern of the specimen.

There are several apertures in the column which often range in size from 30-500 μm . The first aperture in the column is the condenser aperture. This defines the electron

probe and since as it is at the top of the column it is crucial that it is aligned with the optical axis of the microscope. The next aperture is the objective aperture, so called as it is situated near the back focal plane of the objective lens. This is often used to enhance diffraction contrast and to enable Foucault imaging (see section 2.4.2). The final aperture is the selected area aperture which allows diffraction patterns to be collected from specific areas of the sample.

All electron lenses use a vertical magnetic field (0.5-1.0T for a typical objective lens) in order to either focus or diverge the electron beam. When the specimen itself is sensitive to magnetic fields then, due to its position within the objective lens, it is not possible to study magnetic characteristics with the objective lens excited. A possible solution to this is to leave the objective lens unexcited and use the condenser lenses in order to form the image. This, however, only facilitates low resolution studies and in order to image magnetic structures, with a reasonably high resolution, it is necessary to physically modify the objective lens. In the JEOL 2000-FX this is achieved by replacing the original objective lens with a split pole-piece lens which creates a field free specimen area (Tsuno and Taoka, 1983). In the PHILIPS CM20 a field free specimen area is achieved by the incorporation of additional lenses above and below the objective, Fig 2.2. These are referred to as the upper and lower Lorentz lenses and can be used instead of the objective lens in order to achieve field free magnetic imaging with a point resolution of 2.1nm, or a line resolution of 1.0nm.

2.2.3 The Recording of Images

Electron microscopy images can be recorded on either photographic plates, a video camera or a slow scan CCD camera. In this project the photographic plates are CEA Reflex-15 and while they offer a high resolution they are time consuming to both prepare and develop. In the case of experiments where time dependent effects are present (some of which will be described in chapter 6 of this thesis) micrographs do not allow a complete understanding of the physical processes involved. In such experiments it is advantageous to use a TV pick-up / video system which allows experiments to be recorded in real time. The system on the CM20 comprises of a camera with a RCA silicon intensifier target tube (SIT), viewing a single crystal YAG screen. Images are

acquired using an Agar camera control unit and are contrast enhanced by an Arlunya image processor unit (TF 6000). The signal is fed into a μ -matic video recorder or alternatively can be captured by a PC with frame grabbing facilities. It is possible to increase the signal to noise ratio by integrating over many frames, either statically or dynamically. Once recorded the experiment can be played back at a later date and detailed off-line image analysis carried out. The signal to noise ratio of the video camera, however, is significantly less than that of micrographs, even when integrating over frames, and it is standard to record both micrographs and videos of significant experiments. In the near future (early 1996) the CM20 at Glasgow will be equipped with a slow scan CCD camera. As well as eliminating the need for inconvenient photographic processing this will allow high resolution images to be acquired and on-line analysis of data.

2.2.4 Aberrations in a CTEM

Electron lenses have aberrations which limit the resolution attainable in various ways. As in an optical microscope the aberrations in the objective lens are by far the most important. Hall (1953) lists a total of eight third-order aberrations for a magnetic lens, these include spherical aberrations, astigmatism, and chromatic aberration.

Spherical aberration is the chief defect in a typical objective lens. In Fig 2.3 electrons leaving a point P on the object at an angle α to the axis arrive at the Gaussian image plane at a distance $\Delta r_i = MC_s \alpha^3$ away from the Gauss image point P'. A pencil of semi-angle α thus gives rise to a disc of confusion of radius Δr_i in the image plane. Referred back to the object, the corresponding disc of confusion has a radius of,

$$\Delta r_s = C_s \alpha^3 \quad (2.1)$$

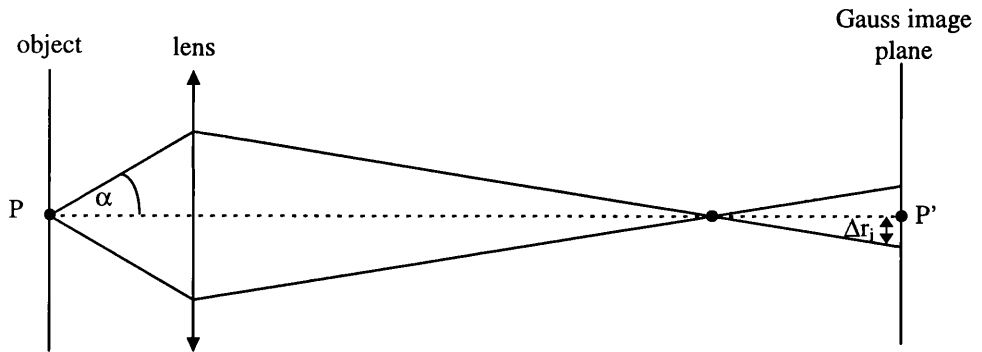


Fig 2.3: Illustration of spherical aberration

Astigmatism is caused by defects in the pole piece of the lens which result in an asymmetrical lens field. This effectively leads to different focal lengths for paraxial rays but can be corrected for by the use of a stigmator. This device, which can be either an electrostatic or magnetic slug type, works by introducing astigmatism which is equal and opposite to that created by the magnetic lens. This can result in near cancellation of the lens astigmatism and allows a higher resolution to be obtained.

The final third order aberration, which will be considered in this section is chromatic aberration. This is a consequence of the focal length of a magnetic lens being dependent on the energy of the electrons. Any spread in the energy, caused by either instabilities in the beam voltage or from the specimen itself, therefore result in a blurring of the image. This also results in a disc of confusion, which is given by,

$$\Delta r_c = C_c \alpha \frac{\Delta E}{E} \quad (2.2)$$

where ΔE is the energy spread and C_c is the chromatic aberration constant.

A more detailed review of aberrations in magnetic lenses is given by Hirsch et al (1965)

2.3 OBSERVATION OF MAGNETIC DOMAINS BY ELECTRON MICROSCOPY

2.3.1 Electron Beam and Specimen Interaction

Some important aspects of Lorentz electron microscopy are well described by a purely classical model (Chapman, 1984). Fig 2.4(a) shows, schematically, a cross-sectional

view through a thin ferromagnetic film which contains three magnetic domains, with directions of magnetisation, perpendicular to the plane of the page.

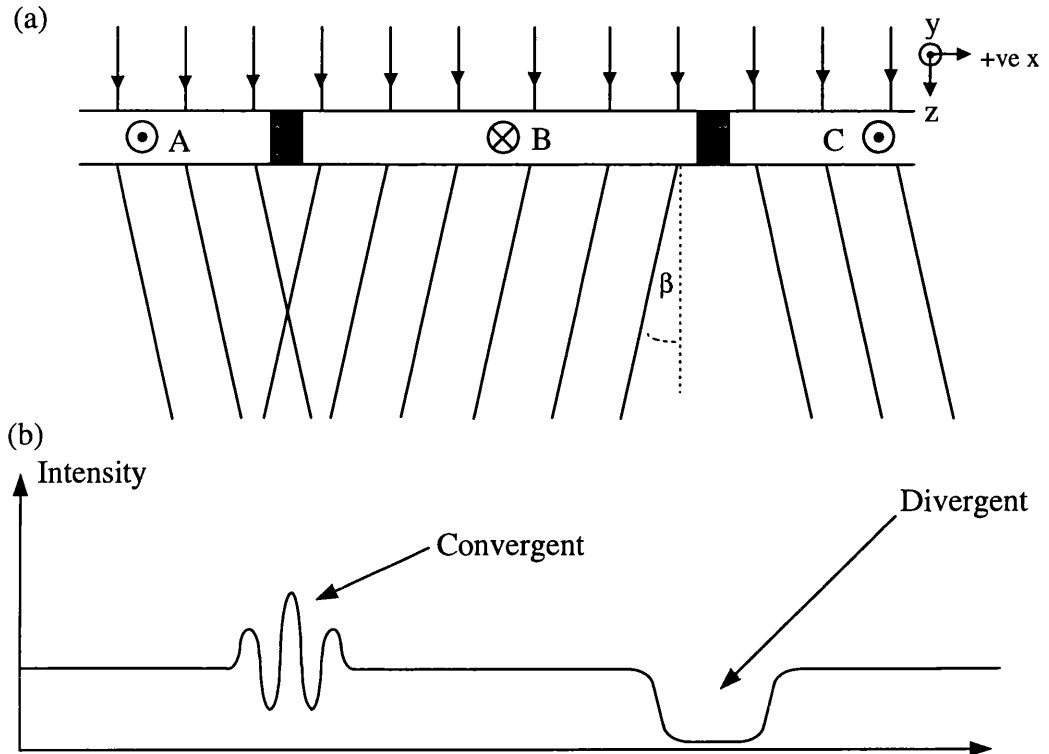


Fig 2.4: (a) Definition of deflection angle for electrons passing through a thin film (b) Schematic of magnetic contrast generation for Fresnel mode with an over-focused imaging lens

A parallel electron beam, incident perpendicular to the plane of the film, experiences a Lorentz deflection through an angle, given by,

$$\beta_x(x) = \frac{e\lambda}{h} \int_{-\infty}^{+\infty} B_y(x,z) dz \quad (2.3)$$

where $B_y(x,z)$ is the y-component of magnetic induction at point (x,z) , e the electronic charge, λ the electron wavelength and h is Planck's constant. Assuming that the film is of a constant thickness, t , and there is no stray field emanating from the film, then equation 2.3 becomes,

$$\beta = \frac{eB_s \lambda t}{h} \quad (2.4)$$

where B_s is the saturation induction, $B_s = \mu_0 M_s$. The Lorentz deflection angle is significantly smaller than the first Bragg angle ($\approx 10^{-2}$ rad) of a typical magnetic material. For example, say that the accelerating voltage is 100keV then the electron wavelength is 3.7 pm. For a film of thickness of 70nm with saturation induction of 1.5T β is only 0.1mrad.

A quantum mechanical description of the electron-specimen interaction was provided by Aharonov and Bohm (1959) and can be understood by considering Fig 2.5.

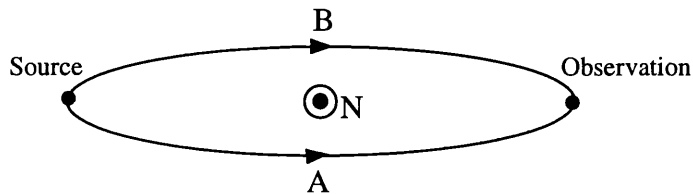


Fig 2.5: Illustration of two paths of the same length which enclose magnetic flux N

Electrons which travel along different paths of equal length and with the same start and end points (such as paths A and B in Fig 2.5) suffer a phase difference which is proportional to the magnetic flux enclosed by the two paths. This phase shift is given by,

$$\phi = \frac{2\pi eN}{h} \quad (2.5)$$

where N is the flux enclosed and all other symbols are as before.

In the case of a plane wave incident on a thin ferromagnetic film (as shown in Fig 2.4) the phase shift between any two points x_1 and x_2 will be,

$$\Delta\phi(x) = \frac{2\pi e t}{h} \int_{x_1}^{x_2} B_y(x) dx \quad (2.6)$$

It is therefore correct to think of ferromagnetic specimens as pure phase objects and thus Lorentz microscopy as a branch of phase contrast electron microscopy.

2.4 CTEM MODES

2.4.1 The Fresnel Mode

The Fresnel mode of Lorentz electron microscopy is an out-of focus imaging technique which reveals domain walls as either bright or dark bands. Considering Fig 2.4(a) again, it can be seen that the magnetisation in domains A and C lead to a deflection of the electron beam in a positive x direction. The magnetisation in domain B, however, results in a deflection of equal magnitude but in the negative x direction. When the image forming lens is slightly defocused by $\pm\Delta Z$ then the image forming plane is no longer coincident with the specimen plane and the magnetisation adjacent to the domain wall has either a convergent (bright walls) or a divergent (dark walls) effect on the electron wave. The contrast which would arise from Fig 2.4(a), when the imaging lens is over focused ($-\Delta Z$), is shown in Fig 2.4(b). This contrast is highly dependent on the defocus (ΔZ) value and can be inverted by moving the imaging lens from over-focused to under-focused. The fringes, which can arise in the convergent wall, are only present when the electron source is coherent and are due to interference effects between electron waves which originate from adjacent domains. Magnetisation ripple also gives rise to contrast in Fresnel images and assuming the directionality of contrast is orthogonal to the average direction of magnetisation this allows a qualitative assessment of domain structures.

The principal advantages of the Fresnel mode are the ease with which it is implemented and the high contrast which can arise at domain walls. The main disadvantage is the requirement that the imaging lens be defocused which results in a poor resolution and difficulties in relating magnetic structure with topographical contrast. A non-linear transfer function also makes it difficult to deduce quantitative information from Fresnel images. An example of a typical Fresnel image is given in Fig 2.6 which shows two areas of opposite directions of magnetisation, separated by a domain wall.

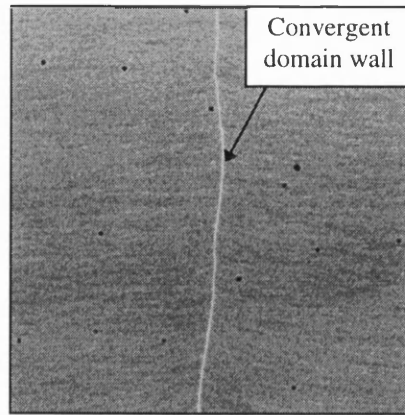


Fig 2.6 Fresnel image showing domain wall contrast

2.4.2 The Foucault Mode

As the Foucault mode of Lorentz electron microscopy is a standard magnetic imaging mode it is mentioned within this chapter even though it is not implemented in the experimental chapters of this thesis. The mode relies on the fact that electrons passing through a given domain are deflected by the same angle and so are all imaged at the same point near the back focal plane of the image forming lens. If the objective aperture, which is also situated near the back focal plane, is deliberately off-set in order to block out those electrons which arise from a particular domain then this domain has zero intensity in the image. Domains with magnetisation in the opposite sense, however, have the strongest intensity while those with other directions have intermediate grey levels. The positioning of the objective aperture can be manipulated in order to “map” in different directions and it is standard to always collect at least two images which have orthogonal mapping directions. Although this technique is relatively simple to implement and does not suffer from the same poor resolution which limits Fresnel imaging, the intensity variations which can be brought about by small movements in the positioning of the objective aperture make it ill-suited for quantitative studies.

2.4.3 Low Angle Diffraction

As discussed in the previous section, with respect to Foucault imaging, all electrons passing through a given domain are deflected by the same angle and so are imaged at the

same point near the back focal plane of the image forming lens. In the mode of low angle diffraction the configuration of the post-specimen lenses are changed so that this plane is projected onto the viewing screen. This is of interest for magnetic studies when the central spot, which is unscattered by the crystal lattice, is considered. In a sample which contains several domains the central unscattered spot is split into several sub-spots. Each of these sub-spots corresponds to a different direction of magnetic induction in the sample. The intensity of the spots is indicative of the relative fractions of induction in the sample, which have a direction which lie perpendicular to a line which joins the spot with the position of an undeflected beam. (see Fig. 2.7)

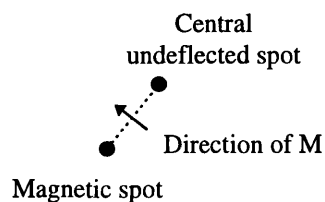


Fig 2.7: Schematic illustration of a low angle diffraction pattern

2.5 STEM MODES

Due to the principal of reciprocity, as described by Cowley (1969), any imaging mode which can be performed on a CTEM can also be implemented on a Scanning Transmission Electron Microscope (STEM). Although it is often simpler to implement many of the standard magnetic imaging modes, such as Fresnel and Foucault, on a CTEM the versatility of a STEM often allows modes which would be otherwise impractical. One of these is differential phase contrast (DPC). This technique, which was first suggested by Deckers and de Lang (1974), requires a configured detector split into quadrants and contrast is achieved by taking the difference signal from opposite segments. The technique has been developed for studying magnetic materials predominantly by Chapman et al (1983), at the University of Glasgow. As a large fraction of the results, within this thesis, were acquired using the DPC mode it and its implementation will be covered extensively in later sections within this chapter (Sections 2.5.1 and 2.5.3).

2.5.1 Scanning Transmission Electron Microscopy

Image formation in a STEM differs markedly from that in a CTEM. In the former instrument a small, often coherent, probe of electrons is scanned in a regular raster across the specimen and some portion of the scattered or unscattered beam is detected. In contrast with a CTEM the detected signal is collected sequentially, and from this a digital image is constructed. The physical size of each sample point is usually defined by the probe size.

In the scanning mode of the PHILIPS CM20 the illumination of the specimen is controlled by the two condenser lenses and, depending on whether a field free specimen area is required, either the objective or upper Lorentz lens. Although the upper Lorentz lens is the final pre-specimen lens and demagnifies the source onto the specimen it is not this lens which is varied to focus the probe. The reason for this is that focusing a lens often results in small thermal changes in the lens core which in turn results in a thermal drift. Since the upper Lorentz is immediately above the specimen even small thermal changes in the lens characteristic could result in blurring of the final image due to thermal drift. To limit this problem the upper Lorentz lens is set to a pre-determined value and in STEM it is the second condenser lens, which is considerably further away from the sample, which is varied in order to focus the probe onto the specimen plane. The electron beam is rastered over the scan area by the scan coils, see Fig 2.2. After passing through the sample de-scan coils compensate for the raster motion so that in the absence of a specimen there is no lateral movement. The beam is then finally projected onto the detector, which is sited in the far field with respect to the specimen.

Another important property of the microscope, when operating in STEM, is the coherent probe size, d_c . This is determined by aberrations in the probe forming lenses and also from diffraction effects due to the probe forming aperture,

$$d_c^2 = \left(\frac{1}{2} C_s \alpha_o^3 \right)^2 + \left(\frac{1.22\lambda}{\alpha_o} \right)^2 \quad (2.7)$$

where C_s is the third order spherical aberration coefficient of the imaging forming lens and α_o is the probe forming angle.

From this the optimum α_0 can be calculated by differentiating with respect to α_0 and setting the derivative equal to zero. This leads to an expression for α_0 ,

$$\alpha_0 = \left(\frac{4\lambda}{C_s} \right)^{\frac{1}{4}} \quad (2.8)$$

For the CM20, operating with the Lorentz lens, this gives an the optimum value for α_0 of 1.1 mrad.

Substituting eqn 2.8 back into eqn. 2.7 gives,

$$d_c = 1.3(C_s\lambda^3)^{\frac{1}{4}} \quad (2.9)$$

and when working with the upper Lorentz on is approximately equal to 3.3 nm. The incoherent probe size, d_i , is simply the demagnification of the extended source by the pre-specimen lenses and is fixed by geometrical considerations to be approximately equal to 1nm. The total probe size is calculated by adding d_i and d_c , either linearly or quadratically .

In the specifications of the CM20 it is stated that a probe angle of 2mrad results in a probe size of 5nm and a probe current of 0.5nA. This performance is not yet achievable however, due to electronic instabilities, though at present the probe size / resolution is more than sufficient to study the majority of magnetic structures.

The CM20 is effectively fitted with three projector lenses (the intermediate lens and the two projector lenses) which allows a wide range of camera lengths to be used. This is of considerable benefit as it means that the diameter of the emergent beam can be easily matched to the physical dimensions of the detector.

The detector which is fitted to the CM20 is a sensitive eight segment photodiode (Oxford Instruments) and is shown schematically in Fig 2.8(b). This detector geometry allows the option of implementing modified DPC (MDPC) which will be discussed in Section 2.5.3. Firstly however a general discussion of standard DPC will be given.

Standard DPC requires only a four segment detector, Fig 2.8(a), and allows two orthogonal maps of magnetic induction to be collected simultaneously. Each segment is a p-n junction in silicon separated by inactive strips $\approx 200\mu\text{m}$ wide.

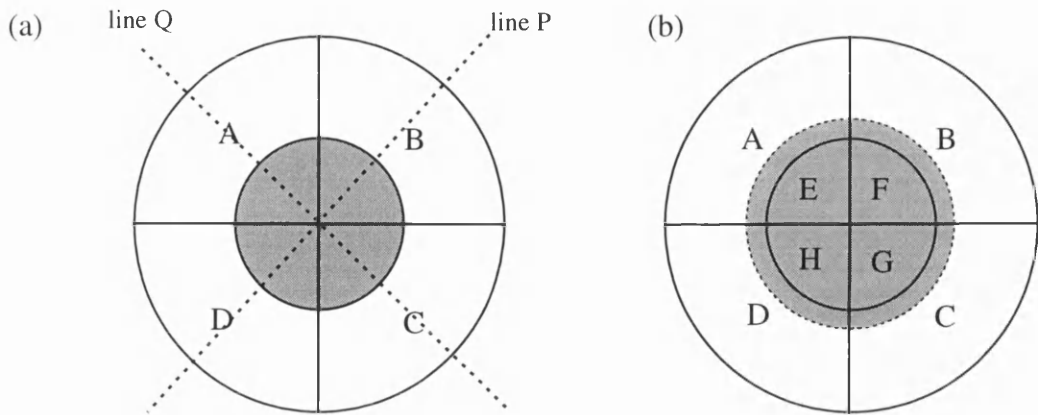


Fig 2.8: (a) Schematic of four segment detector geometry, (b) Schematic of eight segment detector geometry (fitted to CM20)

In the absence of a specimen the post-specimen lenses, Fig 2.2, are used to centre the electron beam on the detector. Since there are equal amounts of current falling on each of the segments the difference signals, A-C and D-B, are zero. If however a magnetic specimen is present the beam is deflected by the Lorentz deflection angle β and the signals on each segment are not equal. Provided that the deflection is small, compared to the probe angle, then the difference signal of A-C is proportional to the component of in-plane magnetic induction which lies along line P in Fig 2.8(a). Similarly the D-B signal is proportional to the component of magnetic induction along line Q, also in Fig 2.8(a). The two difference signals provide orthogonal maps of magnetic induction and from these we have a complete quantitative description of the in-plane magnetic induction.

Although this classical argument explains the generation of magnetic contrast in the DPC mode, a more rigorous quantum mechanical approach is often required to explain the finer issues of the mode. Such an approach is undertaken in the following section.

2.5.2 Image Formation in a STEM

Image formation within a STEM may be described in terms of the wavefunction propagation of the electron beam through the electron optical system and the beam /

specimen interaction. The electron wavefunction incident on the specimen can be described as $\psi_0(\underline{r})$, where \underline{r} is the position vector in the plane of the specimen. Alternatively the wavefunction of the incident wave can be described in terms of the Fourier transform of the wavefunction at the aperture,

$$\psi_0(\underline{r}) = \text{FT}(\Psi_0(\underline{k})) \quad (2.9)$$

where FT denotes the Fourier transform and \underline{k} is the position vector in reciprocal space. $\Psi_0(\underline{k})$ takes the form,

$$\Psi_0(\underline{k}) = \underset{\substack{\uparrow \\ \text{pupil function}}}{A(\underline{k})} \exp \left\{ -2\pi i \left[\underset{\substack{\uparrow \\ \text{spherical aberration term}}}{\frac{C_s \lambda^3 k^4}{4}} - \underset{\substack{\uparrow \\ \text{defocus term}}}{\frac{\Delta z \lambda k^2}{2}} \right] \right\} \quad (2.10)$$

The above equation contains three main terms; (a) the pupil function, $A(\underline{k})$, of the probe forming aperture which is 1 within the aperture and 0 outside it, (b) a term to take account of the spherical aberration of the probe forming lens (C_s is the third order spherical aberration coefficient as discussed in Section 2.2.4) and (c) a term to take account of the defocus effect of the probe forming lens.

The modulation of the electron wave which results from the wave / specimen interaction may be described by a transmission function given by,

$$h(\underline{r}) = \exp\{-i\phi(\underline{r})\} \quad (2.11)$$

where $\phi(\underline{r})$ is the phase change which results due to the interaction and may be either magnetostatic or electrostatic in origin. For the purposes of this discussion however the electrostatic contribution is assumed to be negligible.

Upon exiting the sample the electron wavefunction can be written as,

$$\Psi(\underline{r}, \underline{r}_0) = h(\underline{r})\psi_0(\underline{r} - \underline{r}_0) \quad (2.12)$$

where \underline{r}_0 is the positional vector of the point where the probe is centred.

As the STEM detector is in the far field with respect to the specimen plane, the electron wave function at the detector is given by the Fourier Transform of the $\Psi(\underline{r}, \underline{r}_0)$ i.e.,

$$\Psi_d(\underline{k}, \underline{r}_0) = \text{FT}(\psi(\underline{r}, \underline{r}_0)) \quad (2.13)$$

As with all wavefunctions the amplitude, or the intensity, of this is given by the modulus squared and can be expressed as,

$$I(\underline{k}, \underline{r}_0) = |\psi_0(\underline{k}, \underline{r}_0) * H(\underline{k})|^2 \quad (2.14)$$

In STEM the detector response also affects the actual signal recorded and it is possible to take this into account with the detector response function, $R(\underline{k})$. This gives the recorded signal as,

$$j(\underline{r}_0) = \int I(\underline{k}, \underline{r}_0) \cdot R(\underline{k}) d\underline{k} \quad (2.15)$$

If a quadrant detector is used as a simple split detector then the detector response is given by,

$$\begin{aligned} R(\underline{k}) &= 1 \text{ for } \underline{k}_x > 0 \\ &= -1 \text{ for } \underline{k}_x < 0 \end{aligned} \quad (2.16)$$

Detailed calculations for a split detector (Cowley(1976) and Morrison(1981)) show that the output signal is proportional to the differential of the phase of the object,

$$j(\underline{r}_0) \propto \nabla \phi(\underline{r}_0) \quad (2.17)$$

The conclusion of the arguments in Section 2.3.1 was that a magnetic specimen could be thought of as a pure phase object with a phase proportional to the integrated magnetic induction, Eqn. 2.6. This together with the result of Eqn. 2.17, indicates that the recorded signal from a quadrant detector is directly proportional to the component of the integrated magnetic induction.

2.5.3 Modified Differential Phase Contrast (MDPC) Imaging

Despite the ability of the DPC mode to provide quantitative micromagnetic information there still exists an inherent problem that the phase function of a real specimen contains both magnetic and non-magnetic contributions. One source of non-

magnetic contrast is the crystallites of which many films are composed and, in certain samples, this can dominate, concealing magnetic structure. It is, however, possible to modify the detector geometry and so make substantial changes to the efficiency with which different spatial frequencies are transferred to the image. This is significant when it is realised that the spatial frequency of the crystallite contrast is often substantially greater than that of the magnetic contrast. By detecting the lower frequency components of the image with a greater efficiency, than the high frequency components, it is therefore possible to increase the magnetic signal at the expense of that which arises from the crystallites. This preferential detection of different spatial frequencies can be achieved by using the 8 segment detector, which is shown in Fig 2.8(b), and is fitted to the PHILIPS CM20. The only portions of the electron distribution which carry information, in a difference image, are those parts which are involved in the overlap between the unscattered and diffracted beams. For low frequency components the overlap is at the edge of the unscattered cone and collecting difference signals from the annular quadrants in Fig 2.8(b) therefore results in the preferential detection of low frequency components of the image. The post specimen lenses are set so that the radius of the bright field cone is only slightly greater than the radius of the inner four quadrants and the annular difference signals are collected. When implementing MDPC imaging the most important consideration is the value of κ . This is defined as the ratio of the inner annulus K_i of the detector to the radius of the bright field cone K_α . The ratio can be varied by manipulating the post specimen lenses and Fig 2.9 shows the dependence of the signal to noise ratio on κ .

Although this simple argument demonstrates the physical considerations which result in an eight segment detector being able to preferentially collect the low frequency component, a full wave-optical discussion of the imaging properties is given by Chapman et al (1990).

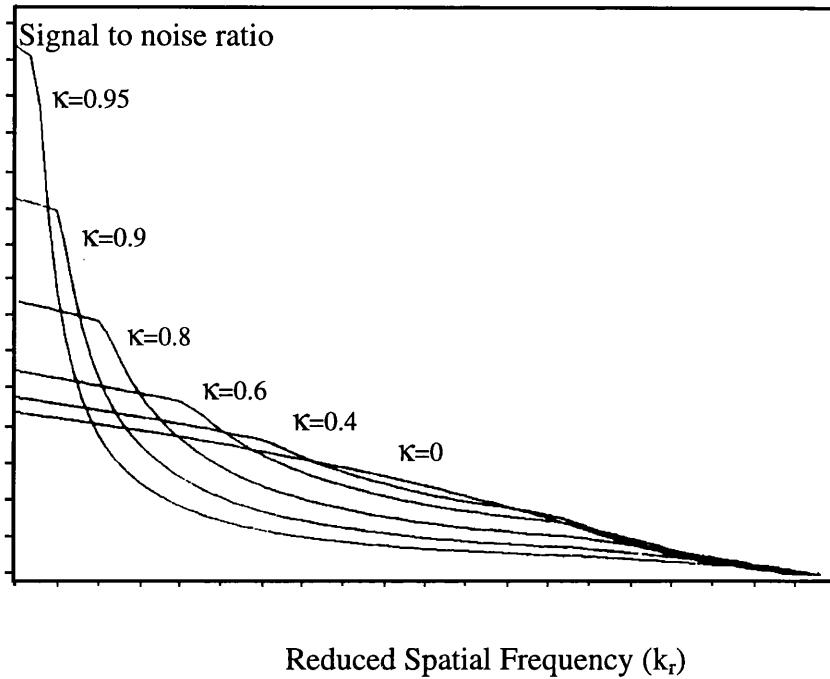


Fig 2.9: Variation of signal to noise ratio with reduced spatial frequency for detectors with different values of κ . (Chapman et al, 1990)

2.6 KERR MICROSCOPY

The Kerr effect was developed by Kerr (1876) and, as mentioned in Section 2.1, it utilises the effect whereby the plane of polarisation of light is rotated by reflection off a magnetic material. A microscope, which utilises the Kerr effect, is used to collect results in Chapter 8, where domain structures in FeNbSiN fluxguides are studied. The final sections of this chapter therefore deal with the implementation of Kerr microscopy with respect to these studies.

2.6.1 The Magneto Optical Rotation

The rotation of the plane of polarisation of light can be explained in terms of the Lorentz force acting on light-excited electrons. Fig 2.10 shows, schematically, linearly polarised light incident on a magnetic material with a magnetisation perpendicular to the horizontal plane of the material.

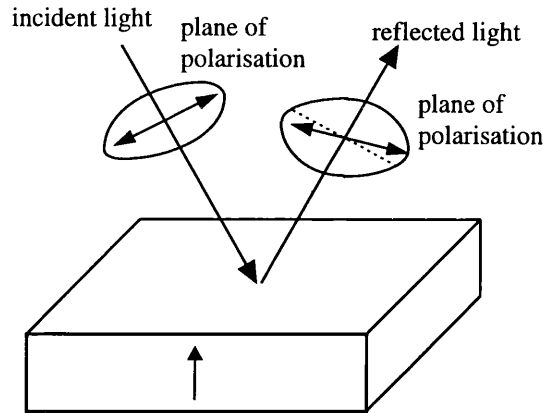


Fig 2.10: Schematic illustrating the Polar Kerr effect

In the case of the Kerr effect the incident light induces electrons to oscillate parallel to its plane of polarisation, the plane of the electric field of the light. The Lorentz force, which arises from the magnetic moments within the material, introduces a secondary component of vibrational motion, for reflected light, which is perpendicular to both the original motion and the direction of magnetisation. This motion is proportional to both the magnitude and direction of magnetisation and can therefore be used to image magnetic contrast. In order to predict the observed contrast it is necessary to consider the dielectric permittivity tensor. This has been done by several authors (for example Voight, 1920) and will not be considered within this thesis. We will however consider the results from a Fortran program (Mansuripur, 1990) which uses the dielectric permittivity tensor in order to predict the contrast from FeNbSiN. The observed contrast is dependent on both the Kerr rotation of the material and its reflectivity. Thus samples are often coated with dielectric interference materials, such as ZnS, in order to enhance Kerr contrast (Kranz and Hubert, 1963).

The previous explanation of the generation of Kerr contrast was for the case where the magnetisation was perpendicular to the horizontal plane of the material. This is referred to as the polar Kerr effect and is strongest for perpendicular incidence. There are however three other Kerr effects which also rotate the plane of polarisation of incident light. These are (a) the transverse Kerr effect, where both the plane of polarisation and the plane of incidence are transverse to the magnetisation, (b) the (parallel) longitudinal Kerr effect, where the polarisation and plane of incidence are both parallel to the

magnetisation and finally, (c) the (orthogonal) longitudinal Kerr effect, where the polarisation is orthogonal but the plane of incidence parallel to the direction of magnetisation.

2.6.2 Implementation of Kerr microscopy

As already previously mentioned, the implementation of Kerr microscopy is directed towards studying domain structures in FeNbSiN fluxguides. Since this material has an in-plane magnetisation it is not possible to utilise the polar Kerr effect as an imaging tool. We therefore only consider the longitudinal and transverse Kerr effects, both of which can be implemented on the optical microscope of Fig 2.11.

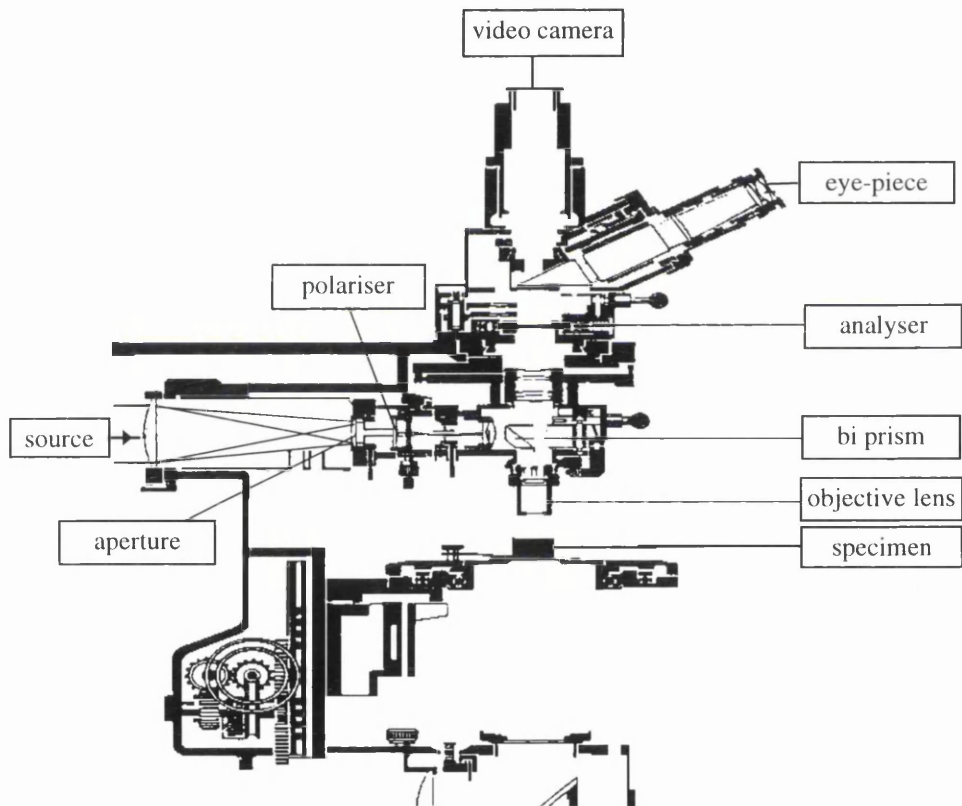


Fig 2.11: Schematic cross-section of the optical microscope used for Kerr microscopy in Chapter 8

The light source for this microscope is an incandescent lamp which can be filtered in order to attain the optimum Kerr rotation for the particular material under study. At low

magnifications a light defuser is often incorporated with the filter in order to give a uniform illumination of the sample. After filtering, the light passes through a polariser and is then incident on the specimen at an angle of $\approx 60^\circ$. After reflection from the sample the light passes through an analyser which is a few degrees off the crossed position with the polariser. A prism can now be inserted to allow the image to be viewed via the eyepieces of the microscope. Alternatively the image can be collected by a video camera which sits on top of the microscope. The signal from this is processed by a Hewlett Packard work station which can perform image averaging over many frames, subtraction of images, contrast expansion, linear and non-linear filtering and various other noise filtering algorithms. There are a pair of orthogonal electromagnets situated under the sample. These allow both magnetising experiments and saturation of the sample. By subtraction of the image of the saturated state from one of interest it is possible to remove both topography and non-uniform light illumination. An example of such an image is given in Fig 2.12. The bright and dark areas correspond to regions with a direction of magnetisation parallel (or antiparallel) to the sensitivity direction as indicated on the figure.

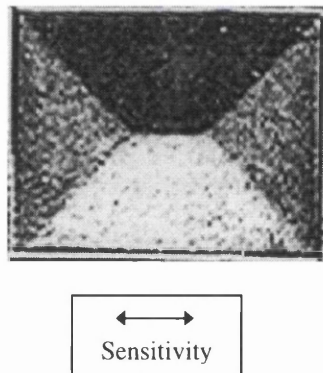
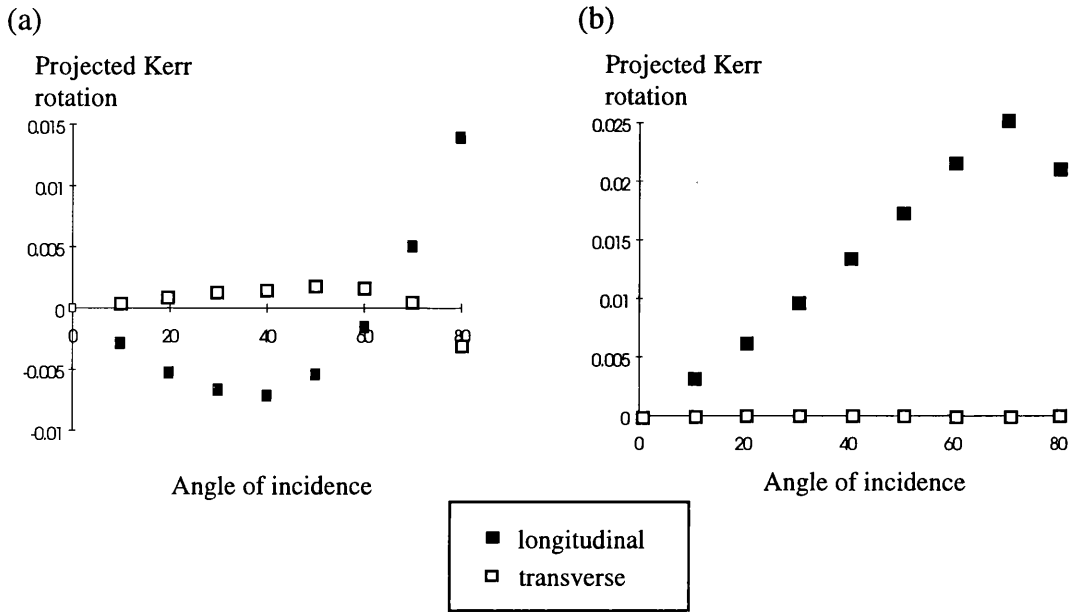


Fig 2.12: Typical Kerr image formed by subtraction of saturated state.

2.6.3 Choosing Which Kerr Effect To Use

In order to optimise the Kerr microscope for studying FeNbSiN it is necessary to consider which type of Kerr effect to use (transverse or longitudinal) and also the plane of polarisation of incident light. If the polariser is set to be parallel to the plane of incidence then $p=1, s=0$ light is incident on the sample while if it is orthogonal $p=0, s=1$ is the polarisation (Jenkins and White, 1981). Whether to use $p=1, s=0$ or $p=0, s=1$ can be

assessed by using a program written by Mansuripur (1990). Several material parameters for FeNbSiN were inserted into this program and the output file gave the Kerr rotation and the reflection coefficient for both types of illumination as a function of incident angle. Figs 2.13(a-b) show the projected Kerr rotation on the analyser which is plotted, versus incident angle, for FeNbSiN.



Figs 2.13: Projected Kerr rotations of FeNbSiN for varying angle of incidence (a) for $p=1, s=0$, (b) for $p=0, s=1$ light

The incident angle is set at $\approx 60^\circ$ by the numerical aperture of the microscope. Therefore considering the graphs, for a 60° incidence, it is seen that $p=1, s=0$ gives a small rotation for both the longitudinal and transverse Kerr effects. For light with $p=0, s=1$, however, the longitudinal component is large while the transverse is zero. Since the maximum Kerr signal is sought and it is undesirable to have both longitudinal and transverse Kerr effects present it was decided to use the longitudinal Kerr effect with $p=0, s=1$ for studying FeNbSiN.

Although the maximum Kerr rotation is predicted to be only a few tenths of a degree away from the crossed analyser / polariser situation the maximum Kerr signal is actually observed at a difference of a few degrees. This is because when the analyser and polariser are almost crossed the signal is very weak and is swamped by shot noise from the processing electronics.

Several image processing techniques were used in order to maximise the contrast possible from the raw Kerr image. These will be discussed in detail in Chapter 8.

2.7 SUMMARY

The magnetic imaging techniques which have been reviewed in this chapter will now be implemented in the experimental chapters of this thesis. These enable studies to be made of spin-valves materials, in the case of Lorentz microscopy, and fluxguides, in the case of Kerr microscopy.

CHAPTER 3: CHARACTERISTICS OF SINGLE PERMALLOY LAYERS IN THE NANOMETRE RANGE

3.1 INTRODUCTION

In this chapter we investigate the magnetic properties of thin permalloy ($\text{Ni}_{80}\text{Fe}_{20}$) films in the thickness range of 5 to 20 nm. The films were prepared by UHV magnetron sputtering and were deposited on specially prepared substrates which facilitated electron microscopy. Using both the Fresnel and DPC imaging modes, the generation and growth of domains, together with the development of magnetisation ripple, have been studied as a function of layer thickness, field strength and direction. The principal motivation for this study is as a prelude to the spin-valve multilayer, which often contains thin ($\approx 8\text{nm}$ thickness) layers of permalloy, and is studied in Chapters 4-7.

3.2 ALLOYS OF NICKEL AND IRON

Permalloy is only one composition in the Ni-Fe binary system of alloys which combine a relatively high saturation magnetisation (0.9-1.05 T) with a high permeability. This has led to the system being investigated by a number of authors, for a variety of applications, and consequently there is a large pool of literature about the subject. The stoichiometry of any alloy is often of vital importance when tailoring properties to particular needs. This is particularly true for the magnetic properties of the Ni-Fe alloys. When considering a ferromagnetic material for applications, such as a magnetic sensor, the magnetostriction constant and the inherent magnetocrystalline anisotropy are two important parameters. The former is significant in that any structuring of the material inevitably induces stress. This stress often varies between structures, even of the same design, so that magnetic properties are unpredictable. Fig 3.1(a) shows the dependence of the magnetostriction constant, λ , on the stoichiometry of films prepared by Bozorth and Walker (1953). It can be seen, from this plot, that the magnetostriction constant, in the $\langle 111 \rangle$ direction, is approximately equal to zero for a composition of $\approx 80\%$ nickel.

Magnetocrystalline anisotropy is also important as this causes local easy axis fluctuations in a polycrystalline material, and thus the directionality of any induced easy axis

deteriorates. Magnetocrystalline anisotropy can be thought of as a dispersion in the induced anisotropy direction and Fig 3.1(b), shows the dependence of this on the percentage nickel in the alloy for films prepared by Smith (1961). It is noted that a minimum occurs at $\approx 82\%$ Ni and it is because of this together with the small λ that the composition of $\approx 80:20$ (permalloy) is very attractive for many applications.

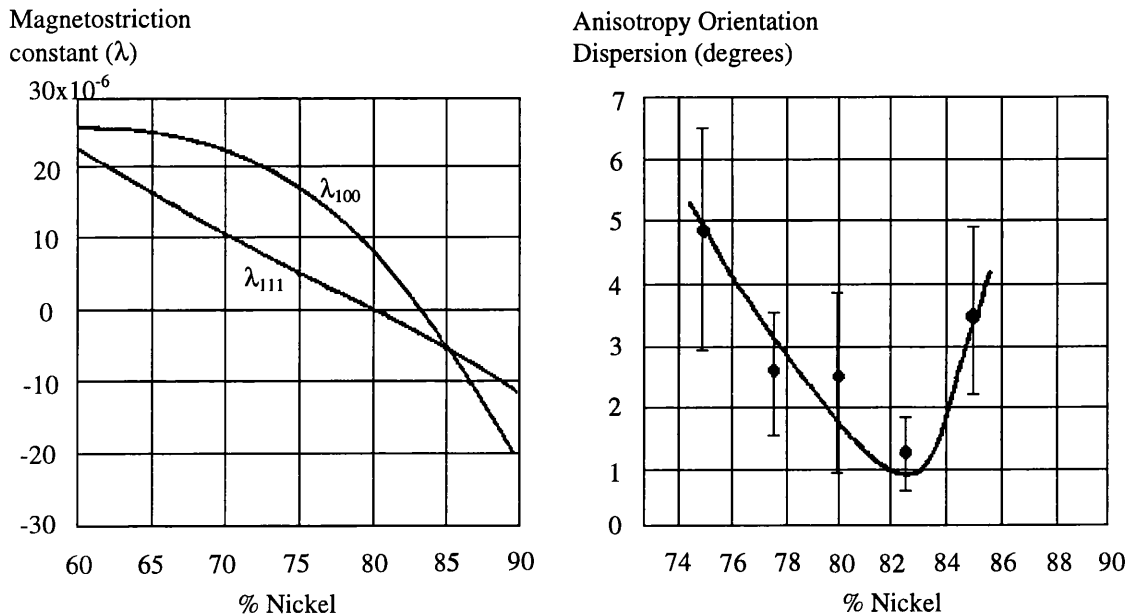


Fig 3.1: The dependence on Ni concentration of (a) magnetostriction constant (Bozorth and Walker, 1953), (b) anisotropy orientation dispersion (Smith, 1961).

3.3 SPECIMEN PREPARATION

Thin films of permalloy can be prepared by a variety of techniques. Initial experiments, by other authors, simply involved vacuum evaporation of the alloy onto a substrate and a review of the properties of such films can be found in Prutton (1964). Another possible deposition technique, which was also used in many initial experiments, is electrodeposition and involves using the substrate as an electrode, immersed in a bath of Ni and Fe solutions (Wolf, 1962). Other established techniques, which are also reviewed by Prutton (1964), include thermal decomposition and chemical reduction. The relatively new deposition technique of molecular beam epitaxy (MBE) offers the possibility to grow very ordered films, with a very high degree of flatness and a general review of this technique is given by Farrow (1990). Finally there is magnetron sputter deposition which is the technique used to prepare all the films studied in this thesis.

Magnetron sputtering involves the acceleration of ions, usually Ar^+ , through a potential gradient and the bombardment of the ions into the “target” or cathode. This causes atoms to be ejected from the target which are then attracted to the substrate, which is often grounded. The film therefore grows through deposition at the substrate. The permalloy films described in the following sections were grown by J.C.S. Kools (Philips Research) and an Ar-pressure of 5mTorr was used during growth, the background pressure being 8×10^{-8} Torr. The growth rate was $\approx 0.2\text{nm/s}$ and all films were deposited in a field of 120 Oe, which induced anisotropy by preferential pair ordering (Chikazumi, 1964). The films were sputtered onto a 3nm seed layer of Ta. It has been shown that such a seed layer enhances $\langle 111 \rangle$ growth and therefore minimises the effect of magnetocrystalline anisotropy and magnetostriction for permalloy films, (Nakatani et al, 1994 and Jérôme et al, 1994).

The films which are studied in this thesis, were sputtered onto supported Si_3N_4 substrates which are suitable for transmission electron microscopy. Both planar and cross-sectional views of the substrate are shown, schematically, in Figs 3.2(a) and (b) respectively.

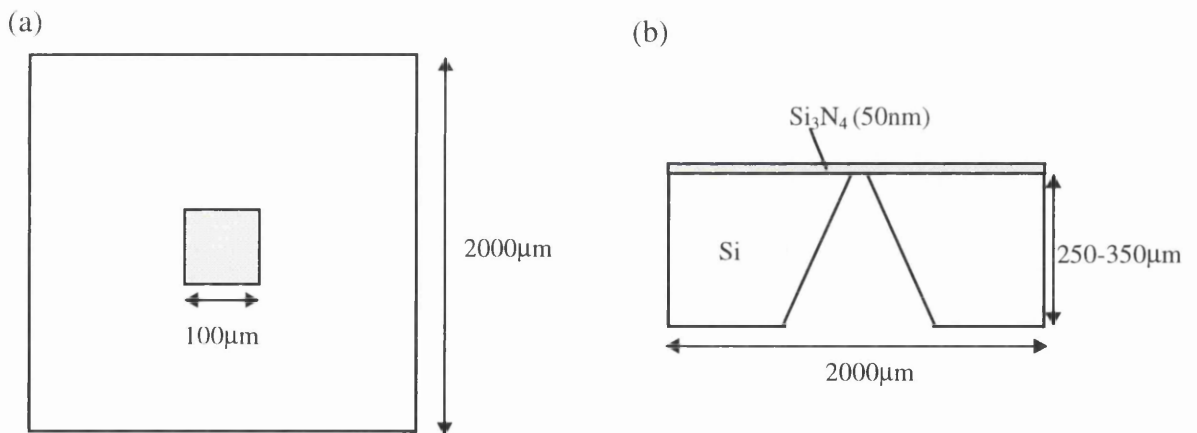


Fig 3.2: Schematic illustration of (a) planar view of substrate, (b) cross-section through substrate

These substrates are made by first depositing a Si_3N_4 layer (in the thickness range of 10-100nm) on a Si substrate. The Si is then preferentially etched in the $\langle 111 \rangle$ direction at sites, determined by a lithographically defined mask on the bottom Si surface. The separation of these sites is typically $2000\mu\text{m}$ and this results in a matrix of pyramidal holes separated by this distance. The holes are, however, still covered, on one side, by the continuous layer of flat Si_3N_4 and a film can now be deposited on top of this. The wafer is

then split up into single windows which are immediately suitable for investigation in the electron microscope. For a more in depth description of the processes involved see Jacobs and Verhoven (1986). The local surface roughness of the Si_3N_4 was measured, by H. Mullen at Philips Research, using a Topometrix Atomic Force Microscope (AFM). The average height variation, which is a measure of the roughness of the membrane, was found to be 0.6 nm. Although this is somewhat rougher than bulk Si (0.25-0.35nm), studies carried out by J.C.S. Kools established that, at least in the case of spin-valves, this did not significantly perturb the magnetic properties of the films.

Permalloy films of 5, 6, 8, 10, 13 and 20nm thickness were deposited on such substrates for the TEM experiments described. Detailed magnetic observations were made on the 5, 10 and 20nm films with the others only being used to determine the relationship between grain size and layer thickness.

3.4 MAGNETISATION RIPPLE AS A FUNCTION OF FILM THICKNESS

Although the composition of permalloy is such that we are near the minimum in the magnetocrystalline anisotropy it still plays a small role in determining the local easy axis direction. This results in local fluctuations in the magnetisation vector which leads to magnetisation ripple. Various authors (Fuller and Hale, 1960 and Hoffmann, 1968) have considered the magnetostatic energy of ripple which arises from fluctuations which are either transverse, Fig 3.3(a), or longitudinal, Fig 3.3(b), with respect to the average direction of the magnetisation.



Fig 3.3: Illustration of (a) transverse ripple, (b) longitudinal ripple

The conclusion of these calculations was that the magnetostatic energy which results from transverse ripple is greater than that from longitudinal. This was in agreement with Fresnel images from the electron microscope (Hale et al, 1959) which showed ripple contrast

orthogonal to the average direction of magnetisation, indicative of longitudinal ripple. An example of magnetisation ripple is shown in Fig 3.4, which is a Fresnel image of a 10nm permalloy film. Although the previous discussions allow us to deduce the direction of magnetisation within the film, Fresnel imaging does not allow a true quantitative assessment of the ripple to be made.

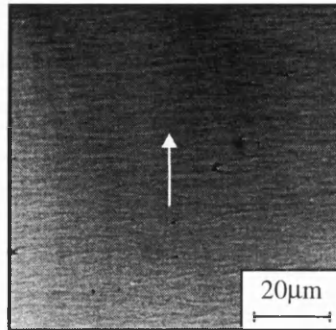


Fig 3.4: *Fresnel image of ripple with the deduced direction of magnetisation superimposed*

The DPC mode of electron microscopy allows a more quantitative study of the ripple in permalloy films to be carried out. Figs 3.5(a-c) show DPC images, for 5, 10 and 20nm films respectively, all of which have been deposited on a Ta seed layer. Fig 3.5(d) shows a 10nm film, but without the seed layer. Ripple was observed in all films studied but was particularly pronounced in the thinner films. However, the contrast was stronger for thicker films, as the Lorentz deflection angle was larger.

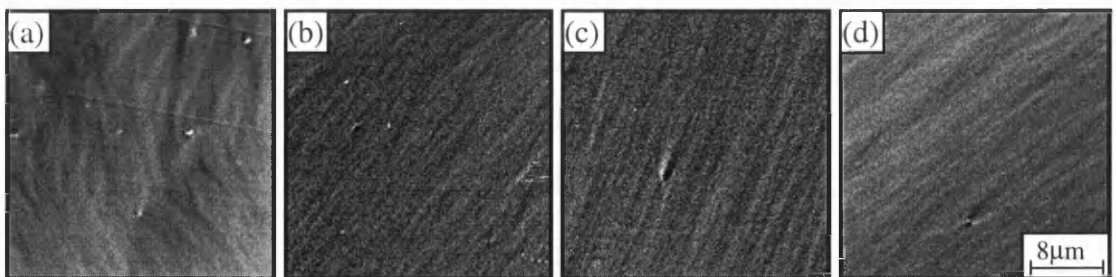


Fig 3.5: *DPC images of ripple in permalloy films, (a) 5nm (with seed), (b) 10nm (with seed), (c) 20nm (with seed), (d) 10nm (without seed)*

The spatial frequency distribution of the ripple can be quantified, at least to an extent, by taking the Fast Fourier Transform (FFT) of the ripple images. An example of the FFT of ripple is shown in Fig 3.6(a), which is for the ripple in a 20nm thick film (Fig 3.5(c)). By considering the distribution of Fig 3.6(a) it is possible to define the half angle, variation θ

(k_y) , of the ripple spectrum, Fig 3.6(b). $\theta(k_y)$ is the angle between the y-axis and a line drawn between zero frequency and the point, $P(k_x, k_y)$ where the intensity falls to 75% of the value $P(0, k_y)$.

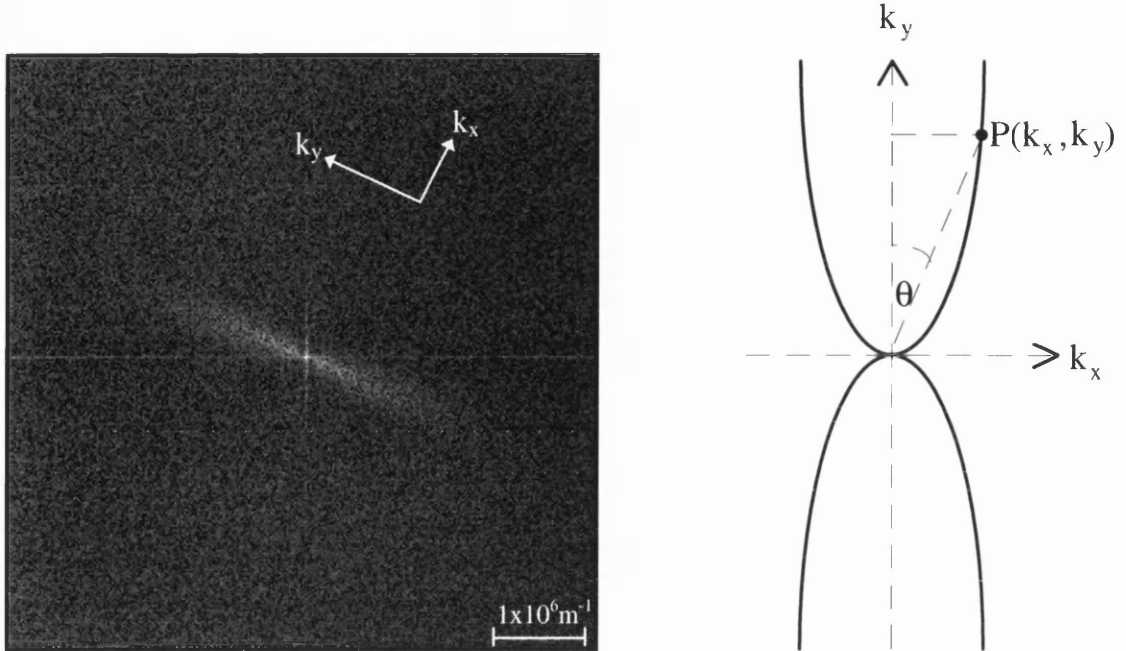


Fig 3.6: (a) Fourier transform of DPC image for a 20nm thick film, (b) Schematic definition of the ripple half angle, $\theta(k_y)$.

It is noted that $\theta(k_y)$ is only a measure of the component of magnetisation transverse to the average direction and does not give any information about that which is parallel to it. $\theta(k_y)$ is a strong function of spatial frequency and Fig 3.7 shows this dependence for films of various thickness. In order to achieve this plot it was necessary to take line scans, along the k_x direction, through the FFT at different distances from the central peak. The distributions were then passed through a low pass filter which removed the high frequency components and thus allowed the width at different values of k_y to be estimated. From these widths θ was determined as a function of k_y .

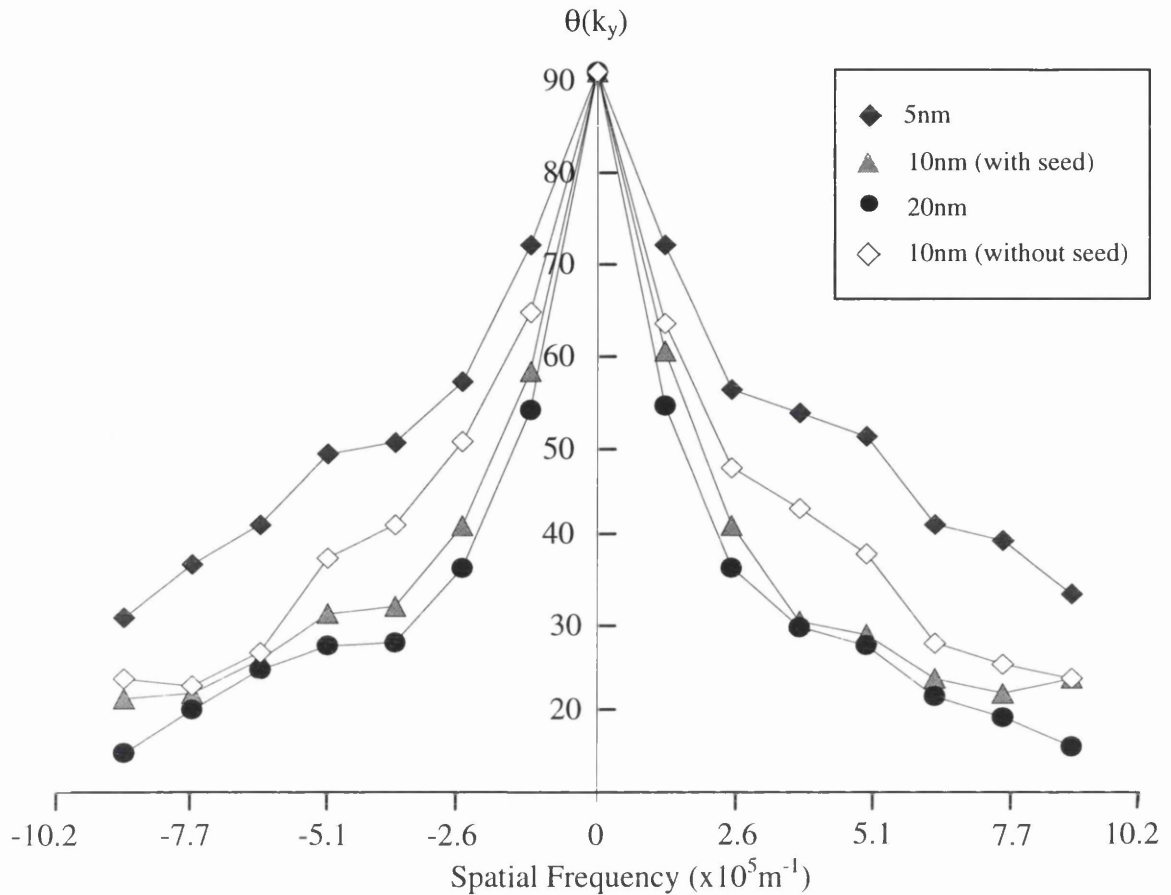


Fig 3.7: Graph of half angle vs spatial frequency for various film thicknesses

It can be seen that the thinner films generally have a larger $\theta(k_y)$ for all frequencies of ripple. When considering the distribution for a 10nm film without the Ta seed layer it is observed that $\theta(k_y)$ is generally greater, for all frequencies, than the equivalent film deposited on the seed. This was not obvious from direct observation of the ripple images themselves but is expected due to the fact that, when compared with other crystallographic directions, the $\langle 111 \rangle$ orientation, in permalloy, has a near negligible magnetocrystalline anisotropy (see Fig 3.1(b)). Thus in the case of $\langle 111 \rangle$ textured films there is less grain-to-grain fluctuations in the anisotropy direction and consequently less magnetisation ripple.

The amount of easy axis dispersion can also have an effect on the macroscopic properties of these films. It has recently been shown (Kools et al, 1995) that the increase in magnetisation ripple associated with films under 20nm thickness results in a rounding of the M-H loops for fields along the hard axis.

3.5 IN-SITU MAGNETISING EXPERIMENTS

The reversal mechanisms of single layer permalloy films have been studied by a variety of authors (for example Conger and Essig, 1957) and in this section we repeat these experiments as a prelude to investigating the reversal mechanisms of complete spin-valve structures.

It is possible to apply fields, in the plane of the sample, in both the JEOL 2000FX and the Philips CM20 electron microscopes, while imaging the specimen. In the JEOL 2000 this may be achieved by using a specially designed magnetising stage which has small coils situated within the specimen rod, Fig 3.8 (Hefferman et al, 1991). The field is generated by passing a current through the coils and has a maximum value of ≈ 100 Oe at the specimen. There are also facilities to rotate the specimen, within the rod, so as to align it with respect to the applied field. The field introduces a DC tilt of the electron beam at the specimen which can be corrected for by using the electrical beam tilts within the microscope.

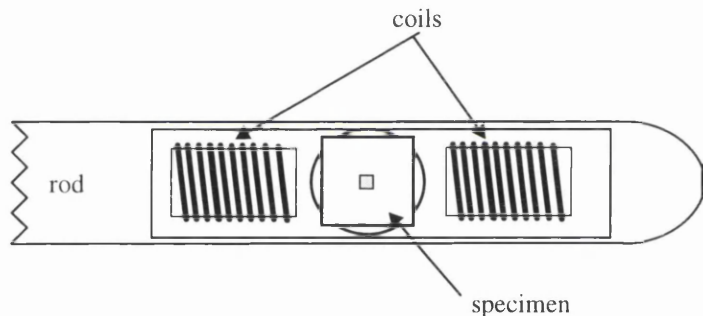


Fig 3.8: Schematic of magnetising stage for JEOL 2000

In the CM20 it is also possible to use a specially designed magnetising stage where the coils are mounted within the microscope, close to the specimen, rather than within the rod (Nicholson and Chapman, 1995). This stage is capable of producing ≈ 100 -200 Oe at the specimen. As already mentioned in Chapter 2 the CM20 is equipped with an objective lens as well as Lorentz lenses and in the standard magnetic imaging modes the objective is mechanically switched off. It is however possible to weakly excite the lens and by tilting the sample bring a component, from the lens field, into the plane of the sample. This avoids shifting the electron beam, as the applied field is parallel to it, and also allows the application of much larger fields (maximum vertical = 6800 Oe) than that available with the magnetising stage (Chapman et al, 1995 and McVitie et al, 1995).

3.5.1 Easy Axis Reversal Mechanisms

The reversal of magnetisation in a permalloy film, when the applied field is perfectly aligned with the easy axis, is one of simple wall motion. This is shown in Fig 3.9(a-c) for a 10nm film and is due to the fact that the applied field exerts no torque on the magnetisation which is parallel to it. Thus up to the field required to nucleate a domain wall the only force is on the components of magnetisation which are not aligned with the applied field. These are the ripple components of magnetisation and so an increase in dispersion is often observed as the applied field approaches that required for wall nucleation. When a wall is nucleated then the magnetic moments within the wall, which are at an angle to the applied field, experience a torque which tends to align them with the field direction. Due to exchange coupling the reorientation of these moments also results in the rotation of moments adjacent to the wall and in this way the wall is propagated through the sample, flipping the magnetic moments sequentially as it goes.

In the absence of pinning points the wall tends to be approximately parallel to the easy axis, as in Fig 3.9(b), and its motion can be described in terms of the domain wall inertia, damping, and stiffness of the material (for example Kittel and Galt, 1956 and Smith, 1958)

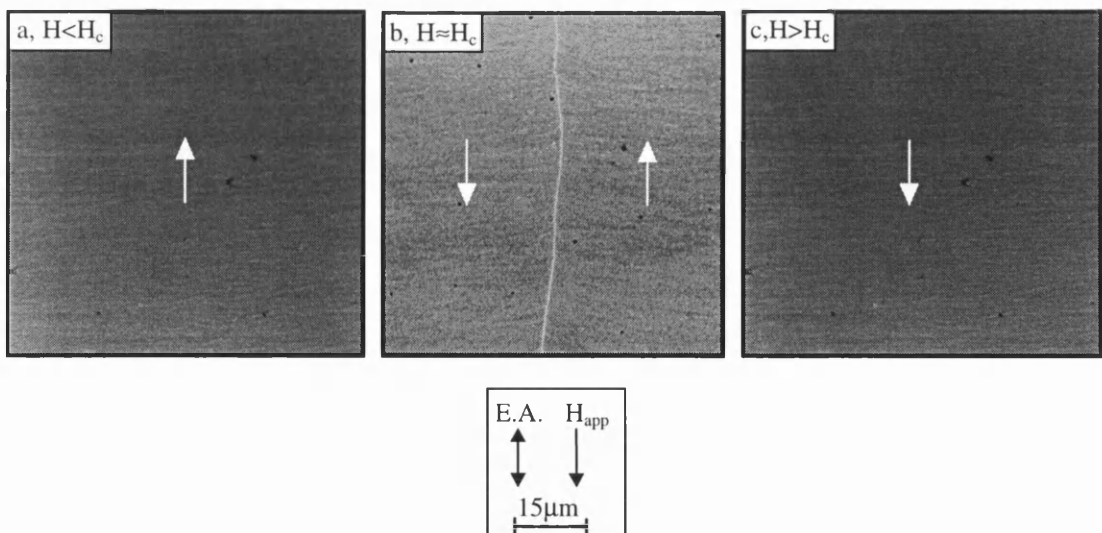


Fig 3.9: Reversal of 10nm film for a field applied parallel to the easy axis.

In many films imperfections tend to retard domain wall motion and it is often necessary to increase the applied field in order to make the wall move through the sample.

As already described the reversal of 10nm films, with or without a seed layer tended to be dominated by one 180° wall, most likely of Néel type, sweeping across the film. The orientation of the wall tended to be parallel to the easy axis though it was possible, by misaligning the applied field with the easy axis by a few degrees, to cause the switching wall to vary in direction. The large dispersion in the 5nm film made it difficult to define an average easy axis with which to align the applied field. The observed reversal was, however, broadly similar to that of the 10nm films, though domain wall motion was not so obvious and on occasion the increase in dispersion led to areas of magnetisation rotating towards the field direction. In the case of the 20nm film the switching wall was predominantly parallel to the easy axis, Fig 3.10, but unlike those of the thinner films the wall had cross-tie characteristics. These are indicated on Fig 3.10 where they manifest themselves as either vortices or Bloch lines. It is noted that the density of these features is substantially lower than that of a typical cross-tie wall and this may be assigned to the fact that for this thickness of film the majority of wall is still Néel type. (see Fig 1.3)

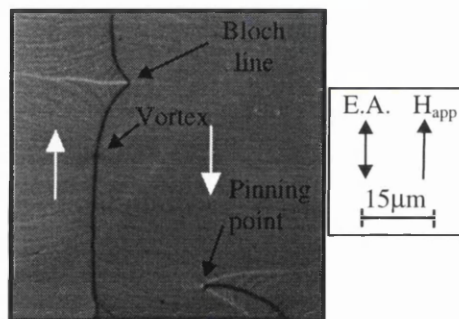


Fig 3.10: Switching wall for easy axis reversal in a 20nm thick film

Also noted on Fig 3.10 is a pinning point. In this particular reversal an inclusion, within the film is acting as a pinning point and is holding a domain wall from a previous switch. Frequent pinning of domain walls by inclusions was observed for all film thicknesses and hamper the reversal by lowering the average domain wall velocity. Pinning results in a perturbation of the magnetisation around the pinning site. Figs 3.11(a)-(c) show DPC images of a wall / inclusion interaction within a 10nm thick film. In Fig 3.11(a) the domain wall is predominately straight and only just incident on the inclusion. Upon increasing the field, Fig 3.11(b), there is substantial wall bowing around the pinning site. This perturbation becomes more pronounced with increasing fields, Fig 3.11(c), before finally being overcome.

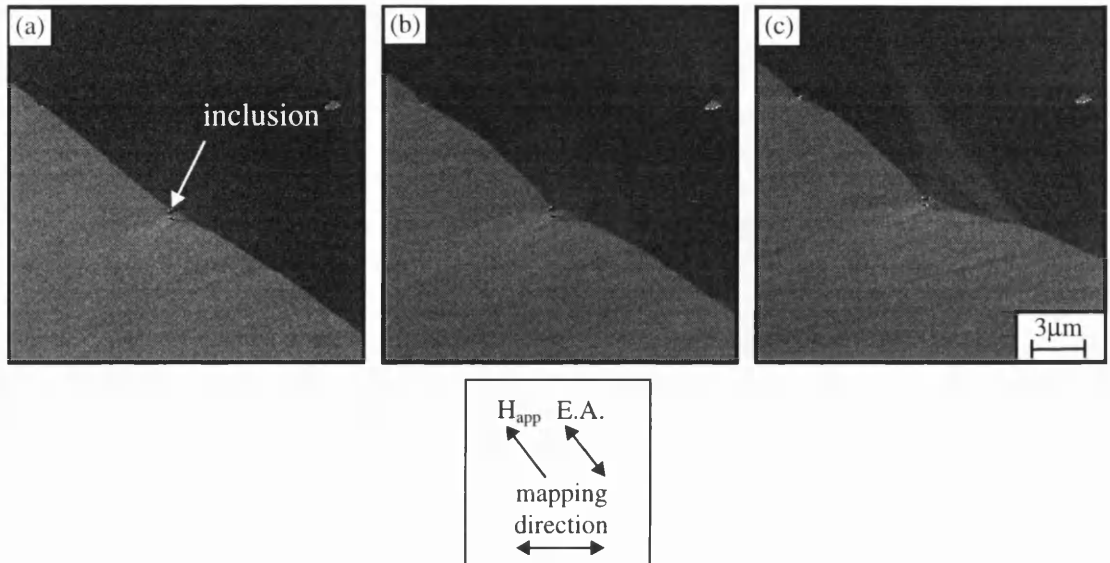


Fig 3.11: DPC images showing an inclusion / wall interaction

In some cases the inclusion exerts a sufficiently strong hold on the domain wall that it is not possible for the wall to break free. This results in the generation of a 360° wall by a process which is illustrated, schematically, in Fig 3.12. Initially an approximately straight 180° domain wall is moving parallel to the field and the easy axis, Fig 3.12(a). This wall becomes pinned on the inclusion, Fig 3.12(b), and the wall bows at either side of the pinning point. Upon increasing the field the wall bends further around the inclusion to make a V and at the same time a secondary, lower angle wall, is introduced behind the pinning point, Fig 3.12(c). This lowers the magnetostatic energy associated with the wall at the inclusion.

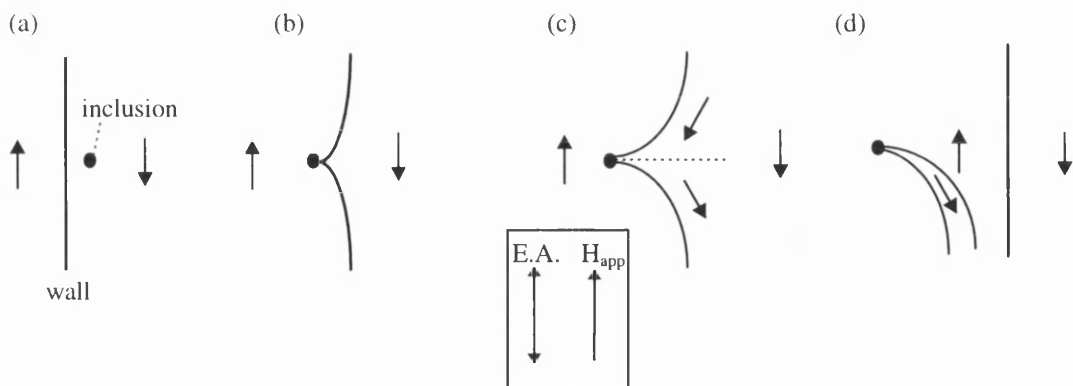


Fig 3.12: Illustration of how a 360° wall can be generated by an inclusion.

Further increasing the applied field results in a section of the wall, on one side of the inclusion, becoming detached and thus moving freely across the film, switching the magnetisation. Part of the original wall and the secondary wall now come close together

and form a 360° structure. The DPC images of Fig 3.13 illustrate the introduction of the secondary wall, immediately behind the pinning point, as depicted in the schematic of Fig 3.12(c). The film thickness here is 10nm.

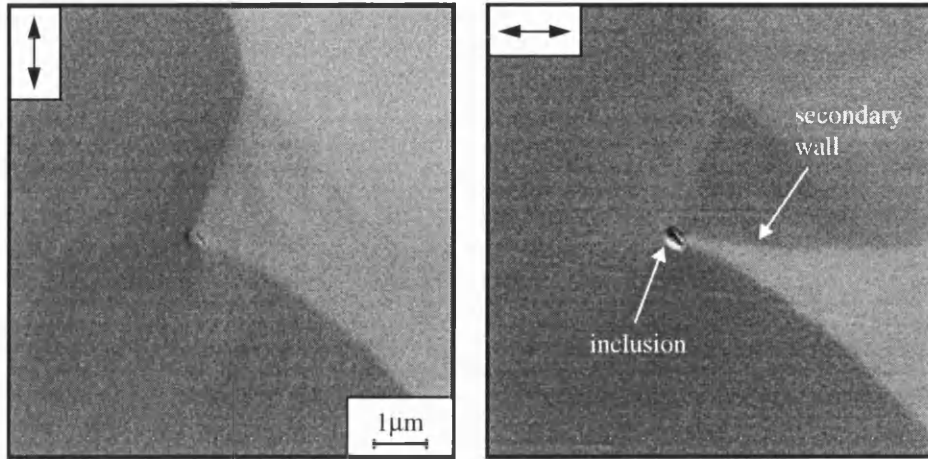


Fig 3.13 : Orthogonal DPC images showing the presence of a low angle secondary wall immediately behind the inclusion.

It was observed that 360° wall type structures are relatively common in the permalloy films but it is stressed that they are always associated with a pinning point. Since upon reversal of the field, domain structures may develop from such walls their existence serves to lower the field required to reverse the magnetisation. Consequently, due to the unpredictability of the formation of 360° walls the range of field values required for reversal is also increased. Possible sources of the inclusions will be discussed in Section 3.6.

3.5.2 Hard Axis Reversal Mechanism

The hard axis is simply defined as the direction which is orthogonal to the easy axis. If the magnetisation within a film is initially single domain and along the easy axis then a field applied along the hard axis results in the coherent rotation of magnetisation, towards the direction of the applied field. Figs 3.14 (a-f) show the response of a 20nm film to fields applied along the hard axis. The effective field which arises from the induced anisotropy, H_K , in a permalloy film of this thickness, is typically $\approx 2-3$ Oe. When the applied field was

approximately equal to H_K the magnetisation was parallel to the hard axis, Fig 3.14(a). (The number quoted with each figure is the applied field in Oersted.)

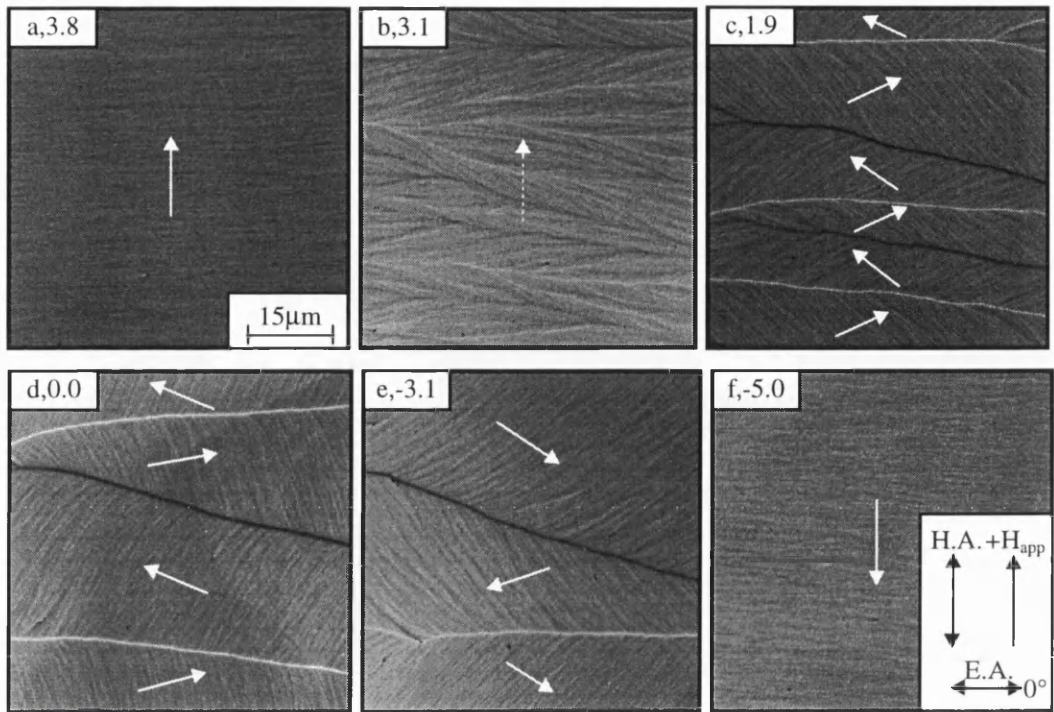


Fig 3.14(a-f): Hard Axis reversal for a 20nm film

Since the easy axis is uniaxial magnetisation which is aligned along the hard axis feels no net torque. Thus on decreasing the applied field the magnetisation is presented with a choice, which Prutton (1964) described as a “schizophrenic” condition. The magnetisation can either return to its original direction or can rotate to lie at 180° to this. The deciding factor on which rotation is chosen is the contribution to the easy axis direction from the magnetocrystalline anisotropy. As already discussed this varies from crystallite to crystallite and causes local fluctuations in the easy axis direction. In some areas of the film this results in making the rotation to 0° favourable while in others the rotation to 180° is the preferred option. We therefore observe the creation of what is often termed the “fish bone” pattern as different areas rotate to the two anti-parallel directions, Fig 3.14(b). In the fish bone pattern the walls between different areas are initially of a low angle but as the field is reduced to zero this increases, Fig 3.14(c-d). It is also noted that as the field is decreased the wall density becomes less. Upon applying a field in the opposite direction (-ve H_{app} as indicated on the figure.) there is substantial domain wall motion as the magnetisation aligns with the applied field, Figs 3.14(e-f).

If the applied field were exactly aligned with the hard axis then the reversal process would not have involved domain wall motion. Instead there would initially be nucleation of low angle walls in a “fish bone pattern” and then, as the applied field was reduced to zero, these would develop into 180° walls. Upon applying a field in the opposite direction the average wall angle would then decrease as the magnetisation rotated towards the applied field. The dominant reversal process would be the coherent rotation of magnetisation within each domain. In order to observe this, however, the applied field must be aligned with the hard axis to within $\approx 0.1^\circ$. This was not possible in the electron microscope where at best a 0.5° alignment can be achieved. The small stray field from the objective lens also makes it very difficult to observe the expected hard axis reversal of films which typically have a coercivity of a few Oe. Films of all thicknesses had very similar hard axis reversal mechanisms and due to the way in which the walls were created there were no walls with cross-tie characteristics.

3.6 INCLUSIONS WHICH PERTURB THE MAGNETIC CHARACTERISTICS

In Section 3.5.1 the perturbation by inclusions of the easy axis reversal mechanism was discussed. In this section we now turn our attention to the chemical composition of the inclusions and discuss possible sources of the contamination. A dark field image of a typical inclusion responsible for the pinning of domain walls is shown in Fig 3.15 and has a typical dimension of around $0.3\mu\text{m}$.

The chemical make-up of such defects in the films was initially investigated using Energy Dispersive X-ray analysis but since some “light elements” were present an accurate estimate of chemical composition could not be obtained (Nicholson, 1994). This was not the case, however, for parallel electron energy loss spectroscopy (PEELS), which is sensitive to “light elements”, and was therefore used to probe the chemical make-up of the inclusions (Egerton, 1992). PEELS is performed by analysing the energy distribution of initially monoenergetic electrons, after they have interacted with the specimen. An energy window is set and divided into many channels, of different energy, which are then filled with electron counts from a spectrometer. The energies are characteristic of the type of atom present and from the relative number of counts in each channel it is possible to estimate the composition of the sample at the point where the electron probe is focused.

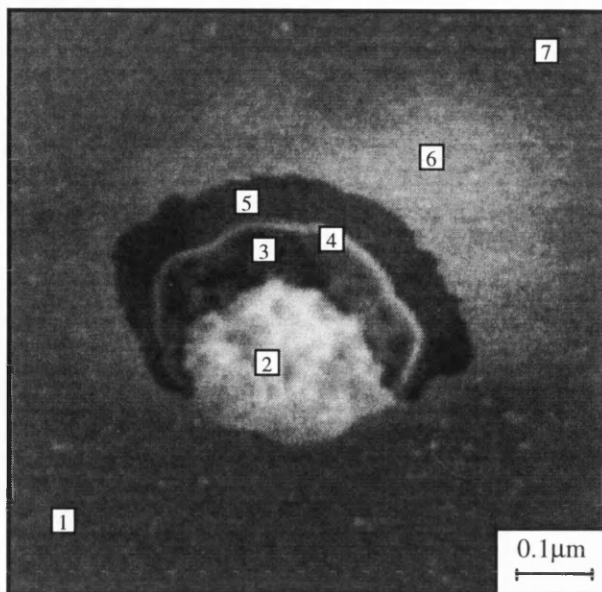


Fig 3.15: A typical inclusion within a 10nm film

The electron probe was focused at the points marked 1 to 7 on Fig 3.15 and spectra collected. Fig 3.16 shows typical spectra collected from points 1, 3 and 6 and as can be seen, there are three main peaks. These arise not only from Fe and Ni, as would be expected, but also from oxygen.

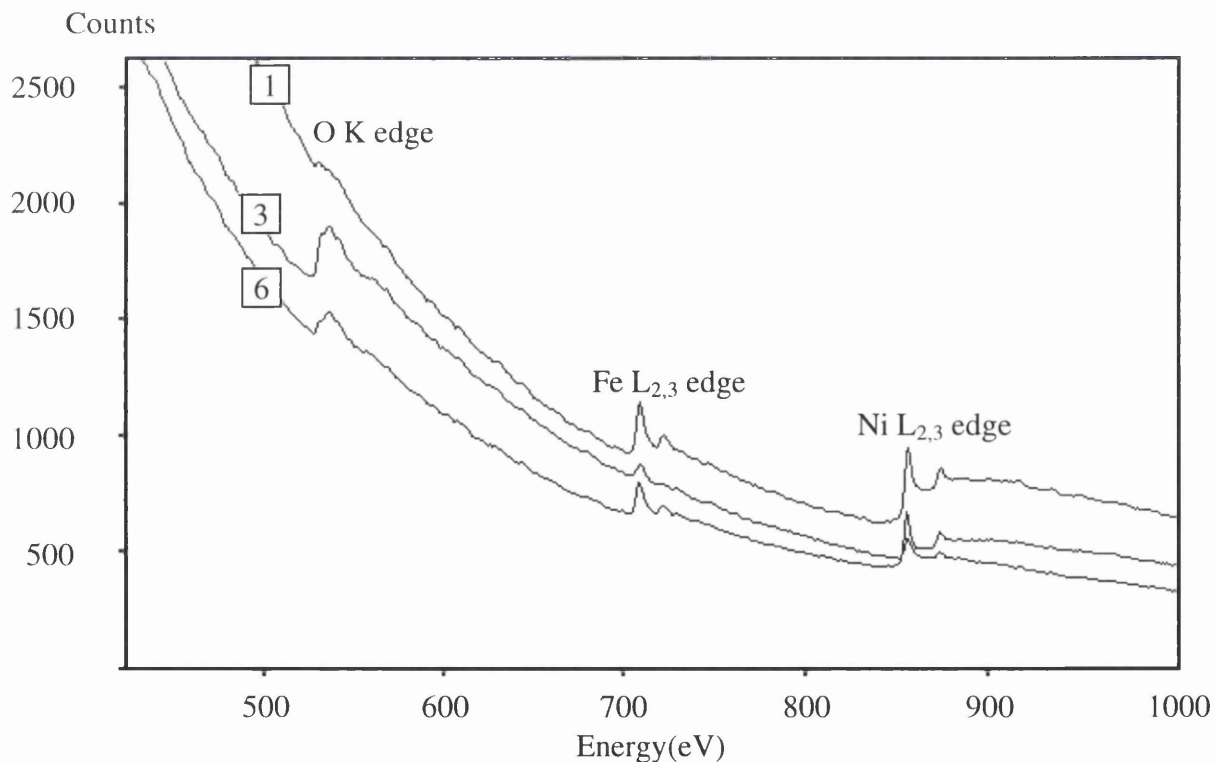


Fig 3.16 : PEELS spectra from areas 1,3 and 6

Fig 3.17, shows a plot of the percentage oxygen at the different sample points, as well as the percentage Ni in the NiFe alloy.

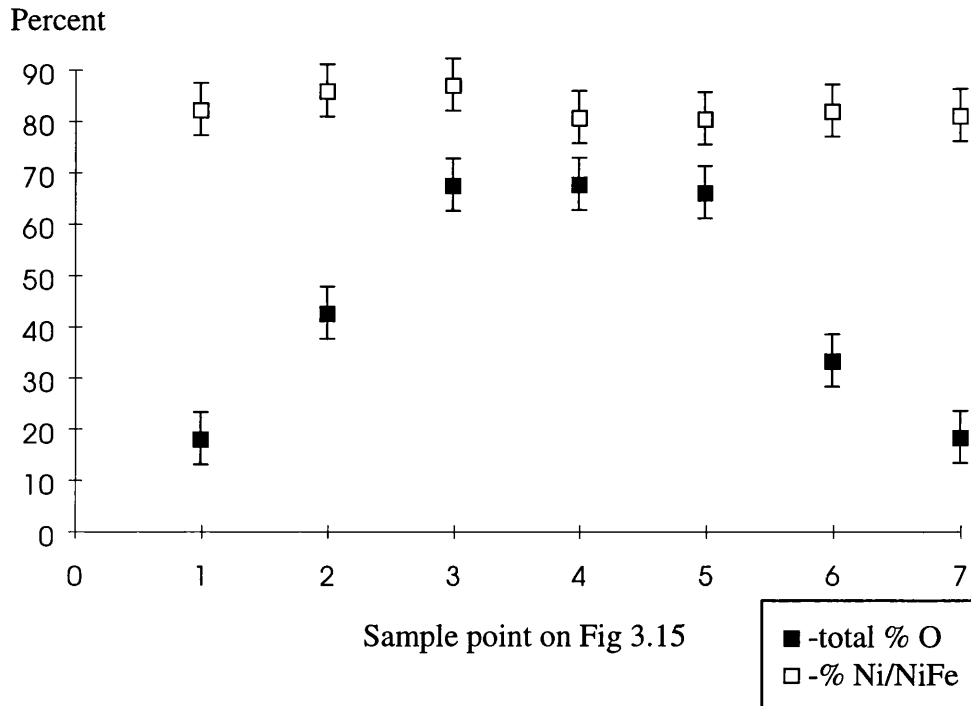


Fig 3.17: The %O and %Ni/NiFe at the sample points indicated on Fig 3.15

From this graph it is noted that there is a sharp increase in oxygen content at the inclusion, while the Ni:Fe ratio remains approximately constant throughout. This was found to be typical for inclusions within these films. A suggested cause (Gillies et al, 1995) of these contaminants was that during previous depositions there had been a build up of material on the shutter between the target and the source. When depositing a new set of films opening and closing the shutter may have resulted in oxidised fragments becoming incorporated within the film. Another possible source could simply be contamination which has resulted from the sputtering apparatus not being in a sufficiently high class of clean room. In retrospect this is the most probable cause as the apparatus has since been moved to a higher class clean room and the average number of inclusions in the films has decreased.

3.7 THE CRYSTALLINE STRUCTURE OF PERMALLOY

In the previous section it was demonstrated that the technique of PEELS was capable of examining the chemical make-up of inclusions which are approximately $0.3\mu\text{m}$ in size. Such an examination of the local microstructure of materials is relatively simple using electron microscopy. In the case, however, when parameters for the entire film are required, such as average grain size, texture, or bulk magnetic properties such as coercive field, M-H loops etc. then the electron microscope is not the most suited of analytical instruments. It is however still possible to investigate some of these parameters and in this section we examine the average grain size, and the texture of the permalloy films.

The bright field images of Fig 3.18(a-c) show the grain structure in 5, 10 and 20nm films respectively, all of which have been deposited on a Ta seed layer. Fig 3.18(d) shows a 10nm film, which has not been deposited on the seed layer.

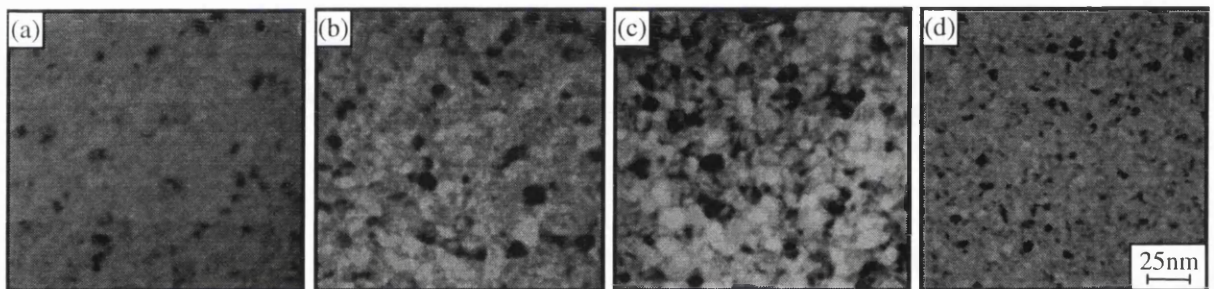


Fig 3.18(a-d): Bright field images showing the grain structure of films with thicknesses; (a) 5nm (with seed), (b) 10nm (with seed), (c) 20nm (with seed), (d) 10nm (without seed)

The bright field images of the crystallite structure allow an estimate of the in-plane grain size to be determined as a function of film thickness. This has been done for films of a variety of thicknesses, 5, 6, 8, 10, 13 and 20nm, and the results are shown in Fig 3.19. It can be seen, from this plot, that the average grain size is approximately equal to the film thickness until around 10nm, where after the in-plane grain size tends to $\approx 10\text{-}11\text{nm}$.

It can also be seen, from Fig 3.19, that the absence of a seed layer resulted in a reduction of the average grain size by a factor of two (≈ 4.5 as opposed to $\approx 9\text{nm}$). These results are in reasonable agreement with what has been found using X-ray diffraction on similarly prepared films (Neerincx et al, 1995).

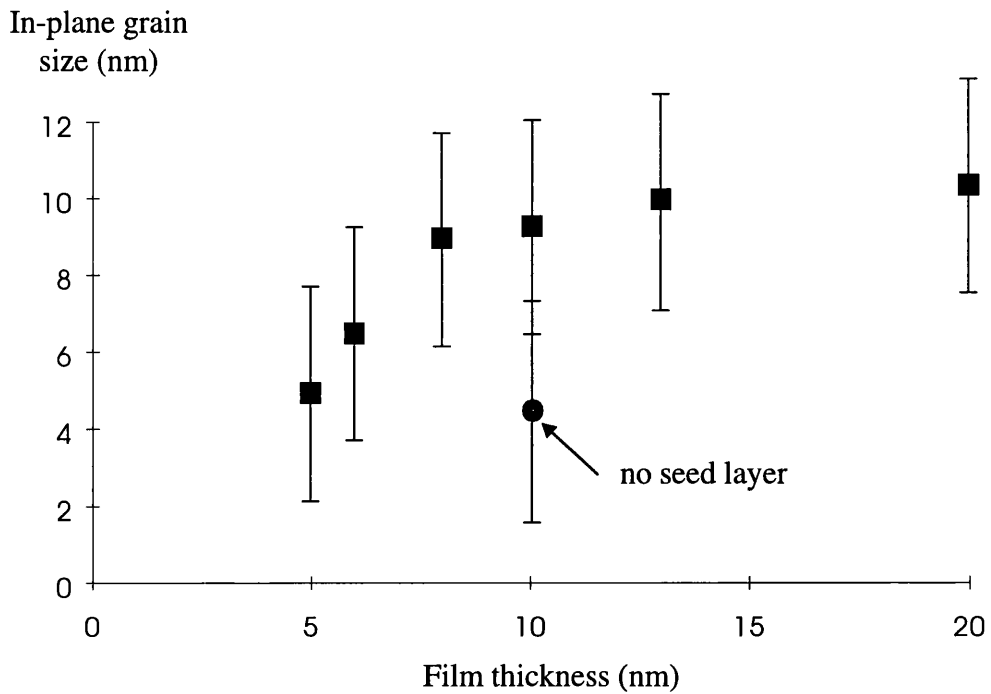


Fig 3.19: Average in-plane grain size as a function of layer thickness

The development of grain size in permalloy films of this thickness can have strong implications for the electron transport properties of the films. The scattering from grain boundaries plays a significant role and this has been considered in detail by Rijks et al (1995).

The influence of the seed layer on the texture, in the plane of the film, can be qualitatively assessed by considering the diffraction patterns from the films. Figs 3.20(a) and (b) show diffraction patterns from two 10nm films. One has been deposited on a Ta seed layer, Fig 3.20(a), while the other has been deposited directly onto Si_3N_4 . By taking linescans through these, it is obvious that the (220) ring is very much brighter for the film with the seed layer. The linescans shown in Fig 3.20 have had the diffuse scattering removed by subtracting a parabolic fit to the distribution. This reveals the Bragg diffraction rings but it is important to note that the linescans are merely to illustrate the qualitative differences in the diffraction patterns and it would not be correct to make quantitative comparisons. The increased intensity, however, in the (220) ring for the film deposited on Ta is sufficiently strong to conclude that this arises from increased $\langle 111 \rangle$ texture rather than from any non-linearities in the transfer function of the photographic film. For a complete study of the texture of the film it would be necessary to record diffraction patterns at different tilt angles.

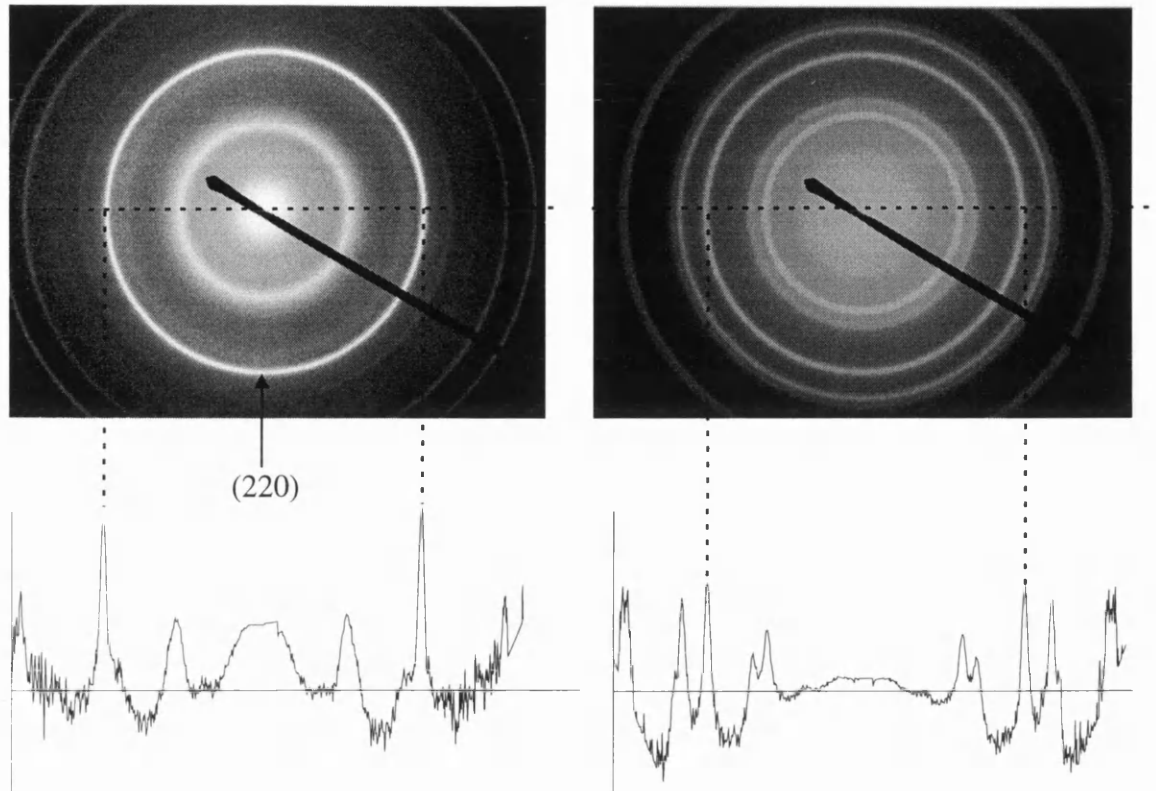


Fig 3.20: Diffraction patterns from (a) 10nm with seed, (b) 10nm without seed.

3.8 SUMMARY

In this chapter thin permalloy films in the thickness range of 5-20nm have been investigated. Magnetisation ripple was observed in all films studied and by considering DPC images of the ripple it was apparent that the spatial frequencies present were dependent on the film thickness. The ripple spectrum was partially quantified by analysis of the Fourier Transforms of DPC images. Typical hard and easy axis reversal mechanisms were observed upon applying an external field to the films. Interactions between domain walls and inclusions were also studied and, in particular, the mechanism for the creation of 360° walls, via this interaction, was looked at in detail.

CHAPTER 4: FREE LAYER REVERSALS IN SPIN-VALVES WITH CO-LINEAR EASY AXIS AND BIASING DIRECTIONS

4.1 INTRODUCTION

In this chapter the free layer reversal mechanism of spin-valves which have parallel easy axis and biasing directions are investigated. Marked differences from the behaviour observed in the single permalloy layers of chapter 3 are identified and complex 360° wall structures, which are not associated with a pinning point, are studied in some detail. A description of their structure is given and a theory involving the compensation of charges from the biased layer is suggested to explain stability. The work has a direct bearing on the performance of spin-valves as sensors as the way the magnetisation changes under the influence of an applied field affects noise characteristics.

4.2 REVIEW OF SPIN-VALVES

Although the basic make-up of a typical spin-valve was covered in Section 1.4.3 it is worthwhile to review a few of the fundamental points before presenting the experimental results of the following three chapters. A typical spin-valve, as was shown in Fig 1.5, basically consists of two ferromagnetic layers (usually permalloy) separated by a Cu spacer layer. The Cu spacer layer is sufficiently thick (2-3nm) to avoid exchange coupling between the ferromagnetic layers but does allow weak ferromagnetic coupling between them (Rijks et al, 1994). This causes a parallel alignment between the magnetisations of the two layers in the absence of an applied field. The first ferromagnetic layer, which is referred to as the free layer, is magnetically soft and typically requires $\approx 5-10$ Oe in order to overcome the ferromagnetic coupling. The second layer, referred to as the biased layer, is exchange coupled to either FeMn, TbCo or NiO and, depending on which of these materials is used, requires $\approx 100-600$ Oe for reversal. The magnetoresistance of a spin-valve is proportional to the cosine of the relative angle between the magnetisations in the two ferromagnetic layers (Dieny et al, 1991). In the zero field state of parallel alignment a low resistance state is obtained, while in the antiparallel state, which can be brought about by the application of a small

external field, a high resistance state is obtained. This change in resistance can be understood by the two current model, as introduced in Section 1.4.3, and is reflected in the magnetoresistance curve of Fig 1.6. The transition between states (a) and (b), as marked on Fig 1.6, is due to the reversal of the free layer and by monitoring the spin-valve resistance it is possible to use this switch in order to sense magnetic fields.

The spin-valves studied in this thesis were all prepared in a similar way to that of the permalloy films in chapter 3. That is to say they were sputter deposited onto supported Si_3N_4 membranes in the presence of a ≈ 120 Oe external field. As for the single layers, deposition in the presence of a field induces an easy axis by preferential pair ordering. Thus the two ferromagnetic layers have parallel easy axes, in the same direction to that of the field applied during sputtering. In a spin-valve, however, the deposition field has the additional effect of defining the biasing direction. This direction, which is also parallel to the direction of the deposition field, is the direction of constraint which is brought about by the exchange coupling between the biasing layer and the adjacent ferromagnetic layer. As previously stated only FeMn and TbCo biased spin-valves are studied in this thesis. In the case of FeMn Hempstead et al (1978) showed that a 50:50 composition gave the maximum biasing field and in this thesis all FeMn layers are of this composition. In the case of TbCo both the strength and the directionality of the biasing field are strong functions of composition and film thickness. In this thesis, however, the Tb composition is limited to either 32 or 35% and the layer thickness to either 10 or 12nm. The reversal of biased layers in spin-valves which are biased by either FeMn or TbCo differ markedly and are studied in detail in chapter 6.

The optimisation of the properties of spin-valves is facilitated by gaining an understanding, on a micromagnetic level, of the free layer reversal mechanism. Thus during this chapter we focus on the free layer reversal of spin-valves and consider in detail the implications of what is observed, with respect to the application of the spin-valve as a magnetic field sensor.

4.3 MAGNETISATION DISTRIBUTIONS IN THE ABSENCE OF AN APPLIED FIELD

As discussed in chapter 2 the Lorentz deflection which is experienced by an electron beam is due to the magnetic induction integrated along the electron path. Thus, due to the nature of transmission electron microscopy, it is not possible to image magnetic contrast from only one layer in a spin-valve structure. It is therefore necessary to consider the possibility of contrast arising from both ferromagnetic layers and in order to de-lineate this it was decided to study the micromagnetic structures of not only a complete spin-valve but also those of the separate constituent magnetic layers. As mentioned previously, the most common material used for the ferromagnetic layers is permalloy. Because of this the separate constituent layers, which are studied in this thesis, are also made from permalloy. Figs. 4.1(a-c) show Fresnel images of the zero field states of (a) a single free permalloy layer 8nm thick, (b) a permalloy layer of the same thickness exchange-biased to FeMn, (c) a complete spin-valve structure, with an 8nm free layer. The reversal mechanisms of the single layer of biased permalloy are investigated in chapter 6 but at present it is only the zero field Fresnel images which are considered.

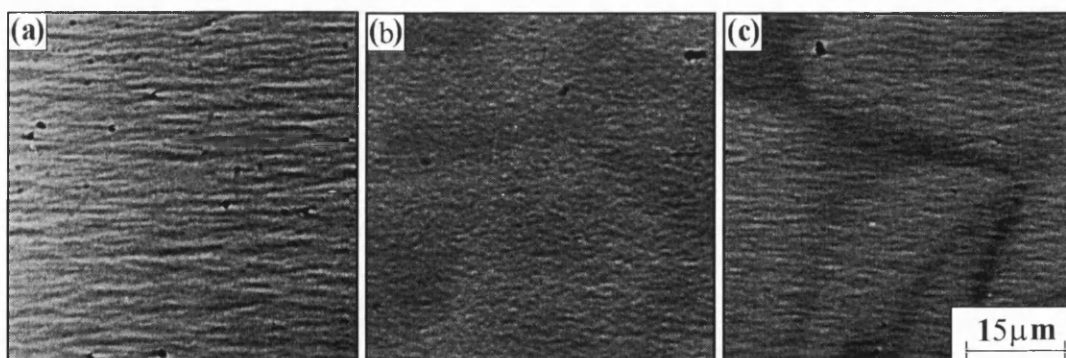


Fig 4.1: *Fresnel images showing the zero field state of (a) 8nm permalloy film, (b) 8nm biased permalloy film and (c) spin-valve with 8nm free layer.*

In general all specimens were single domain across the whole field of view in zero applied field. In all cases, however, magnetisation ripple could be observed in the Fresnel images providing qualitative information on the magnetisation dispersion

present. It is important to note that, for films of a constant thickness, imaged with the same lens defocus, the Fresnel contrast observed depends on the magnitude of the dispersion. The larger scale somewhat-diffuse contrast seen in the background of some of these and other Fresnel images arises from diffraction effects due to the texture of the film. Such contrast therefore contains no magnetic information and should be disregarded.

As for the isolated permalloy layers studied in the previous chapter the contrast which arises from the ripple in Fig 4.1(a) was found, as expected, to be predominantly transverse to the magnetisation direction. Figs. 4.1(b) and (c) were recorded under identical imaging conditions and whilst ripple can be seen it is immediately apparent that the contrast is markedly reduced. Thus dispersion in both the single biased layer and the spin-valve structure, as a whole, is much smaller than that in an equivalent free permalloy layer. Also noteworthy is the fact that the directionality in the biased permalloy was less pronounced, although a mean direction could still be defined and appeared to be transverse to the expected mean direction of magnetisation. The same was true for the spin-valve structure where the magnetisation in both the free and biased layers were parallel, with the ripple contrast once again lying predominantly perpendicular to this common direction.

The Fresnel images of Figs 4.1(a-c) show that while the ripple contrast imaged in a complete spin-valve structure arises predominately from the free layer there is a contribution from the biased layer. It is therefore wise to exercise constraint when deducing the direction of magnetisation from the ripple if, as is often the case during magnetising experiments, the free and biased layer magnetisations are not aligned. It was, however, found that upon applying fields, of the magnitude required to overcome the coupling field, that the biased layer magnetisation was unaffected. Thus in the following magnetising experiments any domain structures which arise come solely from the free layer. We shall return to the zero field states of the constituent magnetic layers in the discussion of section 4.5.

4.4 FREE LAYER REVERSAL MECHANISMS FOR FIELDS PARALLEL TO THE BIASING DIRECTION

In this section the free layer reversal mechanisms of three types of spin-valves are studied. These structures, which are referred to in this thesis, as spin-valve types (i), (ii) and (iii), are variations on the same generic structure, as shown in Fig 1.5, and differ only in either the type of ferromagnetic material used, or by the addition of extra layers to enhance the GMR amplitude. They do, however, have different sensitivity and noise characteristics and this makes it important to consider the specific application before deciding on which type of spin-valve to use. The three types, which are described in the table of Fig 4.2, are; (i) a spin-valve, biased by FeMn and without any GMR amplitude enhancing layers at the permalloy/Cu interfaces, (ii) a spin-valve biased by TbCo which has Co at both permalloy/Cu interfaces and (iii) a spin-valve, biased by FeMn, which uses a NiFeCo alloy instead of permalloy as the ferromagnetic material. The magnetising experiments, in the following sub-sections, investigate the response of these spin-valves to fields applied parallel to the biasing direction.

Type	Layer thicknesses(nm)	Layer composition(%)
(i)	Ta ₅ /NiFe ₈ /Cu _{2.3} /NiFe ₆ /FeMn ₈ /Ta ₅	Ta/Ni ₈₀ Fe ₂₀ /Cu/Ni ₈₀ Fe ₂₀ /Fe ₅₀ Mn ₅₀ /Ta
(ii)	Ta ₈ /NiFe ₄ /Co _{1.5} /Cu _{2.3} /Co _{1.5} /NiFe ₄ /TbCo ₁₂ /Ta ₅	Ta/Ni ₈₀ Fe ₂₀ /Co/Cu/Co/Ni ₈₀ Fe ₂₀ /Tb ₃₂₋₃₅ Co ₆₈₋₆₅ /Ta
(iii)	Ta ₅ /NiFe ₈ /Cu _{2.8} /NiFe ₆ /FeMn ₈ /Ta ₅	Ta/Ni ₇₅ Fe ₁₉ Co ₆ /Cu/Ni ₇₅ Fe ₁₉ Co ₆ /Fe ₅₀ Mn ₅₀ /Ta ^{``} / Ni ₆₆ Fe ₁₈ Co ₁₆ / Cu / Ni ₆₆ Fe ₁₈ Co ₁₆ / ^{``} / ^{``}

Fig 4.2: Table of layer thicknesses and compositions of different types of spin-valves

4.4.1 Type (i) Spin-valve

As mentioned previously the type (i) spin-valve is biased by FeMn and has permalloy for both the ferromagnetic layers. Figs. 4.3(a-l) are Fresnel images showing the effect of applying a small field anti-parallel to the biasing direction of a type (i) spin-valve.

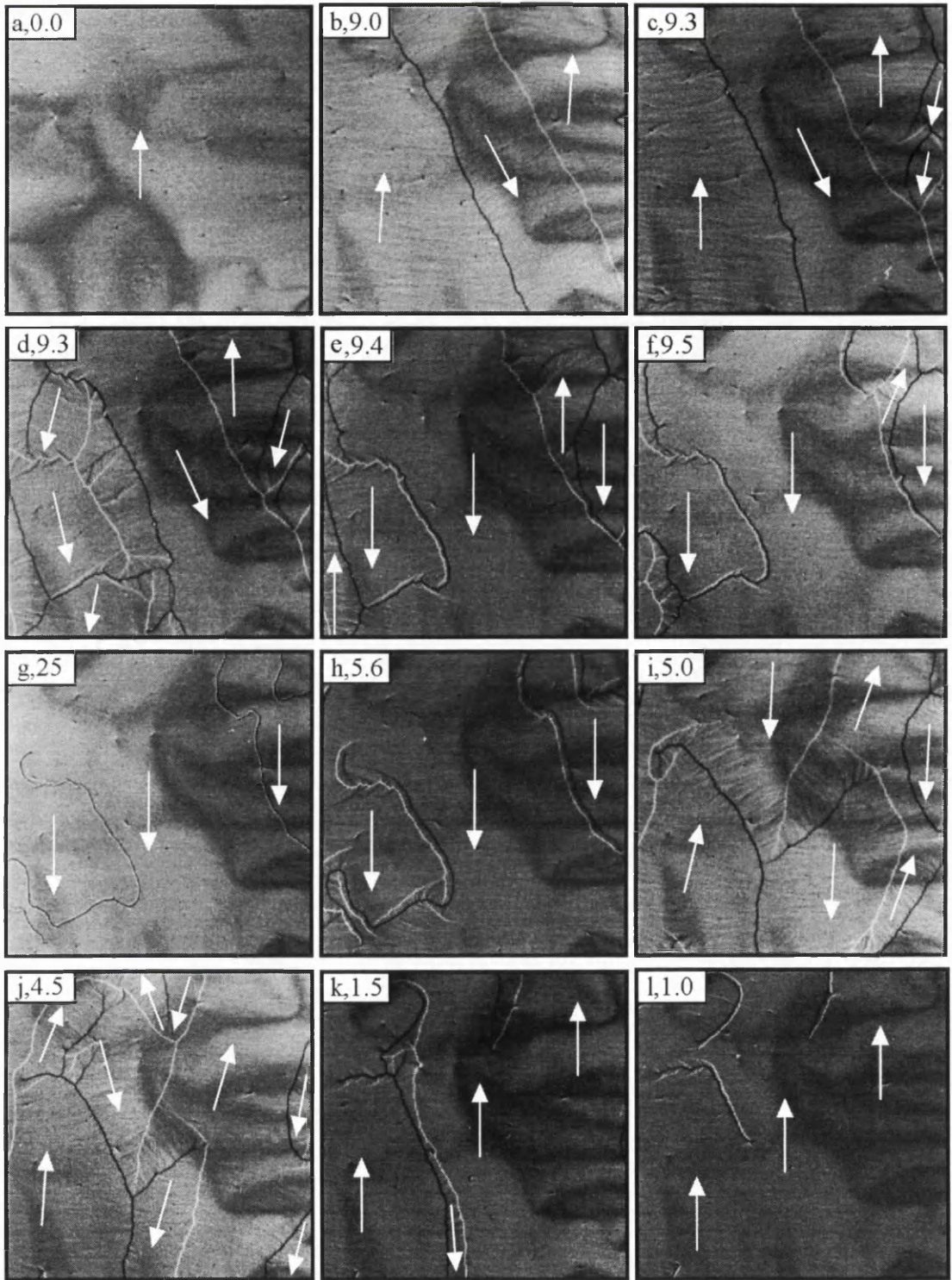


Fig 4.3(a-l): Fresnel images showing the reversal of the free layer in a type(i) spin-valve ($t_{Cu} = 3\text{nm}$) with the approximate directions of magnetisation superimposed. The field is applied antiparallel to the biasing direction and the number quoted with each figure is the applied field in Oe.

The spacer layer thickness, t_{Cu} , for this particular spin-valve was 3.0 nm and as the maximum field applied was very much smaller than the biasing field we assume that all changes take place in the free permalloy layer. As noted previously, the zero field state (Fig. 4.3(a)) was constrained to be single domain with low contrast ripple. On application of a field the ripple contrast increased and at a field of 9.0 Oe domain walls moved into the field of view (Fig. 4.3(b)). The walls were not parallel to the field direction (coincident with the easy axis of the free layer) but were inclined at $\approx 25^\circ$ to it. On increasing the field slightly (Fig. 4.3(c)) there was modest wall motion but in general the walls were neither as straight nor as mobile as those in the single isolated permalloy layers, studied in chapter 3. No obvious pinning sites could be discerned in the images. As well as the retarded wall motion further wall nucleation occurred, as is apparent on the right-hand side of Fig. 4.3(c). Fig. 4.3(d) shows that there was a similar occurrence within the unreversed region on the left-hand side of the region under study, at the same field, but after a time of say a few 100 seconds. It is worth emphasising that around the critical switching field, time-dependent effects, indicative of thermally assisted processes, were often apparent. It is, however, important to note that since changes to domain structure occur over such small increases in field any instability in the current source, used to generate the fields in Fig 4.3, could also have resulted in the change in states between Figs 4.3(c-d). Thus a domain structure of much greater complexity than was ever observed in a single isolated layer developed as the reversal in the spin-valve proceeded. Further small field increases (Figs. 4.3(e) and (f)) resulted in the shrinking of unfavourably oriented domains but, rather than there being complete annihilation, substantial numbers of 360° wall structures formed. These were in the form of irregular lines or loops although many had sections lying approximately parallel to the direction of the walls which appeared at the onset of the reversal process. The 360° structures persisted to field values much greater than those required to switch the bulk of the film, Fig 4.3(g), and indeed were observed on occasion even after the application of fields >100 Oe. Such structures have been observed in other films and are formed when walls of opposite chirality come together (Heyderman et al, 1994).

Relaxation of the external field led to the opening out of the 360° structures, providing the mechanism for the spin-valve to return to parallel alignment, Figs. 4.3(h-k). Again the switching involved the generation of complicated domain structures with walls

inclined at various angles with respect to the applied field direction and the easy axis. On lowering the field further to 1.0 Oe, Fig. 4.3(l) the return of the magnetisation to its original direction was complete everywhere except for within a few remaining 360° structures. These remained in existence following the complete removal of the external field. As before, the structures themselves were irregular and frequently changed orientation along their length. Small scale orientation changes, indicative of strong local pinning, can be seen very clearly in the higher magnification DPC image shown in Fig. 4.4.

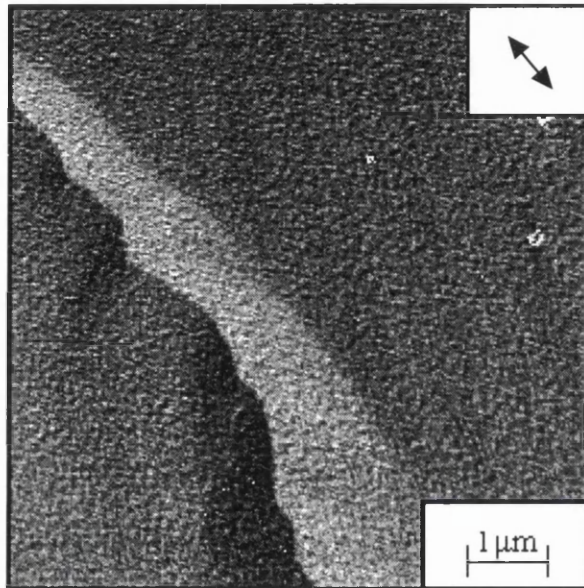


Fig 4.4: DPC image showing irregularities in a 360° wall structure. The arrow indicates the component of induction mapped.

One final point of note is that although the 360° structures in Figs. 4.3(g) and (l) were similar in character, the total length of 360° wall was much larger in the former case, i.e. when the applied field forced the spin-valve into an anti-parallel aligned state.

The reversal processes in spin-valves which have other spacer layer thicknesses, between 2.0 and 3.0nm, generally followed similar lines as that shown in Fig 4.3(a-l). A feature which was frequently observed in these spin-valves was the creation of 360° loops. Fig. 4.5 is an extract from a magnetising sequence, of a spin-valve with $t_{Cu}=2.2\text{nm}$, where the formation of the 360° loops can be seen clearly. As was the case for the spin-valve with $t_{Cu} = 3.0 \text{ nm}$, low mobility walls, Fig. 4.5(a), did not simply

move together and annihilate but remained substantially fixed whilst approximately orthogonal walls nucleated between them, Fig. 4.5(b). These evolved into a "chain-like" structure which in turn split into a set of 360° loops, Figs. 4.5(c) and (d).

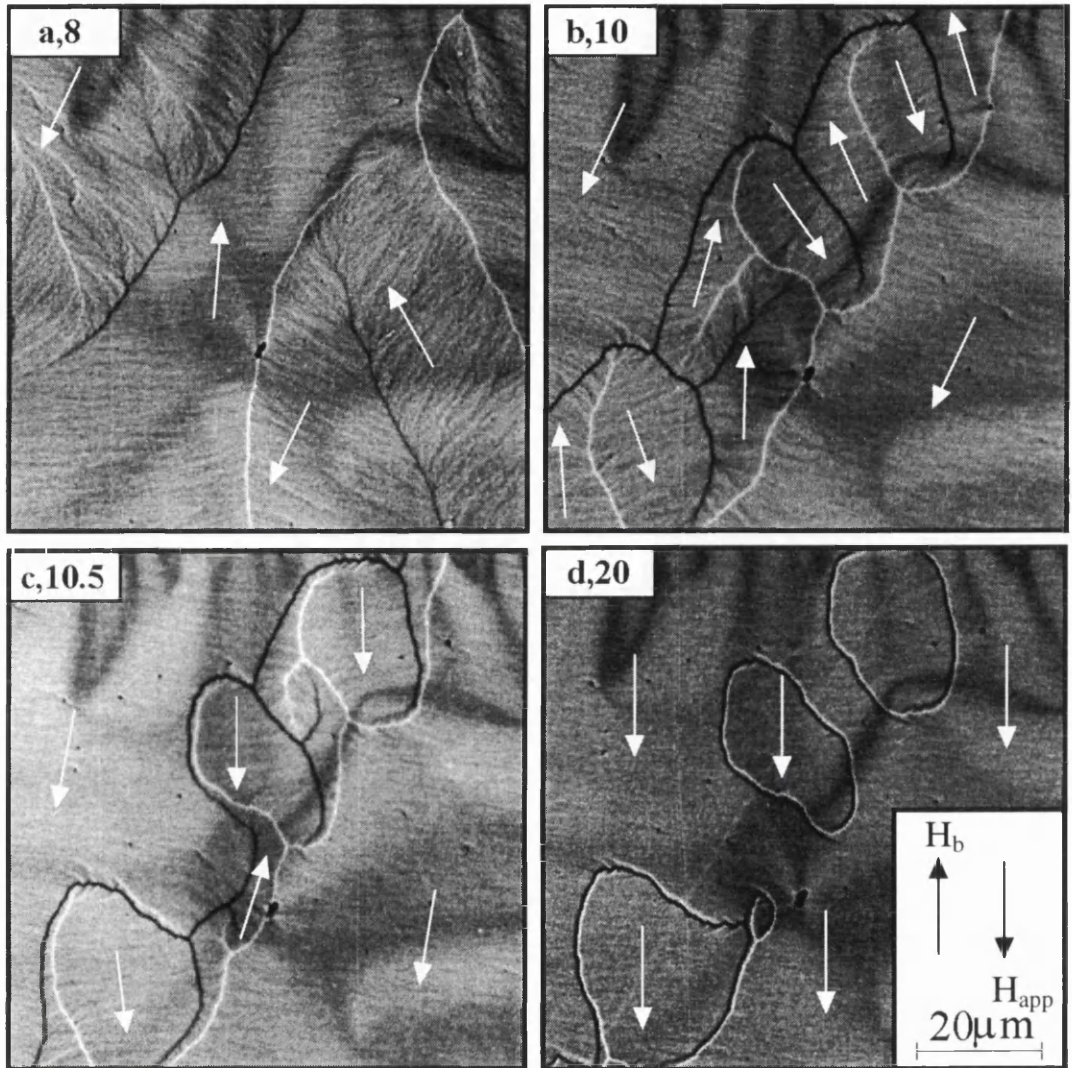


Fig 4.5(a-d): Fresnel images showing an extract from an easy axis reversal of a spin-valve ($t_{Cu} = 2.2\text{nm}$) demonstrating the creation of a chain structure and the subsequent formation of 360° loops. The approximate directions of magnetisation have been superimposed and the number quoted with each figure is the applied field in Oe.

We return to the issue of the total length of 360° walls in spin-valves with different spacer thicknesses in section 4.5 and discuss possible reasons for their stability. We do,

however, note here that the probability of forming complex 360° structures was strongly dependent on the applied field being perfectly aligned with the biasing direction.

Similar switching processes to those described above were observed when fields were applied to reverse the free layer in spin-valves, which were biased by TbCo but did not have thin Co layers at the interfaces. As before the reversal mechanism involved a complicated domain structure, Fig 4.6(a), and often resulted in 360° structures being left in the remanent state, Fig 4.6(b)

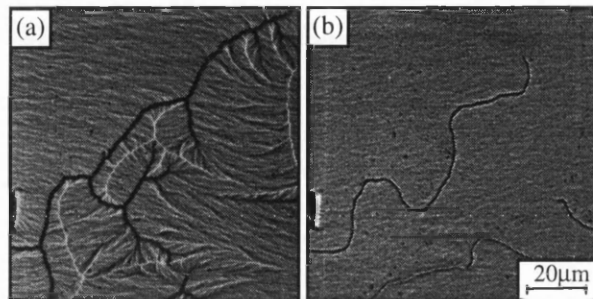


Fig 4.6: (a) *Complicated switching structure for a spin-valve biased by TbCo but with no Co at the interfaces and (b) 360° walls which form in the remanent state.*

4.4.2 Type (ii) Spin-valve

The type (ii) spin-valves which were defined earlier in this chapter are biased by TbCo and have Co layers at both permalloy/Cu interfaces. This follows the work of Parkin et al (1991) who discovered that very thin layers of Co ($\approx 1.5\text{nm}$) at these interfaces enhanced the GMR amplitude. A typical free layer reversal of a type (ii) spin-valve is shown in Figs 4.7 (a-l). As expected the zero field state, Fig 4.7(a), was forced to be single domain by the ferromagnetic coupling between the free and biased layers. As the applied field was increased there was an increase in dispersion and domain nucleation occurred at $\approx 11.6\text{ Oe}$, Fig 4.7(b). The domain walls were more erratic in nature than those in the type (i) spin-valve and the reversal domains had a “fern-like” texture about them.

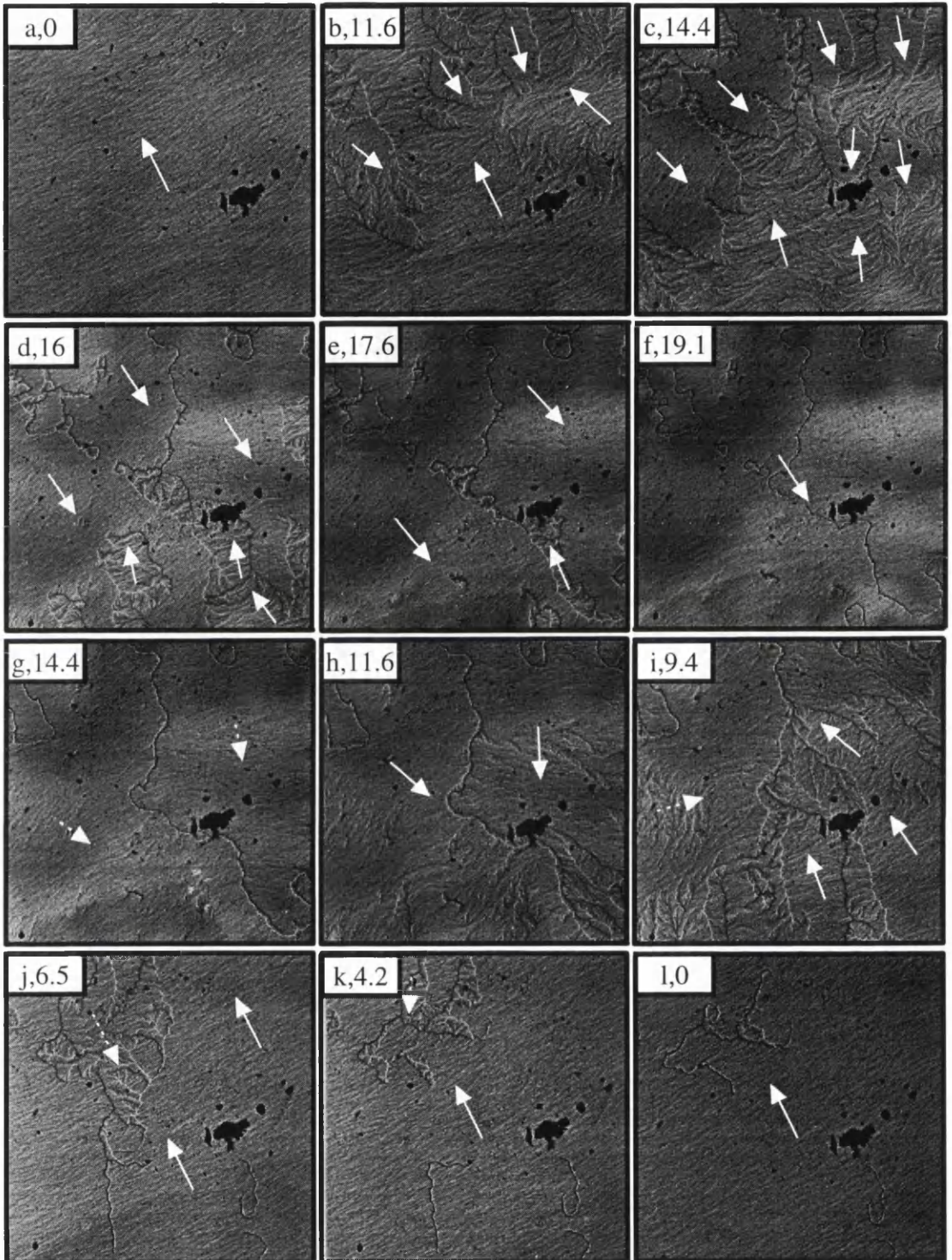
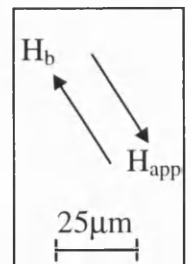


Fig 4.7: Fresnel images showing the reversal of the free layer in a type (ii) spin-valve ($t_{Cu} = 2.8\text{nm}$) with the approximate directions of magnetisation superimposed. The field is applied antiparallel to the biasing direction and the number quoted with each figure is the applied field in Oe.



As the field was increased, Fig 4.7(c), the structures developed so that approximately 40% of the spin-valve had the magnetisation of the free layer aligned anti-parallel to that in the biased layer. As was the case for the type (i) spin-valve the dispersion in areas where the magnetisation of the free layer had not yet reversed was significantly higher than those which were already anti-parallel aligned. A progressively larger fraction of free layer became anti-parallel to the biased layer as the applied field was increased, Figs 4.7(d-e). Full anti-parallel alignment was not, however, achieved due to the large number of 360° walls which were present in the otherwise saturated state of Fig 4.7(f). As before these structures were extremely stable and existed even for fields as great as 100 Oe. As the applied field was relaxed the free layer magnetisation returned to its original parallel alignment with the biased layer, Figs 4.7(g-l). The magnetisation within the areas which were last to become anti-parallel were the first to return to a parallel alignment and when the applied field was reduced to zero, Fig 4.7(l), the majority of the spin-valve had returned to its parallel state. As in the type (i) spin-valve some 360° walls were still present in the zero field state and it is noted that the total length of 360° walls was less when the magnetisation in the two permalloy layers were parallel rather than anti-parallel.

4.4.3 Type (iii) Spin-valve

The type (iii) spin-valves which were defined earlier in this chapter are biased by FeMn and utilise a NiFeCo alloy, instead of permalloy, as the ferromagnetic layer material. The exact composition of the alloy must be such that the magnetostriction constant is approximately zero and this corresponds to a stoichiometry which is situated on the zero magnetostriction line of Fig 4.8. It has been known for some time that as the fraction of Co in a NiFeCo alloy is increased, while maintaining a 4:1 ratio for Ni:Fe, the anisotropy field also increases, (Wolf, 1962). The dependence of the anisotropy field on the stoichiometry of the alloy is indicated by shading on Fig 4.8. This is a crucial parameter for a spin-valve as the permeability of the free layer plays an important role in determining both the output and the sensitivity of a spin-valve sensor, (Folkerts et al, 1995).

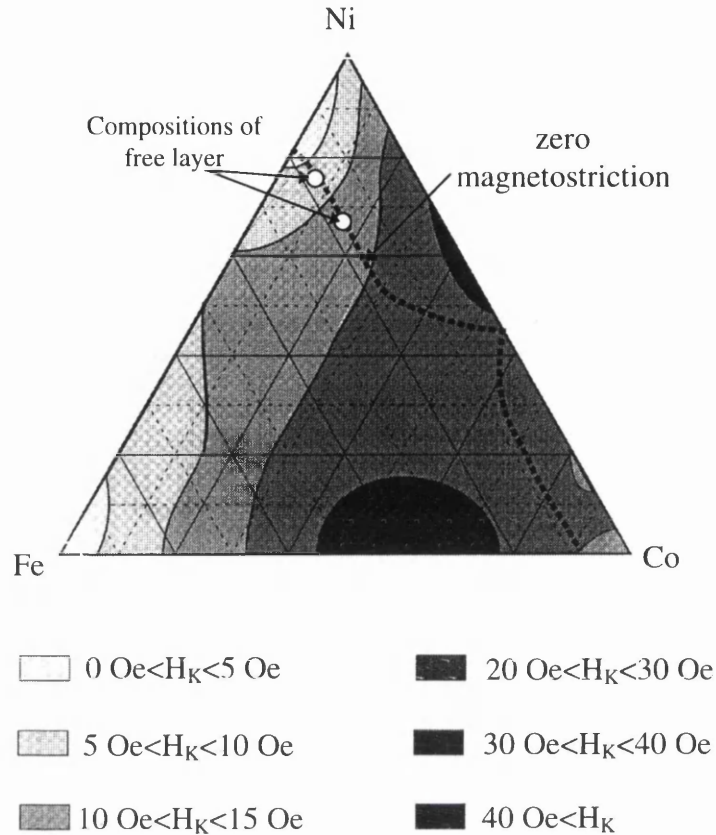


Fig 4.8: *Dependence of the anisotropy field on the composition of NiFeCo films, (Wilts and Humphrey, 1968)*

In this thesis we limit ourselves to studying the free layer reversal of only two compositions, $\text{Ni}_{75}\text{Fe}_{19}\text{Co}_6$ and $\text{Ni}_{66}\text{Fe}_{16}\text{Co}_{18}$, on the zero magnetostriction line. Both of these compositions had similar free layer reversal mechanisms which were more reminiscent of isolated permalloy switches rather than those of the spin-valves described previously. Figs. 4.9(a-h) show the free layer reversal for the $\text{Ni}_{75}\text{Fe}_{19}\text{Co}_6$ spin-valve. As expected the zero field state was constrained to be single domain by ferromagnetic coupling, Fig 4.9(a). As the applied field approached that required for free layer reversal there was an increase in dispersion and then the introduction of a domain wall, at an angle to the easy axis and biasing directions, Fig 4.9(b). Without further increasing the applied field the domain wall moved through the free layer. This phenomenon is known as magnetisation creep and is discussed in detail, with respect to biased layer reversals, in chapter 6. Such behaviour has been reported previously (for a discussion see Street

and Brown, 1994 or Folks and Street, 1994) and in this experiment resulted in making it difficult to record images that showed the development of the reversal process. It was, however, possible to retard the domain wall motion, and therefore record the wall movement on photographic film. This was done by decreasing the applied field at important points in the reversal process in order to “freeze” the magnetisation and allow images to be recorded. Unlike the magnetising sequences for the previous spin-valves these states should be thought of as “snap-shots” in time rather than states which are brought about by an increasing field.

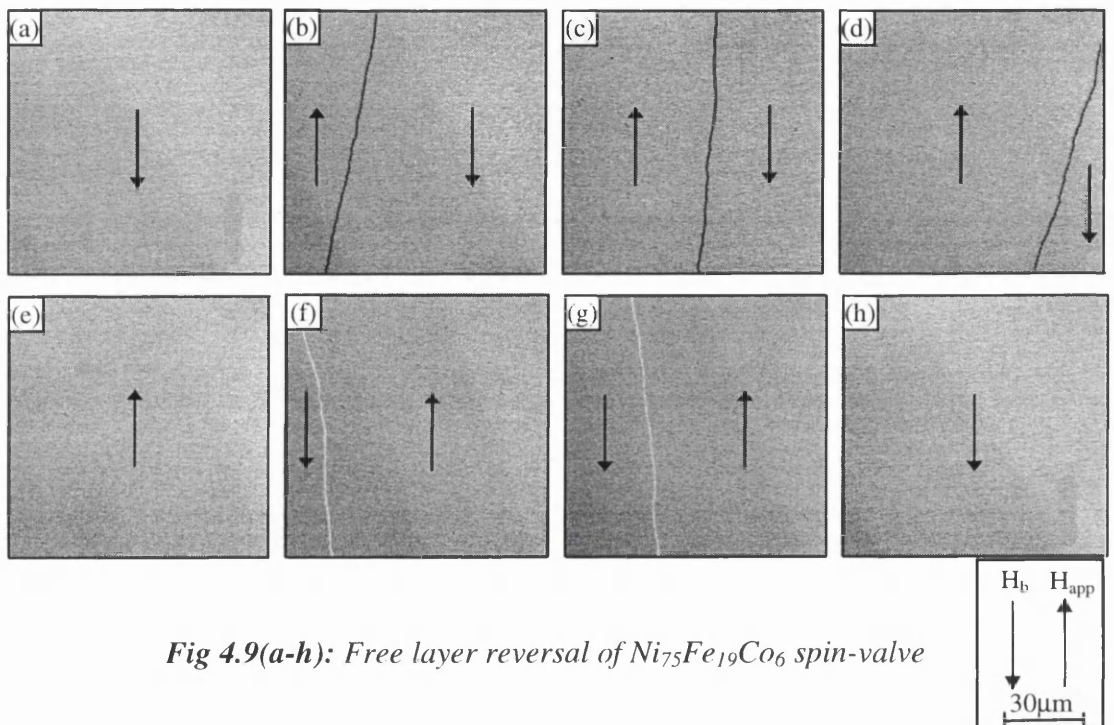


Fig 4.9(a-h): Free layer reversal of $Ni_{75}Fe_{19}Co_6$ spin-valve

As already mentioned the reversal process of the $Ni_{75}Fe_{19}Co_6$ spin-valve began with the introduction of a wall at an angle to the biasing direction, Fig 4.9(b). As the reversal process developed the wall swept through the free layer, Figs 4.9(b-d), until there was complete anti-parallel alignment between the free and biased layer magnetisations, Fig 4.9(e). This simple switching mechanism is similar to that of the easy axis reversal in the isolated permalloy layers of chapter 3. Upon relaxing the applied field a similar reversal was observed, Figs 4.9(f-g), as the magnetisation of the free layer returned to parallel alignment with that of the biased layer, Fig 4.9(h). Upon repeated reversal of the free layer it was possible to occasionally form a 360° structure but the total wall length was very much reduced as compared to that in the permalloy spin-valves.

A somewhat similar free layer reversal was observed for the $\text{Ni}_{66}\text{Fe}_{16}\text{Co}_{18}$ spin-valve. The reversal of this spin-valve, Figs. 4.10(a-l), again showed the phenomenon of magnetisation creep and the images are “frozen states” brought about by a reduction in the applied field from that required to bring about the reversal.

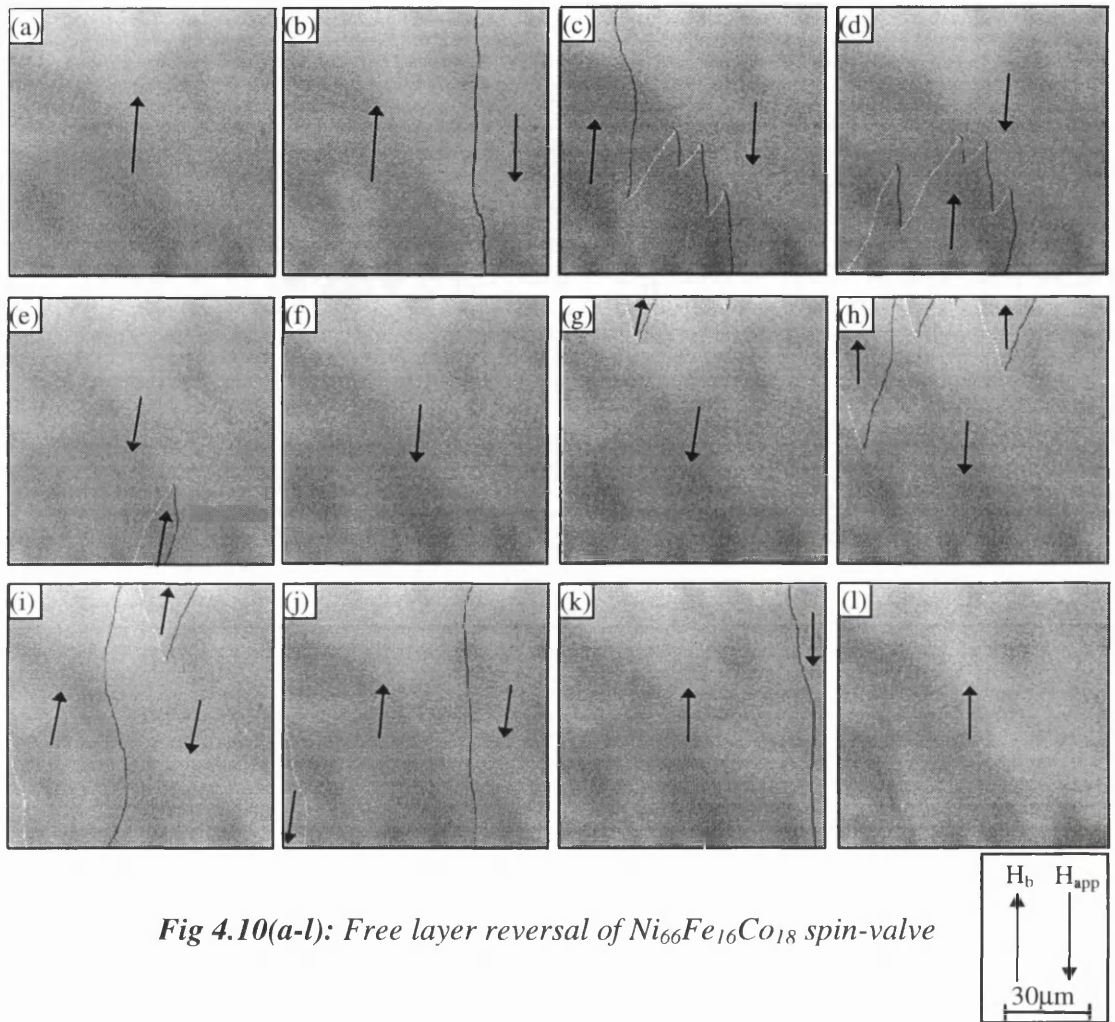


Fig 4.10(a-l): Free layer reversal of $\text{Ni}_{66}\text{Fe}_{16}\text{Co}_{18}$ spin-valve

The reversal started with the introduction of a rather erratic wall, approximately parallel to the easy axis / biasing directions, Fig 4.10(b). This wall moved through an area of the free layer while leaving a “zig-zag” boundary between areas of parallel and anti-parallel alignment, Fig 4.10(c). The reversal developed to leave a small region of un-reversed free layer, Fig 4.10(e), which finally was overcome as full anti-parallel alignment was achieved, Fig 4.10(f). Upon reversing the applied field small reverse domains were nucleated at the top of the area under study, Fig 4.10(g). These moved through the sample, Fig 4.10(h), until a large fraction of the window had returned to parallel

alignment. The wall direction in Fig 4.10(i) is very erratic and this tends to imply either many local pinning points or alternatively, a large dispersion in anisotropy. As the sequence develops it was observed that the remainder of the reversal is dominated by a single domain wall, Figs 4.10(j-k), which sweeps across the area under study. Although the walls in this reversal are slightly more complicated than those of $\text{Ni}_{75}\text{Fe}_{19}\text{Co}_6$ they do still resemble those of an isolated permalloy layer. What is most striking in these reversals is the absence of 360° wall structures. In section 4.4.1 it was noted that the probability of forming 360° structures in spin-valves was highly dependent on the exact alignment of the applied field with the biasing direction. In order to confirm that the simple reversal mechanisms of the NiFeCo alloys were not due to such a misalignment the free layer magnetising cycle was repeated for field directions which were at small angles to the approximate direction of the deposition field. This intentional misalignment varied, in steps of 1° , between $\pm 10^\circ$ but at no angle was it possible to generate reversal mechanisms, which were similar to those observed for the type (i) or (ii) spin-valves. We therefore conclude that a simpler free layer reversal mechanism is a characteristic of the two NiFeCo alloys studied in this section.

4.5 DISCUSSION AND COMPARISON OF SPIN-VALVE PROPERTIES

From the results presented in the preceding three sections it is very clear that there are distinct differences between the free layer reversal processes occurring in spin-valve structures and those in isolated permalloy layers. Before considering the reversal processes, however, let us discuss the zero field states which were presented in section 4.3. The fact that ripple in permalloy exchange-biased to FeMn is reduced is not surprising as the orientation of the magnetisation is clearly constrained by the pinning layer. However, that a comparable reduction in dispersion in the spin-valve as a whole is seen in zero field was not expected and must be due to the weak coupling favouring parallel alignment between the layers. This results in a better alignment of free layer magnetisation with the biasing direction in zero field, a decrease in the magnitude of local fluctuations of magnetisation and a consequent reduction in observed ripple. Support for this comes from the fact that in the presence of a field sufficient to initiate magnetisation reversal (and hence overcome the effect of coupling), substantial ripple,

more akin to that seen in isolated permalloy in zero field, is present in the spin-valve structures (Figs. 4.3(c) and 4.5(a)).

The origin of the coupling between the free and the biased layer has been variously ascribed to "pin-holes" and "orange-peel" magnetostatic coupling (for a discussion, see Kools^A, 1995). In the former case thin continuous columns of magnetic material join the two films leading to local exchange coupling whilst the latter, following Néel (1962), builds on coupling due to magnetic surface charges which are induced in adjacent layers separated by a non-flat interface. In both cases local behaviour will vary from point to point across the structure although the degree of localisation is more pronounced in the former case.

Whilst differences in the ripple spectrum are marked it is the differences in the switching mechanisms for the free layer of spin-valve types (i) and (ii), compared with a single isolated permalloy layer, that are of primary concern. Repetition of the free layer reversal experiments for a type (i) spin-valve showed that the initiation of the reversal process usually involved the introduction of walls inclined to the easy axis, albeit not always at $\approx 25^\circ$. For a given Cu spacer thickness, however, similar angles were found in all specimens. Thus it is clear that these angles are in some way characteristic of the structure and are not a consequence, for example, of pinning by an inclusion just outside the area imaged. Further evidence for this comes from the structure seen in Fig. 4.3(d) which is shown in a somewhat different form in Fig. 4.11. Here domains are coded according to the direction of magnetisation within them as deduced from the magnetisation ripple. Black regions have magnetisation unchanged from the original direction whilst the grey regions have magnetisation which is directed towards the field but does not appear to be coincident with it. It is noteworthy that these latter domains can be further subdivided according to whether their walls are inclined at $+25^\circ$ or -25° . Close examination of other images in the magnetisation sequences confirms the importance of walls at these angles.

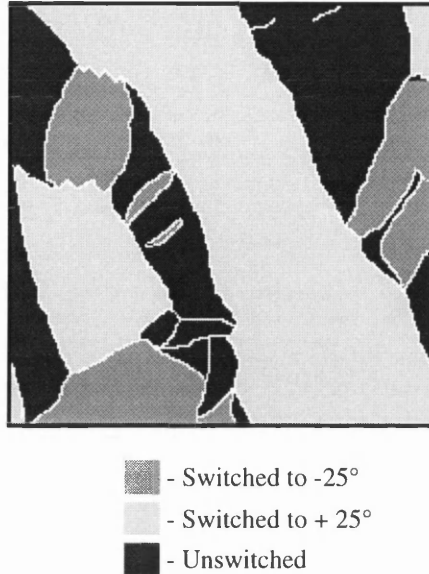


Fig 4.11: Schematic depiction of the domain structure observed in Fig. 4.3(d)

The fact that walls exist inclined at both positive and negative characteristic angles is presumably a consequence of easy axis dispersion whereby magnetisation in different regions can rotate clockwise or anti-clockwise towards the field. Furthermore, it must be assumed that although both the applied field and the anisotropy in the free layer favour magnetisation alignment parallel to their common direction, this is not achieved, at least not at the fields where switching occurs, because of the residual torque associated with coupling to the exchange-biased layer. Further experiments involving spin-valves with different Cu spacer thicknesses may help to explain these angles (see future work).

We turn now to the 360° wall structures which are a characteristic feature of the reversal of both the type (i) and type(ii) spin-valves. The existence of such structures in single isolated permalloy layers has been known for some time and they are usually associated with a clearly visible pinning point such as an inclusion (Smith et al, 1962 and chapter 3 of this thesis). This is not the case here where complex 360° wall structures exist and change their direction frequently despite a total absence of obvious topological pinning sites. This is more in accordance with observations in thin coupled magnetic films of other types (Heyderman et al, 1991, Heyderman et al, 1994 and Schäfer et al, 1993). In the case of the spin-valve the proximity of the biased layer leads to a marked reduction in wall mobility, followed by the generation of complex domain

structures which subsequently collapse to form 360° structures. Repetition of the magnetisation cycle shows that there is a strong tendency for rather similar structures to form in the same places within the specimen suggesting that there are locations where 360° structures are significantly stabilised. The high fields required for their annihilation provide further evidence for this.

Fig. 4.12 shows high magnification Fresnel and DPC images of two 360° structures. From analysis of the contrast in the images a simplified model of a 360° loop is given in Fig. 4.13(a). It can be seen that the structure carries considerable magnetic charge and the local charge distributions at various points in the structure are indicated schematically on the figure. The charge density appears to be greatest at the top and bottom of the loop (locations A and B) and it is here that the greatest irregularity is often observed with the simplified structure of Fig. 4.13(b) locally developing a zig-zag pattern, Fig. 4.13(c). This is related to the case of transitions between bits in magnetic recording media where the magnetisation meets head-on. Various authors have calculated the magnetostatic energy at such boundaries and found that the energy is substantially reduced by forming a saw-tooth structure (Hsieh et al, 1971).

Magnetostatic energy considerations also provide a plausible explanation of why 360° structures are stabilised in a spin-valve structure if the coupling mechanism is of the Néel type. In this case undulations in the biased layer give rise to charges and a saving in total magnetostatic energy can be achieved if positive and negative charges associated with the 360° wall structure are positioned over charges of the opposite sign in the biased layer. We note that the above argument suggests that, as the coupling increases with a decrease in Cu spacer layer thickness, we might expect that spin-valves with thinner spacer layers would support a greater density of 360° wall structures. Analysis of results from spin-valves with 2.2 nm and 3.0 nm Cu spacer layers, augmented by a few results from samples with greater layer spacings, suggests that this is indeed the case.

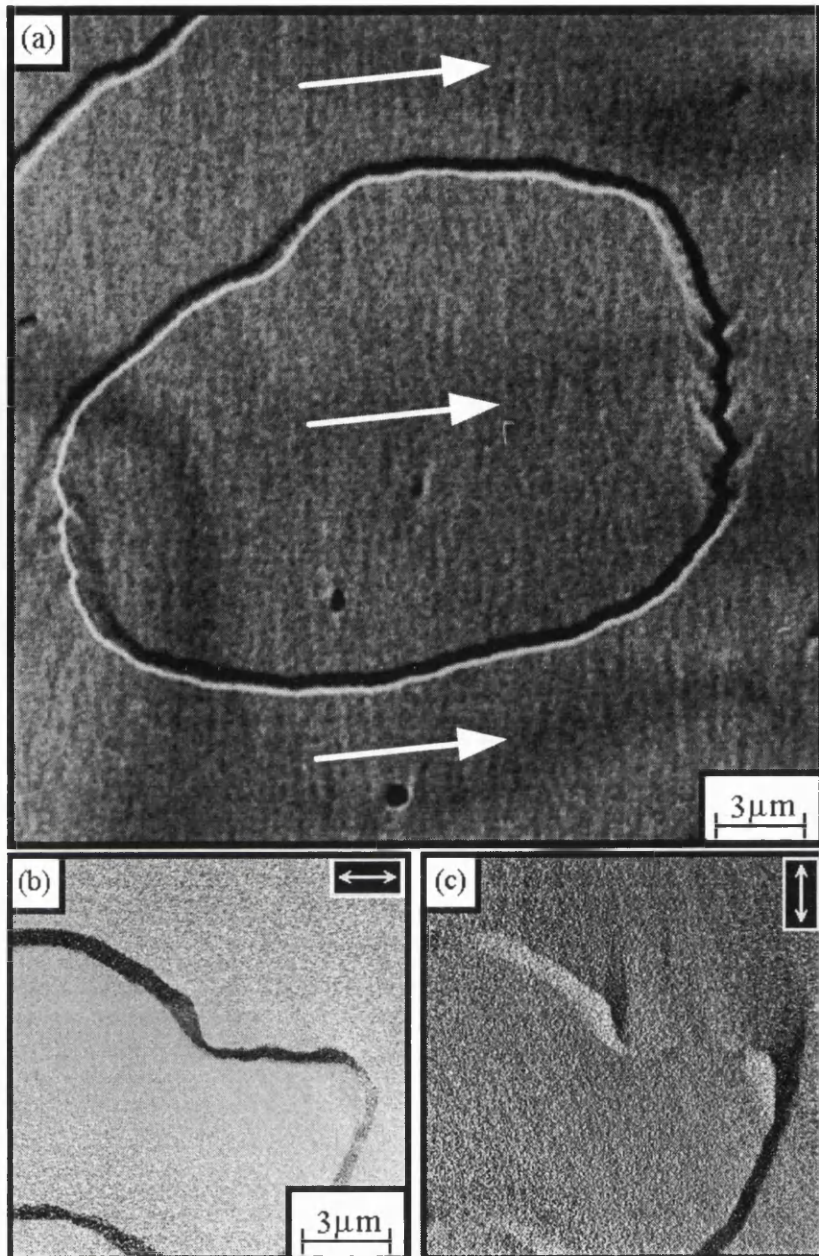


Fig 4.12: (a) Fresnel image of a 360° loop; (b), (c) DPC images with orthogonal mapping directions of a 360° loop observed in the free layer of a spin-valve ($t_{Cu}=2.2nm$)

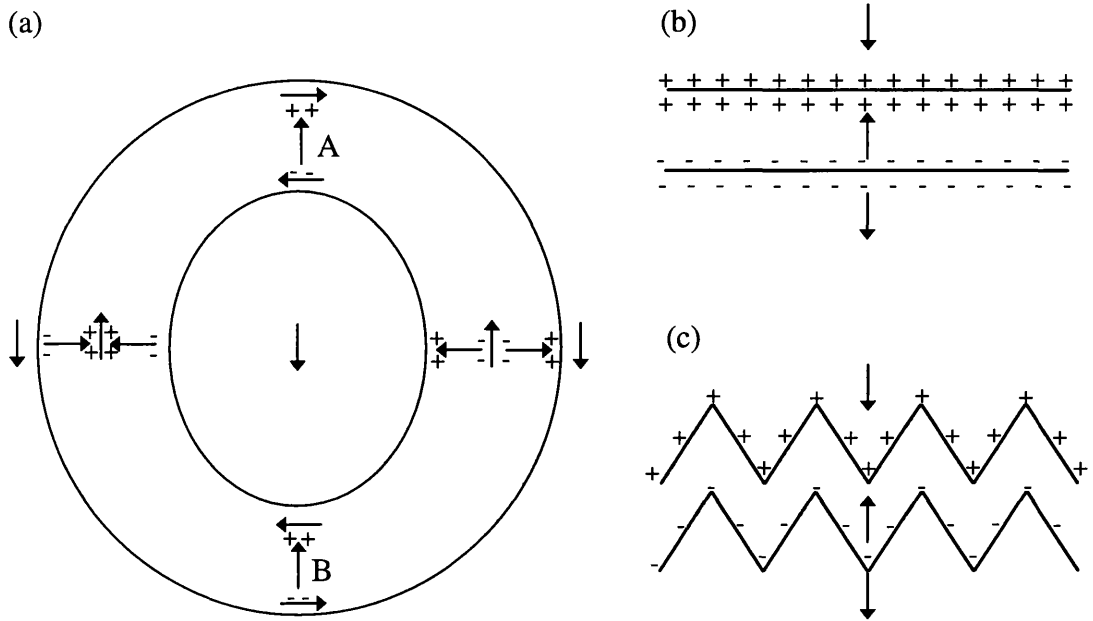


Fig 4.13: (a) Simplified schematic of a 360° loop, (b) charge distribution for a straight section of loop in the vicinity of A and B, (c) equivalent distribution in a saw tooth structure.

The large number of domain walls which were involved in the free layer reversal of type (i) spin-valves, Figs 4.3(a-l), make it far from an ideal sensor material. A sensor made from such a spin-valve would suffer from discrete jumps in magnetoresistance which would inevitably result in either Barkhausen noise, or distortion, in the output of a working head (Folkerts et al, 1994). The free layer reversal of type (i) spin-valves does, however, occur for relatively low fields ($\approx 5-10$ Oe) and the spin-valves are therefore sensitive to weak magnetic fields. Thus, for the type (i) spin-valves studied in this chapter, it is correct to say that they would make noisy but sensitive magnetic sensors. Possible ways of improving the noise characteristics of these spin-valves will be discussed in chapter 5.

As already mentioned the type (ii) spin-valves also have a strong tendency to form 360° wall structures. This again must be attributed to proximity of the biased layer to the free layer. What is interesting, however, about the free layer reversal of type(ii) spin-valves are the domain walls which were observed before the formation of the 360° structures. This may be attributed to the presence of Co at the permalloy/Cu interfaces which greatly affects the domain structures involved in the reversal of the free layer. In particular the domain walls of type (ii) spin-valves are more erratic than those of type

(i). This is probably due to the fact that, unlike permalloy, it is difficult to define an easy axis in Co during sputtering. Consequently this leads to the crystallite anisotropy, which is characteristically strong in Co, playing a major part in deciding the local direction of any easy axis in the Co layers. As the Co layer is polycrystalline in nature, at least in the plane of the sample, this means that the crystallite contribution to anisotropy is essentially random and although the Co layer is relatively hard, compared to permalloy, the dispersion within it is greater. Due to exchange coupling between the Co and the free layer any dispersion in the Co is replicated in the adjacent permalloy layer. This results in a deterioration of the easy axis of the free layer as a whole. Such a decrease in the directionality of the anisotropy inevitably leads to more erratic wall structures. As already mentioned, the presence of thin Co layers at the permalloy/Cu interfaces increases the GMR amplitude and for many applications this is the ultimate aim. The Co does, however, also increase the “stiffness” of the free layer and consequently reduces the sensitivity of the spin-valve. The different wall structures involved in the free layer reversal of type (ii) spin-valves may also alter the noise characteristics with respect to the type (i) spin-valves. In summary type (ii) spin-valves are less sensitive than type (i) but display an increased GMR amplitude. A possible compromise between these two structures is to use only one Co layer, situated between the biased layer and the Cu spacer layer (ten Berge et al, 1995). This results in a relatively soft free layer while the GMR ratio is still enhanced, though obviously not to the same extent as when two Co layers are present.

Type (iii) spin-valves display a property which is of considerable interest when considering which type of spin-valve to use as a sensor material. The free layer reversal appears to be very much simpler than those of the other spin-valves and for the compositions studied in this thesis there appeared to be an almost complete absence of 360° wall structures. This is significant as the absence of 360° walls in the free layer reversal will inevitably lead to less noise in the output of a working sensor. The reason for the reduction in numbers of 360° walls is not entirely clear but it may be associated with the increase in anisotropy which is brought about by the addition of small amounts of Co to the alloy, Fig 4.8. An increase in anisotropy would certainly discourage domains which were not either parallel or anti-parallel to the biasing direction and consequently would reduce the probability of forming the complicated switching

structures which were observed for type(i) and (ii) spin-valves. The wall momentum is significant in the reversal of type (iii) spin-valves and when recording the “frozen states” of both Figs 4.9(a-h) and 4.10(a-l) it was often necessary to increase the field above that which was previously applied in order to re-start domain wall motion. The increased dispersion in anisotropy which is associated with Co, as discussed with respect to type (ii) spin-valves previously, is probably the reason for the slightly more erratic wall structures observed in type (iii) spin-valves. An advantage of adding Co to the alloy is an increase in the spin-valve effect by a factor of 1.12 and a decrease in the AMR amplitude due to the free layer reversal. Since AMR contributions to the total MR are non-linear this has the affect of increasing the linearity of the sensor, (Kools^B et al 1995). The major disadvantage, however, is that the anisotropy field of the free layer is increased, Fig 4.8. This results in a decrease in sensitivity and is an important consideration when considering which composition of alloy to use as the ferromagnetic material. It has been found by other authors (Kools^C et al 1995) that increasing the Co composition results in an increase in the signal to noise ratio of the sensors, though it is noted that these measurements are not for spin-valves with co-linear easy axis and biasing directions.

The table of Fig 4.14 summarises the properties of the three spin-valves studied in this chapter for fields applied parallel to the easy axis / biasing direction.

Type	Structure	Characteristics
(i)	Ta/NiFe/Cu/NiFe/FeMn/Ta	Sensitive to weak magnetic fields but also potentially noisy due to complicated free layer reversal which involves many 360° walls.
(ii)	Ta/NiFe/Co/Cu/Co/NiFe/FeMn/Ta	Lower sensitivity but increased GMR amplitude. Wirey “fern like” domain walls caused by Co layers. Many 360° wall structures.
(iii)	Ta/NiFeCo/Cu/NiFeCo/FeMn/Ta	Slightly reduced sensitivity than permalloy spin-valves but potentially reduced noise. Vast reduction in the numbers of 360° walls and an overall simpler free layer reversal.

Fig 4.14: Summary table of spin-valves studied in chapter 4

4.6 THE APPLICATION OF FIELDS ORTHOGONAL TO THE BIASING DIRECTION

In the prototype head geometries which have so far been fabricated the stray field, from the passing disk or tape, has been directed so as to be parallel to the biasing direction (Tsang et al, 1994, Folkerts et al, 1994 and Freitas et al, 1994). For this reason the experiments of the preceding sections are, from an applications point of view, the most interesting. It is, however, also interesting to study the free layer response to external fields, which are orthogonal to the biasing direction. In this section we concentrate on the response of type (i) spin-valves to fields orthogonal to the biasing direction and compare these to an isolated permalloy layer.

4.6.1 Rotation of Magnetisation Ripple

As already mentioned in Section 3.5.2 the application of an external field along the hard axis of an isolated permalloy layer, which starts uniformly magnetised along the easy axis, leads to the coherent rotation of magnetisation towards the field direction. Assuming that the contrast, which arises from ripple, is perpendicular to the average direction of magnetisation, M , then it is possible to plot the angle between M and the easy axis as a function of applied field. This was done, using Fresnel imaging, for an isolated permalloy layer (thickness=10nm) as well as for spin-valves with t_{Cu} = 1.5, 2.2 and 3.0nm. The results are shown in Fig 4.15 and as expected the ripple from the single permalloy layer experienced a full rotation of 90° , indicative of M rotating by the same angle from the easy axis. The ripple from the spin-valves, however, only rotated to $\approx 45^\circ$ at a rate which was dependent on the spacer layer thickness. Fig 4.16a-d) shows such a rotation for a spin-valve with t_{Cu} = 3.0nm. The ripple rotated quite freely, Fig 4.16(a-c), until reaching $\approx 45^\circ$, from the easy axis, where after no further rotation was observed and increasing the applied field only led to a decrease in the ripple contrast. This decrease in ripple contrast made it difficult to deduce the direction of M_{free} when the applied field was increased much above that required for a 45° rotation of ripple. Such behaviour would tend to imply alignment between the free layer magnetisation, M_{free} , and the applied field even though the direction of ripple is not indicative of this.

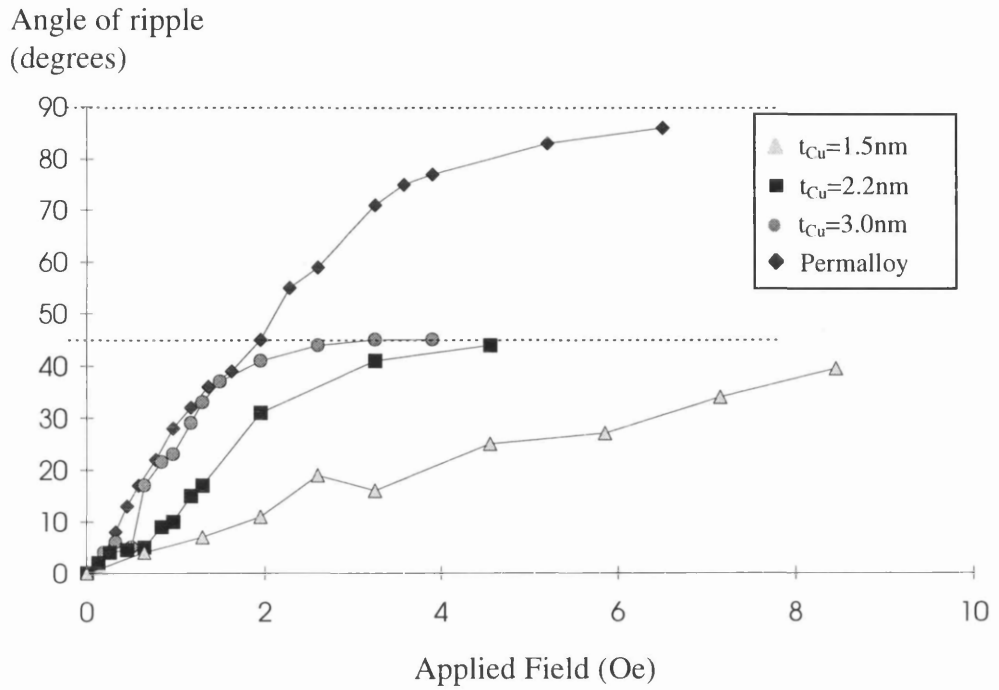


Fig 4.15: Rotation of ripple as a function of applied field, as deduced from Fresnel images. The field is applied orthogonal to the biasing direction

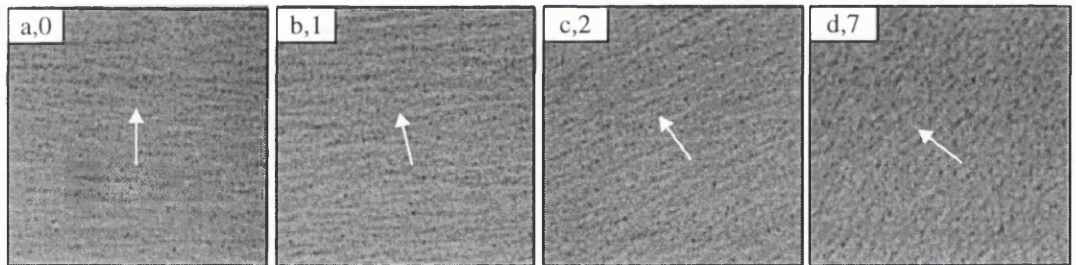
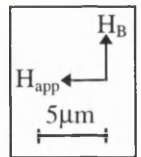


Fig 4.16: Fresnel images showing the rotation of ripple for fields orthogonal to the biasing direction. The number quoted with each figure is the applied field in Oe.



The observed variation in the rate of rotation with t_{Cu} was expected and may be quite simply attributed to the increase in ferromagnetic coupling which arises for a decreasing spacer layer thickness (Rijks et al, 1994). The rotation of the spin-valve ripple to $\approx 45^\circ$ was, however, surprising and could be caused by either M_{free} being constrained to lie within 45° of the biasing direction or by the ripple contrast, as imaged in the TEM, not

always being transverse to the free layer magnetisation. In order to resolve which of these is responsible for this behaviour the technique of low angle diffraction, LAD, was implemented. This technique, which was described in Section 2.4.3, allows the direction of magnetisation to be assessed, independently from magnetisation ripple. It involves imaging the central diffraction spot from the specimen which, due to the Lorentz deflection, is split into sub-spots. From the orientation of these sub-spots it is possible to deduce the different directions of magnetisation which are present. When doing LAD experiments it is advantageous to have an area of free space in order to have a reference beam in each of the diffraction patterns. This was achieved, quite simply, by using a sample which had a small puncture in the Si_3N_4 window. By aligning the electron beam so that half was on the sample and half was passing undeflected through the hole a reference beam was obtained. The sample chosen for this experiment was a spin-valve with $t_{\text{Cu}}=2.2\text{nm}$ and Fig 4.17(a) shows the field of view from where the diffraction pattern was collected. A 20 Oe field was applied parallel to the biasing direction and the low angle diffraction pattern imaged. As the two ferromagnetic layers were initially parallel this caused a large deflection from the sample area and so the diffraction pattern contained two distinct spots, Fig 4.17(b). The approximate centres of these spots have been indicated on the diffraction pattern. The sample was now rotated 20° and the diffraction pattern recorded again, Fig 4.17(c). This was repeated in 20° intervals until the applied field was a full 180° from the biasing direction and the magnetisations from the two layers were anti-parallel, Fig 4.17(k). As can be seen from this sequence of diffraction patterns the rotation of the spin-valve, with respect to the applied field, resulted in the spot, which arises from the sample, also being rotated by a full 180° degrees. This is indicative of M_{free} being free to rotate and the observed decrease in the distance, between the two spots, is a result of a decrease in the net magnetic moment, which occurs for an increasing component of M_{free} , antiparallel to M_{biased} . From Fig 4.17(k) it is noted that there is still a small deflection, even though the spin-valve is in the antiparallel aligned state. This is due to the different free and biased layer thickness (8 and 6nm respectively) which gives a deflection equivalent to a 2nm permalloy film.

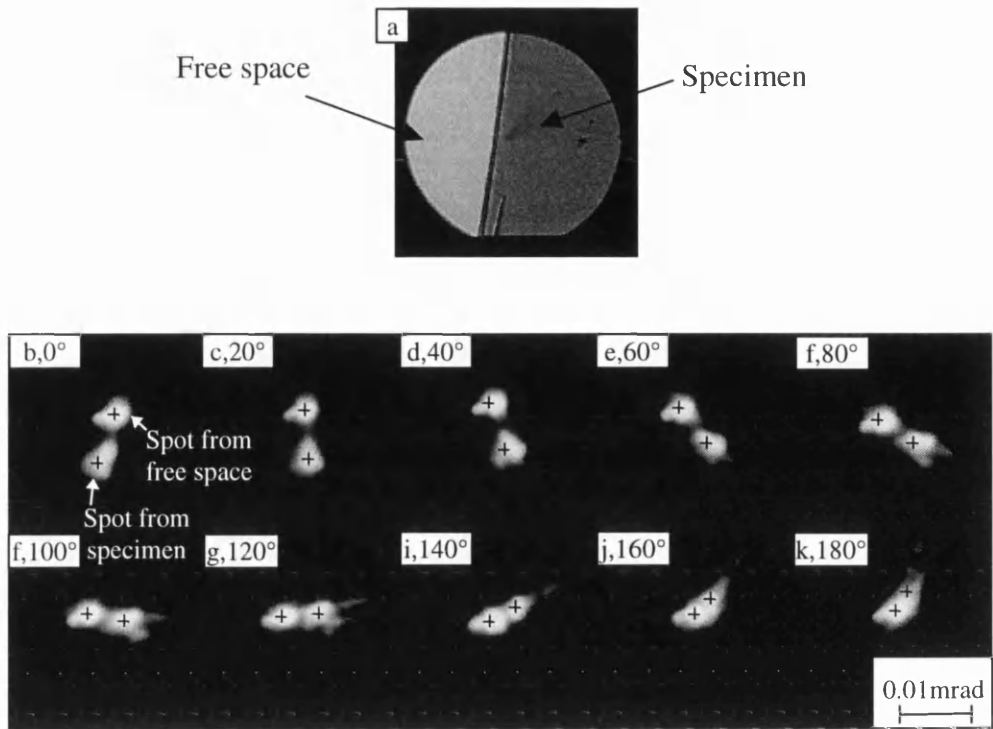


Fig 4.17: Low angle diffraction patterns from a spin-valve when the direction of applied field is rotated away from the biasing direction. The number quoted with each figure is the angle between the biasing direction and the applied field. The approximate centre of each diffraction spot is indicated by a small cross.

The low angle diffraction experiment confirms what others have reported (Kergoat et al, 1995); that the application of external fields, orthogonal to the biasing direction, leads to the coherent rotation of the free layer magnetisation to be aligned with the applied field. The reason why the ripple, as imaged in the TEM, does not also rotate a full 90 degrees must be attributed to the presence of the biased layer. This may cause the direction of ripple contrast to be perturbed so that it is not always transverse to the average direction of M_{free} but instead lies at an intermediate angle. From the results presented in this chapter it is possible that the ripple contrast lies orthogonal to the vector $M_{\text{free}} + M_{\text{biased}}$ rather than only M_{free} . Alternatively the discrepancy between the direction of ripple and the direction of M_{free} may be due to the fact that the recorded image is a superposition of both the free and biased layer states and not simply the ripple arising from M_{free} . It would be interesting to compare these results with experiments using Kerr microscopy

which would have the advantage of only being sensitive to the magnetic induction from one layer in the spin-valve structure.

4.7 SUMMARY

The free layer responses of spin-valves to fields applied either parallel or orthogonal to the biasing direction have been studied in this chapter. In the case of spin-valves where the ferromagnetic layers were permalloy (types (i) and (ii)) the reversal mechanism, for fields applied parallel to the biasing direction, involved many domain walls and the probability of forming 360° wall structures was very high. The reversal of spin-valves with NiFeCo ferromagnetic layers (type(iii)) were found to be relatively un-complicated and 360° walls were rarely observed.

The application of fields orthogonal to the biasing direction led to the rotation of the free layer magnetisation towards the applied field. During such rotations the direction of ripple, as imaged in the TEM, did not appear to rotate with M_{free} and often only rotated to $\approx 45^\circ$ from the biasing direction.

In chapter 5 we discuss possible ways of either reducing, or eliminating, domain walls from the free layer switch and consider both the practical implementation of this and the resultant free layer reversal mechanisms.

CHAPTER 5: THE OPTIMISATION OF FREE LAYER REVERSAL MECHANISMS FOR USE IN GMR SPIN-VALVE HEADS

5.1 INTRODUCTION

In the previous chapter the free layer reversal of spin-valves which had co-linear easy axis and biasing directions were studied. It was observed, from these experiments, that free layer reversals frequently contained many domain walls and, for spin-valves with ferromagnetic layers of permalloy, the probability of forming 360° structures was considerably higher than in the equivalent isolated permalloy layers. As remarked in chapter 4, the presence of a large number of domain walls in the free layer reversal of a magnetoresistive sensor results in Barkhausen noise and distortion in the output of a working head. For this reason we investigate, in this chapter, possible ways of either decreasing or eliminating the number of domain walls involved in free layer reversals.

5.2 UTILISING THE DEMAGNETISING FIELD

The demagnetising energy of a ferromagnetic body may be utilised in a spin-valve in order to encourage the coherent rotation of the free layer magnetisation, M_{free} . The shape of a spin-valve sensor is often rectangular and this results in a demagnetising field which is directed along the long axis of the sensor. The situation is depicted schematically in Fig 5.1 and if the width, w , is sufficiently large, compared with its height, h , then M_{free} lies predominantly along the long axis. In reality, however, w is often not sufficient to overcome the demagnetising effects of shape anisotropy and interactions arising from the biased layer magnetisation. This results in concertina domain structures forming in the free layer which are closely related to those observed in elements of permalloy, (see McVitie et al (1988) for permalloy elements and chapter 9 of this thesis for spin-valve elements.)

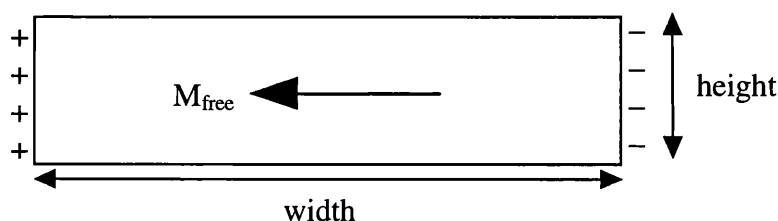


Fig 5.1: Idealised domain structure for $w < h$

As already mentioned in the discussion of spin-valve properties in chapter 4 the easy axes of the ferromagnetic layers and the exchange biasing direction, are defined by the direction of the deposition field. If the spin-valve is rectangular, as in Fig 5.1, then deposition in a field, which is oriented along the short axis of the structure, results in a biasing field of $\approx 150\text{-}250$ Oe which is also directed along this axis, (the exact biasing field is dependent on the thickness of the ferromagnetic layer). This field is sufficiently strong that the majority of biased layer magnetisation overcomes shape anisotropy and lies parallel to the short axis of the sensor. As well as the induced anisotropy, which also favours parallel alignment with the short axis, M_{free} now experiences a coupling field (≈ 10 Oe) in this direction. In some cases, however, the demagnetising energy is sufficiently strong that, in the absence of an applied field, M_{free} does not lie parallel to the biasing direction. Such a situation is advantageous for sensor applications as fields from electrical biasing, which are parallel to the short axis, are therefore at an angle to M_{free} . Electrical biasing, which is often achieved by introducing a small DC off-set on top of the AC sense current, can therefore be used to rotate M_{free} to lie orthogonal to that of the biased layer. This results in stray fields from a passing tape or disk being orthogonal to the average direction of M_{free} and therefore induces rotations of M_{free} in either a clockwise or anticlockwise direction from the zero field orthogonal configuration. Thus the sensor is operated within the most linear part of the MR characteristic and also over the largest dynamic range possible (Heim et al, 1994). Since fields from a passing tape or disk do not induce any domain walls in the free layer there is no Barkhausen noise or distortion in the output of the head.

A typical sensor geometry is depicted, schematically, in Fig 5.2 and has been shown to work by IBM in a prototype disk drive head, (Tsang et al, 1994).

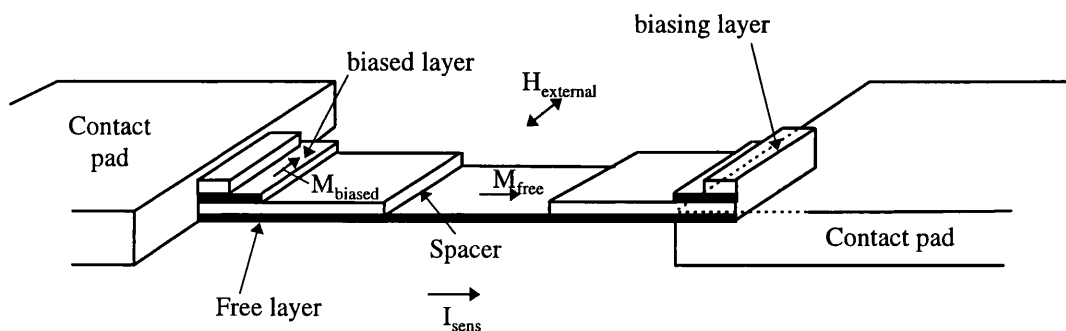


Fig 5.2: Schematic of sensor geometry used by Tsang et al (1994) and Freitas et al (1994)

Freitas et al (1994) have also achieved considerable success with the incorporation of similar sensor geometries into QIC (Quarter Inch Cassette) tape head systems.

5.3 CHANGING THE BIASING DIRECTION

In the sensor geometry of section 5.2 an orthogonal configuration of free and biased layer magnetisations was achieved due to the shape anisotropy of the sensor element and the application of a small biasing field. When, however, the height of the sensor is increased the shape anisotropy is lowered and consequently, even with electrical biasing, it is often not possible to obtain an orthogonal configuration of magnetisation in both ferromagnetic layers. This is the case in the Philips DCC head structure where the active sensor dimensions are typically $80\mu\text{m} \times 10\mu\text{m}$. In such sensors there is a near parallel alignment of magnetisation in the free and biased layers with the height of the sensor and this results in a free layer response, to fields from a passing tape, similar to those observed in chapter 4. For sensors with large heights it is therefore necessary to use another method in order to establish an orthogonal configuration between magnetisations in the two ferromagnetic layers. One possible method is to move from a parallel arrangement of easy axis and biasing directions to one which is perpendicular. For such a configuration the combined effects of the free layer anisotropy and demagnetisation energy often result in a non-parallel alignment between the magnetisation in the two ferromagnetic layers, in the absence of an applied field. Thus, as in sensors with smaller heights, fields from electrical biasing are at an angle to the free layer magnetisation and can therefore be applied in order to obtain an orthogonal configuration of magnetisations in the absence of fields from a passing tape or disk.

One method of attaining an orthogonal configuration of free layer easy axis and biasing directions is to deposit the free layer of the spin-valve in the presence of a field which is parallel to the width of the sensor, after which the field is rotated by 90° and the other layers in the spin-valve are deposited. This results in the induced anisotropy of the free layer being parallel to the width of the sensor (Rijks et al, 1994). While this is satisfactory for prototype head structures, and has resulted in stable DCC heads, it is not a convenient process for head structures which must be mass produced. Thus another method of obtaining a crossed configuration, which is more suited to production, has been developed

by Folkerts et al (1994). This method is only possible for spin-valves biased by FeMn and involves initially depositing the whole spin-valve structure in the presence of a field, directed along the width of the sensor. After deposition the spin-valve is heated above the blocking temperature of FeMn (140°C) and upon cooling, in the presence of a 100 Oe field, directed along the short axis of the sensor, an orthogonal configuration of free layer easy axis and biasing directions is obtained.

It may be thought that an annealing temperature of 140°C would be insufficient to cause any substantial realignment to atom pairs in the free layer. This however may not be the case and initial studies of annealed spin-valves indicate that, even for such low temperatures, the free layer easy axis becomes less well defined after annealing. It has also been found that the ferromagnetic coupling between the layers increases after annealing, (Kools et al, 1995).

In the following sections of this chapter we investigate the free layer reversal of what were termed type(i) spin-valves in chapter 4. These were annealed so that the biasing direction and the free layer easy axis were approximately orthogonal. In the later sections it is shown that, under the right conditions, a coherent rotation of free layer magnetisation can be obtained.

5.4 ZERO FIELD STATES

In this section we use the Fresnel mode of electron microscopy to study the zero field states of spin-valves which have a variety of Cu spacer layer thicknesses. By assuming that, in zero applied field, the ripple is orthogonal to \mathbf{M}_{free} it is possible to deduce the direction of free layer magnetisation. Figs 5.3(a-g) show the zero field states of various spin-valves and the number quoted with each is the thickness of the Cu spacer layer, t_{Cu} , in nanometres. Depending on the value of t_{Cu} we shall term the spin-valves, weakly coupled ($t_{\text{Cu}} > 4.0\text{nm}$), moderately coupled ($t_{\text{Cu}} = 3.0, 3.5\text{nm}$) or strongly coupled ($t_{\text{Cu}} = 2.0\text{nm}$). In the zero field state of any continuous spin-valve multilayer there are two competing energy terms acting on the free layer magnetisation. These are; (a) that which arises from the anisotropy of the free layer and (b) that which arises from the ferromagnetic coupling between the two ferromagnetic layers. For the spin-valves studied in this thesis it was found that, provided the ferromagnetic layers were only relatively weakly coupled, ($t_{\text{Cu}} > 4\text{nm}$) the anisotropy of the free layer was dominant over the coupling field, H_0 . Consequently for weakly coupled

spin-valves, in the absence of an applied field, the majority of M_{free} was aligned with the easy axis, EA_{free} , Figs 5.3(a-c). Due to both the anisotropy field, H_K , and H_0 being relatively small it was possible for domain structures to exist in the zero field states of weakly coupled spin-valves, Figs 5.3(a) and (c).

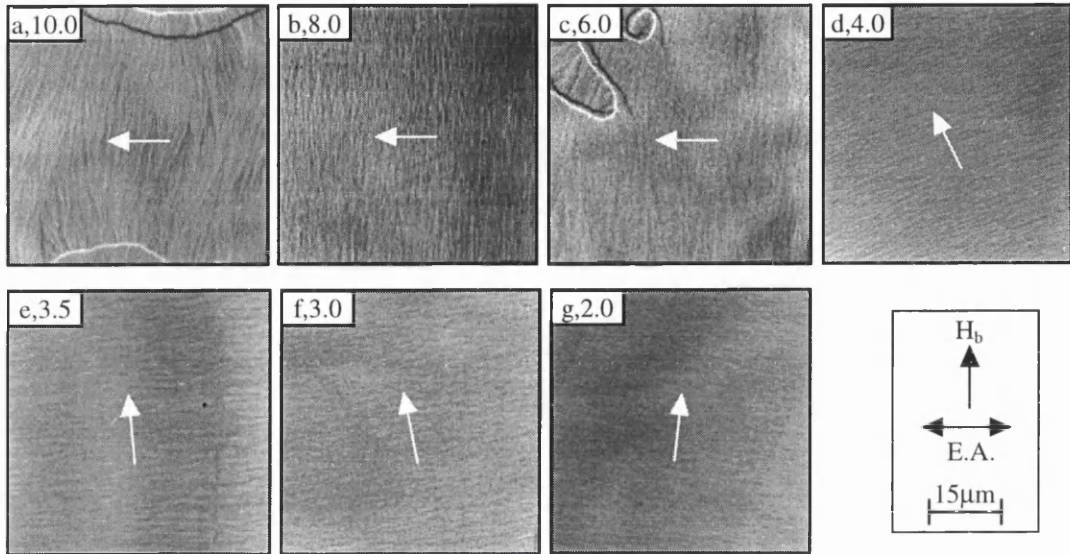


Fig 5.3(a-g): Zero field states of spin-valves with varying Cu spacer layer thickness

The coupling field which occurs between the two ferromagnetic layers increases in strength for decreasing values of t_{Cu} . As t_{Cu} is decreased there comes a point where M_{free} is no longer aligned with the free layer easy axis. This occurs for a t_{Cu} of between 4-6nm and the zero field state of a $t_{\text{Cu}}=4\text{nm}$ spin-valve is shown in Fig 5.3(d). As t_{Cu} was further reduced, to below 4nm, M_{free} tended to be roughly aligned along the biasing direction, as in Figs 5.3(e-g). The relatively large value of H_0 in these spin-valves constrained M_{free} to be single domain in zero applied field. It is important at this point to make a brief note about the zero field states which are shown in Figs 5.3(e-g). In the case of spin-valves, with $t_{\text{Cu}} < 4\text{nm}$, the direction of ripple after annealing often implied a direction of M_{free} which was not parallel to the direction of the annealing field. This unusual result could be corrected for by re-annealing and for some of the states shown in Fig 5.3(e-g) this has been done. Since this affects both the coupling between the ferromagnetic layers and the anisotropy of the free

layer, the micrographs of Fig 5.3(e-g) should be regarded as a guide to the zero field states rather than what is always observed. It is also important to realise that the results in Fig 5.3(e-g) are for continuous films which differ from a working sensor in that there is no contribution from shape anisotropy. In a structured sensor this extra contribution would allow M_{free} to be aligned along EA_{free} even when H_0 is significantly increased.

5.5 FRESNEL STUDIES OF FREE LAYER REVERSAL MECHANISMS FOR FIELDS THAT ARE PARALLEL TO THE BIASING DIRECTION.

As with parallel spin-valves the free layer reversal mechanism, when the easy axes and the biasing directions are orthogonal, is of vital importance when considering sensor applications. In the following sections we therefore consider the free layer reversal for orthogonal spin-valves when the applied field is parallel to the biasing direction.

5.5.1 Spin-valves with Weakly Coupled Ferromagnetic Layers

The free layer response of a weakly coupled spin-valve, $t_{\text{Cu}}=10\text{nm}$, is shown in Figs 5.4(a-l). Upon applying a +3.0 Oe field, aligned approximately anti-parallel with the biasing direction, M_{free} coherently rotates to be aligned with the field direction, Fig 5.4(a). Relaxation of this field results in the coherent rotation of M_{free} back towards one direction of the free layer easy axis, Figs. 5.4(a-d). Upon applying a field in the opposite direction the continued rotation of M_{free} is obtained and alignment with H_{app} is reached for a field value of -3.0 Oe, Fig 5.4(g). When this field is relaxed M_{free} does not coherently rotate towards one direction of the easy axis and instead different areas rotate in either a clockwise or an anti-clockwise sense. This inevitably leads to domain wall nucleation between areas of different sensed rotations, Fig 5.4(i). Increasing H_{app} in a positive sense again results in the rotation of M_{free} towards the field direction and the creation of 360° loops in the final state, Fig5.4(l). These loops are not particularly stable and can be annihilated by the application of moderate fields (typically $\approx 20\text{-}40$ Oe).

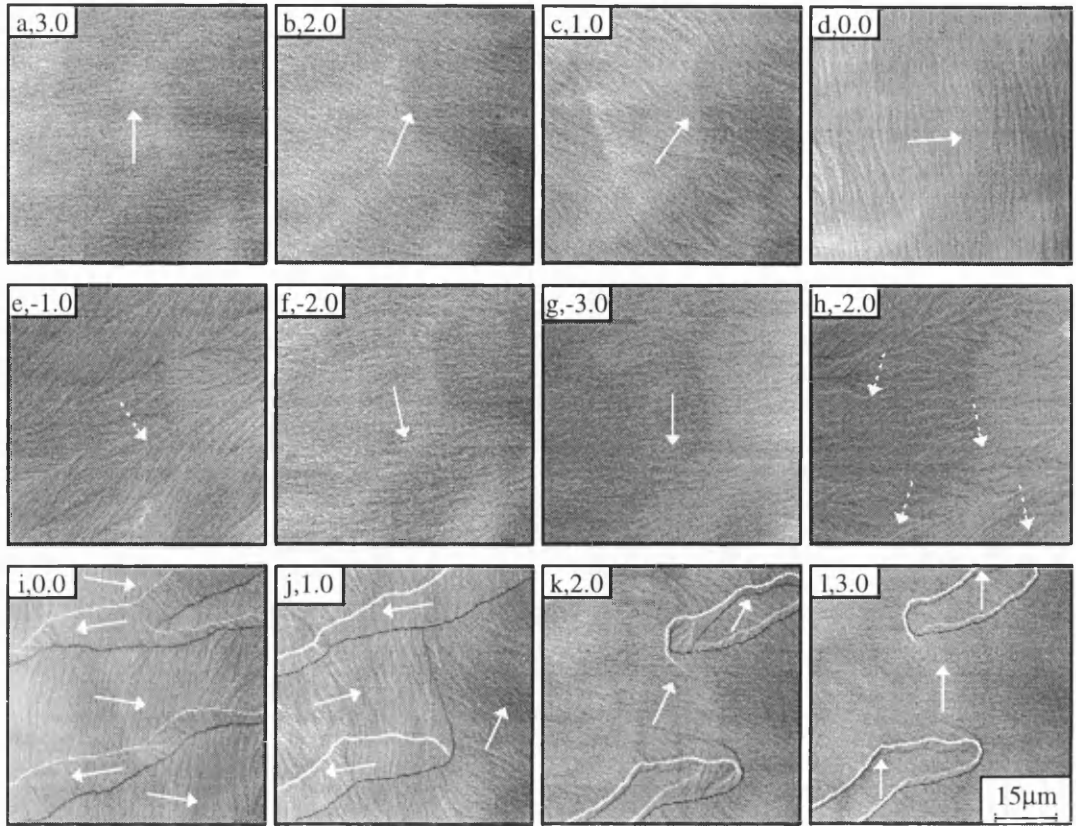
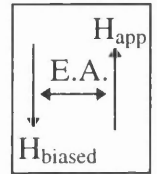


Fig 5.4(a-l): Free layer reversal of a weakly coupled spin-valve ($t_{cu} = 10\text{nm}$)



Although the coherent rotation of M_{free} which is observed in Figs 5.4(a-g) may seem a departure from that of a permalloy hard axis reversal this may not be due to the presence of the underlying biased layer. Such a reversal may be explained in terms of a slight misalignment between the hard axis of the free layer and H_{app} , together with a small stray field from the objective lens of the electron microscope. Saying this, however, it is noted that 360° loops, which are a characteristic feature of spin-valve reversals, are present in Fig 5.4(l). This suggests that although the general free layer reversal is similar to that which could be observed for an isolated permalloy layer the presence of domain walls may result in stray fields which interact with charge distributions in the biased layer.

An important point to take from the magnetising sequence of Fig 5.4(a-l) is that unlike the more strongly coupled spin-valves of chapter 4, where the easy axes and the biasing direction were parallel, the application of a field orthogonal to the direction of M_{free} , leads to the coherent rotation of ripple by a full 90° . In the spin-valves of chapter 4 the application of fields orthogonal to the zero field direction of M_{free} led to the ripple rotating by only $\approx 45^\circ$ from the original direction.

5.5.2 Spin-valves with Moderately Coupled Ferromagnetic Layers

In the case of the spin-valves studied in chapter 4 deposition in a field ensured a perfect alignment between the free layer easy axis and the biasing direction. When orthogonal spin-valves are fabricated the exact orientation of the biasing direction with respect to the free layer easy axis is determined by the accuracy with which the post-deposition annealing field is aligned. Since this is aligned by eye there may be a significant error ($\approx 10^\circ$) in the orientation of the biasing direction. While this will probably have little effect on free layer reversals of spin-valves where the anisotropy of the free layer is dominant the situation may be different when the spacer layer thickness is reduced and the coupling becomes stronger. One could envisage that a slight mis-alignment for spin-valves with $t_{\text{Cu}} < 4.0\text{nm}$ would result in the coherent rotation of M_{free} for fields applied along the hard axis of the free layer. We, however, will not investigate the influence of variations in the exact biasing direction and will instead assume that for moderately or strongly coupled spin-valves that the biasing direction is equivalent to the direction of M_{free} in zero field.

The direction of M_{free} in zero field, or the biasing direction as it will now be referred to, can be determined experimentally by a simple method. Fields are applied at small angles to the approximate annealing direction and, as will be shown later, this results in the rotation of different fractions of M_{free} towards the field direction, in either a clockwise or an anticlockwise sense. Due to dispersion in the easy axis and or dispersion in the biasing direction perfect alignment of H_{app} will result in approximately 50% of M_{free} rotating in a clockwise sense while the remainder rotates in an anti-clockwise sense. When this is observed it is assumed that the applied field is exactly parallel to the average biasing direction.

Using the above method H_{app} was aligned with the biasing direction of a moderately coupled spin-valve ($t_{\text{Cu}}=3.0\text{nm}$). The resulting free layer reversal mechanism, for fields applied in this direction, is shown in Figs 5.5(a-l). As expected, in the absence of an applied field, M_{free} was single domain, Fig 5.5(a). As H_{app} is increased, in a negative direction, there is a large divergence in ripple, Fig 5.5(b), followed by the rotation of M_{free} ,

in different areas of the film, either in a clockwise or an anticlockwise sense, Fig 5.5(c-d). Further increases in H_{app} , in the negative direction, lead to the continued rotation of M_{free} towards the direction of field, Fig 5.5(e), and the formation of 360° walls between areas of opposite sensed rotations. These walls prevent the otherwise complete antiparallel alignment of magnetisation in the ferromagnetic layers, Fig 5.5(f). Relaxation of the applied field results in the coherent rotation of M_{free} in the left hand side of the window towards the biasing direction, Fig 5.5(g-l). This, however, is not the case in the right hand side of the window where decreasing the applied field results in a large increase in dispersion, Fig 5.5(h).

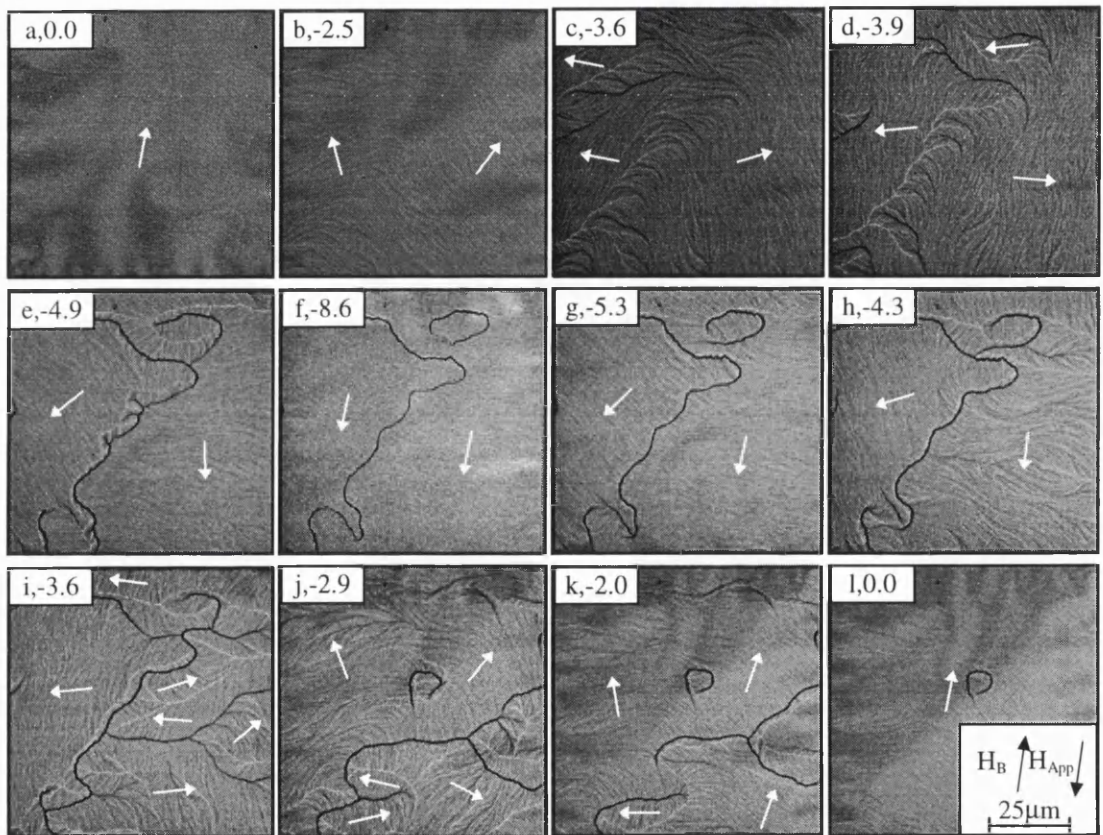


Fig 5.5(a-l): Free layer reversal for a moderately coupled spin-valve ($t_{Cu}=3.0nm$)

Unlike the switch to an antiparallel state a complicated domain structure is generated, Fig 5.5(i), though further reducing the applied field results in M_{free} returning to an almost complete parallel alignment with the biasing direction, Fig 5.5(l).

When the magnetising sequence of Fig 5.5(a-l) is compared with that of a spin-valve, where the easy axes and the biasing direction are parallel, several differences are noticed.

In the case of parallel spin-valves domain nucleation was the dominant process and domain walls appeared to be of low mobility. The process was, however, unpredictable in that reverse domains suddenly appeared when the applied field was comparable to that of the coupling field. When the easy axes and biasing directions are orthogonal the reversal process is often dominated by the coherent rotation of M_{free} , within different areas of the film. In regions which experienced a coherent rotation of M_{free} the rotation is not single sensed, in that M_{free} rotates $0^\circ \rightarrow 90^\circ \rightarrow 180^\circ \rightarrow 90^\circ \rightarrow 0^\circ$ rather than a full 360° . In areas where complete coherent rotation is not observed M_{free} initially rotated $0^\circ \rightarrow 90^\circ \rightarrow 180^\circ$ but upon relaxation of H_{app} domain nucleation is observed. This is due to different areas within this region rotating in either a clockwise or an anticlockwise direction and so inevitably leads to a complicated structure, such as Fig 5.5(i). From the magnetising sequence of Fig 5.5 it is concluded that for a crossed spin-valve there appears to be less erratic jumps in M_{free} than in the equivalent parallel spin-valve and consequently the MR response should have reduced noise. This is indeed the case and prototype DCC head structures show an increase in signal to noise ratio of around 20dB when orthogonal spin-valves are used instead of parallel, Kools (1995). It is worth noting that for prototype spin-valves heads, with exactly orthogonal easy axes and biasing directions, the yield of heads which have the lowest noise characteristics is rather low. In light of the previous magnetising experiment this may be due to some sensors having an easy axis / field geometry which gives single sensed coherent rotation of M_{free} , while in others a geometry which results in domain nucleation may exist.

5.5.3 Spin-Valves with Strongly Coupled Ferromagnetic Layers

Reducing the spacer layer thickness of a spin-valve below 2.5nm results in strong coupling between the two ferromagnetic layers. Thus for $t_{\text{Cu}} = 2.0\text{nm}$, which in this thesis is a strongly coupled spin-valve, the free layer is significantly stiffer than for those with greater t_{Cu} . Consequently the sensitivity of such a spin-valve is lowered though it is still possible to achieve an anti-parallel alignment of magnetisations in the two ferromagnetic layers. In this section we investigate the free layer response of a strongly coupled spin-valve for fields anti-parallel to the biasing direction. Again an exact alignment of H_{app} with

the biasing direction was achieved by using the method described in section 5.5.2. The resulting response of a spin-valve with $t_{Cu} = 2.0\text{nm}$, to an applied field which was within $\approx 1^\circ$ of the biasing direction is shown in Figs 5.6(a-n).

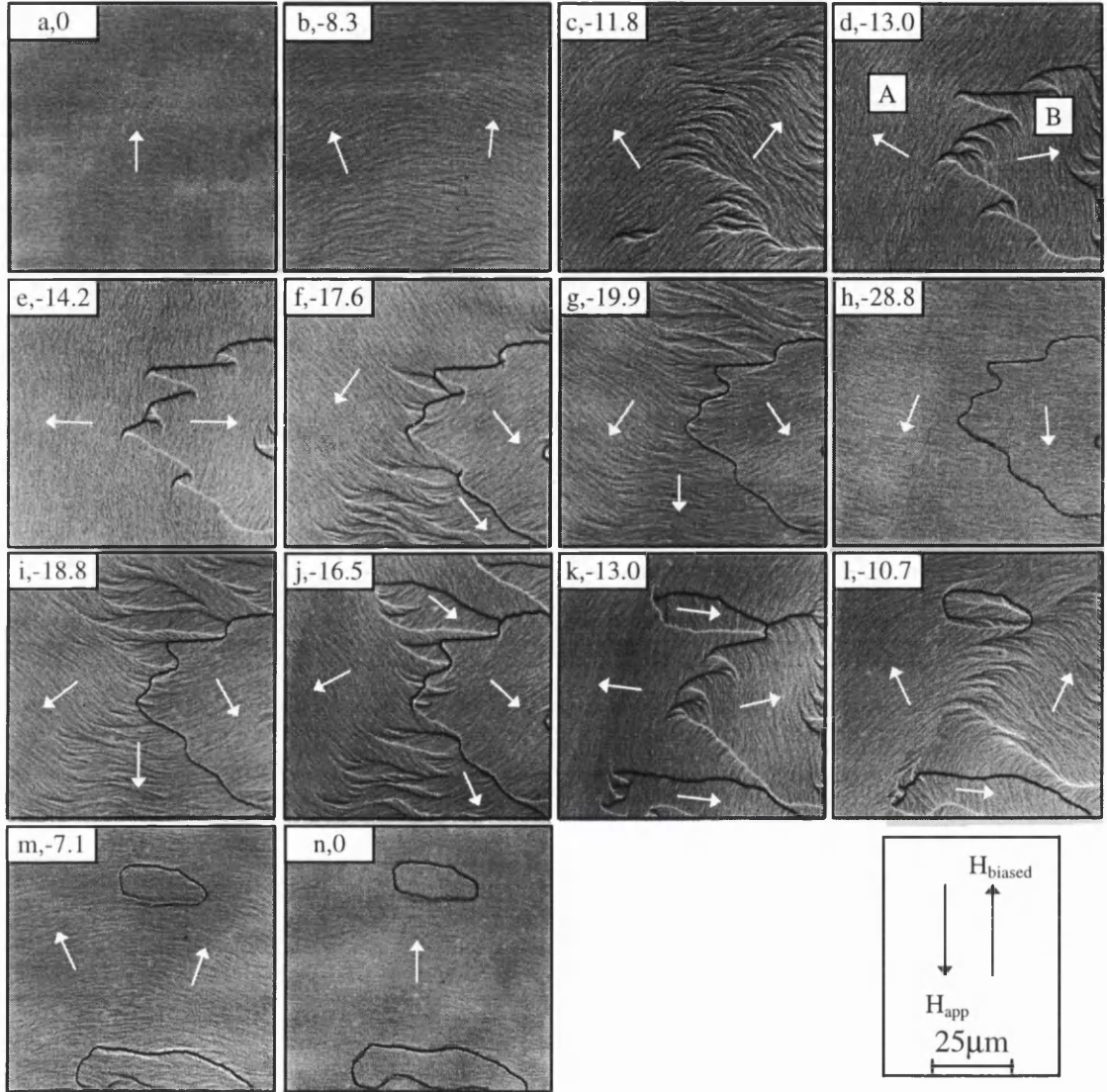


Fig 5.6(a-n): Reversal of free layer in a strongly coupled spin-valve

Upon increasing H_{app} in a negative direction a large increase in ripple is observed, Fig 5.6(b). As for the moderately coupled spin-valve this divergence in M_{free} is followed by the nucleation of walls, Fig 5.6(c), as M_{free} rotates in either a clockwise or an anti-clockwise sense towards the direction of H_{app} . As this rotation continues the average wall angle increases and in Fig 5.6(d) a zigzag wall structure is formed between the two areas of opposite sensed rotations. These areas are labelled as area A and area B on Fig 5.6(d). As

H_{app} is further increased in a negative direction small domains, with low angle walls, nucleate within area A, Fig 5.6(f). These appear to have the same direction of M_{free} as that of area B. Increasing H_{app} further negative leads to a decrease in ripple and eventual alignment of M_{free} , in both areas, Fig 5.6(h). As for the moderately coupled spin-valve a 360° wall is located at the boundary between areas which rotated in different senses. As H_{app} is relaxed there is again nucleation of some small domains in area A, Fig 5.6(i-j). When $H_{app} = -13.0$ Oe, Fig 5.6(k), the majority of area B is seen to have rotated in an anti-clockwise sense where as the majority of area A has rotated in a clockwise sense. As we relax H_{app} further the previously formed 360° boundary wall unwinds, Fig 5.6(l). We do, however, form some new 360° walls which again are at the boundaries between areas of opposite sensed rotations, 5.6(m-n).

On the whole the free layer reversal of a strongly coupled spin-valve is similar to that of one which is moderately coupled. The fields required for free layer reversal were, however, higher due to the presence of increased coupling between the two ferromagnetic layers.

5.6 THE APPLICATION OF FIELDS AT SMALL ANGLES TO THE BIASING DIRECTION

In the previous sections of this chapter the free layer reversal of spin-valves, for fields applied parallel to the biasing direction were investigated. In the case of moderately and strongly coupled spin-valves it was found that, depending on the specific area of the film, M_{free} could rotate towards the field direction in either a clockwise or an anti-clockwise direction. It is, however, possible to encourage the single sensed rotation of M_{free} , in all areas, by varying the angle between H_{app} and the biasing direction. This angle will be referred to as the off-set angle, θ , and in this section the value of θ required for coherent rotation will be established.

The biasing direction of a spin-valve with a copper spacer layer of 2.0nm was determined using the technique described in section 5.5.2. The off-set angle was then varied in steps of 0.5° between $\pm 4^\circ$ from anti-parallel to the biasing direction. As expected fields in these directions led to the rotation of M_{free} which, depending on the exact area of the film, were

either in a clockwise or anti-clockwise sense. The relative fraction of each rotation was dependent on θ and Figs 5.7(a-m) show single micrographs which were taken from magnetising sequences at different off-set angles.

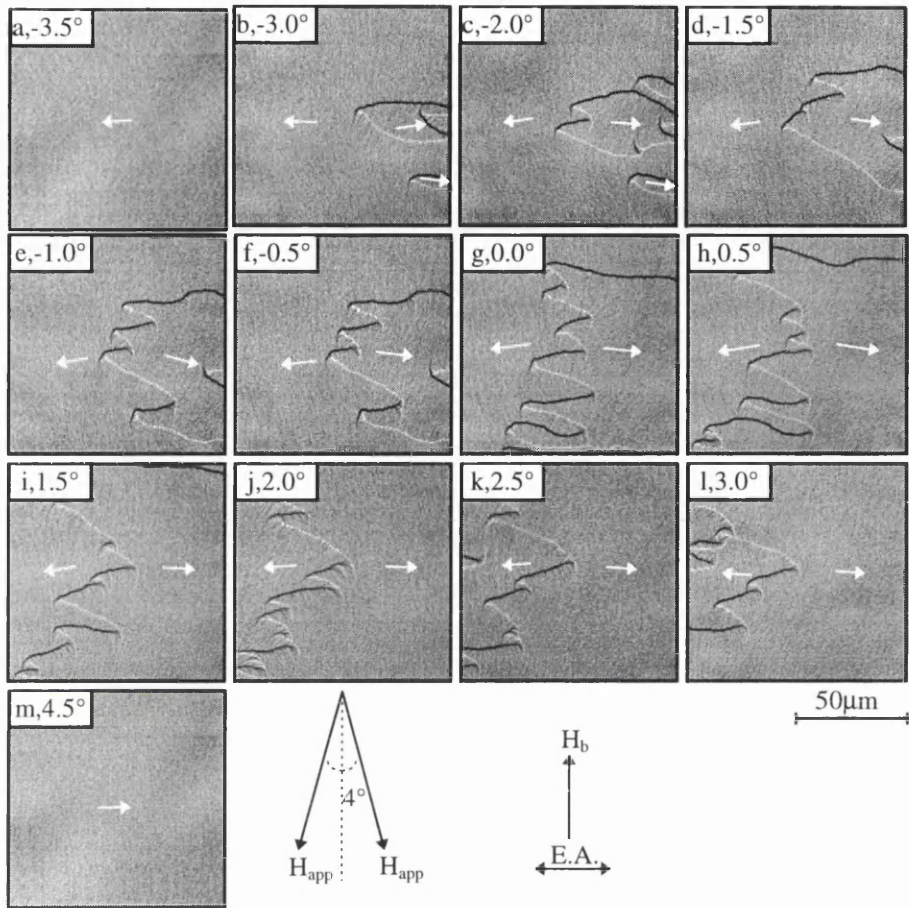


Fig 5.7(a-m): Mid reversal states for a -15 Oe field applied at small off- set angles

These micrographs represent how M_{free} rotates as a function of θ and were taken when $H_{\text{app}} = -15$ Oe. From Fig 5.7(a) it is seen that an off-set angle of $\theta = -3.5^\circ$ leads to the coherent rotation of M_{free} in an anti-clockwise sense. As θ is increased to -3° , Fig 5.7(b), there is a small area in which clockwise rotation of M_{free} is observed. As θ is further increased a larger fraction of M_{free} rotates in a clockwise sense, Figs 5.7(c-g). When $\theta = 0^\circ$, H_{app} and the biasing direction are perfectly aligned, and approximately 50% of M_{free} rotates in a clockwise sense rather than anti-clockwise. As one would expect making θ positive results in a larger fraction of M_{free} rotating in a clockwise manner, Figs 5.7(h-l), and full clockwise rotation is achieved for $\theta = 4.5^\circ$, Fig 5.7(m).

From the observations of chapter 4 it was clear that the ripple contrast in a biased layer of permalloy is much reduced when compared to that of a single permalloy layer. The

magnetisation ripple which did exist however may be thought of as a dispersion in the biasing direction of a spin-valve. Thus for fields parallel to the biasing direction we can interpret the rotation of M_{free} in either a clockwise or an anti-clockwise sense as being due the combined effects of dispersion in the biasing direction and the free layer easy axis.

It is possible to obtain quantitative information from the micrographs of Fig 5.7(a-m) by a simple method developed at Glasgow University. Initially the images are digitised and fed into edge detection software which detects domain walls as edges. Further processing allows the pixels within each domain to be assigned either a “0”, if M_{free} rotates in an anti-clockwise sense or a “1” if it rotates in a clockwise sense. Thus binary images similar to Fig 5.8(b) may be constructed from which it is simple to deduce an accurate estimate of the fraction of M_{free} which reverses in an anti-clockwise direction as a function of θ .

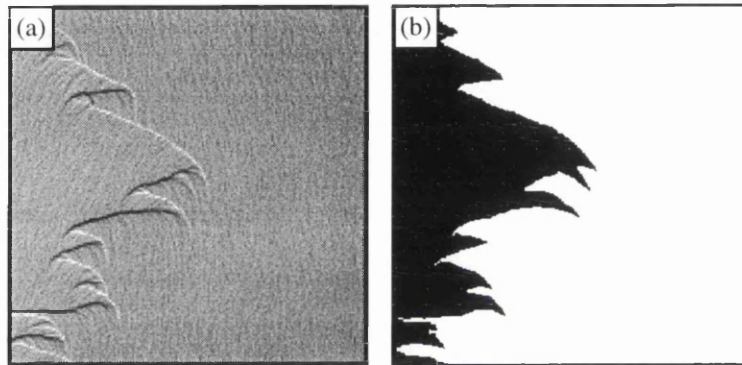


Fig 5.8: (a) Typical image to be analysed, (b) resulting binary image

Binary images were constructed from the states of Figs 5.7(a-m) and used to deduce the fraction of M_{free} which rotates in an anti-clockwise direction as a function of θ , Fig 5.9. From this graph it is estimated that for the spin-valve studied here, where $t_{\text{Cu}}=2.0\text{nm}$, there is a combined dispersion in the biasing direction and the free layer easy axis of $\approx 3\text{-}4$ degrees. Such experiments have not been carried out quantitatively for moderately coupled spin-valves though would certainly be of interest.

The fact that coherent rotation of M_{free} can be achieved by an intentional misalignment of H_{app} , with respect to the biasing direction, is of great significance for the application of spin-valves as MR sensors. Such rotations would lead to practically noise free sensors and for this reason the coherent rotation of M_{free} will be studied in greater detail in the next section of this chapter.

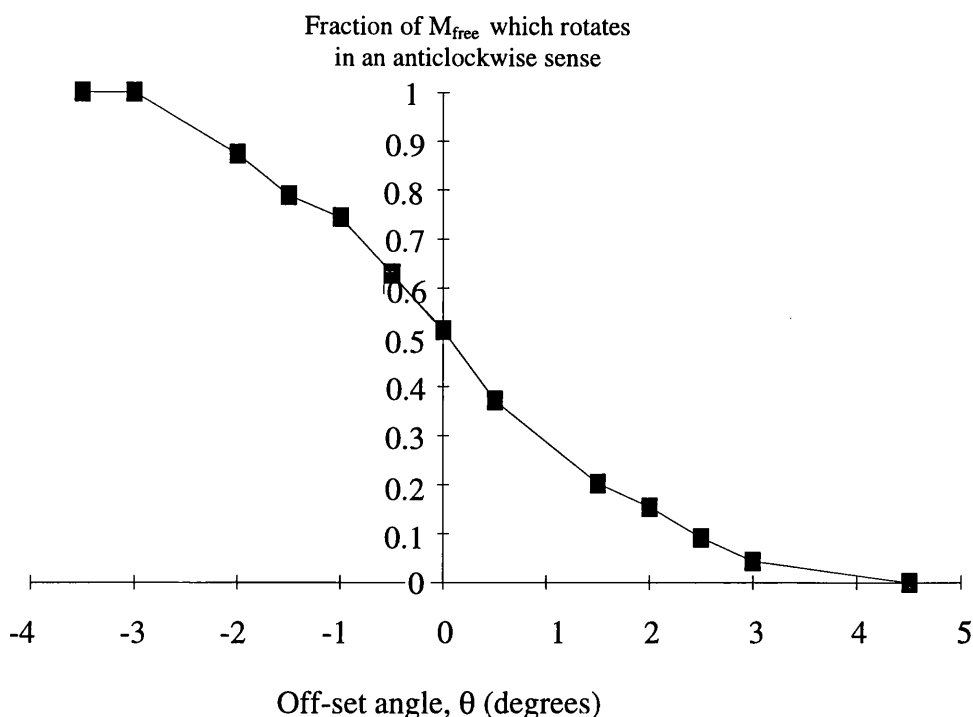


Fig 5.9: Fraction of M_{free} which rotates in an anticlockwise sense vs off-set angle θ

5.7 THE COHERENT ROTATION OF FREE LAYER MAGNETISATION

In the previous section it was established that for a spin-valve with $t_{Cu} = 2.0\text{nm}$ the coherent rotation of M_{free} could be obtained by deliberately off-setting the biasing direction and H_{app} by $\approx 3-4^\circ$. In this section we investigate further the coherent rotation of M_{free} and by using both the Fresnel and DPC modes of electron microscopy, monitor how M_{free} varies as a function of H_{app} .

Since in this section the only magnetic contrast which will be imaged is that of magnetisation ripple it is sensible to use a spin-valve which displays a large amount of ripple but also has a zero field direction of M_{free} which is approximately parallel to that of the deposition field. Thus the spin-valve chosen for this experiment has $t_{Cu} = 3.5\text{nm}$ and Figs 5.10(a-s) show Fresnel images of the coherent rotation of M_{free} when there is an off-set angle between the biasing direction and H_{app} .

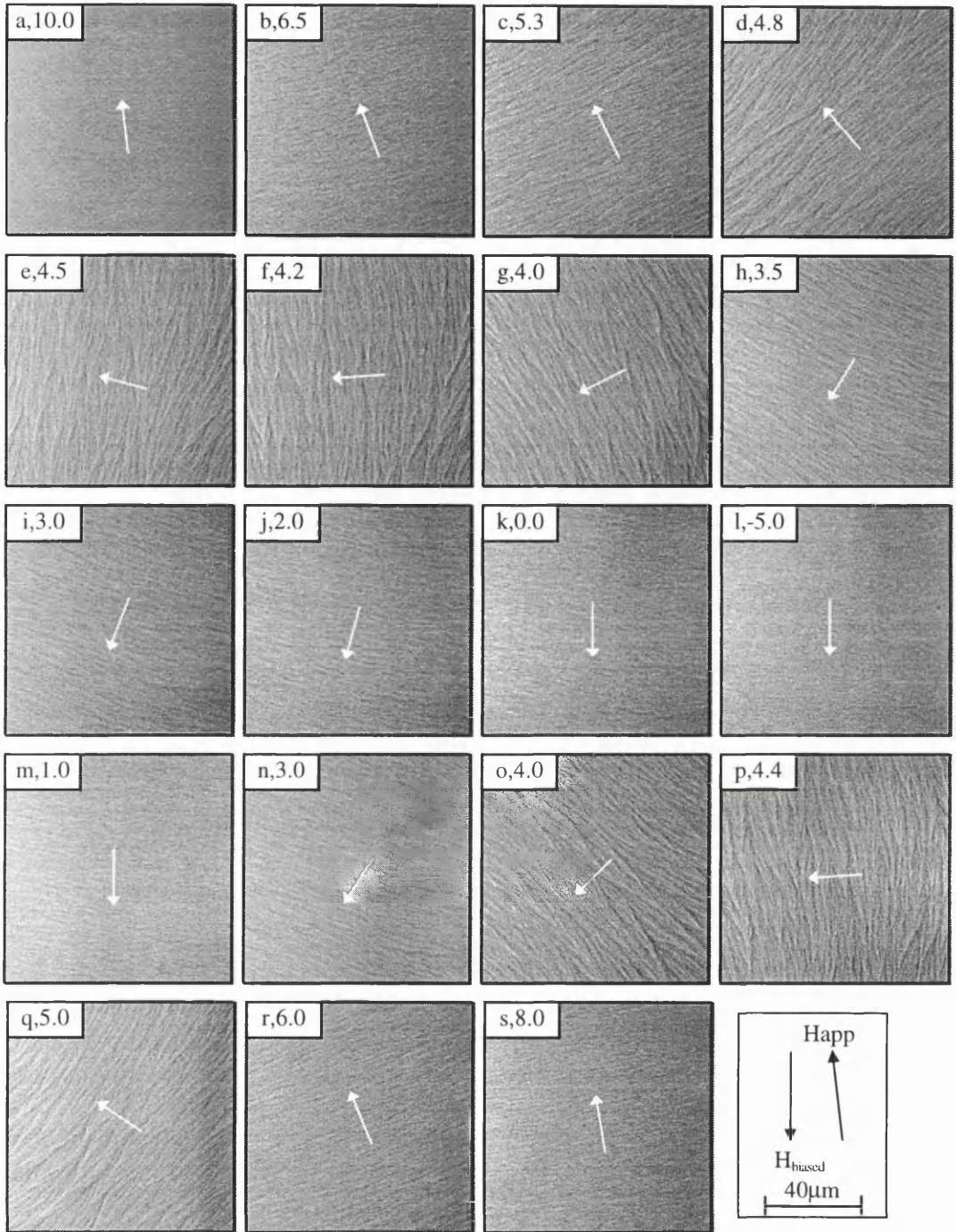


Fig 5.10(a-s): Fresnel images showing the coherent rotation of M_{free}

This magnetising sequence shows that although there is no introduction of domain walls for the free layer reversal there is a very large increase in dispersion when M_{free} is approximately orthogonal to the bias field direction. This is the direction of the free layer easy axis and the large increase in ripple is observed for both decreasing, Figs 5.10(c-h), and increasing field values, Figs 5.10(o-q). It is noted that the rotation of ripple is one sided

i.e. M_{free} rotates $0^\circ \rightarrow 90^\circ \rightarrow 180^\circ \rightarrow 90^\circ \rightarrow 0^\circ$ rather than $0^\circ \rightarrow 90^\circ \rightarrow 180^\circ \rightarrow 270^\circ \rightarrow 360^\circ$. This phenomenon of one sided rotation is observed in all spin-valves when the condition for coherent rotation is satisfied and can be understood quite simply by considering the schematic of Fig 5.11. If there were no dispersion in either the free layer easy axis or the biasing direction then any non-zero value of θ would lead to the single sensed coherent rotation of M_{free} . When, however, dispersion is present then the off-set angle must be greater than the maximum dispersion in order to ensure coherent rotation.

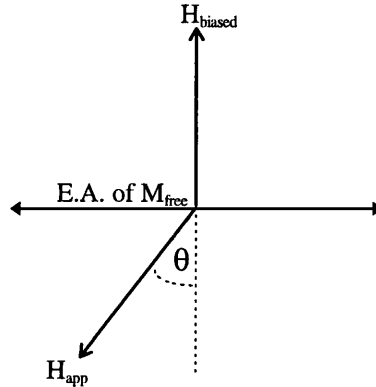


Fig 5.11: Illustration of H_{app} / biasing direction geometry for coherent rotation.

The observed increase in magnetisation ripple as M_{free} approached the free layer easy axis is probably due to the fact that at this point the applied field exactly cancels out that which arises from ferromagnetic coupling. Thus the only torque acting on M_{free} , at this point, is that which arises from dispersion. Consequently the intensity of ripple is comparable to that observed in an isolated permalloy layer rather than that of a free layer in a spin-valve.

As was discussed in previous chapters Fresnel imaging is not particularly well suited to quantitative studies of magnetic structures. Therefore in order to gain a more quantitative understanding of how M_{free} rotates, under the application of an external field, the previous experiment was repeated using the DPC mode of electron microscopy. Using the 8 segment detector which was described in chapter 2, Fig 5.12(a), it is possible to collect maps which are sensitive to magnetic induction in four different directions. These directions are indicated in Fig 5.12(b) and during the following magnetising experiment all four signals are collected simultaneously. From the four collected images, that which shows maximum sensitivity closest to the direction of ripple is chosen to represent the magnetisation distribution. These are shown in Figs 5.13(a-n) where single sensed rotation of M_{free} , is observed.

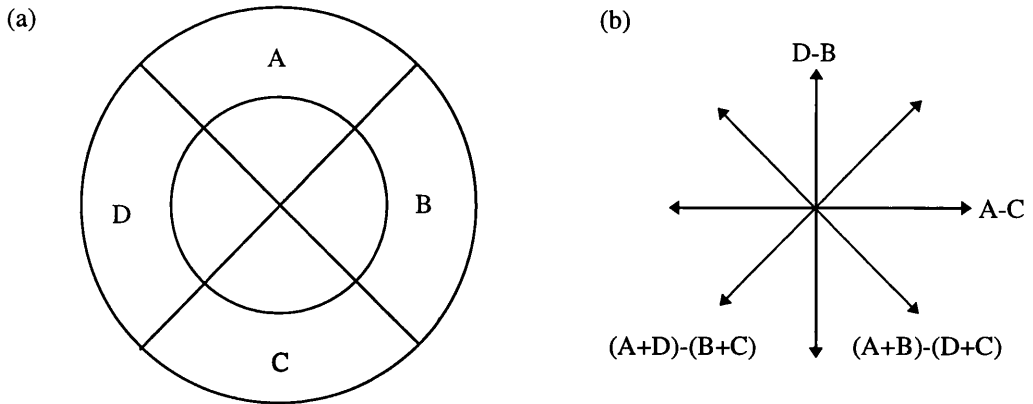


Fig 5.12: (a) 8 segment DPC detector, (b) mapping directions for various signals.

The mapping direction is never more than 22.5° away from the average direction of ripple and next to each image is the Fast Fourier Transform (FFT) of the DPC image. These allow us to study the spatial distribution of the free layer ripple as M_{free} rotates.

In the zero field state of Fig 5.13(a) the magnetic contrast from the free layer ripple is relatively weak. This is illustrated in the FFT of the state which shows only a narrow spread in the direction of M_{free} . Upon the application of a field M_{free} is observed to rotate in an anti-clockwise direction, Figs 5.13(a-g). As in the Fresnel images of Figs 5.10(a-s) the rotation of M_{free} results in changes to the fine structure of the magnetisation ripple. In particular when M_{free} is at intermediate angles between being parallel and anti-parallel to the biasing direction there is significantly more ripple than in the zero field state. This is illustrated in several of the FFTs (e.g. Figs 5.13(e)) which show a wider distribution than that of the zero field state. Increasing H_{app} leads to the continued rotation of M_{free} in an anti-clockwise direction and at the maximum negative field, Fig 5.13(g), M_{free} is anti-parallel to the biasing direction. The ripple in this state is comparable to that of the zero field state, Fig 5.13(a). As expected when H_{app} is relaxed there is a clockwise rotation of M_{free} and as before an increase in dispersion is observed when M_{free} is approximately parallel to the free layer easy axis, Fig 5.13(i). Relaxing H_{app} further leads to the continued

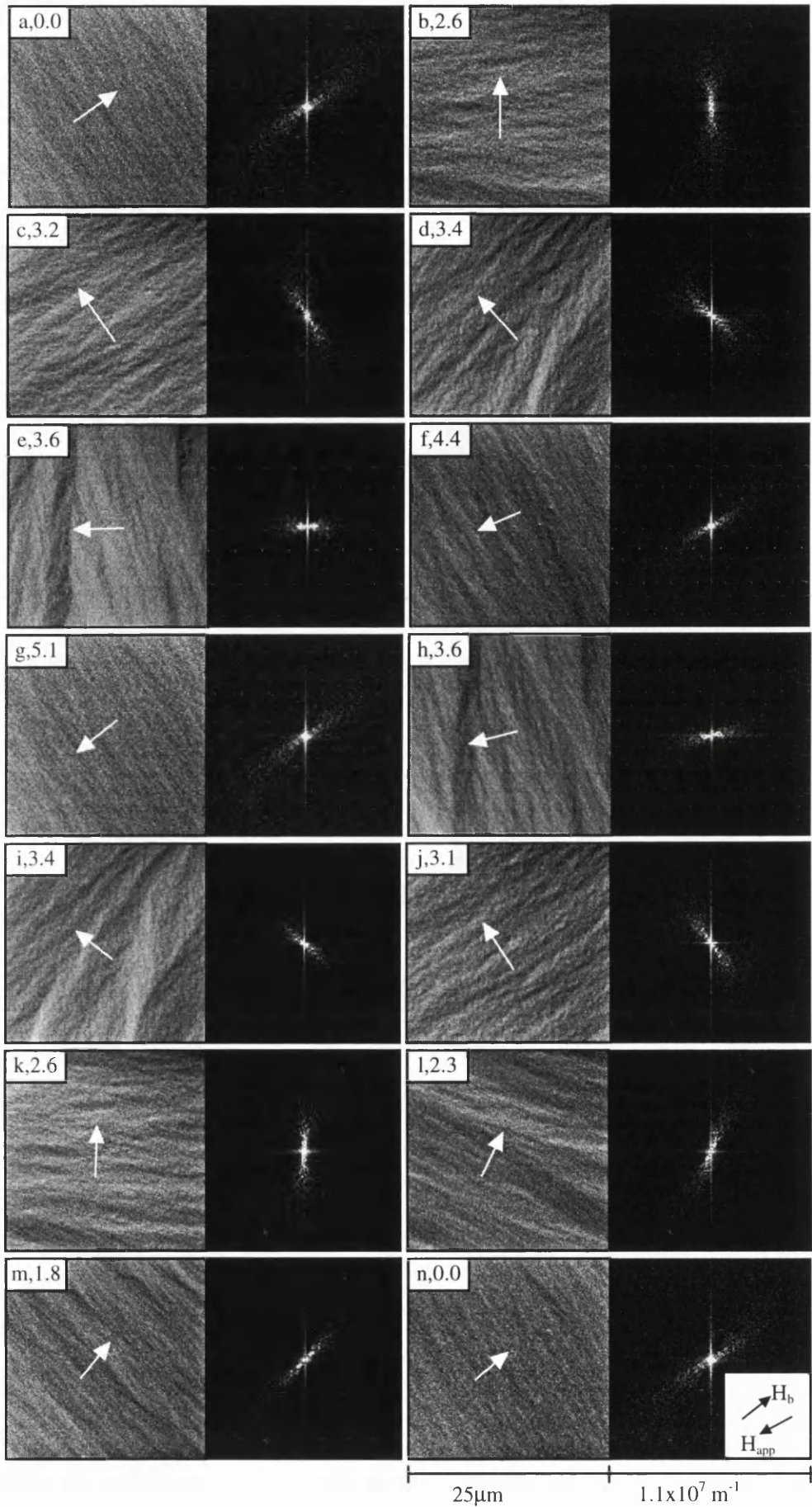


Fig 5.13(a-n): The coherent rotation of M_{freec} in real and spatial frequency space

rotation of M_{free} and in the zero field state of Fig 5.13(n) M_{free} returns to its original direction.

The FFTs in Figs 5.13(a-n) give information about both the dispersion and the average direction of M_{free} . Analysis similar to that carried out in chapter 3 to quantify the ripple in isolated permalloy films could also be attempted for the FFTs of Fig 5.13(a-n). It is however felt that the ripple intensity is insufficient in many of the images that such analysis would not be accurate. At the present time the problem of analysing the ripple spectrum and extracting quantitative information about the spread of M_{free} is being considered by the statistics department at Glasgow University. The average direction of M_{free} can, however, be easily deduced from linescans through the FFTs and the resulting data has been used to deduce the free layer reversal hysteresis loop of Fig 5.14.

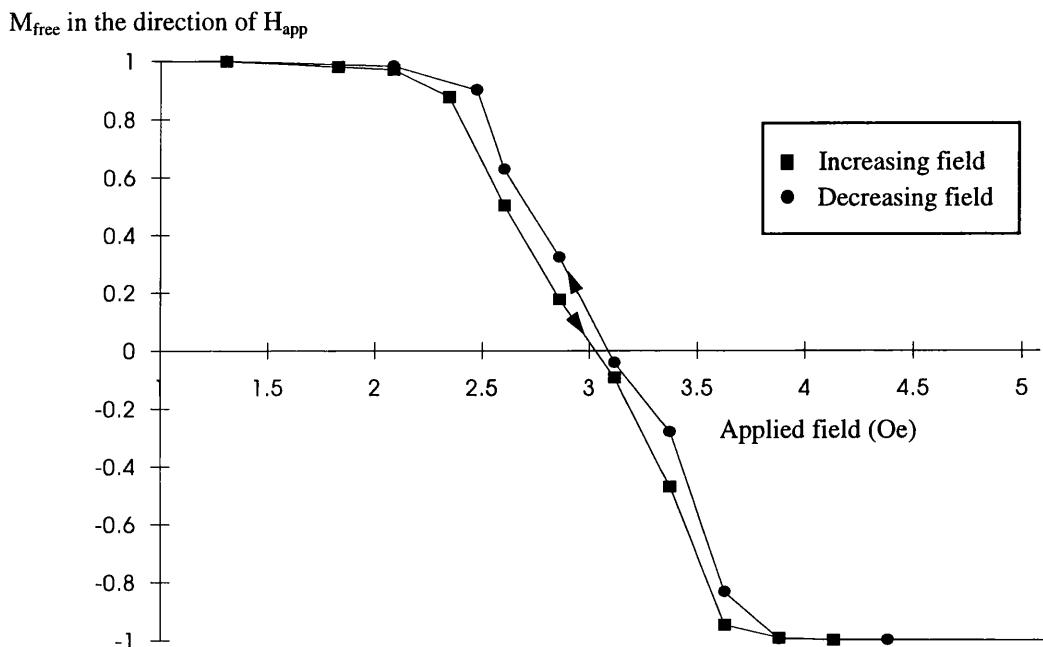


Fig 5.14 : *Deduced hysteresis loop for the coherent rotation of M_{free}*

This appears to show that even when there are no domains involved in the easy axis reversal there is still a small amount of hysteresis present. It is, however, important to note that any mechanical backlash in the tilt mechanism of the microscope would also result in the widening of the hysteresis loop in Fig 5.14.

5.8 DOMAIN WALL PROFILES OF 180° WALLS IN SPIN-VALVES

In sections 5.5.2 and 5.5.3 it was shown that upon applying a field which is aligned with the biasing direction some areas of the free layer in a spin-valve rotate in a clockwise sense while the remainder rotates in an anti-clockwise sense. At the boundary of oppositely sensed rotations domain walls were nucleated and as the reversal progressed the change in angle of M_{free} across the boundary gradually increased until a 360° wall was formed. In this section, we pause the reversal when there is a wall angle of approximately 180° and by using DPC obtain high magnification maps of the magnetic induction across the wall. These maps are analysed to obtain domain wall profiles and from these typical domain wall widths can be estimated. To enable a comparison a profile for a 180° wall in an isolated permalloy film, which is the same thickness as the spin-valve free layer (8nm), is also obtained.

The ripple on either side of the wall is used to ensure that the wall angle is approximately 180° and in the spin-valves the wall is approximately orthogonal to the biasing direction. Figs 5.14(a) and 5.14(b) are a pair of MDPC images with mapping directions approximately parallel and orthogonal to the wall direction respectively. These are for a spin-valve with $t_{\text{Cu}}=3.5\text{nm}$ and since the majority of the magnetic contrast is in Fig 5.14(a) it is this image which is used to calculate the wall profile. By considering Figs. 5.14(a-b) it can be seen that at this high magnification both magnetic and crystallite contrast are present in the DPC images. The crystallite contrast is, however, random and so can be minimised in the wall profile by taking an average over many linescans ($\approx 30-50$) from within one area. It is important that the length of the area over which the profile is averaged is completely orthogonal to the wall. In Fig 5.14(a) two such areas have been chosen, marked A and B, and Figs 5.15(a) and 5.15(b) show the resulting wall profiles. The value for wall width, w , may be obtained by performing a least squares fit of $\tanh(2x/w)$ to the profile. This has been done and the value of w required for the best fit, together with the standard deviation, δ , is quoted with each figure. In the case of the spin-valve areas A and B have similar average wall widths, $w= 150$ and 146 nm respectively and when profiles from walls in other spin-valves were taken it was found that the average wall widths were always similar. From these studies there was no evidence to suggest a relationship between t_{Cu} and the width of a 180° wall in a spin-valve.

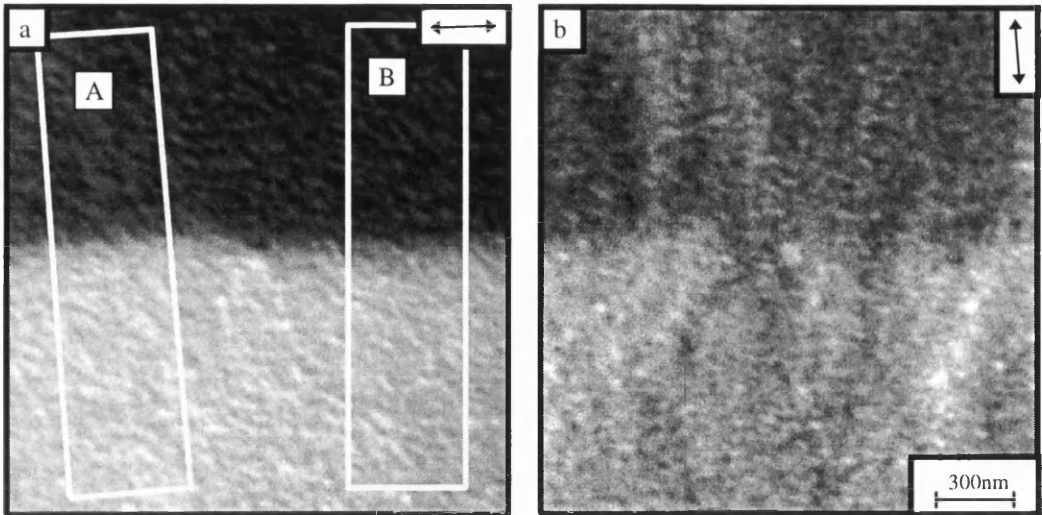


Fig 5.14(a-b): MDPC maps of a 180° wall in a spin-valve with $t_{Cu}=3.5nm$

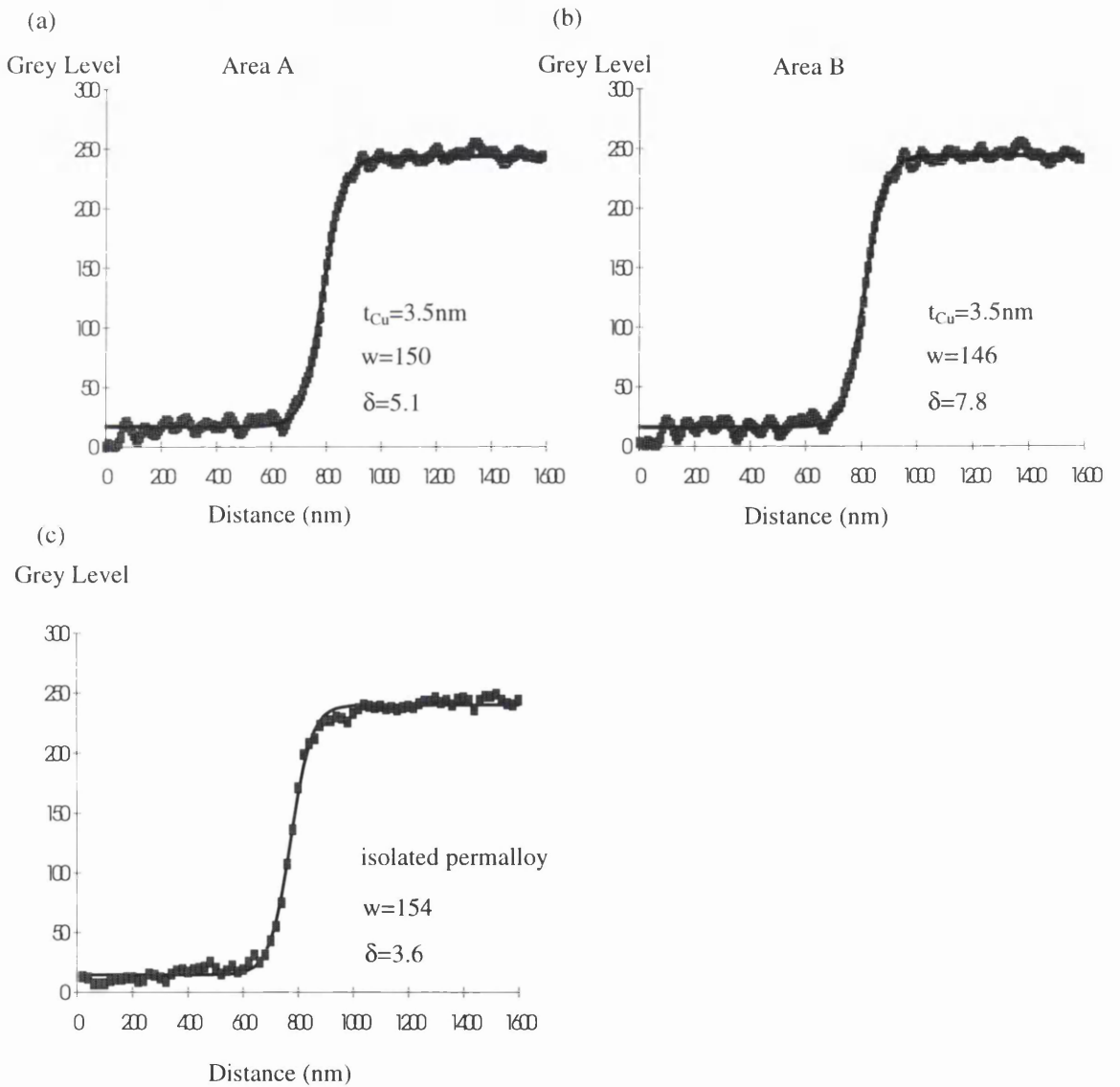


Fig 5.15: (a-b) 180° wall profiles in a spin-valve (c) an isolated permalloy layer

The profile of a 180° wall, in an isolated permalloy layer, Fig 5.15(c), allows an estimate of w in permalloy which is the same thickness as the free layer of a spin-valve. From the fit of $\tanh(2x/w)$ in Fig 5.15(c) the wall width is estimated as 152nm. This is in good agreement with the value of $\approx 157\text{nm}$ as predicted by Hubert et al (1969) for an 8nm permalloy film. Upon fitting $\tanh(2x/w)$ to lower magnification images domain wall widths of $\approx 166\text{nm}$ were obtained. This was caused by relatively long tails in the wall which had the effect of increasing the value of w in the $\tanh(2x/w)$ fitting function.

If the underlying biased permalloy layer has any affect on the wall profile then it would probably be most obvious in the tails of the wall. In retrospect it would therefore have been better to collect the images of Fig 5.14(a,b) at a lower magnification and so allow a comparison of the tails. It would be interesting to study if the underlying biased layer has any affect on the width of the tails and if so whether the wall direction, with respect to the biasing direction, also plays a role.

5.9 HIGH RESOLUTION MDPC STUDIES OF 360° WALLS

With the exception of the type (iii) spin-valve in chapter 4 all spin-valves tend to have a far greater probability of supporting 360° structures than single permalloy layers. Possible reasons for this were suggested in chapter 4 and in this section we now go on to study the structure of a typical 360° wall in more detail. The wall which is studied was nucleated in an orthogonal spin-valve with $t_{\text{Cu}} = 3.5\text{nm}$ and was brought about by applying fields which were parallel to the biasing direction. The distribution of magnetic induction through the wall is studied using DPC imaging where the mapping directions are chosen to be approximately parallel and orthogonal to the average wall length.

Figs 5.16(a-b) show DPC images of a 360° wall at a relatively low magnification. There is no applied field at the time of acquisition and since M_{free} is orthogonal to the average wall length there is considerable bucking of the wall. As in the previous section average wall profiles were made and these, which are from area A in Fig 5.16(a), are shown in Fig 5.17.

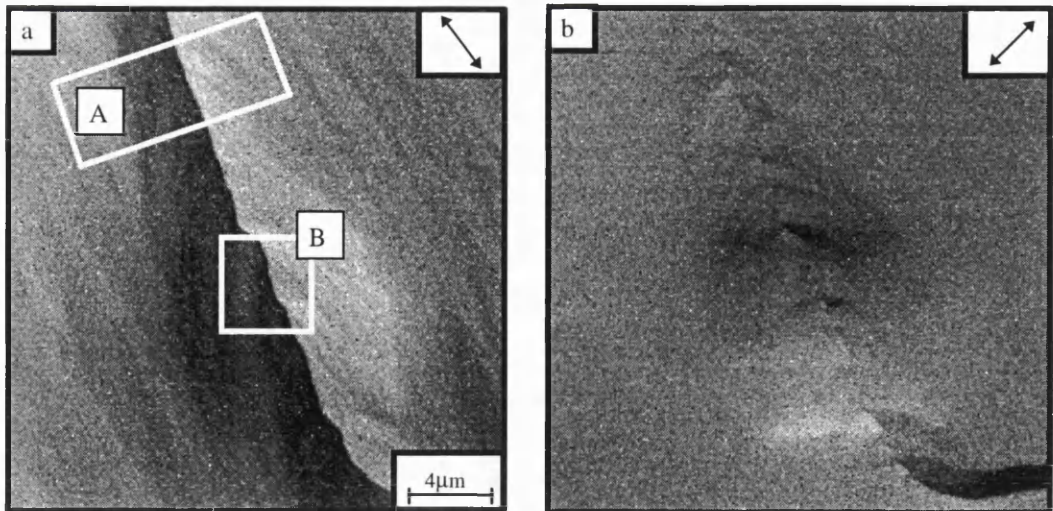


Fig 5.16(a-b): Maps sensitive to magnetic induction (a) parallel to the wall, (b) orthogonal to the wall

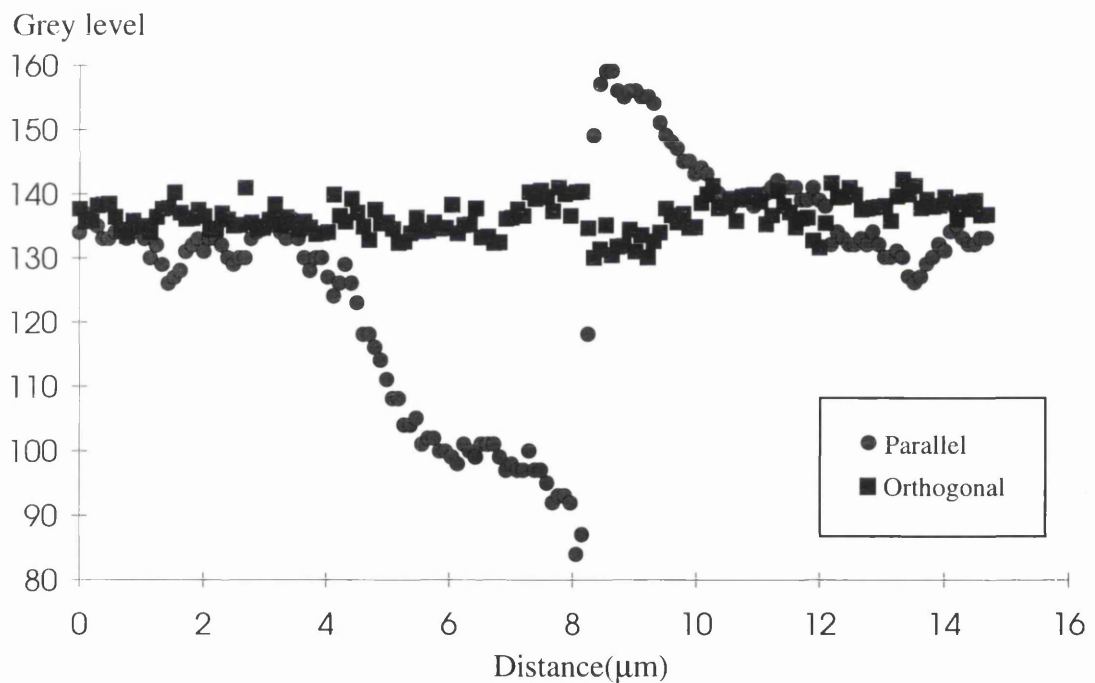


Fig 5.17: Averaged linescans for both mapping directions from area A on Fig 5.16

As can be seen from both the DPC images and the linescans, there is strong magnetic contrast in the map which is parallel to the wall. This, however, is not the case for the map which is orthogonal where only very weak magnetic contrast can be seen. As shall be shown later, this is due to a nulling of the Lorentz deflection from the sample by stray fields which arise from the charge density associated with the wall. It is obvious from Fig

5.17 that although the 360° wall has very long tails ($\approx 4\mu\text{m}$) there is not a smooth rotation of M_{free} through the wall. A wall core exists, where M_{free} rotates over a large angle in a relatively short distance, and this is shown in the higher magnification maps of Figs 5.18(a-b). The scan area here is that which is marked as B on Fig 5.16(a).

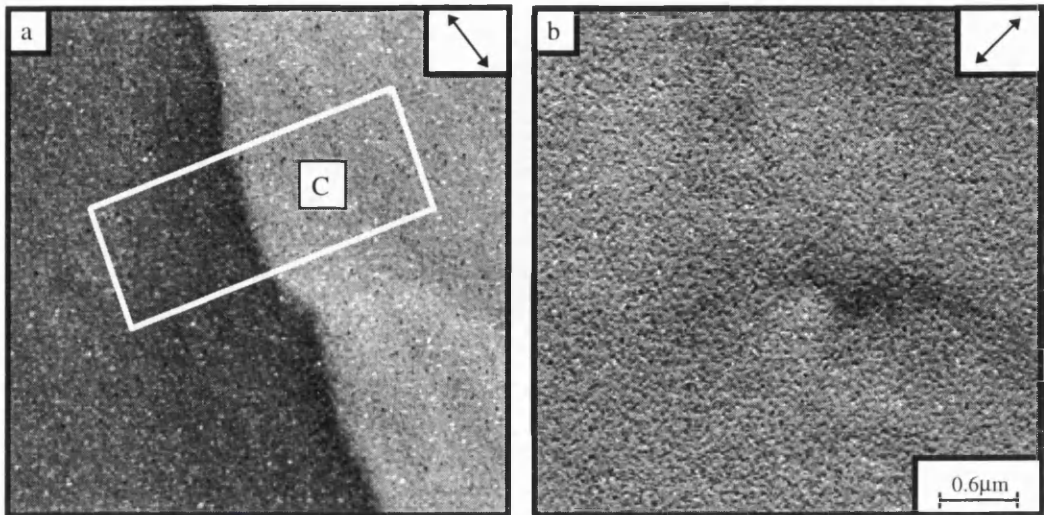


Fig 5.18(a-b): High magnification maps of Area B as marked on Fig 5.16(a)

Again averaged linescans from both mapping directions can be taken and these, which were averaged from the area marked C on Fig 5.18(a), are shown in Fig 5.19.

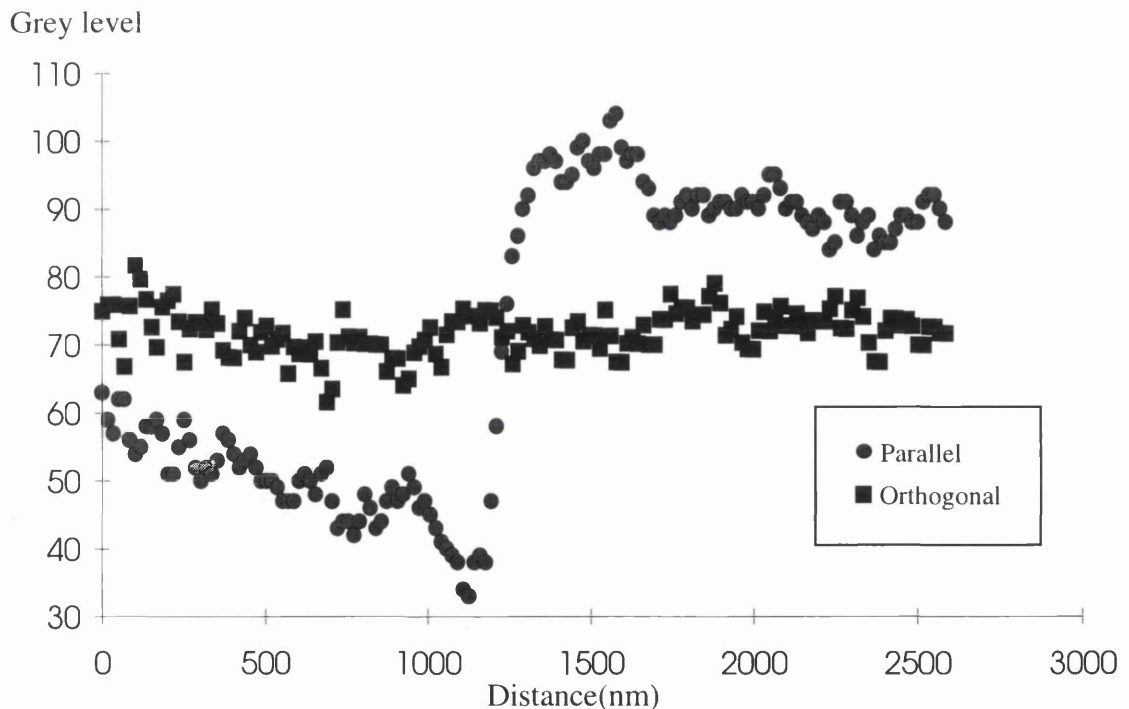


Fig 5.19: Averaged linescans for both mapping directions from area C on Fig 5.18

From the above linescans and those of Fig 5.17 it is possible to draw a simplified schematic of a 360° wall, Fig 5.22. This schematic is a planar view of the wall structure and is not to scale.

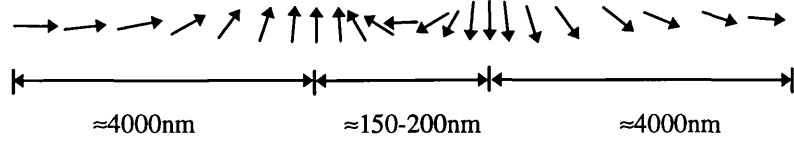


Fig 5.22: Schematic planar view of a 360° wall

In the core of the 360° structure there is a rotation of M_{free} through an approximate angle of 180° . The core width is approximately equal to the width of a 180° wall, as established in section 5.8, and the long tails which occur on either side of the wall each extend over $\approx 4\mu\text{m}$. M_{free} rotates by $\approx 90^\circ$ in each of the tails.

As previously mentioned there is only relatively weak magnetic contrast in the DPC image which is sensitive to magnetic induction orthogonal to the wall. This is due to the stray field generated by poles distributed along the wall and can be understood from the following. Using the coordinate system defined in Fig 5.23, the field at point, $r'(x', y', z')$, which arises from a free pole density $\rho(r)$, is given by eqn 5.1

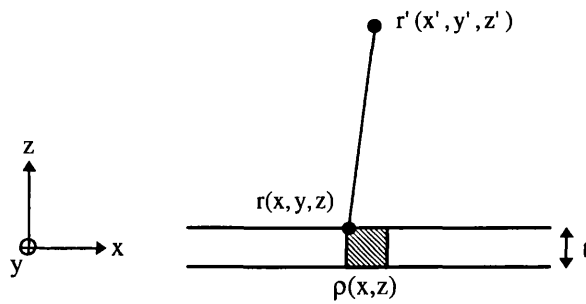


Fig 5.23: Definition of coordinate system

$$\underline{H}(r') = \int \frac{\rho(\underline{r})d^3\underline{r}(\underline{r}'-\underline{r})}{4\pi|\underline{r}'-\underline{r}|^3} \quad (5.1)$$

Assuming a perfectly straight wall in the y direction the stray field, $\underline{H}(x', z')$, is given by,

$$\underline{H}(x', z') = \int_{x=-\infty}^{\infty} \int_{y=-\infty}^{\infty} \int_{z=-\frac{t}{2}}^{\frac{t}{2}} \frac{\rho(x, z)(\underline{x}' - \underline{x})}{4\pi[(x' - x)^2 + (y' - y)^2 + (z' - z)^2]^{\frac{3}{2}}} dx dy dz \quad (5.2)$$

The component of the Lorentz deflection to which the map orthogonal to the wall is sensitive, $\beta(x')$, can be found by integrating the magnetic induction along the electron path,

$$\beta(x') = K \left[\int_{-\infty}^{+\infty} (H_x(x', z') + M_x(x')) dz' \right] \quad (5.3)$$

where K is a constant of proportionality. Substituting eqn 5.2 into eqn 5.3 and integrating w.r.t. y gives,

$$\gamma(x') = \int_{z'=-\infty}^{\infty} \int_{x=-\infty}^{\infty} \int_{z=-\frac{t}{2}}^{\frac{t}{2}} \frac{-\rho(x, z)(x' - x) dz dx dz'}{2\pi[(x' - x)^2 + (z' - z)^2]} + \int_{z'=-\infty}^{\infty} M_x(x') dz' \quad (5.4)$$

where $\gamma(x')$ has been substituted for $\beta(x') / K$. Within the film $\rho(x, z)$ is independent of z , i.e. $\rho(x, z) = \rho(x)$, and so integrating eqn 5.4, with respect to z' , gives,

$$\gamma(x') = \int_{-\infty}^{+\infty} \int_{z=-\frac{t}{2}}^{\frac{t}{2}} \frac{\rho(x)(x' - x) dz dx}{2|(x' - x)|} + M_x(x')t \quad (5.5)$$

Recalling that,

$$\rho(x) = -\frac{dM_x(x)}{dx} \quad (5.6)$$

and substituting this into eqn 5.5 gives a deflection equal to,

$$\gamma(x') = \frac{t}{2} \left[-\int_{-\infty}^{x'} \frac{dM_x(x)}{dx} \cdot dx + \int_{x'}^{\infty} \frac{dM_x(x)}{dx} \cdot dx \right] + M_x(x')t \quad (5.7)$$

which evaluates as,

$$\gamma(x') = \frac{t}{2} \left[-M_x(x') + M_x(-\infty) - M_x(x') + M_x(\infty) \right] + M_x(x')t \quad (5.8)$$

Replacing $\gamma(x')$ with $\beta(x')/K$ and assuming that sufficiently far away from the wall $M_x(x')$ is perfectly orthogonal to the wall eqn. 5.8 becomes,

$$\beta(x') = KM_s \quad (5.9)$$

Where M_s is the saturation magnetisation of the free layer. Since eqn. 5.9 has no spatial dependency there should be no magnetic contrast in the DPC image which is sensitive to magnetic induction orthogonal to the wall. In reality this is not quite the case since local deviations to the wall direction result in a non-cancellation of the Lorentz force, in the direction orthogonal to the wall, and subsequently contrast in DPC images with this mapping direction. Since in the parallel maps we have no deflection from the stray field the magnetic contrast is strong and we can assume this to be a true description of how M_{free} rotates across the 360° wall.

5.10 CHANGES IN MAGNETIC STRUCTURE OF A STRONGLY PINNED 360° WALL AS M_{free} COHERENTLY ROTATES

In sections 5.5.2 and 5.5.3 we reported that when H_{app} was perfectly aligned with the biasing direction the nucleation of 360° walls was frequently observed. These walls occurred between areas of differently sensed rotations and upon relaxing the applied field tended to unwind. Occasionally, however, a 360° wall may be nucleated which is particularly stable and does not unwind. One way of increasing the probability of forming such a wall is to nucleate a 360° structure and then slightly rotate the applied field so that

coherent rotation is favoured. In this case the width of the wall can be studied as M_{free} coherently rotates about it. In this section we again use the DPC mode of electron microscopy in order to study how both the width and the structure of a stable 360° wall varies as fields are applied at a few degrees off anti-parallel to the biasing direction. The spin-valve used for this study had a copper spacer layer of 3.5nm. As was shown in section 5.9, there is very little magnetic contrast in the DPC map which is sensitive to magnetic induction orthogonal to the average direction of a 360° wall. For this reason, in this section, only maps which are parallel to the wall direction are considered. A sequence of MDPC images, with the relevant mapping direction, is shown in Figs 5.24(a-o). These show the behaviour of a 360° wall as M_{free} is relaxed from a constraining field, anti-parallel to the biasing direction. In the anti-parallel state of Fig 5.24(a) the wall has a similar white / black contrast to that of the wall in section 5.9. Due to M_{free} being orthogonal to the wall it is buckled along its length. As H_{app} is relaxed from 10.0 Oe to 3.0 Oe the width of the wall increases to such an extent that it would be incorrect to describe it as a single 360° wall. We shall therefore describe it as two separate walls which have been labelled as wall A and wall B on Fig 5.24(c). The increase in the width of the structure which occurs during the relaxation of the constraining field between 10.0 and 3.0 Oe is due almost entirely to the movement of wall B. During this part of the reversal wall A is static. When H_{app} is equal to 2.7 Oe, Fig 5.24(i), there is a dramatic increase in both the position and structure of wall A. In this transition region wall A appears to have a lower angle and the width of the whole structure is $\approx 9\text{-}10\mu\text{m}$. As H_{app} is decreased below 2.7 Oe further changes in the position and angle of wall A are observed and in the zero field state of Fig 5.24(o) the 360° wall is reformed. If we were to consider only the two extreme images of this sequence, Fig 5.24(a) and 5.24(o), without the knowledge of the intermediate states, our principal observation would be that the contrast of the 360° wall has become inverted. With the benefit of the intermediate images we can see that although the two states are similar they are only related structures and are not the same 360° wall. If Figs 5.24(a-o) are studied carefully we see that M_{free} does not necessarily always rotate by the same amount over walls A and B. In Figs 5.24(a-f) wall B appears to be a lower angle wall and can move more freely than wall A. In Figs 5.24(g) and 5.24(h) the two walls have a similar high angle of rotation and consequently both appear as sharp transitions.

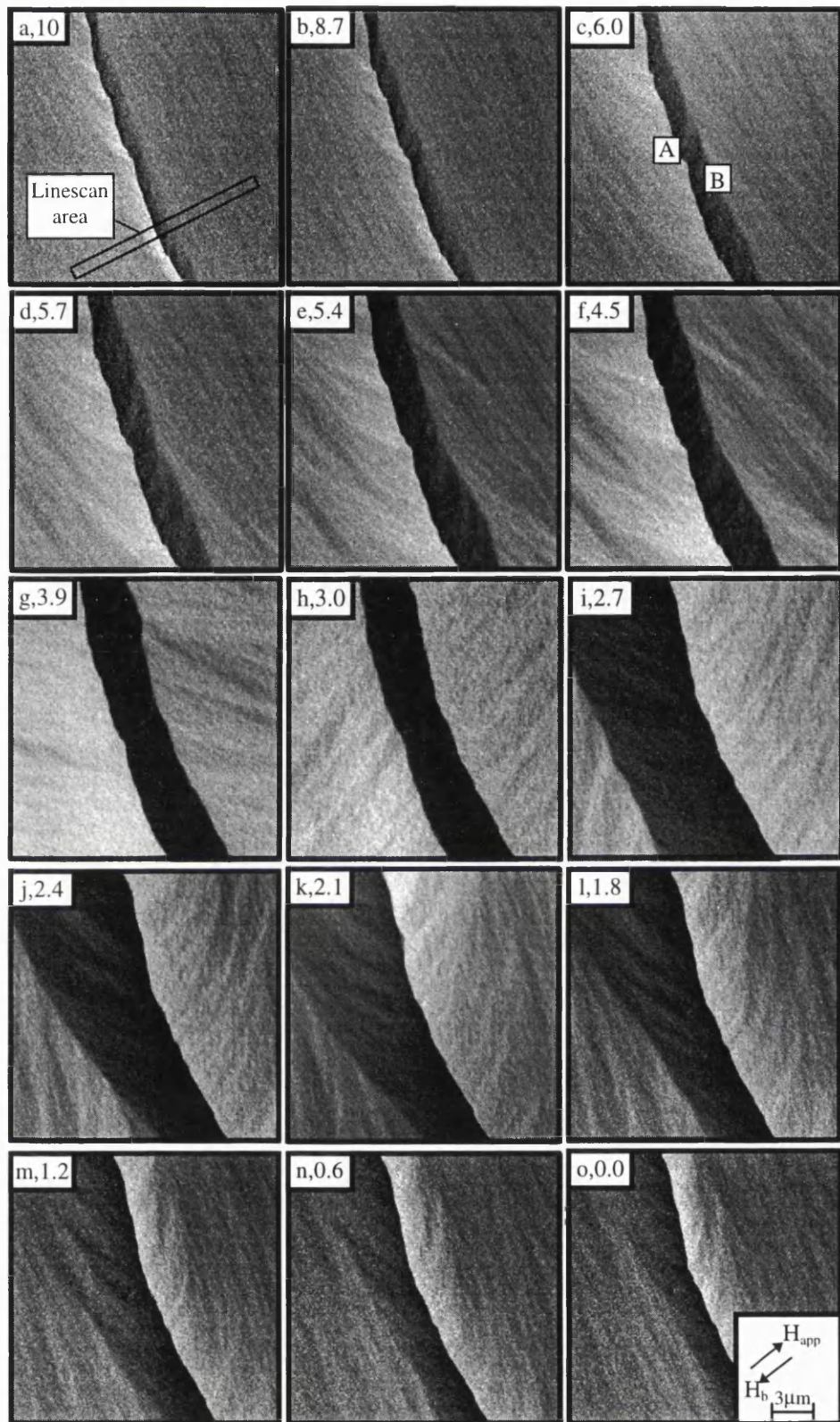


Fig 5.24(a-o): DPC images of a 360° wall as M_{free} rotates around it

It is noted that when both walls have high angles of rotation there is little wall motion. For example between the states of Figs 5.24(g) and (h) there is practically no wall motion for

an decrease in H_{app} of 0.9 Oe. When H_{app} is decreased to below 3.0 Oe wall A becomes unstable and a lower angle wall, further away from wall B, forms in its place. Further decreases in H_{app} result in wall A moving closer to wall B.

As in previous sections it is possible to take linescans through the structure in each of the images shown in Figs 5.24(a-o) and so study the width of the structure as a function of H_{app} . Again we reduce the noise by averaging over an area, which has been marked on Fig 5.24(a), and is approximately orthogonal to the original wall length. Due to the changes which occur in the wall structure as H_{app} is relaxed it is not clear what the best definition of wall width is. It is, however, decided to define the width of the structure as that equivalent to the width of the black area in the DPC images. Fig 5.25 shows a plot of this width as a function of H_{app} .

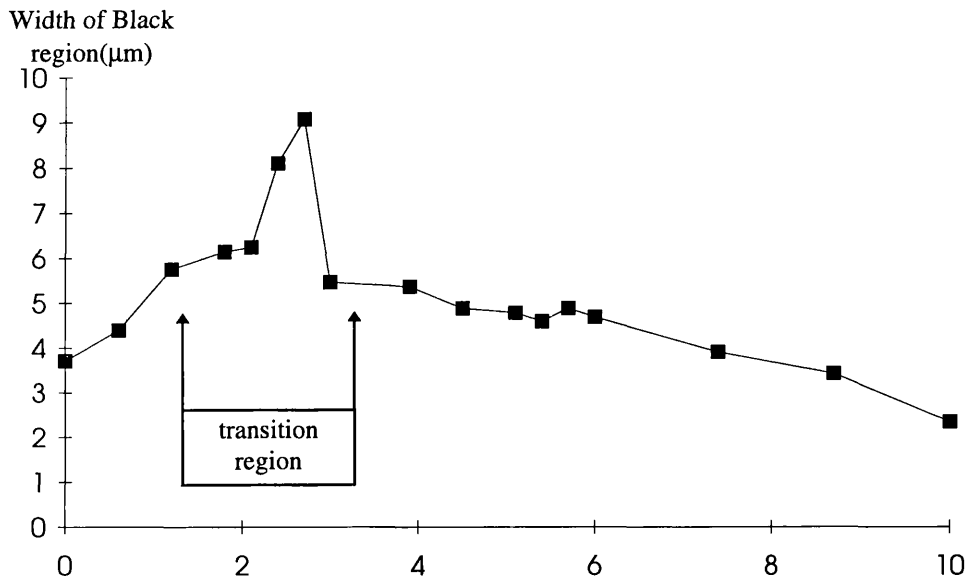


Fig 5.25: Width of black region vs H_{app} in a spin-valve with $t_{Cu} = 3.5nm$
Applied Field (Oe)

As is obvious from the DPC images and the plot of width versus H_{app} , there is a dramatic increase in width in the regime where wall A changes its structure. This dramatic increase would almost certainly lead to Barkhausen noise in the output of a working sensor and this experiment illustrates that even when the majority of M_{free} coherently rotates the existence of a single 360° wall will cause significant jumps in M_{free} . We observe in Fig 5.25 that outwith the transition region there is a gradual decrease in wall width as the magnitude of H_{app} is increased. It is probable that if $|H_{app}|$ is increased to be substantially greater than the

coupling field we would observe a decrease in the rate of change of width as the free poles, associated with the 360° structure, are forced closer together.

5.11 SUMMARY AND CONCLUSIONS

In this section the free layer reversal mechanisms of spin-valves with crossed easy axes and biasing directions have been investigated extensively. A criterion for the coherent rotation of M_{free} has been established and changes which occur in the ripple structure during such a rotation have been studied. When walls were observed in the free layer reversal they have been characterised using the DPC mode of electron microscopy and this enabled wall profiles to be deduced. It was found in these experiments that the presence of a biased permalloy layer did not significantly change the wall width of a 180° wall in the free layer of a spin-valve. High resolution profiles of 360° walls were obtained and these allowed an accurate estimate of how M_{free} rotates through a 360° wall.

CHAPTER 6: BIASING MECHANISMS IN SPIN-VALVE STRUCTURES

6.1 INTRODUCTION

In order to develop maximum GMR amplitude in a spin-valve it is necessary to be able to switch the magnetisation of the free layer while maintaining the original direction of magnetisation in the biased layer. To generate anti-parallel alignment it is therefore necessary that the switching field of one of the ferromagnetic layers is greater than the other. Attempts to use ferromagnetic layers with different coercivities have met with limited success, primarily due to interlayer coupling which prevents a full anti-parallel state being generated, (Dieny et al, 1991 and Kergoat, 1995). In order to reach the much desired state of complete anti-parallel alignment it is therefore necessary to exchange bias one of the ferromagnetic layers. The biasing mechanism of this layer plays an important role in determining both the maximum GMR and the sensitivity of the spin-valve. In this chapter we will consider spin-valves biased by FeMn and TbCo, which were grown by J.C.S. Kools and P.P. Freitas respectively. We will briefly mention the use of NiO as a biasing mechanism but no results will be presented for this type of spin-valve.

6.2 BIASING MECHANISMS

The effect of an anti-ferromagnetic FeMn layer, grown in the γ -phase, on top of a permalloy layer has been known for some time and was utilised in order to produce a barber-pole type structure by Hempstead et al (1978). γ -FeMn has a tetrahedral spin structure (Jungblut et al, 1995) and deposition on a permalloy layer results in direct exchange between the moments in the permalloy and the FeMn. This results in unidirectional biasing which shifts the hysteresis loop of the permalloy by a field, H_b . The maximum biasing field is present for a stoichiometry of 50:50 and is inversely proportional to the permalloy layer thickness (Malozemoff, 1988). For permalloy thicknesses of around 10nm the biasing field is typically 150-250 Oe and is sufficiently large for the majority of applications. Unfortunately, however, FeMn has a typical resistivity of $\approx 95\mu\Omega\cdot\text{cm}$ which,

when compared with permalloy, typically $\approx 30\mu\Omega\cdot\text{cm}$, results in shunting of the sense current and consequently a lower GMR amplitude than could otherwise be achieved.

Amorphous ferrimagnetic TbCo films have also been proposed as an alternative candidate for biasing MR heads, since it was found that over a restricted composition range they exchange couple to permalloy (Cain et al, 1988). A resistivity of $\approx 200\text{-}500\mu\Omega\cdot\text{cm}$ reduces the problem of current shunting though the biasing field is dependent on many parameters and is often difficult to control. An advantage of TbCo over FeMn is that the biasing mechanism is stable to higher temperatures (typically stable up to 160°C rather than 105°C (Folkerts et al, 1995)). This is not only significant for the processing technology used to prepare spin-valve sensors but also for the situation where commercial heads could be accidentally exposed to high temperatures. Unfortunately, however, when TbCo is cooled after temperatures in excess of 180°C the biasing mechanism does not return. Thus the creation of orthogonal spin-valves by post deposition annealing, which was discussed in chapter 5 with respect to FeMn biasing, is not possible.

In order to obtain reasonable exchange coupling between TbCo and the adjacent permalloy layer it is necessary that the Tb content leads to a compensation temperature which is close to room temperature. This results in the rare-earth and transition metal sublattices compensating and exchange coupling occurring. It has been found by other authors that unidirectional exchange coupling occurs for a Tb content of 25-30% while uniaxial coupling occurs for a Tb content $>30\%$, (Freitas et al 1995). Strong exchange coupling occurs when the TbCo film is sufficiently thick so that away from the interface there is vertical magnetisation. Such a situation is depicted schematically in Fig 6.1 and leads to a stabilisation of the in-plane component of TbCo which exists at the interface.

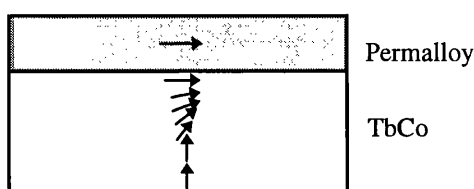


Fig 6.1: Schematic of magnetisation at permalloy/TbCo interface

The thickness of the TbCo layer often ranges from $\approx 10\text{nm}$ to 50nm and as with FeMn the exchange field is inversely proportional to the adjacent permalloy layer thickness. The substrate voltage during sputtering also influences the biasing field by altering the fraction

of in-plane anisotropy of the TbCo film (Cain et al 1988 and Freitas^A et al 1994). The TbCo biasing mechanism will be discussed further in section 6.4 where reversal mechanisms of TbCo/permalloy layers are presented.

Although the increased resistivity of TbCo is certainly an advantage over FeMn an ideal biasing layer would be an insulator. This would allow further increases in the GMR amplitude by confining the sense current to the NiFe/Cu/NiFe layers thus increasing the spin-dependent scattering. One insulating layer which displays exchange coupling to an adjacent permalloy layer is NiO. This is an antiferromagnet and unlike other possible oxide biasing mechanisms (for example CoO) it remains antiferromagnetic substantially above room temperature. For an exchange coupled system the blocking temperature is the temperature at which exchange biasing ceases to exist. In the case of an antiferromagnet this coincides with the Néel temperature and for thin film NiO this is ≈ 200 °C. This compares with ≈ 33 °C for CoO, (Carey and Berkowitz, 1992). Initial studies using NiO found that the strongest biasing fields were obtained by depositing the NiO layer at elevated substrate temperatures (Carey and Berkowitz, 1992). In order to avoid interlayer mixing, which would be caused by such a deposition, it is necessary to grow the spin-valve as an “inverted” structure where the NiO is the first layer rather than the final layer. More recent studies, however, have succeeded in growing spin-valves with NiO on both the top and bottom of the multilayer stack (Plaskett et al, 1994 and Egelhoff et al, 1995). While the resulting double symmetric spin-valve structures exhibit large GMR amplitudes (21%) the sensitivity is poor (≈ 0.4 %/Oe) and the coercivity relatively large. A variation on the symmetrical spin-valve structure is to use NiO as the biasing mechanism for the first fixed layer but FeMn for the second. This reduces the problem of weak biasing from the NiO layer on top of the stack and results in an MR of $\approx 13\%$ (Anthony et al, 1994).

The main problem with using NiO biased spin-valves in heads is that the exchange biasing field is at best typically 80-100 Oe and consequently linearisation of the sensor often also results in the rotation of the biased layer magnetisation (ten Berge et al, 1995).

6.3 FeMn BIASED SPIN-VALVES

In this section we present in-situ magnetising experiments on a layer of permalloy exchange biased by FeMn. Marked differences are noted from the reversal mechanisms of isolated permalloy layers. Since the fields required for biased layer reversals are typically greater than those available using either magnetising stages in the Philips CM20 or the JEOL 2000 electron microscopes, the objective lens field of the CM20 was used.

Figs 6.2(a-h) show Fresnel images of a biased layer reversal mechanism for an 8nm permalloy layer with FeMn (8nm) deposited on top.

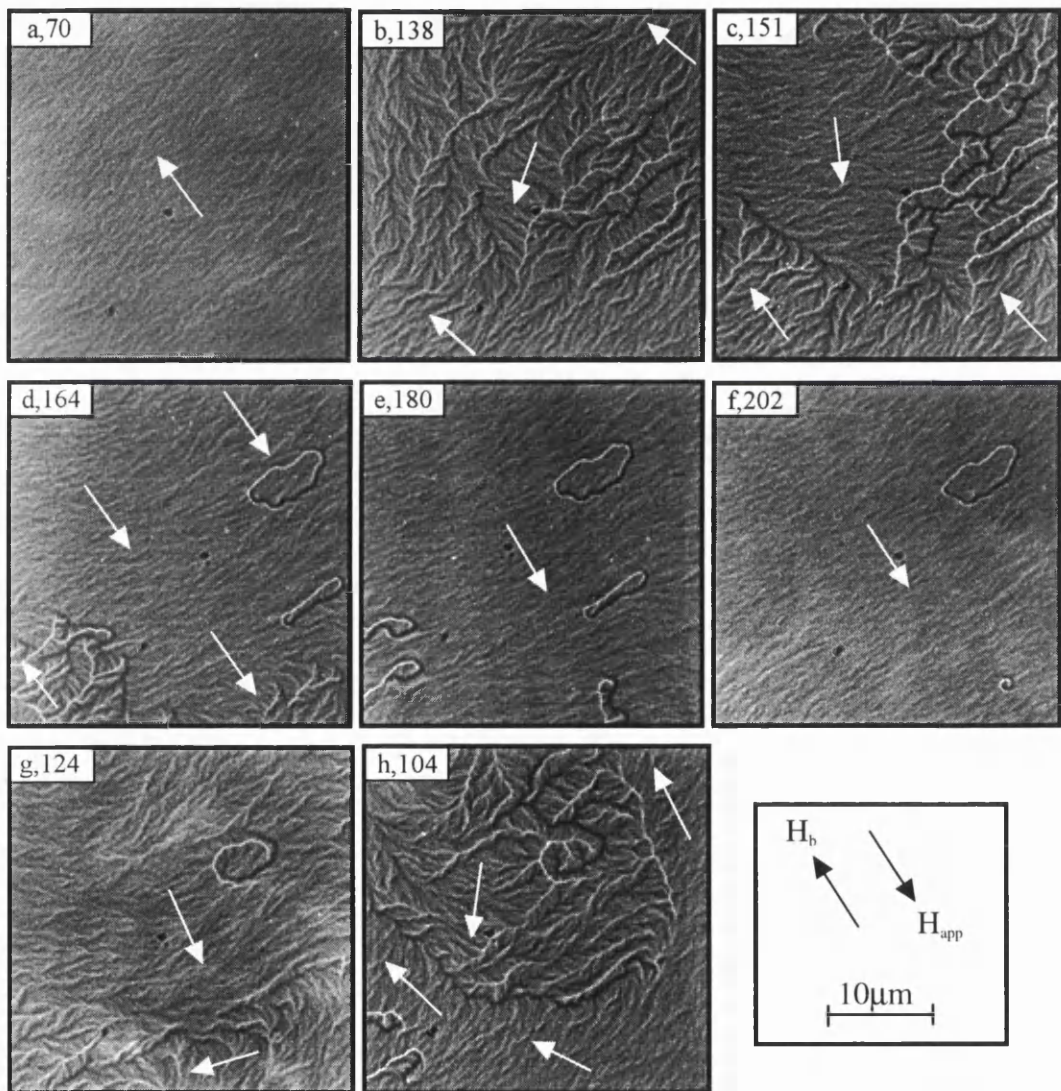


Fig 6.2(a-h): Fresnel images showing the magnetising cycle for a layer of biased permalloy with the approximate directions of magnetisation superimposed. The number quoted with each figure is the applied field in Oe.

Application of a field anti-parallel to the biasing direction led to no change in the magnetic structure until the field value exceeded ≈ 100 Oe. Beyond this field, there was an increase in ripple contrast followed by the nucleation and propagation of small irregular domains, Fig 6.2(b). These domains were only a few microns in width and it is apparent from Fig. 6.2(b) that many orientations of the magnetisation vector can be found over the field of view shown in the image. With a further increase in field (Fig. 6.2(c)) the reversed area grew in size leaving a complex distribution of small domains around its periphery. Wall mobility was low and the increase in reversed area proceeded only slowly with field (Fig. 6.2(d)). Fig 6.2(d) also shows that domain walls did not always annihilate as domains with an unfavourable orientation of magnetisation shrank but that irregular 360° loops could remain in areas otherwise completely reversed. The final stages of reversal are shown in Figs. 6.2(e) and (f) where it can be seen that 360° loops remained beyond the field values sufficient to reverse the bulk of the film. Upon reduction of the applied field broadly similar processes were observed (Figs. 6.2(g) and (h)) by which the magnetisation returned to the original direction. From these and other experiments it was observed that there was considerable hysteresis and that the areas which first returned to their original orientation tended to be those which had been the last to reverse under the influence of an increasing field. These areas presumably were those where the local pinning to the FeMn was strongest. For fields of ≈ 70 Oe the permalloy layer had usually returned to its original single domain state although on occasions 360° loops formed which remained in existence down to zero field. When the biased layer was part of a complete spin-valve structure the mechanism for reversal was very similar to that described above. From the above it is clear that the presence of the FeMn dramatically influences the domain structures created during the switching process and very complex distributions of small domains form, particularly around the transition region between the switched and the unswitched regions. The nature of these domains can be seen more clearly from higher magnification DPC images which reveal two main domain types. The first type, which was commonly observed for biased layer reversals, is shown in Fig. 6.3(a) and is one of a pair of DPC images with the corresponding magnetic induction distribution, superimposed. There are many different directions of magnetisation within this image, emphasising the fact that this switch is erratic in nature, with some areas reversing before others. The second, Fig 6.3(b), which

was observed less commonly, shows a boundary region which can be thought of as a series of small flux vortices.

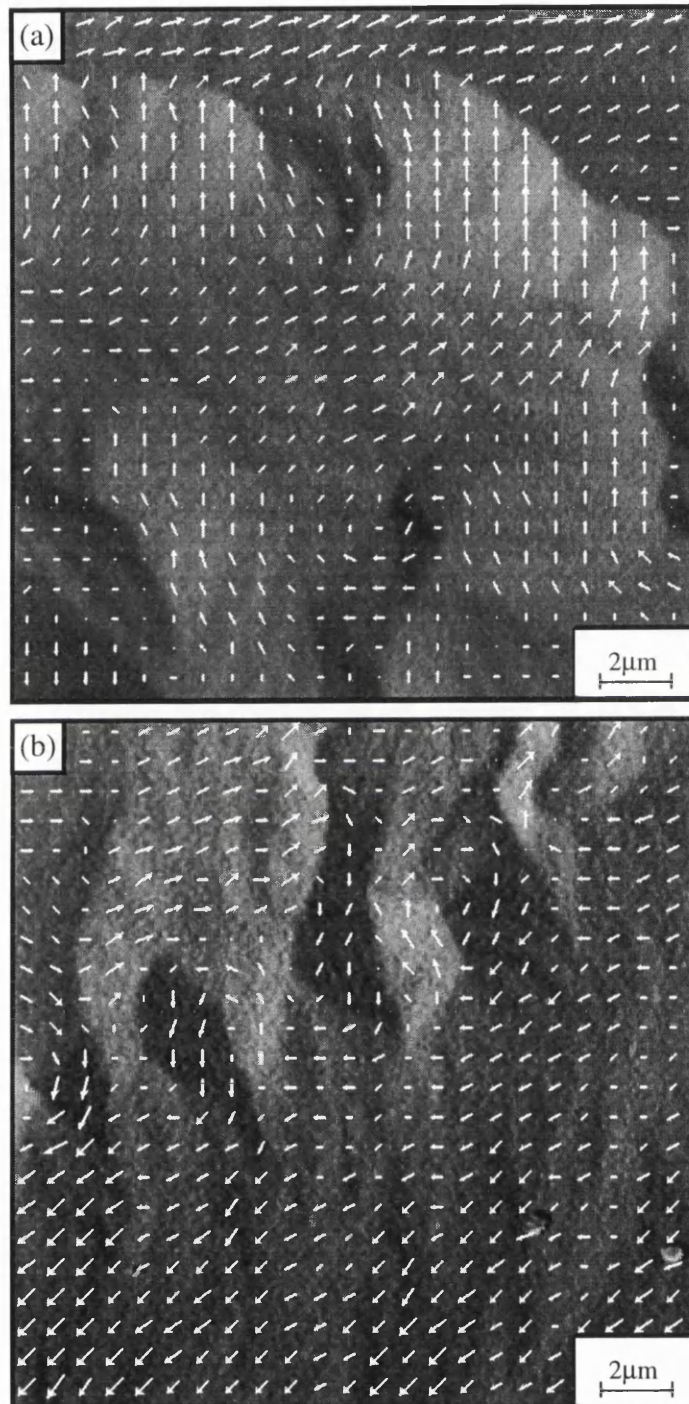


Fig 6.3: Single DPC images and superimposed induction maps, showing (a) a typical domain structure during reversal of the biased layer, (b) vortex structures at the boundary between switched and unswitched regions.

In some ways this is more reminiscent of a cross-tie wall (Ploessl et al, 1993) where small vortices, often referred to as Bloch lines, are found separating sections of Néel wall with opposite polarities. It is clear that these walls are quite unlike the Néel walls which were observed in the reversal of isolated permalloy layers that were reported in previous chapters.

Upon studying complete spin-valve structures the presence or otherwise of the free layer appears unimportant for the biased layer reversal. The above results show clearly that the effect of the FeMn biasing layer is not simply to shift the hysteresis loop by a constant field but to completely change the switching mechanism. One of the main features of the reversal process is the wide field range (≈ 50 Oe) over which reversal for fields parallel to the biasing direction takes place. This is indicative of non-uniform coupling across the specimen.

6.4 TbCo BIASED SPIN-VALVES

Although thick TbCo films, similar to those used for magneto optic applications have strong perpendicular anisotropy, thin films of the correct composition and thickness deposited on top of permalloy can exhibit a curling of the magnetisation vector at the interface. This interfacial curling is described by a micromagnetic model suggested by Smith et al (1991) and explains the domain structures observed in amorphous TbCo/permalloy films (Cain and Kryder, 1990). The model postulates the formation of a Bloch wall within the TbCo layer as the mechanism for exchange anisotropy and in the case of unidirectional biasing this is stabilised by a strong vertical component of m_{TbCo} below the wall, (see Fig 6.1). For spin-valves prepared by Freitas^B et al (1994) the width of this Bloch wall is ≈ 8 nm and so layer thicknesses of 10-12 nm are required for stabilisation. Small variations in the Tb content can result in a decrease in the vertical anisotropy of the TbCo layer and consequently may change the biasing mechanism from being unidirectional to uniaxial. A typical uniaxial, or symmetric, MR loop is shown in Fig 6.4. The direction of magnetisation in both ferromagnetic layers is shown schematically on this figure.

For spin-valves biased by TbCo it is important that the compensation temperature is around room temperature in order to minimise fringe fields. If this is not taken into consideration the TbCo layer can have an adverse effect on the free layer reversal mechanism by

increasing the coercivity and so reducing the sensitivity of the sensor, Freitas^C et al (1994). In the case of uniaxial TbCo problems can also arise if the spin-valve is exposed to large vertical fields as the biased layer no longer remains single domain (see later). This not only lowers the maximum GMR amplitude obtained upon subsequent reversals but could also have the effect of making the sensor output more noisy.

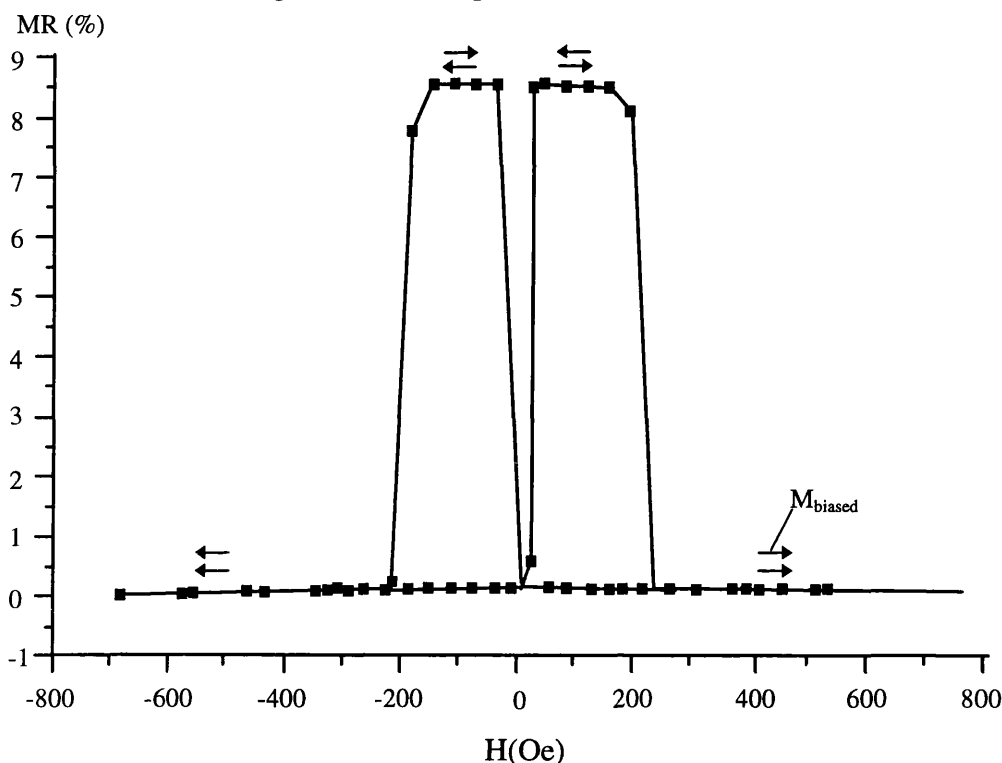


Fig 6.4: Symmetric MR response, measured at room temperature, for a uniaxial $Tb_{32}Co_{68}$ biased spin-valve.

The biased layer reversal of TbCo spin-valves in this thesis will be limited to uniaxial spin-valves. This is due to the fact that unidirectional spin-valves require very large in-plane fields (>600 Oe) in order to reverse the biased permalloy layer. While the vertical field required to generate such in-plane fields can be applied using the objective lens of the CM20 its magnitude, even when used with high tilt angles, is too large for out of plane components of magnetisation to be ignored.

6.4.1 Biased Layer Reversal of a Uniaxial Biased TbCo Spin-valve

In this section we apply a moderate vertical field (≈ 680 Oe) and by tilting the sample around the correct axis bring a component of field into the plane of the spin-valve which is

anti-parallel to the biasing direction. As the component of field in the plane of the film is substantially greater than the coupling field (≈ 200 Oe as opposed to $\approx 5-15$ Oe) it is reasonable to assume that when such fields are applied the free layer is single domain and that any domain structures come from either the biased NiFe and/or the TbCo layer. The introduction of a component of field, anti-parallel to the biasing direction but equal in magnitude to the biasing field, results in the rapid reversal of the biased layer magnetisation. When $H_{app} \approx 200$ Oe a domain structure, similar to that of Fig 6.5(a), is nucleated. These structures are not well pinned and without increasing H_{app} the domain walls creep through the unswitched material. In order to take micrographs it is therefore necessary to reduce the component of field along the biasing direction and so retard domain wall motion. The images of Figs 6.5(a-f) are therefore “remanent” states where the applied field is reduced to ≈ 50 Oe after a field of ≈ 200 Oe was used to encourage domain wall motion.

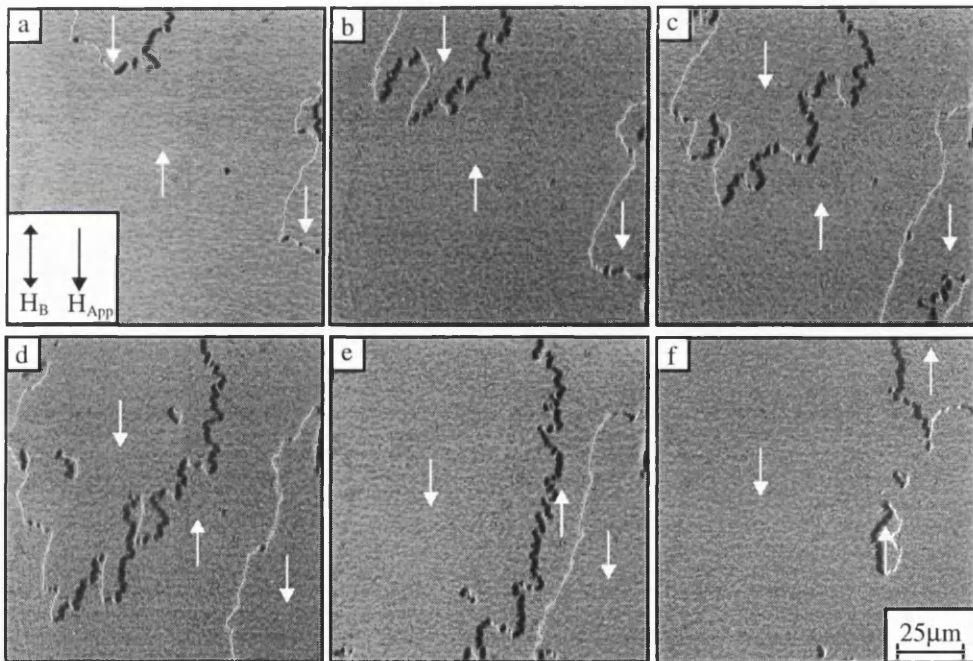


Fig 6.5(a-f): Biased layer reversal for a uniaxial TbCo biased spin-valve

The field is reduced to 50 Oe rather than zero as this prevents any domain structures forming in the free layer which could cause interpretation problems. Unlike the biased layer reversal of FeMn spin-valves, the magnetisation in areas which switch do not return to the original biasing direction if the field is relaxed. In the case of Fig 6.5(a) the majority of m_{biased} is directed towards the top of the page whereas by Fig 6.5(f) the majority is

biased towards the bottom. If instead of pausing the biased layer reversal to take micrographs H_{app} is slowly increased the same domain structures as shown in Figs 6.5(a-f) can be observed but as the life-time of each state is so short there is not sufficient time for them to be photographed. Fig 6.6 shows a high magnification Fresnel image of a domain in the biased layer and illustrates how erratic the domain walls are. Such erratic structures are characteristic of materials which display a form of magnetic creep where the energy barriers for domain wall motion are lower than that for domain nucleation (Labruno et al, 1989).

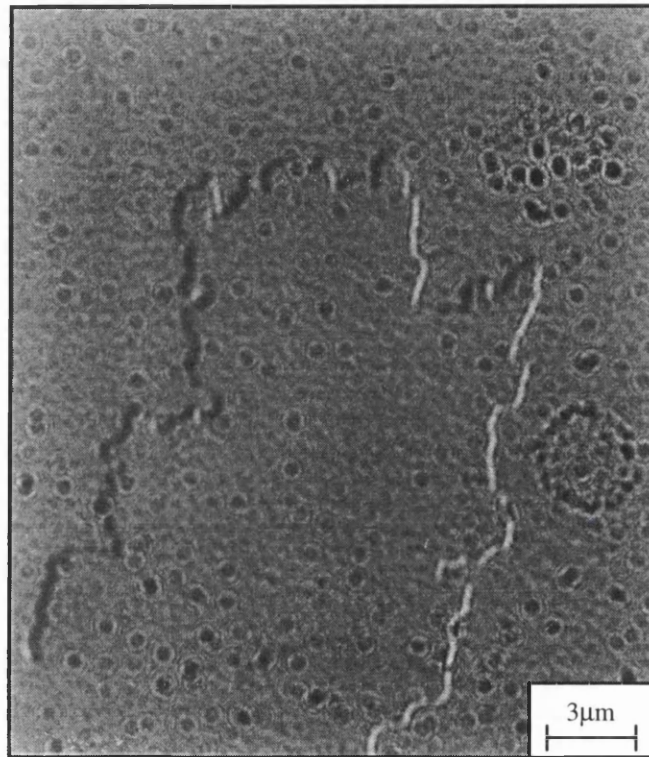


Fig 6.6: *Fresnel image of a domain structure in spin-valve biased by uniaxial TbCo*

The domain walls which are observed in the biased layer differ from those of an isolated permalloy layer in that there does not tend to be a preferred wall angle. In the case of isolated permalloy the component of magnetisation orthogonal to a wall is usually continuous across the wall. This satisfies the condition of $\text{div } \mathbf{M} \approx 0$ and as there are few free poles, there is consequently little or no magnetostatic energy. When the images of Fig 6.5(a-f) are considered it is seen that there are long sections of wall where the magnetisation meets “head on”. For the resulting magnetostatic energy from this structure to be tolerated there must be a greater energy barrier which would be incurred if the magnetostatic energy were lowered. This energy barrier is due to the domain structure in

the TbCo. As large fields are applied to the sample the introduction of walls is caused by the in-plane component of TbCo switching to a direction closer to the applied field. As already mentioned, when the applied field is reduced the TbCo does not re-align with the original biasing direction but instead those areas which are now inclined towards the field direction stay there. Fig 6.7 schematically depicts the situation at a domain wall. The energy needed to flip the TbCo magnetisation of domain 2a to that of the TbCo in domain 1a must be greater than that incurred by the generation of free poles at the domain wall in the permalloy layer.

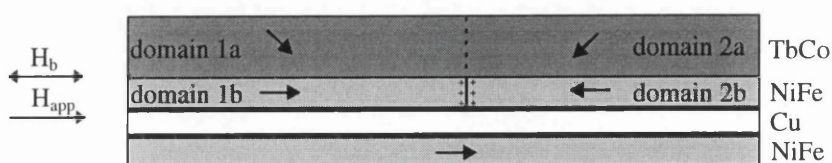


Fig 6.7: Schematic cross-section of a NiFe/TbCo wall

If the field is reduced after switching the biased layer it requires a similar magnitude of field in the opposite direction to re-introduce domains. This, along with the speed at which the reversal occurs is indicative of a very square hysteresis loop, centred on zero. Such a rapid reversal of the in-plane component of TbCo is reflected in the MR data for these samples, Fig 6.4, which shows a correspondingly sharp ΔMR for the reversal of the biased layer.

6.4.2 Detailed Study of Magnetisation Creep

In the previous section we presented results which gave an overall impression of how the biased layer in a uniaxial TbCo spin-valve reversed. We commented how the phenomenon of magnetisation creep prevented a true study of how the biased layer reversed as the applied field was varied. In this section we investigate the development of the magnetic state as a function of time, when the applied field is held constant. For a detailed study of magnetisation creep electron micrographs recorded on film are impractical. It was therefore decided to use video, as described in chapter 2, in order to record the development of the magnetic structure. Off-line analysis of individual images could then be performed by using a computer equipped with a video board capable of grabbing individual frames. Initially the sample was saturated with a ≈ 1000 Oe field in the plane of the specimen, parallel to the original biasing direction. Upon tilting in the presence of a 510 Oe vertical

field an in-plane component, with a magnitude slightly less than H_b , was applied anti-parallel to this direction. The video was started and the reversal of the biased layer recorded. Images were then grabbed at various time intervals and superimposed to create the images of Fig 6.8(a-d). These show the development of the magnetic structure as a function of time for four different values of H_{app} , which are indicated on the figures.

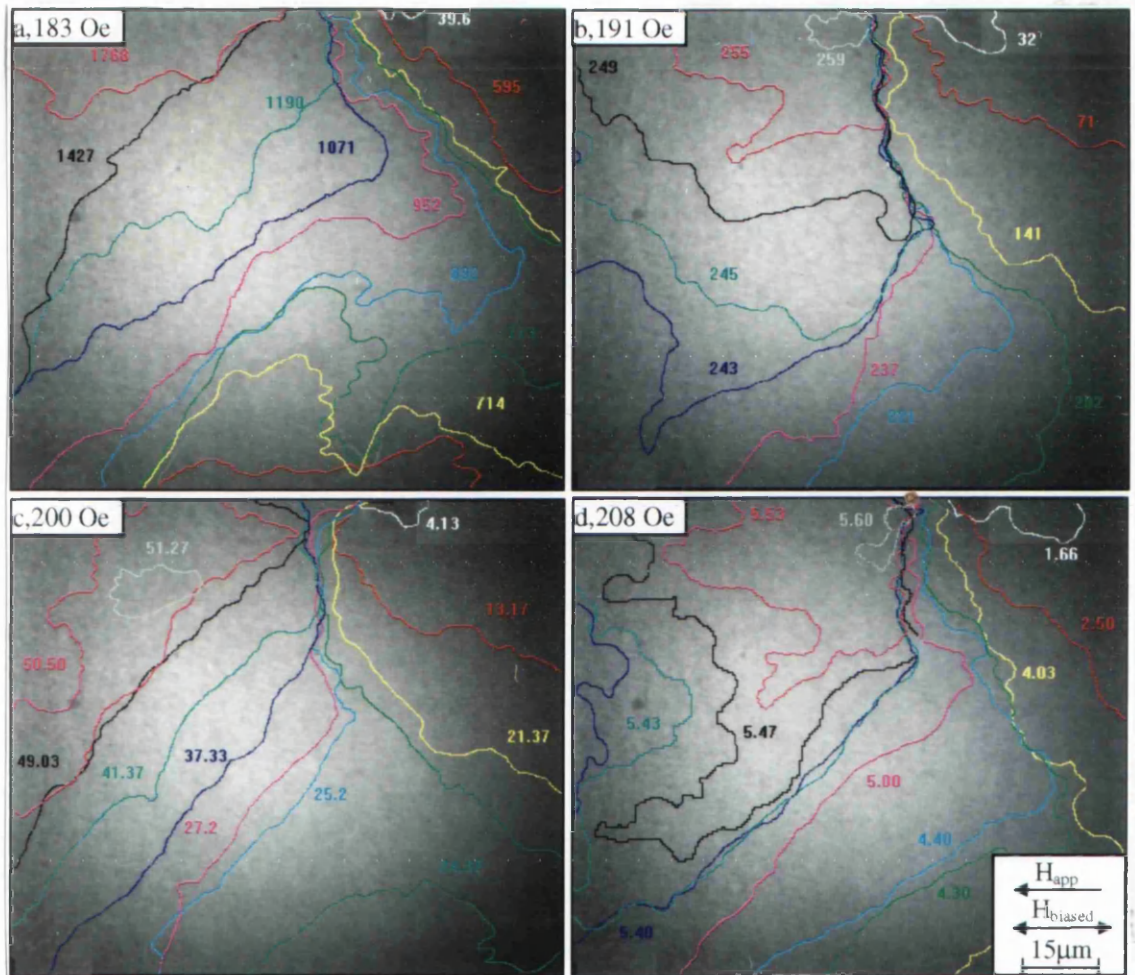


Fig 6.8(a-d): Superimposed images of the development of magnetic structure as a function of time.

In these images the domain walls have been colour coded to represent their positions and the time elapsed, for each colour, is also indicated next to the domain wall. In all of these reversals the first nucleation site is at the top of the field of view and upon close examination of other images a defect could be seen within this area of the film.

The individual frames which were used to create the superposition images of Fig 6.8(a-d) can also be used to deduce the fraction of the biased layer magnetisation which reverses, as a function of time. This was achieved by using binary analysis techniques similar to those

described in chapter 5 and the deduced normalised magnetic moment vs $\ln(\text{time})$ curves, for the four field values, are plotted in Fig 6.9. As one would expect, the switching time decreases with increasing applied field and the kinks, which are seen in all the curves, can be associated with changes in the micromagnetic structure as shown in Figs 6.8(a-d).

Normalised Magnetic Moment

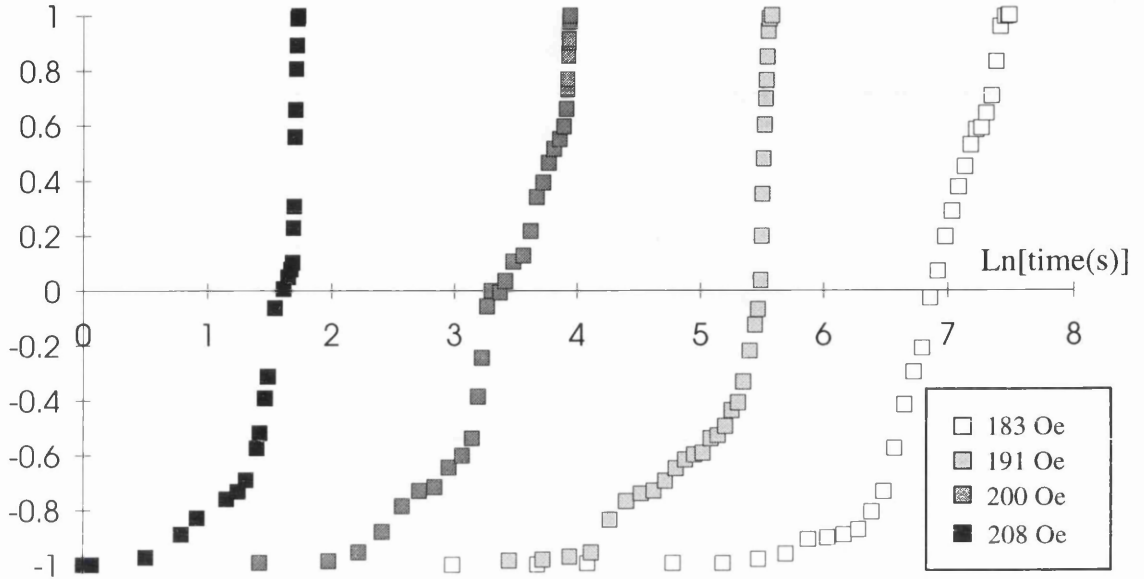


Fig 6.9 : Deduced M vs $\ln(t)$ loops for TbCo/Permalloy layer for different H_{app}

Although the curves in Fig 6.9 have many similarities close examination of the images in Fig 6.8(a-d), reveal what appears to be two different reversal mechanisms. In the case of Figs 6.8(a) and (c), where the applied fields are 183 and 200 Oe respectively, the reversal mechanism proceeds by the nucleation of a domain in the area where, as previously mentioned, a defect exists. As the reversal continues this domain grows and a domain wall moves through the top right of the area under study. This wall has a relatively slow speed and is responsible for the gradual increase in magnetic moment which occurs at the onset of the reversal (Fig 6.9). After approximately 700s (in the case of the 183 Oe reversal) a wall is introduced at the bottom of the area under study. Due to the restricted field of view it is not possible to say whether this is a separate wall or only part of the wall structure which is already present. Due to its orientation, however, it is likely that the latter is true. This section of wall appears to move relatively quickly, compared with that previously introduced, and in the case of the 183 and 200 Oe reversals switches the majority of the

remaining material. It is this wall which is responsible for the sharp change in dM/dt which occurs after an initial period of time has elapsed for all curves in Fig 6.9.

In the case of the 191 and 208 Oe reversals the initial stages of reversal are similar to those described previously with the top right of the area under study switching first and then a section of wall being introduced at the bottom. Instead of this wall sweeping through the film, however, another section of wall is introduced at the left hand side of the window. This section of wall appears to have a higher velocity and moves rapidly through the film. The introduction of this high velocity wall can be illustrated by plotting the normalised magnetic moment vs reduced time; where the reduced time is defined as the time elapsed divided by the time required to achieve zero net magnetic moment. These are shown, for the different applied fields in Fig 6.10.

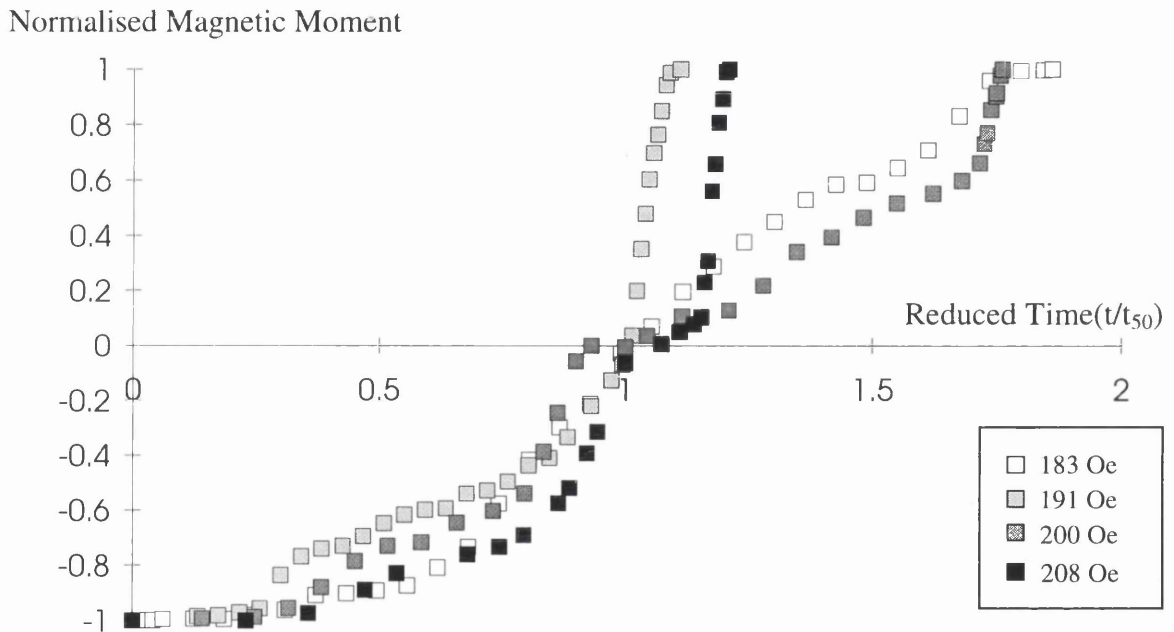


Fig 6.10: Normalised magnetic moment vs reduced time for different H_{app}

The sharp increase in gradient which occurs at a reduced time of approximately 1 for both the 191 and 208 Oe curves is due to the introduction of the high velocity wall in the left hand side of the area under study. There is also a similarly sharp rise in the 200 Oe curve at a reduced time of ≈ 1.7 and this can also be associated with the introduction of a wall in the left hand side of the sample. The reason for fast and slow moving sections of wall is not

entirely clear but we note at this point that the orientation of the wall may play an important role in it determining its velocity (see future work).

The above creep data can be analysed in order to estimate an activation radius for the TbCo/permalloy bi-layer. The method used follows Labrune et al (1989) and invokes the experimentally determined law,

$$t_{50} = C \exp \left[\frac{2V_a M_s (H_0 - H)}{k_B T} \right] \quad (6.1)$$

where t_{50} is the time required for a zero net magnetic moment, H_0 is the coercive field, V_a is the activation volume and all other symbols are as used in previous chapters.

Thus plotting a graph of $\text{Ln}(t_{50})$ versus H , as shown in Fig 6.11, gives a linear relationship where the gradient is equal to,

$$\text{gradient} = \frac{-2V_a M_s}{k_B T} \quad (6.2)$$

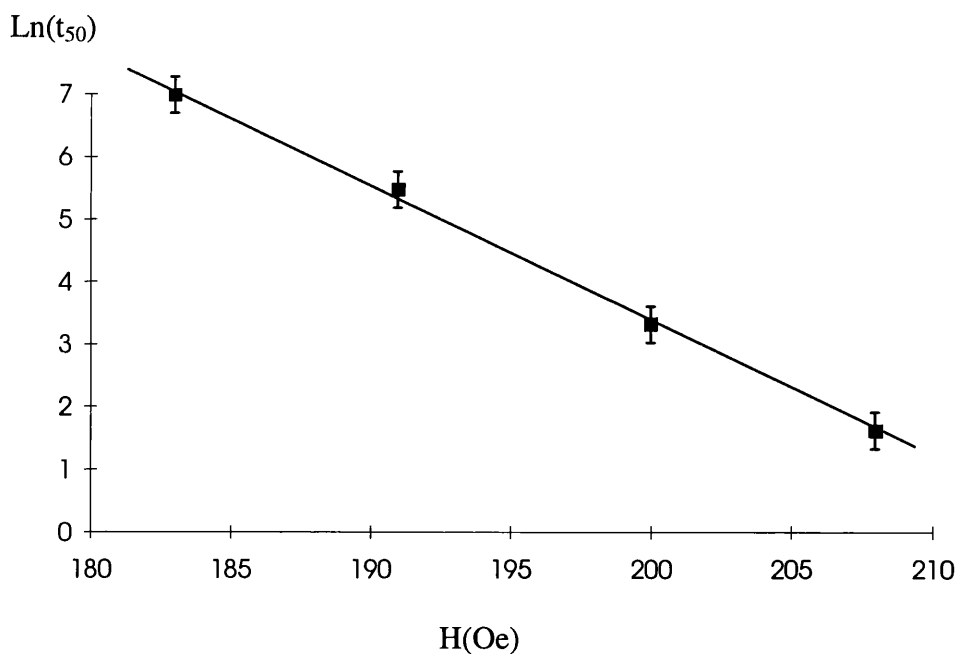


Fig 6.11: Plot of $\text{Ln}(t_{50})$ vs applied field

If $V_a M_s$ is interpreted as $A(M_s^{\text{Py}} t^{\text{Py}} + M_s^{\text{TbCo}} t^{\text{TbCo}} \sin \gamma)$, where A is the activation area, t is the layer thickness and γ is the average angle of M_{TbCo} , with respect to the vertical, then the activation area can be calculated. For the sample considered here M_s^{Py} and M_s^{TbCo} are taken as 0.98T and 0.48T respectively and the layer thicknesses as $t^{\text{Py}} = 6\text{nm}$ and $t^{\text{TbCo}} = 10\text{nm}$. In the next section we will determine a value for γ which is $\approx 22^\circ$ but for now this value is

assumed. Upon substituting these parameters into equation 6.2 an activation area of $7.28 \times 10^{-16} \text{m}^2$ is found. This corresponds to an activation radius of $27 \pm 2 \text{ nm}$.

It is important to note that while the previous study of time dependence in the TbCo/permalloy layer has yielded some interesting results these could be inherently flawed for two reasons. The first reason is the existence of a pinning point at the top of the area under study which quite obviously perturbs the switching mechanism. The second is that the area over which the domain structure can be studied is limited by the size of the Si_3N_4 window ($120 \mu\text{m}^2$ in the case of this sample). This small sampling area may be insufficient for the macroscopic time dependence of the material to be assessed. Ways of overcoming these flaws will be discussed in chapter 9.

6.5 PROBING THE TbCo BIASING MECHANISM USING VERTICAL FIELDS

In this section we deduce information about the uniaxial biasing mechanism of TbCo by considering the remanent domain structures after the application of large vertical fields ($200 < H_{\text{app}} < 6800 \text{ Oe}$). It is helpful, from the point of view of the discussion, and also to help the reader visualise the experiment, that we define polar co-ordinates. The polar angles, θ and ϕ , are shown in Fig 6.12, and are used in this section to describe the remanent states. They are also used extensively in later sections where H_{app} is inclined to the vertical.

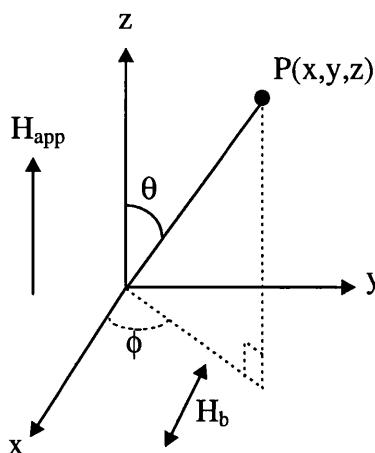


Fig 6.12: Definition of Polar co-ordinates

Figs 6.13(a-l) show the remanent states after the application of a vertical field which increases in magnitude through the sequence.

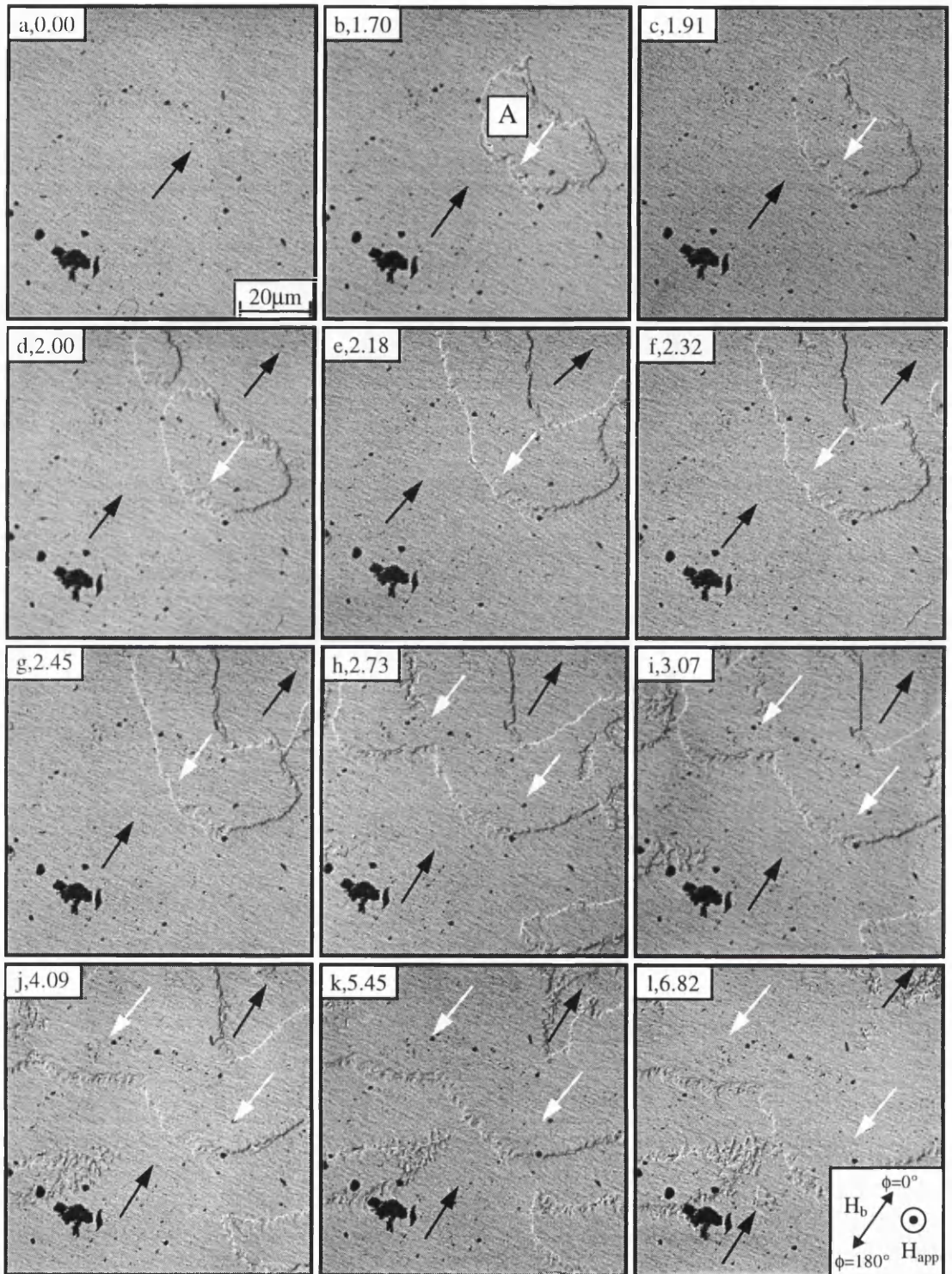


Fig 6.13(a-l): Remanent states after the application of a vertical field. The approximate directions of magnetisation have been superimposed.

This is a type (ii) spin-valve, as defined in chapter 4, and therefore has thin Co layers at the Cu/permalloy interfaces. The TbCo composition is 32% Tb and the value of H_{app} is quoted, in kOe, with each figure caption. Before each vertical field is applied a 6 kOe saturating field is applied at $\theta=30^\circ$, $\phi=0^\circ$ in order to ensure that the sample is uniformly magnetised along the biasing direction. The biasing direction which results from the initialising field is superimposed as a black arrow on the remanent states of Fig 6.13. When the vertical field is less than ≈ 1.6 kOe the remanent states have only one direction of biasing and all layers have a magnetisation directed along the original “black” direction. When 1.6 kOe is exceeded the TbCo magnetisation, m_{TbCo} , no longer returns to just one biasing direction and instead there are two directions of magnetisation in the zero field state. For some areas, which are marked by “white” arrows, the projection of m_{TbCo} lies predominantly along $\phi=180^\circ$ and causes a biasing field in this direction, e.g. area A of Fig 6.13(b). The remainder of Fig 6.13(b), however, still has the projection of m_{TbCo} predominantly along $\phi=0^\circ$ and correspondingly has biasing along this direction. As one increases the magnitude of H_{app} a progressively larger fraction of the biased layer becomes aligned along $\phi=180^\circ$ in the remanent state. This will be returned to at the end of this section but for now we concentrate on the wall structures which are observed in the remanent states. Careful scrutiny of Figs 6.13(b-l) reveals that double domain walls can often be distinguished. This can be seen more easily in higher magnification Fresnel images, such as that shown in Fig 6.14, where two walls, one of which exists in each permalloy layer, have been labelled as wall 1 and wall 2. Such wall structures have previously been observed in double permalloy films (Niedoba et al, 1989 and Heyderman, 1991) and are attributed to stray fields associated with a Néel wall in one layer inducing a secondary, sometimes quasi, wall in the second.

The fact that adjacent walls appear with the same contrast in the Fresnel image of Fig 6.14 is unambiguous evidence that we are observing wall structures in both permalloy layers. The slight separation of the two walls is caused by the fact that the ferromagnetic coupling between the two permalloy layers is relatively weak. This allows the magnetostatic interactions between the walls to dictate their relative positions and the positive poles in the tail of one wall can align with the negative poles in the other. The domains in the biased NiFe/TbCo layers are similar to those described earlier, in the biased layer reversal of section 6.4, but in this case there is no 50 Oe constraining field. This

allows domain structures to exist in the free layer and due to the ferromagnetic coupling a parallel alignment between adjacent magnetisations in the two permalloy layers results. Consequently domain walls in the free layer are in similar places to those in the biased layer.

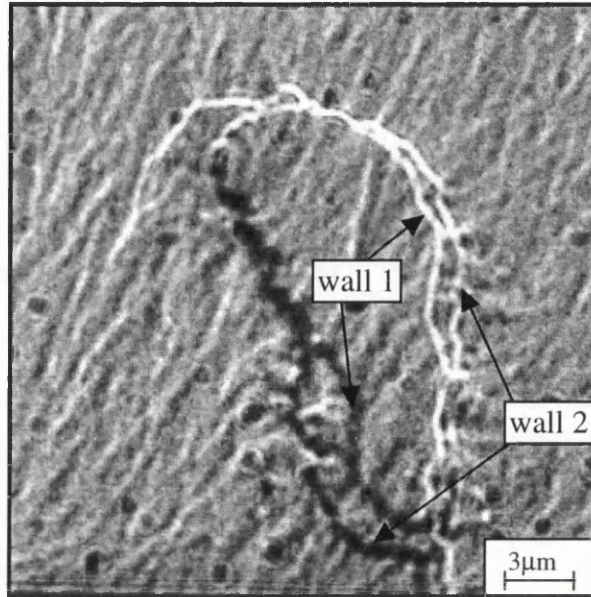


Fig 6.14: *Fresnel image of double walls observed in a remanent state after a vertical field*

The nature of these double wall structures can be further investigated by using DPC imaging. Fig 6.15 shows a DPC image with a mapping direction approximately parallel to the biasing direction.

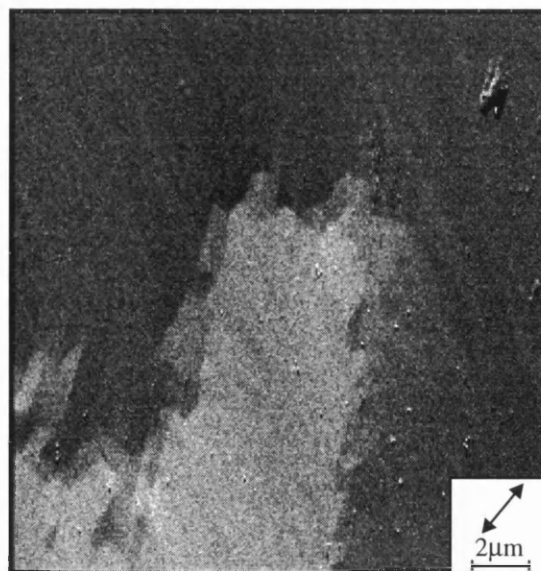


Fig 6.15: *DPC image of domain boundary with mapping direction approximately parallel to the biasing direction.*

Upon studying this image it is noted that instead of an abrupt change in contrast at the domain boundary, as is normally observed for a single wall, there is an intermediate area where the contrast is approximately mid-way between the greyscales of the two domains.

Fig 6.16(a) shows another DPC image of typical domain boundaries but at a higher magnification. Again the mapping direction, as indicated on the figure, is approximately parallel to the biasing direction. The bright field image from this area was also collected and did not show any topographical pinning sites. It also confirmed that the electron probe was sharply focused and that no astigmatism was present.

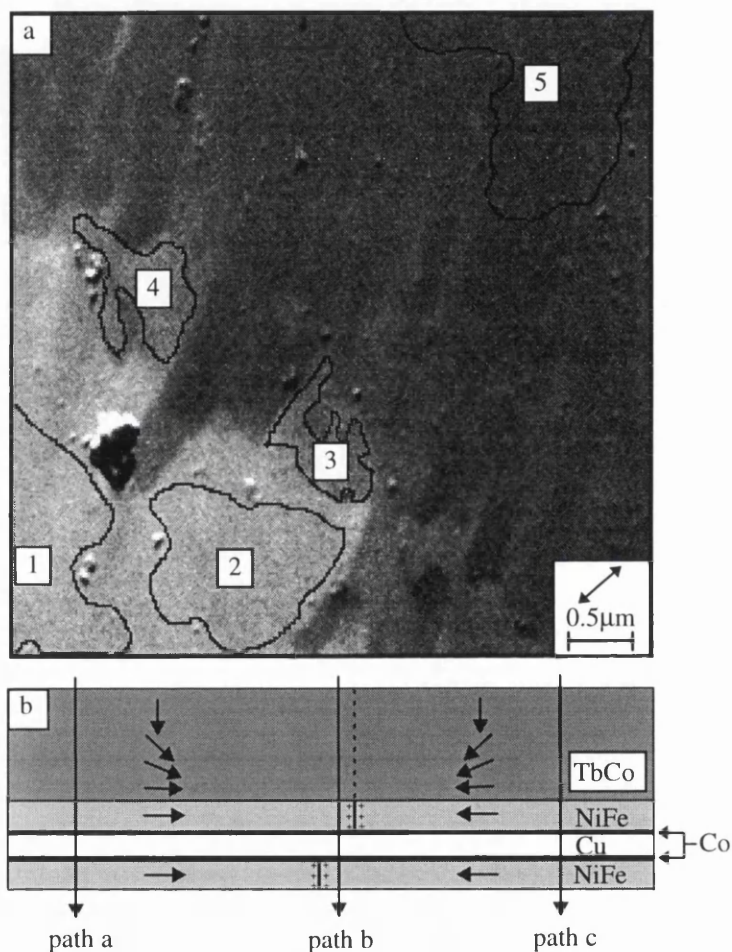


Fig 6.16: (a) High magnification image of domain boundary, (b) Schematic of situation at the boundary

The three distinct grey levels which can be seen in both the DPC images of Fig 6.15 and 6.16(a) can be used to extract quantitative information about the magnetisation in the TbCo biasing layer. The situation at a domain boundary is depicted schematically in Fig 6.16(b).

For the purposes of the forthcoming argument we shall simplify the model of the TbCo magnetisation and assume that there is no curling of m_{TbCo} as the TbCo/NiFe interface is approached. Instead the TbCo magnetisation is assumed to be inclined at an angle to the vertical. We shall also assume that the magnitude of the in-plane component of magnetisation, within the TbCo layer, is independent of which direction of biasing is present. This is a reasonable assumption as the MR loop of Fig 6.4, which is for the sample studied here, is symmetrical. In the case of the spin-valve under study in this section the two permalloy layers are of the same thickness (4nm). If we consider the three paths indicated on Fig 6.16(b) the grey level of each path can be thought of as the Lorentz deflection which arises from the different layers. The path (a) grey level is due to the deflection of the electron beam by the magnetisation in the two permalloy layers (equivalent to 8nm of permalloy) plus the horizontal component of m_{TbCo} . The path (b) grey level is due only to the horizontal component of m_{TbCo} , since the direction of magnetisation in the two permalloy layers are anti-parallel and have no net effect. The path (c) grey level is due to the same Lorentz deflection as that of path(a) but in the opposite direction. From these arguments about the origins of the Lorentz deflection it is possible, with some simple algebra, to derive equation 6.3 which gives the average angle of the TbCo magnetisation, γ , with respect to the vertical.

$$\sin \gamma = \frac{\left[\frac{(s_a - s_c)}{(s_a - s_b)} - 2 \right] [M_{\text{NiFe}} t_{\text{NiFe}} + M_{\text{Co}} t_{\text{Co}}]}{M_{\text{TbCo}} t_{\text{TbCo}}} \quad (6.3)$$

s_a is the grey level for path (a) and similarly s_b and s_c are the grey levels for paths (b) and (c) respectively. In order to obtain a value for γ it is necessary to determine the grey levels for the three paths. In the case of path (a) this was done by averaging over what is marked as areas 1 and 2 on Fig 6.16(a). Similarly areas 3 and 4 were averaged for path (b) and area 5 for path (c). These grey levels are shown in the table of Fig 6.17 and when substituted into equation 6.3 yield a value for γ of $22 \pm 3^\circ$ or a $38 \pm 5\%$ in plane component of m_{TbCo} .

Grey level	Areas	Averaged grey level
S _a	1,2	63±15
S _b	3 and 4	117±17
S _c	5	189±14

Fig 6.17: Table of averaged grey levels

Although in Figs 6.13(a-l) we were able to deduce the direction of magnetisation in the remanent magnetic states we did not consider the actual reason for the existence of domain structures. This may be understood by re-considering the biasing mechanism of uniaxial TbCo. One possible model for the biasing is that as the interface is approached the TbCo does not have a single vertical easy axis but instead has two, inclined at equal but opposite angles to the vertical. This would account for the appearance of domains in the vertical field remanent states. Fig 6.18 shows what the easy axis (EA) geometry may look like near the TbCo/permalloy interface.

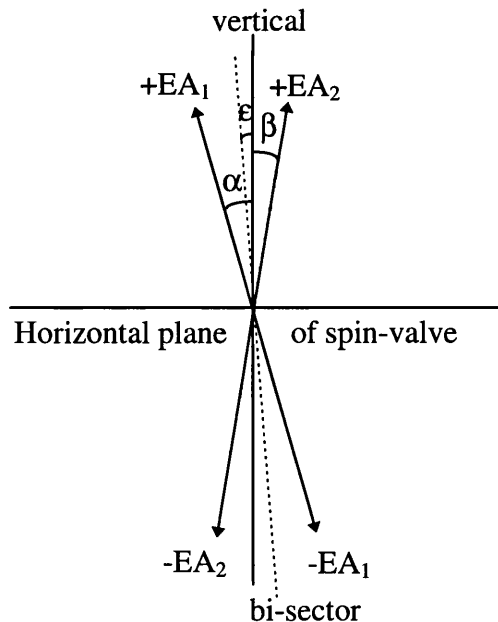


Fig 6.18: Schematic of simplified easy axis geometry of TbCo at TbCo/permalloy interface.

For ease of description we have labelled each EA with a +ve and -ve direction. The average angle that each EA makes with the vertical is likely to be of the same magnitude but for

now they are labelled separately as α and β . We have also labelled the angle that the bisector of EA_1 and EA_2 makes with the vertical as ϵ , though this is not discussed until section 6.6. Since we applied a 6kOe initialising field at $\theta=30^\circ$, $\phi=0^\circ$ it is assumed that initially the average m_{TbCo} , at the interface, is along $+EA_2$.

As with the permalloy films studied in chapter 3 dispersion of magnetisation is caused by variations in the local easy axis and prevents the perfect alignment of m_{TbCo} with the average easy axis. In the case of TbCo there will be a distribution in the angle that the EA makes with the vertical as well as local variations in ϕ . Together these will lead to a conical distribution around the average easy axis direction. The variation about ϕ will not however be investigated in this thesis and we limit ourselves to the distribution of EAs with respect to the vertical. When we apply a small vertical field to the spin-valve m_{TbCo} is drawn towards the vertical but upon reducing H_{app} returns to $+EA_2$. As H_{app} is increased m_{TbCo} becomes progressively closer to the vertical until areas where the dispersion is greatest are closer to $+EA_1$, instead of $+EA_2$. At this point relaxation of H_{app} will lead to domains in the remanent state. If H_{app} is increased further, larger and larger fractions of m_{TbCo} will relax back to $+EA_1$ rather than $+EA_2$ until at an infinite field approximately 50% of m_{TbCo} should flop to each easy axis. It is possible to repeat the binary image analysis of previous sections on the states of Fig 6.13(a-l) and so calculate the relative areas, following the application of a vertical field, which are biased along $\phi \approx 180^\circ$ and 0° . This was done and a plot of the fractional area biased along $\phi \approx 180^\circ$ vs H_{app} is shown in Fig 6.19.

This graph shows that as H_{app} is increased a larger fraction of m_{TbCo} is pulled towards EA_1 and therefore is in general agreement with the suggested model of two easy axes, inclined to the vertical. We note that for the largest field, 6.8kOe, 58% of the magnetisation flopped towards $+EA_1$. This is higher than expected and may be due to slight buckles in the film which results in more than 50% of m_{TbCo} favouring one easy axis at high fields. The hypothesis of two easy axes in the TbCo is also consistent with the Fig 6.4 which shows uniaxial biasing for this sample.

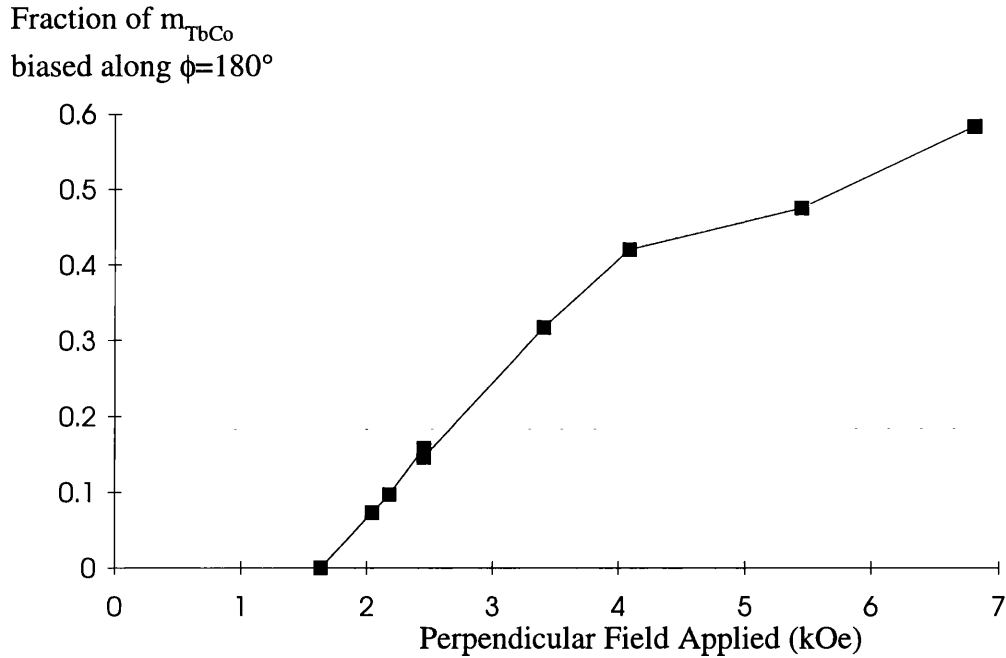


Fig 6.19: Fraction of m_{TbCo} biased along $\phi=180^\circ$ vs applied vertical field (kOe)

6.6 PROBING THE TbCo BIASING MECHANISM USING FIELDS AT SMALL ANGLES TO THE VERTICAL

In this section we apply a 6 kOe field at small angles to the vertical where the component of field, in the plane of the film, is parallel to the biasing direction (i.e. $\phi \approx 0^\circ$ and $-10^\circ < \theta < +10^\circ$). By studying the consequent remanent states we investigate the hypothesis of two easy axes in the TbCo, as suggested in section 6.5.

Unfortunately the sample which was used in previous sections had become contaminated with a non-magnetic material. For consistency, however, it was decided that the present experiment should still be performed using this sample. Although the contamination lowers the aesthetic appeal of the sample the magnetic contrast is still easily distinguishable from that which arises from contamination. The results which are extracted from the following experiment are therefore unaffected by the presence of the contaminant.

As in section 6.5 it is important that we always start from a well defined magnetic state. An initial field of 6 kOe was therefore applied at $\theta=30^\circ$, $\phi=0^\circ$ in order to ensure that all m_{TbCo} started along $+EA_2$. Figs 6.20(a-o) show the remanent states following the application of H_{app} at various angles to the vertical. The number quoted with the image identification letter is θ , the angle to the vertical. In order to avoid any confusion between magnetic contrast and contamination the binary images of these states are shown in Figs 6.21(a-o).

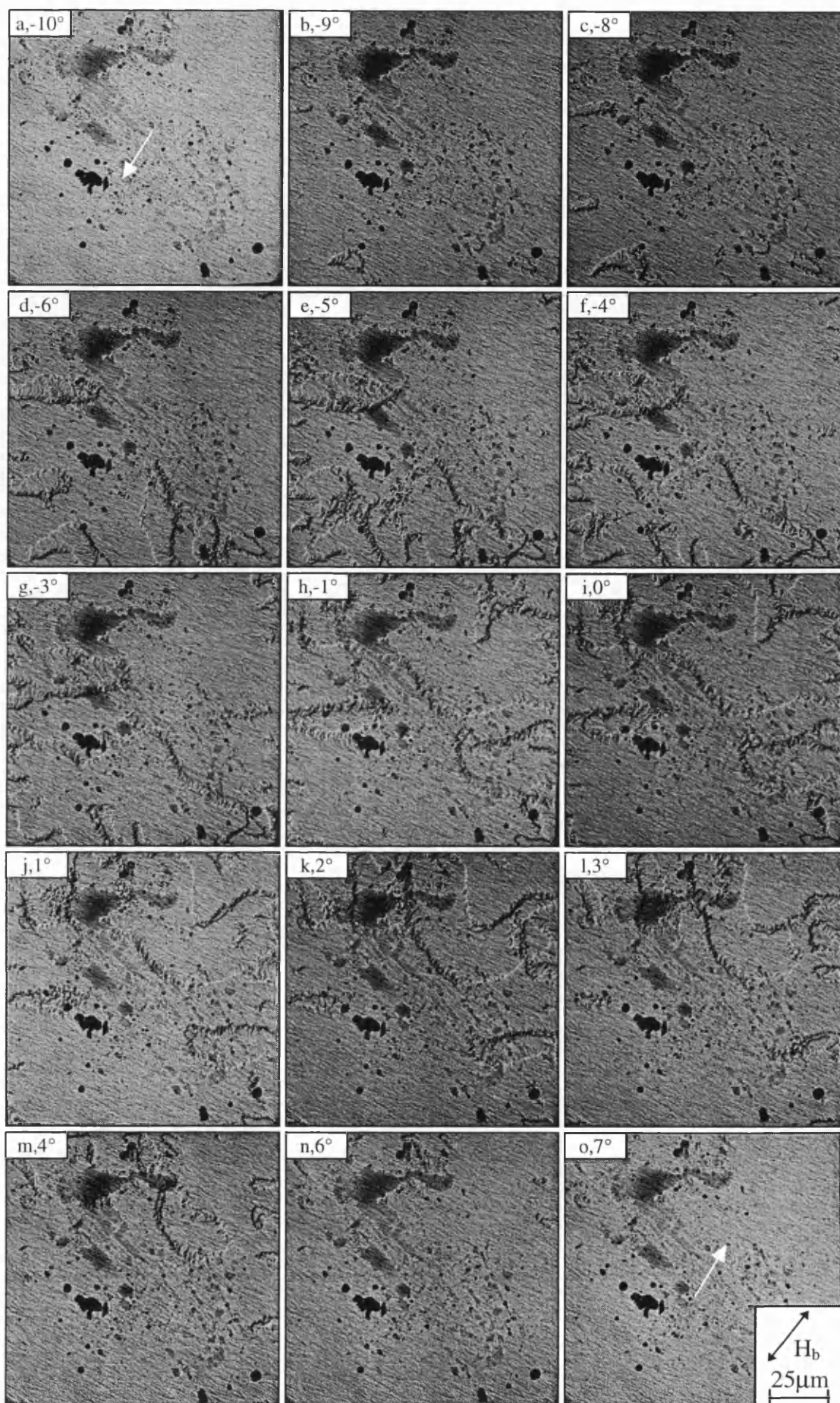


Fig 6.20(a-o): Remanent states after the application of fields at small angles to the vertical.

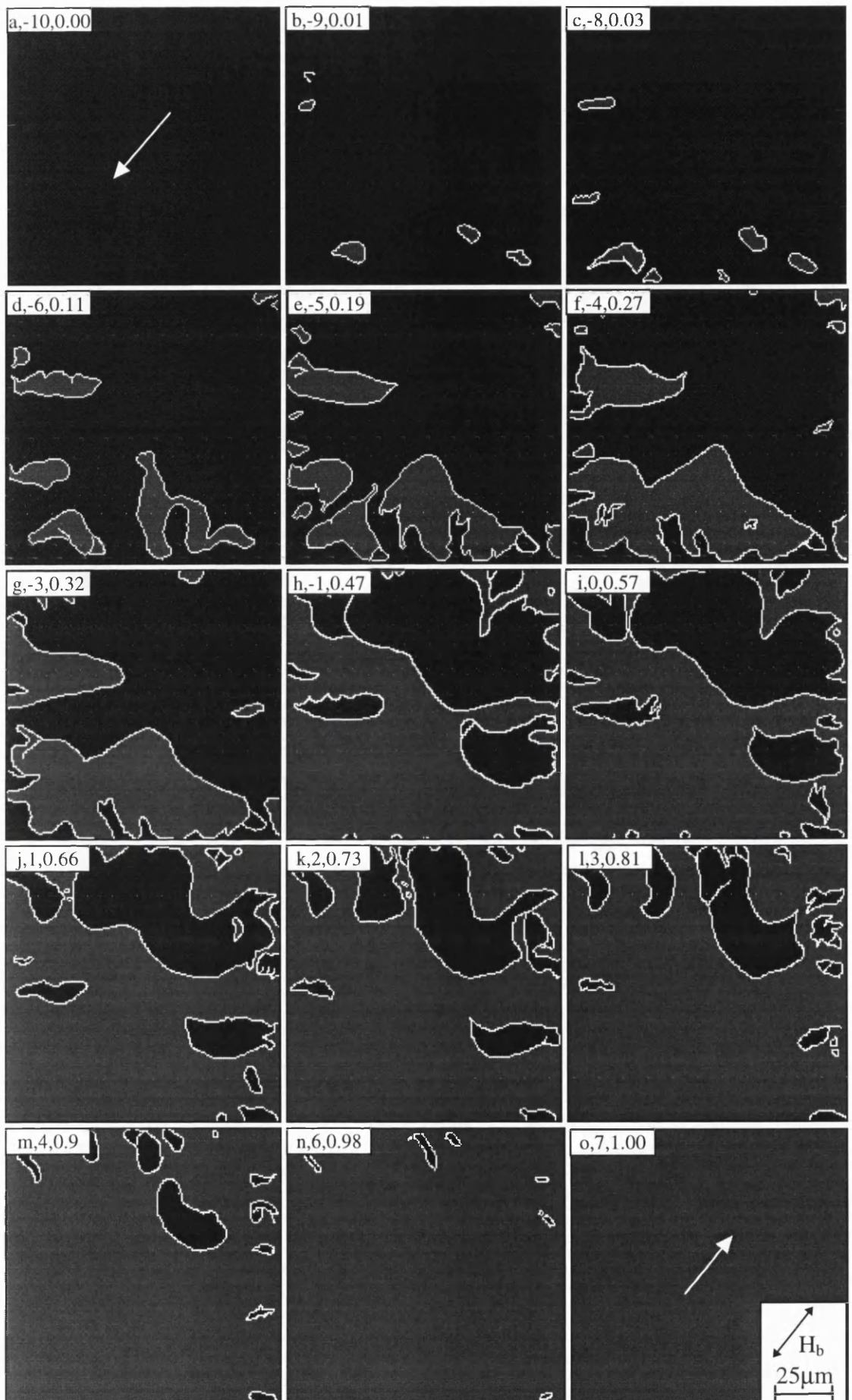


Fig 6.21(a-o): Binary images of Figs 6.20(a-o) which are representative of the remanent states after the application of a field at a small angle to the vertical.

After application of a field at $\theta = -10^\circ$ there are no domains in the remanent state, Fig 6.20(a). This is due to the fact that all m_{TbCo} was pulled from $+EA_2$ to $+EA_1$ and the biasing direction is consequently reversed from $\phi = 0^\circ$ to $\phi \approx 180^\circ$. As θ is increased from -10° , there is a progressively larger fraction of m_{TbCo} which is not reversed by the applied field. When H_{app} is vertical $\approx 50\text{-}60\%$ of m_{TbCo} stays in the original $+EA_2$ direction while the remainder becomes aligned along $+EA_1$. The fraction along $+EA_2$ continues to increase until $\theta = +7^\circ$, Fig 6.20(o), where all m_{TbCo} is along $+EA_2$ and unidirectional biasing with $\phi \approx 0^\circ$ is present in the remanent state. It is again possible to analyse these remanent states by using the images shown in Figs 6.21(a-o). In these images the first number quoted is θ and the second is the fraction of m_{TbCo} which is along $+EA_2$ in the remanent state.

A plot from this binary analysis is given in Fig 6.22 and shows the fraction of m_{TbCo} along $+EA_2$ as a function of θ . It is noted that it is a tilt angle of $\theta = -1^\circ$ rather than $\theta = 0^\circ$ which gives a state where both $+EA_1$ and $+EA_2$ are equally favoured.

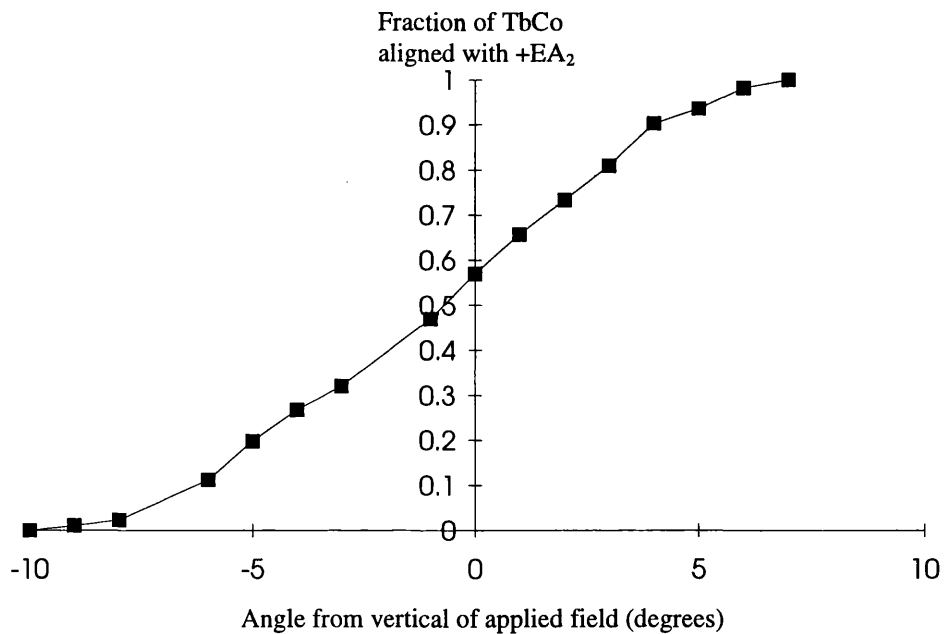


Fig 6.22: Fraction of TbCo in the remanent state which is aligned with $+EA_2$ vs the angle of applied field

As is clear from this experiment and that of section 6.5 there are two distinct biasing directions which can arise after the application of a vertical field. For these directions to be

favoured above others they must offer an energy minimum for the TbCo magnetisation. What is more since an in-plane field of ≈ 200 Oe is required to switch between these states an energy barrier equivalent to this field value must exist between them. From the point of view of the following discussion it is necessary to re-consider the easy axis geometry as shown schematically in Fig 6.18. The angle which the EA_1 / EA_2 bisector makes with respect to H_{app} , is the crucial factor in deciding whether a certain area of the TbCo will relax to $+EA_1$ or $+EA_2$. Due to the initialising field we will assume that all m_{TbCo} starts by lying along a direction close to the average direction of $+EA_2$. Now say, for a particular area of the film, ϵ , is equal to $+5^\circ$ (ϵ , as defined in Fig 6.18, is the angle that the bisector makes with the vertical). If H_{app} is along a direction less than $+5^\circ$, m_{TbCo} , within that area, will align along $+EA_1$ in the remanent state. If however $\theta > +5^\circ$ the magnetisation will relax to $+EA_2$. This means that the difference in the fraction of m_{TbCo} which aligns along $+EA_1$, between two particular values of θ , gives the fraction of m_{TbCo} which has a bisector between these angles. If one considers Fig 6.22 we have a plot of the fraction of m_{TbCo} which aligns along $+EA_2$ as a function of the angle of the applied field. The differential of this, Fig 6.23, gives the relative fractions of TbCo with different bisector angles.

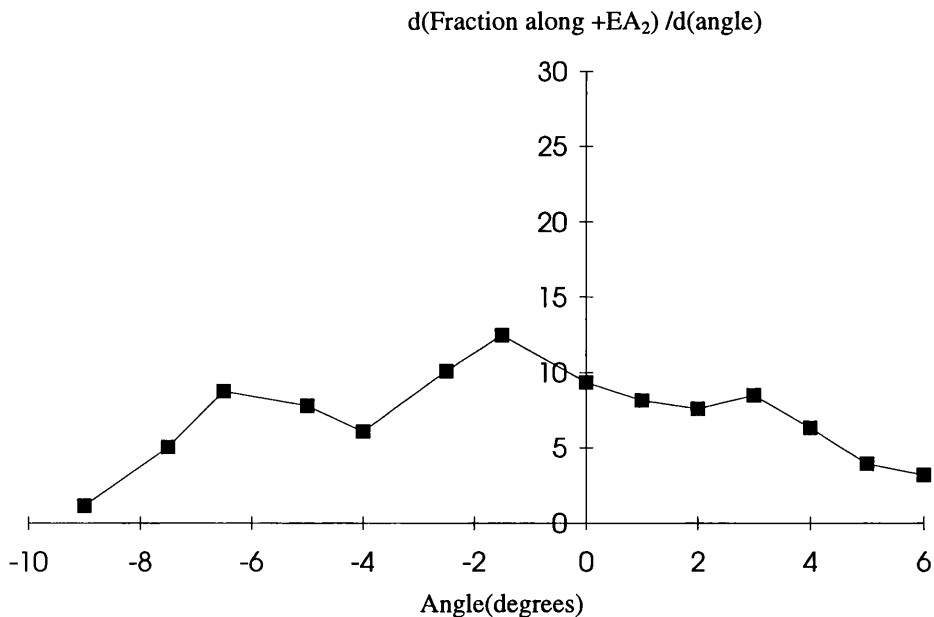


Fig 6.23: Differential of fraction along $+EA_2$ vs angle of applied field

The bi-sector angle is equivalent to the position of the energy barrier between the two easy axes and may be referred to as a “hard axis”. The graph in Fig 6.23 therefore gives the dispersion of the hard axis in the TbCo.

It is however important to note that the observed dispersion in the hard axis could also be due to bends in the Si_3N_4 membrane. Such bends could result in a preferred biasing direction for different areas of the film. It would be interesting to apply a large vertical field to a uniaxial TbCo biased spin-valve deposited on Si. If the MR ratio decreased after the application of such a field then this would be clear evidence for the creation of domains in the remanent state.

6.7 VARYING THE DIRECTION OF THE INITIALISING FIELD

In previous sections the initial magnetic state was brought about by applying a saturating field at $\theta=30^\circ$, $\phi=0^\circ$. This resulted in a state with m_{TbCo} aligned along $+EA_2$ and consequently an initial biasing along $\phi=0^\circ$. We did not, however, consider the possibility of initialising m_{TbCo} along other directions. In the case of having m_{TbCo} along a negative direction of either EA_1 or EA_2 the result will be an in-plane component of m_{TbCo} which is in the opposite direction from that of the positive case. Thus the biasing direction is either $\phi=0^\circ$ for $+EA_2$ and $-EA_1$ or $\phi=180^\circ$ for $-EA_2$ and $+EA_1$. In this section we study the effect of varying the direction of the initialising field on the remanent states which occur after the application of a vertical field.

Figs 6.24 (a,b) show two remanent states of the same sample after different initialising fields were applied.

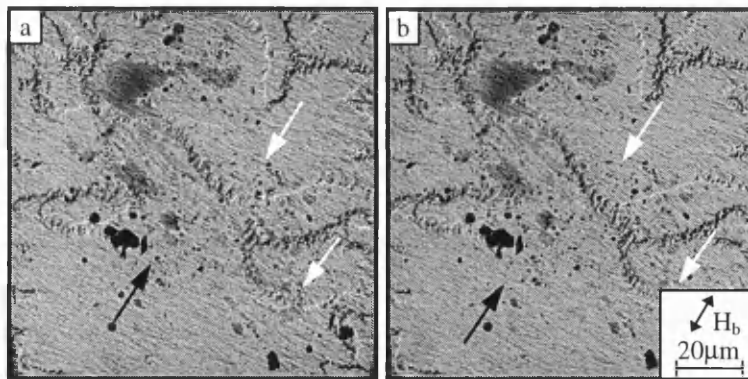


Fig 6.24(a,b): Remanent states after an initialising fields along (a) $+30^\circ$ and (b) -30°

The state shown in Fig 6.24(a) was created by the application of a 6kOe initialising field at $\theta = +30^\circ$ and then a vertical field of + 6 kOe. As seen earlier this creates domain structures in both the free and the biased layers. The remanent state of Fig 6.24(b) was created in a similar way but instead of the initialising field along $\theta = +30^\circ$ it was aligned along $\theta = -30^\circ$. It is noted that the two remanent structures appear very similar with only very slight differences at domain boundaries. In the case of the state shown in Fig 6.24(a) m_{TbCo} is initialised along $+EA_2$, denoted by the black arrow, and then a positive vertical field is applied. We would therefore expect those areas which have a negative bisector angle, to align along $+EA_1$ when the field is relaxed and this results in the creation of domains in the remanent state. In Fig 6.24(b) m_{TbCo} is initialised along $+EA_1$, denoted by the white arrow, and therefore the biasing direction is $\phi \approx 180^\circ$. Upon application of a large vertical field we would expect those areas which have a positive bisector angle to reverse and those with a negative angle to remain along $+EA_1$. This is consistent with what is observed and the fact that the remanent states are so similar indicates that upon relaxation from a +6kOe vertical field the TbCo is “free” to chose which biasing direction to relax to.

It is also possible to vary the direction of initialising field to orientations other than $\pm 30^\circ$.

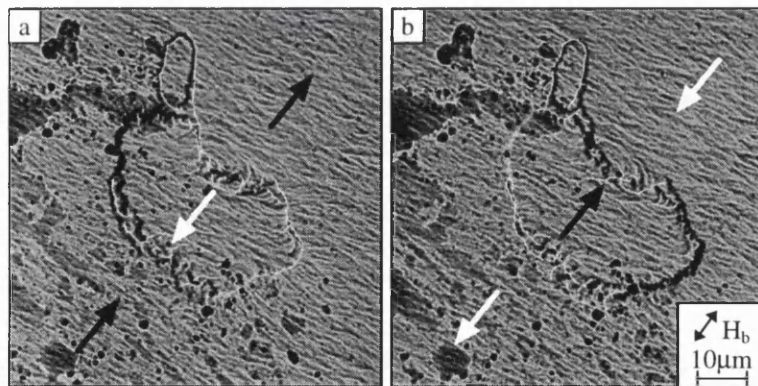


Fig 6.25: Remanent states after (a) initialising along $+EA_2$ and then applying a +2.0 kOe vertical field (b) initialising along $-EA_2$ and then applying a -2.0 kOe vertical field

In the remanent states which are shown in Fig 6.25(a-b) the first was brought about in the same manner as previous experiments, that is a 6kOe field was applied at $\theta = +30^\circ$, to align m_{TbCo} along $+EA_2$, and then a +2.0 kOe vertical field was applied. The second remanent structure however, Fig 6.25(b), was created by applying an initialising field at $\theta = -150^\circ$ and then a vertical field of -2.0 kOe, (Note that unlike Figs 6.24(a-b) Figs 6.25(a-b) only show

a region of the film rather than the whole TEM window). Although the Fresnel imaging mode is not particularly well suited to quantitative analysis, provided the experimental conditions are unaltered, the wall contrast in two magnetic states can give information about the relative senses of magnetisation in adjacent domains.

In Fig 6.25(a) the initialising field leads to a biasing direction predominantly along $\phi=0^\circ$. When a positive vertical field of +2.0 kOe is applied those areas which locally favour +EA₁ will relax towards it when the field is reduced. If, as in Fig 6.25(b), the initialising field is along -EA₂ then the original biasing direction is $\phi\approx 180^\circ$. When a -2.0 kOe vertical field is applied those areas which relaxed to +EA₁ previously should now relax to -EA₁. Comparing Figs 6.25(a) and (b) we see that this is indeed the case and the directions of magnetisation have been superimposed upon the figures. The inverted wall contrast of these two figures is what is expected for the magnetisation directions suggested.

6.8 SUMMARY AND CONCLUSIONS

In this chapter we have studied the reversal mechanisms of the biased layer in both FeMn and TbCo uniaxial biased spin-valves. In the case of FeMn the reversal proceeded by the nucleation of very erratic domain structures which existed on a fine scale (typically a few microns). In the case of uniaxial TbCo the reversal was quite different and the phenomenon of magnetisation creep was prominent during the reversal mechanism. The reversal was dominated by domain wall motion and due to there being relatively few nucleation sites the domain wall density was low. The fact that magnetisation creep was observed is indicative of a small distribution in energy barriers which prevent domain wall motion. The dominance of domain wall motion over nucleation indicates that the magnitude of this energy barrier is lower than that required for nucleation. The walls which did exist were very erratic and typically changed direction over a sub-micron length scale.

Domain structures were observed in the biased layer after the application of a vertical field. These structures were replicated in the free layer and double domain walls existed at the boundaries. DPC imaging was used to study the domain boundaries in fine detail and allowed the in-plane component of magnetisation in the TbCo layer to be estimated. While the creation of domain structure in the biased layer is interesting from a scientific point of view it may also have serious implications for the response of sensors which use uniaxial TbCo as a biasing mechanism. If such sensors are exposed to a large vertical field then the

resulting biased layer domain structure will lower the GMR amplitude attainable upon subsequent free layer reversals. These reversals are also likely to be substantially more noisy due to local pinning of the free layer magnetisation by fields emanating from the biased layer. A model of two easy axes was postulated to account for domain structures in the remanent state but it was noted that the Si_3N_4 membrane could influence the remanent domain structure. Some further studies of films deposited on bulk Si substrates, where the MR amplitude is measured before and after the application of a vertical field, are therefore required to rule out this possibility.

CHAPTER 7: THE STABILISATION OF A MAGNETIC VORTEX USING A VERTICAL FIELD

7.1 INTRODUCTION

In previous chapters we have considered the reversal mechanisms of both ferromagnetic layers within a spin-valve. In this chapter we now turn our attention to the observation of a magnetic vortex which, under the right conditions, can be observed in both the free layer of a spin-valve and in an isolated permalloy layer.

In general thin films of soft magnetic material tend to minimise magnetostatic energy by maintaining a magnetisation in the plane of the film. Stray fields are however generated at domain walls and in the case of permalloy, in the thickness region of 20-80nm, out of plane components give rise to quasi-singularities within the wall. These wall structures are known as cross-ties walls, (see section 1.2.6), and the singularities as Bloch lines, (Ploessl et al 1990). Bloch lines, which are shown schematically in Fig 7.1(a-b), are, depending on the chirality of the neighbouring Néel wall sections, referred to as either (a) circular or (b) crossed.

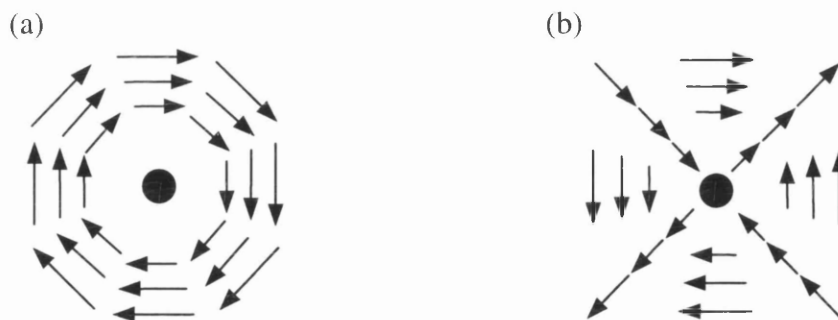


Fig 7.1(a) Circular Bloch line, (b) crossed Bloch line

Since Bloch lines are an integral part of the wall structure they can never become detached from it. The circular Bloch line can however be easily translated along the length of the wall by applying external fields. In the case of permalloy, Bloch lines are often attracted towards pinning points, or inclusions, within the film. Since the inclusions are often non-

magnetic the centring of a Bloch line on such a point eliminates the need for a magnetic singularity and therefore lowers the contribution to the total wall energy.

Another example of a vortex structure is the magnetisation distribution which may occur at the junction of 3 or more domains. This is considered in a publication by Hubert (1988) where the existence of magnetisation swirls in bulk magnetic materials is also communicated. These swirls occur at the corners or edges of a magnetic structure and are a consequence of the minimisation of the magnetostatic energy. Finally it is possible that vortex structures exist in small cubic ferromagnetic elements where the dimension of the element is smaller than the width of a domain wall, (Schabes and Bertram, 1988).

In this chapter we present results which show the existence of a new type of magnetic vortex which exists upon the application of vertical fields to either a continuous 8nm permalloy film or a spin-valve structure with a free layer of 8nm. The vortex structure is not associated with a domain wall though magnetic contrast can be discerned around it.

7.2 CREATION OF THE VORTEX AND INITIAL OBSERVATIONS

The magnetic vortex which is described in this chapter was first observed when a low angle diffraction experiment was carried out on a spin-valve. Due to the need for a reference beam a sample with a hole in the Si_3N_4 window was deliberately chosen. A vertical field of 600 Oe was applied and the orientation of the sample was tilted so as to introduce a component of field orthogonal to the biasing direction. As described in chapter 4 fields in this direction lead to the coherent rotation of the free layer ripple by $\approx 45^\circ$. Further tilting, however, did not lead to a gradual decrease in ripple contrast and instead domain structures were nucleated in approximately the same place as bend contours.

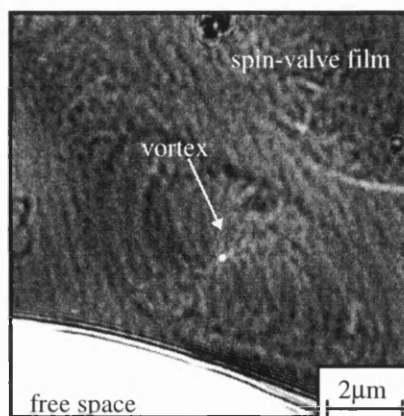


Fig 7.2: A magnetic vortex in a spin-valve

It was at this point that a magnetic vortex could be observed. An example of such a vortex structure is shown in Fig 7.2. The relatively large fields required for the nucleation of the vortex initially suggested that the structure existed in the biased layer. The experiment was therefore repeated using a single biased permalloy layer rather than the complete spin-valve structure. This, however, did not yield any domain structures for fields with components orthogonal to the biasing direction, and coherent rotation of the ripple was observed as the biased layer magnetisation rotated towards the direction of H_{app} . It was therefore necessary to investigate the possibility that the vortex existed in the free layer of the spin-valve. A permalloy layer of the same thickness (8nm) as that of the free layer in a spin-valve was therefore studied. As with the spin-valve structure in which the vortex was first observed the permalloy film was badly buckled. It was again possible to nucleate a vortex in this buckled permalloy layer as shown in Fig 7.3.

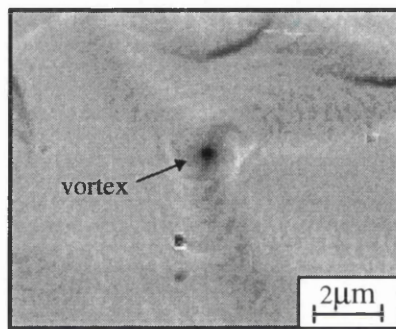


Fig 7.3: Vortex in 8nm buckled permalloy film

Vortices of opposite chirality were equally likely to form in the presence of a vertical field and although it is necessary to tilt the sample to nucleate it, the vortex is also stable when the specimen is brought back to zero tilt. Similar experiments for un-buckled films did not result in the generation of vortices.

7.3 REDUCTION OF THE VERTICAL FIELD AFTER NUCLEATION

In this section a vortex is nucleated in a single layer of buckled permalloy by tilting the sample back and forth, while in the presence of a ≈ 954 Oe vertical field. The vortex is nucleated at a tilt angle of $\approx 8^\circ$ and Figs 7.4(a-g) show Fresnel images of the change in magnetic structure as the applied field is relaxed to zero.

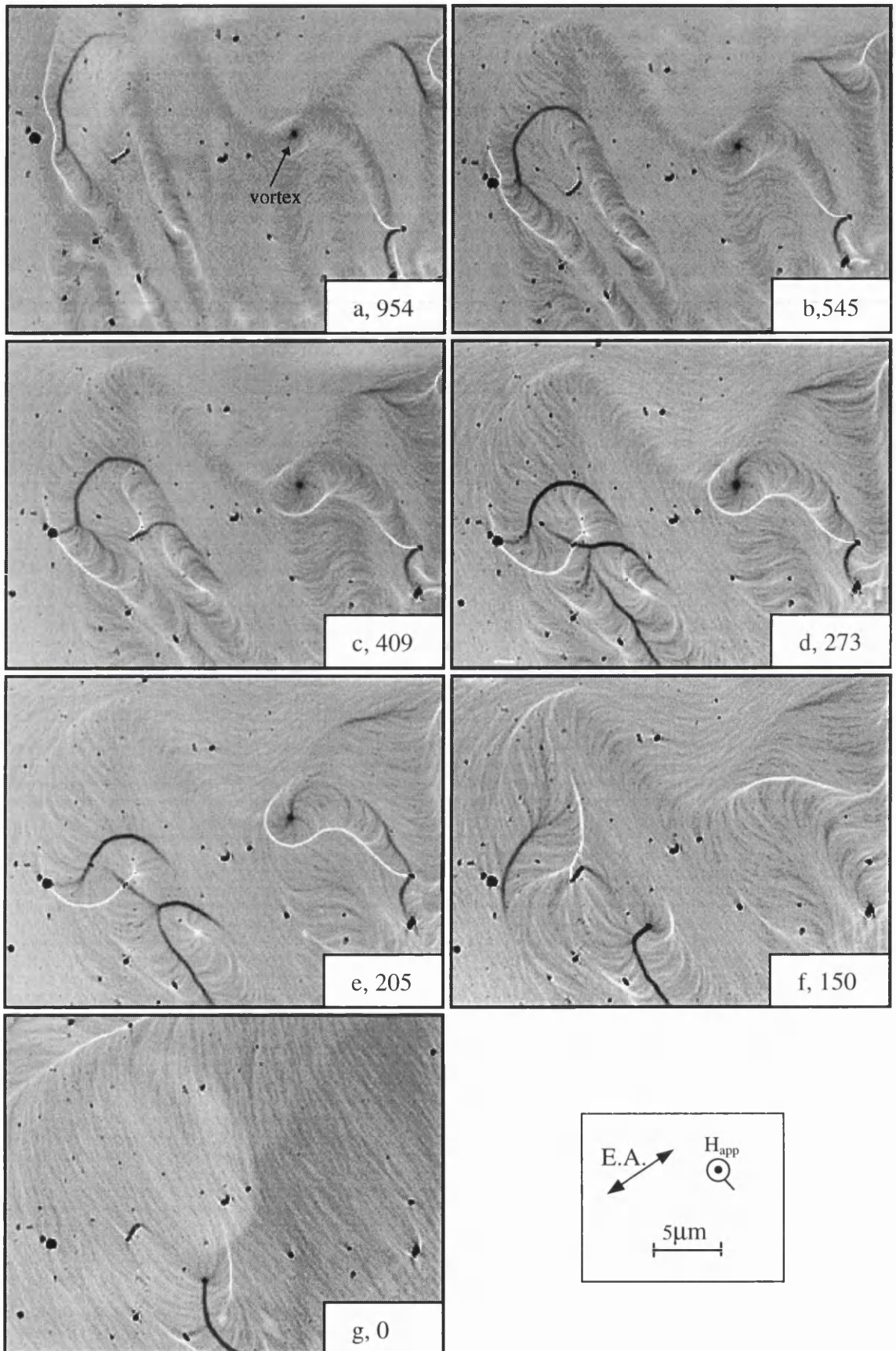


Fig 7.4(a-g): Changes in vortex structure upon relaxation of near vertical field

The vortex core which can be seen in Fig 7.4(a) is imaged as a small dark spot and should not be confused with the non-magnetic contaminants which are also present on the surface of the film. It is noted that apart from the vortex there is also a substantial amount of magnetic contrast in other areas of the film. This contrast takes the form of either domain walls or relatively strong ripple and tends to follow any bend contours in the film. The magnetic states which are presented in Figs 7.4(a-g) are difficult to interpret. It should however be noted that we are only sensitive to components of induction which are orthogonal to the electron beam. Therefore in cases where either strong ripple or wall contrast is observed there must still be substantial in-plane components of magnetisation. Since the field is applied using the objective lens, relaxation of the field leads to a change in the de-focus value and therefore the magnification of the image. The condenser lens is therefore also changed so that the distance between two arbitrarily chosen pieces of contaminant remains approximately constant. As the applied field is relaxed there is an increase in magnetisation ripple, particularly around bend contours, and domain walls are nucleated in several areas, Figs 7.4(c-d). The boundary between the perimeter of the vortex and the rest of the film also becomes more pronounced, Fig 7.4(c-e), and below approximately 200 Oe the vortex becomes energetically unfavourable and collapses, Fig 7.4(f). There are, however, still many different orientations of ripple in the film when a 150 Oe field is present at 8° to the vertical. Relaxation of the field to zero results in the majority of magnetisation returning to be aligned with the easy axis of the film, Fig 7.4(g)

7.4 THE RESPONSE OF A VORTEX TO SLIGHT CHANGES IN THE ORIENTATION OF THE APPLIED FIELD.

In this section a vortex is initially nucleated by tilting the specimen back and forth in the presence of a 680 Oe vertical field. The movement of the vortex is then studied upon further tilting of the specimen which varies the in-plane component of field. The initial state which is nucleated at a tilt of angle -2° is shown in Fig 7.5(a). Again there is magnetic contrast out with that directly associated with the vortex. Large scale ripple is obvious and upon studying other micrographs it is again possible to associate this with bend contours. As the tilt angle is changed to -1° the vortex begins to move along a channel whose presence is revealed by a bend contour. At this tilt angle there does not appear to be a well defined boundary between the perimeter of the vortex and the rest of the film.

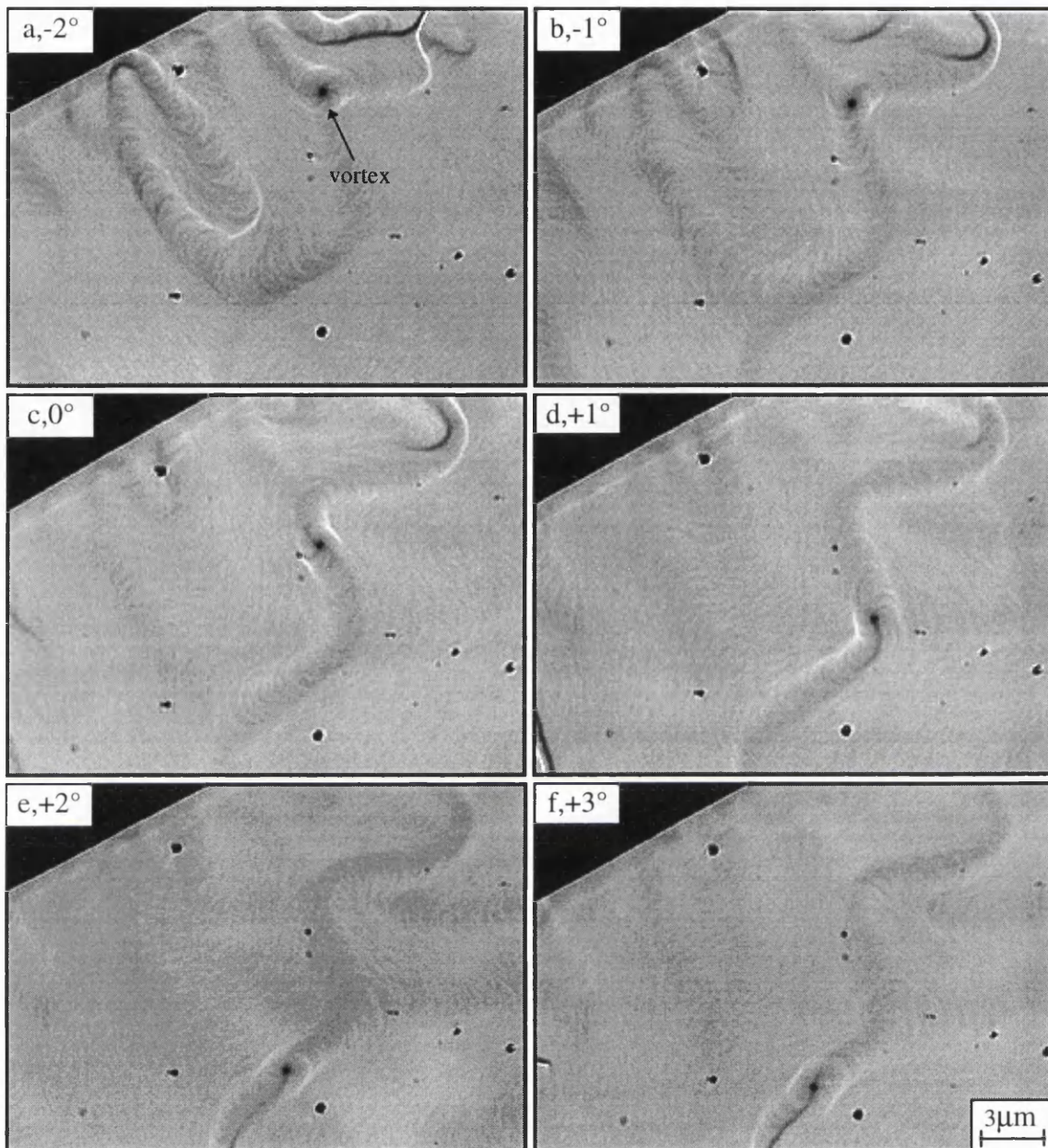


Fig 7.5(a-f): Vortex movement brought about by tilting in the presence of a 680 Oe field

Further changes in tilt angle result in the continued movement of the vortex along the contour and, depending on the position of the vortex, a more pronounced boundary can be observed, Fig 7.5(c). At a tilt angle of $0 \rightarrow 1^\circ$ a section of wall is nucleated which appears to be associated with the core of the vortex, Fig 7.5(c-d). This wall increases in length with increasing tilt angle, Figs 7.5(e), and at a tilt of $+3^\circ$ has relatively strong contrast, Fig 7.5(f). Any further increase in tilt leads to a collapse in the vortex structure. From this and

other experiments it is obvious that when the vortex becomes part of a wall structure it becomes unstable and is very prone to collapse.

Upon tilting back and forth the vortex follows a very similar path. This is illustrated well in the super-position image of Fig 7.6, which has been constructed from a video of the vortex movement produced for increasing and decreasing tilt angles. The black spots indicate the position of the vortex at various stages for an increasing field cycle while the white spots represent the position of the vortex for decreasing fields. As can be seen the vortex is fairly well constrained to a single path and only occasionally deviates from it. This is what would be expected if the vortex is constrained by a bend in the film.

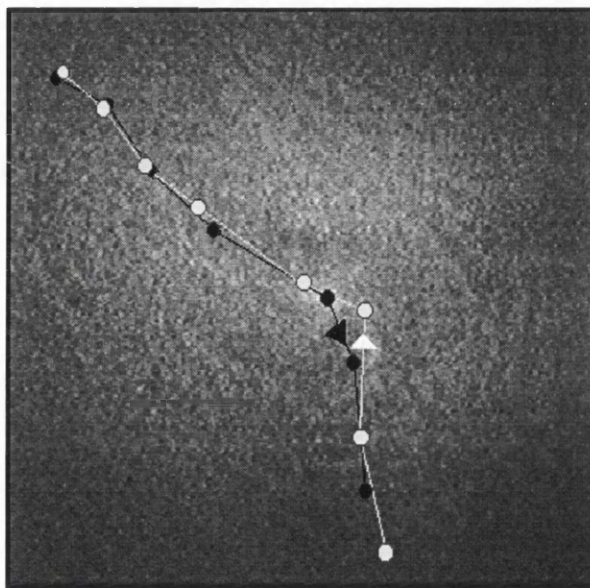


Fig 7.6: Super-position image of vortex movement for increasing and decreasing field.

7.5 THE VORTEX CORE

In the previous sections we utilised the Fresnel mode of electron microscopy in order to study the presence of a magnetic vortex in a buckled permalloy film. In this section we use DPC imaging to study the structure of the vortex in more detail. Figs 7.7(a,b) show two orthogonal DPC maps, at a relatively low magnification, of the vortex structure. Fig 7.7(c) shows the same vortex, but as imaged with the Fresnel mode. As can be seen from Figs 7.7(a-b) DPC reveals the true vortex nature of the magnetic structure. Although the

diameter of the vortex could be estimated from these images it is likely that the width of the structure is dependent on the exact bend contour in which it is formed.

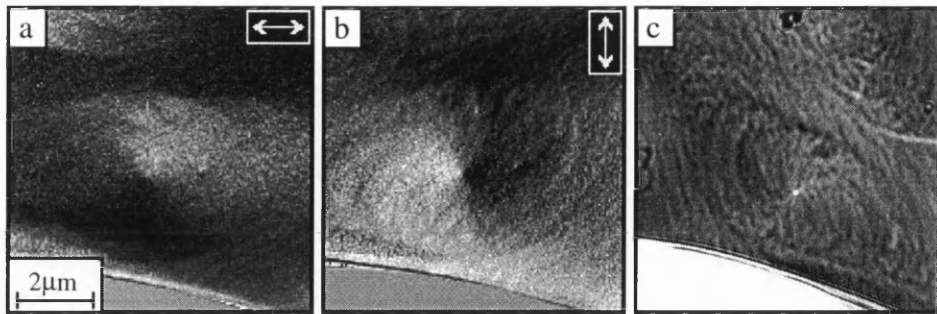


Fig 7.7:(a-b) DPC maps of magnetic induction at magnetic vortex, (c) equivalent Fresnel image of vortex shown in (a-b)

The core of the vortex, which is imaged as either a bright or dark spot in Fresnel, can also be studied using DPC. A DPC image with the overlying map of magnetic induction is shown in Fig 7.8. From this image it can be seen that the core of the vortex does indeed involve a full rotation of at least a component of the magnetisation vector by 360° .

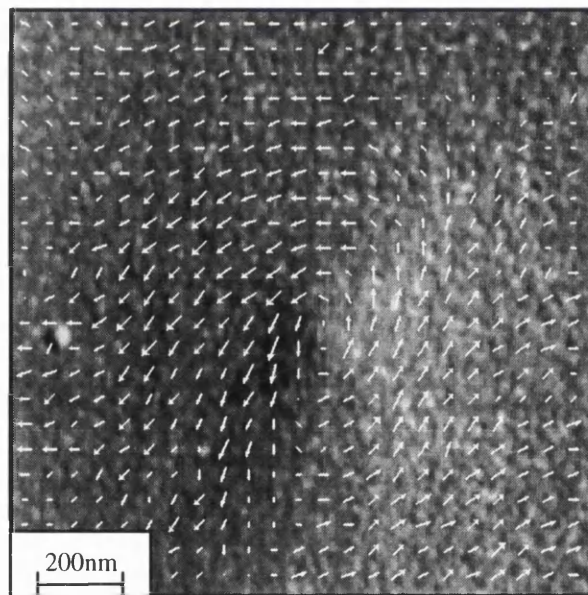


Fig 7.8: DPC image of the centre of a vortex with the magnetic induction overlaid

7.6 DISCUSSION AND CONCLUSIONS

Although magnetic vortices have been predicted to exist in modulated magnetic materials (Bogdanov and Hubert, 1994) their existence in the free layer of a spin-valve was totally unexpected. At first it was thought that the proximity of the two ferromagnetic layers may have a stabilising effect on the out of plane components of magnetisation, but the subsequent observation of a vortex in a single buckled permalloy layer showed that this could not be the case. The vortex structure must therefore be due to the large vertical field which is applied using the objective lens of the CM20. It is reasonable that such a field has a stabilising effect on any out of plane components of magnetisation. When, however, the demagnetising energy for a permalloy film, with a purely vertical magnetisation, is compared with that of the Zeeman energy then it is realised that, even for the maximum fields applied, 954 Oe, the Zeeman energy is approximately ten times smaller than that required for a purely vertical magnetisation. Thus it is clear that the simple explanation of the applied field pulling the magnetisation out of the plane of the film is inadequate. The stabilisation of the magnetic vortex must therefore be due to the combined effect of both the bend contours and the vertical field, rather than the vertical field alone. The fact that vortices are not observed when the Si_3N_4 membrane is taut also adds credence to this statement. From Figs 7.5(a-f) it is true to say that the stabilisation of the vortex is not dependent on the orientation of the bend contour. The problem, however, of why a bend in the film concentrates the vertical field so much that a vortex is stabilised is not at all clear. At the moment the answer to this question is not known and some original thought is required in order to solve it. The experiments presented in this chapter graphically illustrate how the combination of a buckled membrane and a vertical field can severely perturb the magnetic structure of a thin ferromagnetic film. It is therefore wise to exercise restraint when performing magnetising experiments on films with an in plane magnetisation when the applied field is simply brought about by tilting in the presence of a vertical field.

In conclusion a magnetic vortex has been observed in a buckled permalloy film when the film is subjected to a near vertical field. The vortex can be moved by introducing an in-plane component and tends to follow bend contours. The reason for the creation of a vortex is not clear and further experiments are needed in order to develop a fuller understanding of the structure.

CHAPTER 8: DOMAIN STRUCTURES IN FeNbSiN FLUXGUIDES FOR USE IN THIN FILM HEADS

8.1 INTRODUCTION

In thin film magnetic recording heads which utilise a magnetoresistive sensor the distance between the sensing element and the passing tape should be as small as possible. At present the fluxguide material used in thin film yoke type heads is often permalloy and a throathheight of $\approx 3\mu\text{m}$ is required in order to obtain both a sufficient output and a stable domain structure, (Zieren et al, 1993). The throathheight, t_h , of a yoke type head is indicated on the simplified schematic of Fig 8.1; which shows a cross-section through the layers of a magnetoresistive read head.

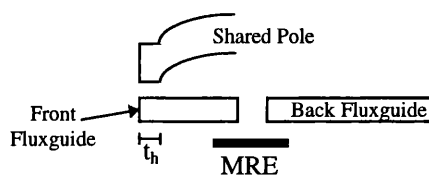


Fig 8.1: Definition of throathheight in a thin film read head

A throathheight of $\approx 3\mu\text{m}$ puts a high demand on the machining accuracy of head polishing techniques and consequently the production of such heads involves the risk of a high yield cost. Fluxguide materials other than permalloy could offer advantages for use in magnetic recording heads due to enhanced magnetic and wear properties. Any alternative fluxguide material should preferably exceed the $\approx 1.0\text{T}$ saturation magnetisation of permalloy. It is also necessary that any alternatives have a permeability of several thousand over the frequency range in which the head is operated (typically a few hundred kHz). It is, however, also important that the fluxguides do not become saturated during the reading process as this would lead to non-linearities in the output of the sensor. A linear relationship between the magnetisation in the fluxguides and the field generated from the passing disk or tape, over a field range of approximately 0-20 Oe, is therefore sought.

One possible replacement material for permalloy, which is studied in this chapter, is $\text{Fe}_{75}\text{Nb}_9\text{Si}_3\text{N}_{12}$. This material is deposited by RF diode magnetron sputtering and has an M_s

of approximately 1.45T with an induced anisotropy is typically 100 Jm^{-3} . Although an increase in M_s allows the fabrication of heads with larger throathheights an increase in noise is also observed. This is indicated on Fig 8.2 where the output for a head with FeNbSiN fluxguides is plotted as a function of fluxguide height. The three regimes which have been marked on this figure, and are depicted schematically in terms of output signal in Fig 8.3(a-c), are; (a) stable, (b) metastable and (c) unstable.

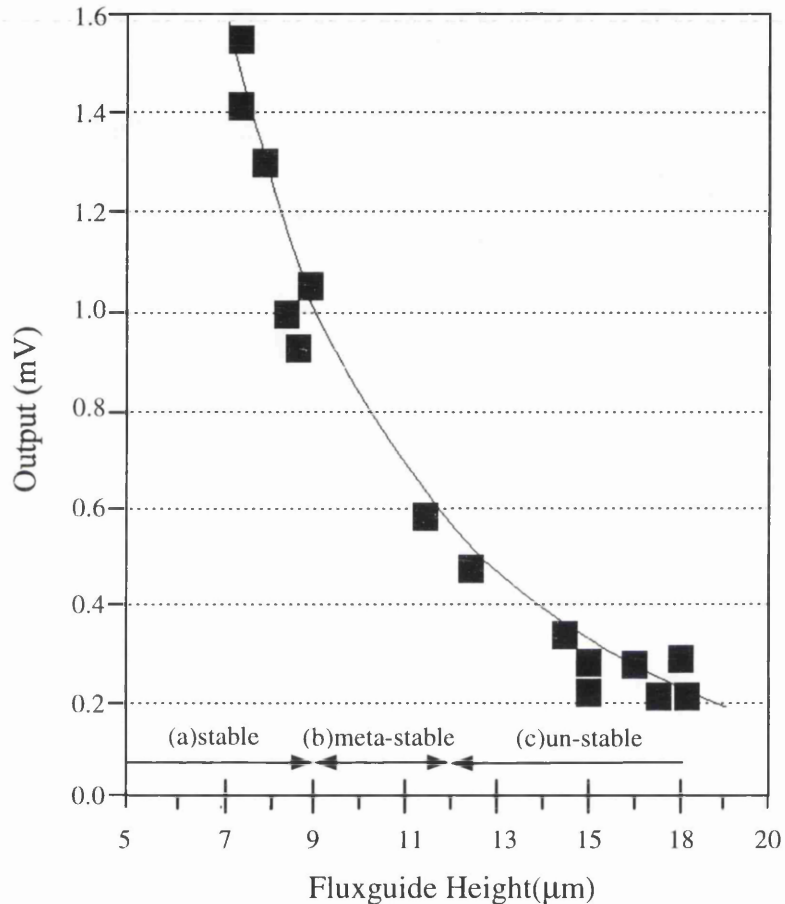


Fig 8.2: Output of DCC head as a function of front fluxguide height, courtesy of G. Somers(1994)

The decrease in stability with increasing throathheight is due to domain instabilities in the fluxguide and is a significant barrier to using heads with larger throathheights. Consequently, from an application point of view, there is a strong motivation for the study of domain structures, as a function of aspect ratio, which is presented in this chapter.

The results in this chapter were collected using the Kerr microscope described in section 2.6 and due to the predicted Kerr signal for FeNbSiN, Fig 2.13, the longitudinal Kerr effect was used.

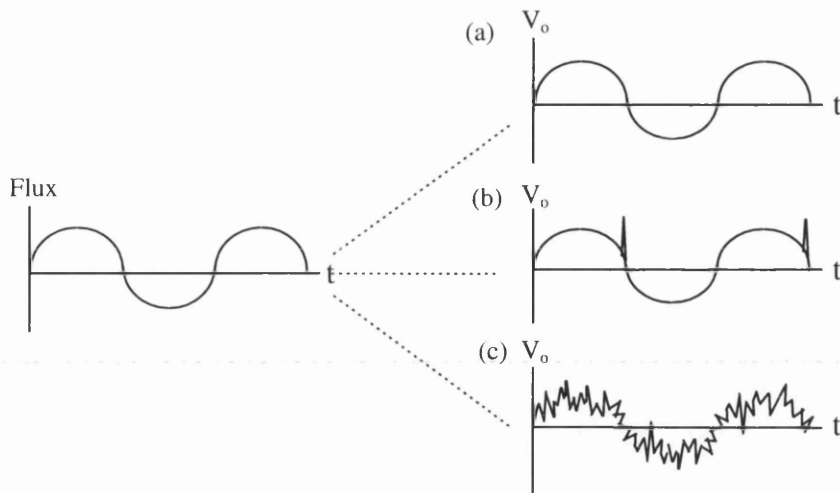


Fig 8.3: Three different output regimes (a) stable, (b) metastable and (c) unstable

8.2 FeNbSi

In recent years the microstructure and magnetic properties of Fe-(Nb, Ta, Zr)-N alloy films have been studied by a variety of authors (Nago et al, 1992, Litake and Shimada, 1992). With the correct processing and composition these films can offer a saturation magnetisation of 1.0-1.9T and permeabilities in the range of 1000-10000. Such magnetic properties make these films strong candidates for replacing permalloy in many thin film magnetic recording heads. The fluxguides studied in this thesis are sputtered FeNbSiN alloy with a stoichiometry near the eutectic composition of the Fe-Nb system. In the as-deposited state the material is amorphous-like but upon annealing at 500°C fine grains of α -Fe and NbN form. From studies of similar systems the α -Fe grains are estimated to be 5-10nm while the nitride grains are considerably smaller (1-3nm), (Nago et al, 1992). The fine nitride grains contribute to suppress the growth of the α -Fe grains which are sufficiently small to average out the magnetocrystalline anisotropy. This reduces the effective magnetocrystalline anisotropy and thereby results in a high permeability. While good soft magnetic properties are obtained for films annealed at $\approx 500^\circ\text{C}$ higher temperatures lead to growth of the α -Fe grains and a deterioration of the magnetic properties. For the FeNbSiN fluxguides studied in this thesis annealing took place at a temperature of 500°C and was in a field of 10 kOe, orientated orthogonal to the tape flux direction.

The fact that FeNbSiN is sputter-deposited rather than electro-deposited makes it possible to introduce lamination layers into the head simply by incorporating another target in the sputtering apparatus. Lamination may allow the front fluxguide to be single domain and so solve the problems of increased Barkhausen noise which are often present in heads with larger throat heights. Other studies have found a dramatic increase in performance due to lamination in both inductive (Lazarri and Melnick, 1971) and magnetoresistive (van Ooyen, 1982) heads.

Due to both the large Fe composition of the FeNbSiN used in this study and the fact that the majority of Fe is present in the form of α -Fe grains it is conceivable that the Kerr rotation would be close to that of pure Fe. The Kerr rotation (polar Kerr effect) for both Ni and Fe, as a function of incident light energy, was determined experimentally by Krinchik et al (1967) and their results are shown in Fig 8.4.

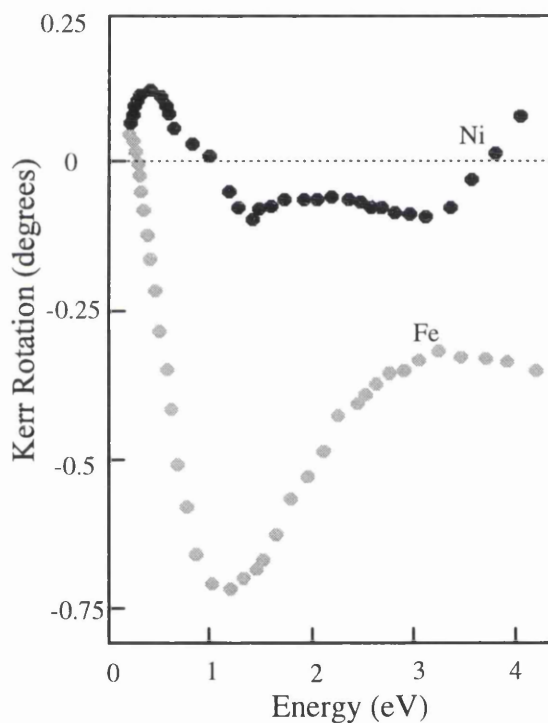


Fig 8.4: Magneto-optic Kerr rotation for Fe and Ni as a function of the energy of incident light, Krinchik et al (1967)

As can be seen the rotation of Fe, is relatively large compared with Ni, particularly for energies of $\approx 1.2\text{eV}$. This explains why it is relatively simple to image magnetic contrast in FeNbSiN whereas for permalloy, which is 80% Ni, contrast is generally weak. Before

performing the experiments described in this chapter several different filters were used to assess whether, as would be expected from Fig 8.4, the magnetic contrast could be enhanced by varying the wavelength of the incident light. Orange, green and blue filters were all tried in combination with a Xe arc source and although with our experimental set-up the wavelength of incident light was not crucial it did appear that orange light gave slightly increased contrast. This is in agreement with Fig 8.4 and in the forthcoming experiments orange filtered light is used as illumination.

Although the maximum Kerr rotation for FeNbSiN is predicted to be only a few tenths of a degree away from the crossed analyser / polariser situation the maximum Kerr signal is actually observed at a difference of a few degrees. This is because with the analyser and polariser almost crossed the signal is very weak and is swamped by shot noise from the camera tube and processing electronics.

8.3 IMAGING MAGNETIC CONTRAST USING THE KERR ROTATION

There are several ways of using the Kerr rotation to image magnetic contrast. Each has advantages and disadvantages but compliment each other to make Kerr microscopy a versatile imaging tool. The four techniques which are used in this study are briefly considered below for the case of imaging magnetic structure in a fluxguide. Examples of the images formed using these techniques are shown in Figs 8.5(a-d):



Fig 8.5(a-d): Examples of magnetic contrast in fluxguides as imaged using (a) raw Kerr contrast, (b) subtraction of the saturated state, (c) subtraction of the tickled state and (d) subtraction of + and - Kerr rotations

a) Raw Kerr contrast

This technique is relatively simple to implement and involves collecting a single frame at optimised gain and black level settings on the video card of the acquiring computer. It is

possible to watch “live” magnetising experiments but the magnetic contrast is very weak, particularly at edges or areas with increased surface roughness

b) Subtraction of the saturated state from the one of interest.

This involves acquiring an image of the magnetic state of interest. A large external field is then applied, in order to saturate the fluxguide, and another image acquired. Upon subtraction of these images the contrast is expanded within the relevant work area. The advantage of this technique is that high magnetic contrast can be obtained, due to the subtraction of both topography and non-uniform illumination. The disadvantage is that sometimes it is difficult to saturate the fluxguide and this can give confusing structures in the subtracted image, particularly at the edge of the fluxguide.

c) Subtraction of a tickled state from the one of interest.

This involves initially acquiring an image of the sample at the field of interest. A small “tickling” field is then applied to the fluxguide and a second image acquired. Upon subtraction of these images changes in the magnetic state are revealed. The advantage of this technique is that even small changes in wall position are obvious. The disadvantage is that not all walls move by equal amounts and static walls are not revealed.

d) Subtraction of + and - Kerr rotations.

This involves acquiring an image with the analyser set at the positive off-set angle which gives the maximum Kerr contrast. The analyser is then rotated to the equivalent negative position and after acquisition a subtraction of the images is performed. The main advantage of this method is that it is not necessary to saturate the fluxguide and so the potential for confusion over magnetic structure as mentioned in b) is not present. Essentially by using + and - rotations the Kerr contrast is doubled. The disadvantage however is that any non uniform illumination is also enhanced.

In the case of the techniques described as (b) and (c) above it is necessary to be able to apply an external field to the sample. This can be achieved relatively simply by three techniques; (i) bring a permanent magnet close to the sample, (ii) pass a current through external magnetising coils, which are situated below the specimen or (iii) pass a current

through a wire which is situated between the substrate and the fluxguide. In the case of a soft magnetic substrate the external coils, which in this set-up are only capable of applying ≈ 80 Oe, are insufficient to move the domain walls in the fluxguide. It is therefore necessary to use either method (i) or (iii) to obtain a change in the magnetic state under the application of a field (see later).

8.4 SAMPLES FOR OBSERVATION

The fluxguide structures which are studied in this thesis were fabricated by L. Postma at the Philips Research Laboratories, Eindhoven. They were fabricated using chemical etching techniques and the mask used to define the fluxguides was designed to give a series of structures of constant width ($70\mu\text{m}$) but varying height. The initial fluxguide height on the mask is $105\mu\text{m}$ and as one moves through the series this decreases in steps of $5\mu\text{m}$ until a height of $20\mu\text{m}$ is reached. The step size then changes to $1\mu\text{m}$ and the series continues down to zero height. Unfortunately, however, due to under etching the in-plane dimensions of the fluxguides may be as much as 10-15% smaller than that of the mask. In the following sections it is the aspect ratio from the mask which is quoted. The reason for not quoting the aspect ratio of the fluxguide, which could be measured from the Kerr image, is that strong edge contrast often arises in subtraction images which makes it difficult to obtain an accurate estimate of the aspect ratio. As mentioned previously it is possible to first deposit a wire under the fluxguides which can then be used to drive the fluxguides. The fluxguides studied here are deposited on an insulation layer of SiO_2 which is grown by CVD on either Si, AlSiMg (ceramic) or NiZn ferrite substrates. Since Kerr microscopy is a surface technique the topography of the sample is of vital importance. Any substrate roughness is, at least to some extent, carried through the insulation layer to the fluxguides. From the observation point of view the smoothness of Si makes it an ideal substrate material. It is however AlSiMg which is used in production and since any increase in roughness may affect the domain structure it is important to also study fluxguides on this substrate. Due to the increase in roughness of AlSiMg, as compared to Si, the Kerr contrast from the fluxguides is weaker. It is however possible to polish the SiO_2 insulation layer, making the fluxguides smoother, but again this is a departure from production methods. The reason for studying fluxguides on ferrite is that due to the flux closure offered by the magnetic substrate it is perhaps possible that a single domain state could be obtained for fluxguides with a larger aspect ratio than that deposited on non-magnetic substrates.

8.5 ZERO FIELD STATES

A final step in the production of thin film heads is to clear the magnetoresistive element of any domain structures by applying a large saturating field orthogonal to the tape flux direction. The remanent states of the fluxguides after such a field are therefore of interest and are considered in this section.

8.5.1 Si Substrate

The remanent states of fluxguides on a Si substrate, after the application of a saturating field orthogonal to the tape flux direction, are shown in Figs 8.6(a-r). The aspect ratio of the fluxguides is quoted with the image identification letter and the images have been formed by the subtraction of the + and - Kerr rotations. While the magnetic contrast is reasonable some of the images are badly shaded due to uneven illumination. For an aspect ratio greater than ≈ 1.29 , a seven domain flux closure structure is observed, Figs 8.6(a-d). This type of solenoidal structure is shown schematically in Fig 8.7(a). In the absence of any induced anisotropy the domain structures which are formed are determined primarily by the shape of the element. In the presence of an induced anisotropy the domain structure is not simply a function of shape and in the case of the fluxguides with an aspect ratio greater than unity this anisotropy is orthogonal to the long axis of the structure. This results in a magnetic state with domains parallel to the short axis and long axis closure domains, Fig 8.7(a). Such structures are similar to those observed in CoNbZr strips where the induced anisotropy is also orthogonal to the strip length, Wimmers et al (1990). As the aspect ratio is decreased below 1.29 a more complicated state is observed, Figs 8.6(e-f). This is somewhat surprising as such a state, which is shown schematically in Fig 8.7(b), apparently has a greater energy. The wall structure in the area A, as marked on Fig 8.7(b), is unclear, from the experimental images, Fig 8.6(e-f), though some in-situ magnetising experiments which are presented in later sections give justification for the state depicted in the schematic.

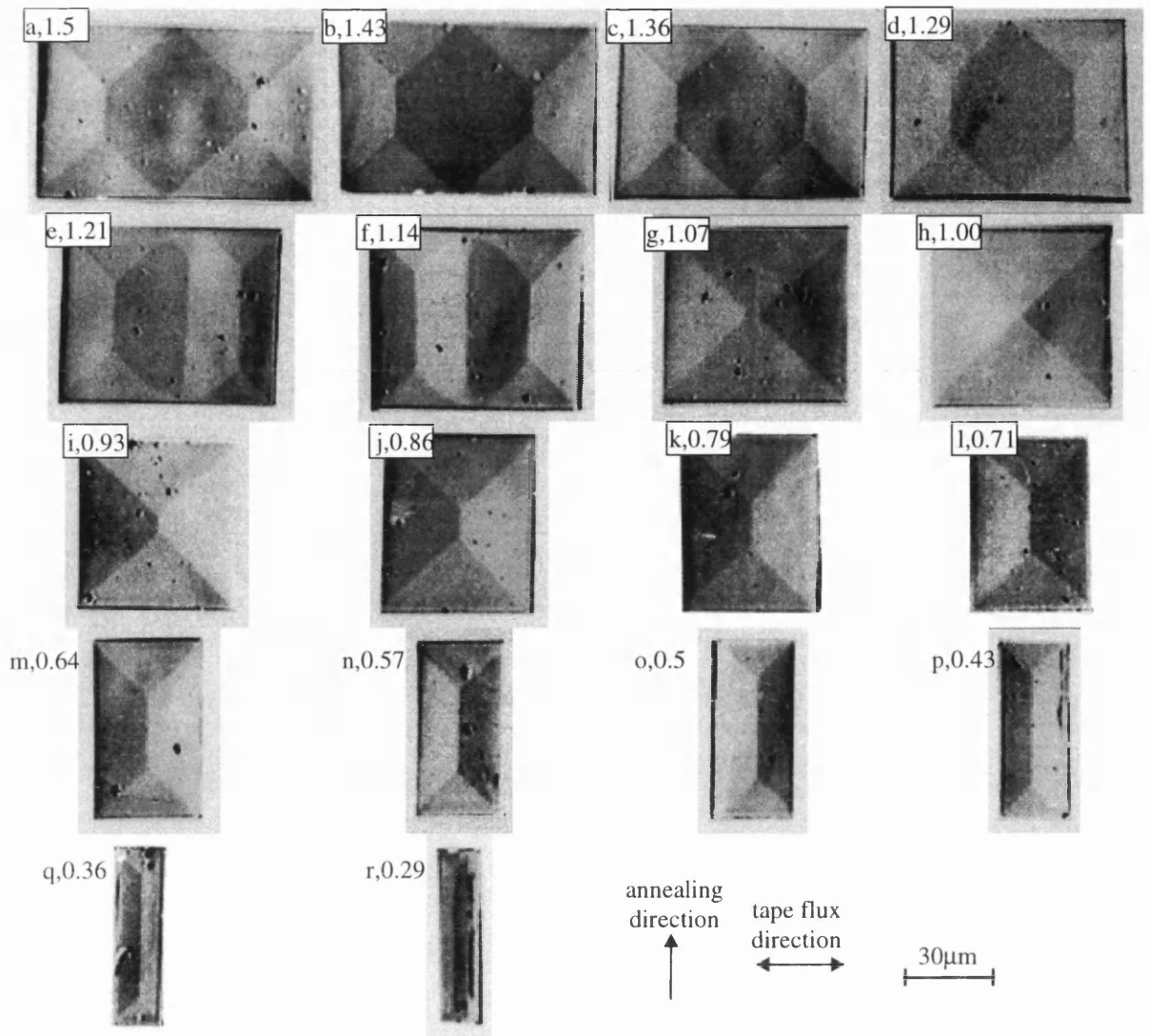


Fig 8.6(a-r): Domain structures in fluxguides on silicon substrate

As the aspect ratio is further reduced towards unity a simple four domain state, with only four 90° walls becomes stable, Figs 8.6(g-i) (shown schematically in Fig 8.7(c)). Reduction below an aspect ratio of unity results in a 180° wall extending along the long axis of the fluxguide, and two closure domains existing at the short ends of the structure, Figs 8.6(j-r)

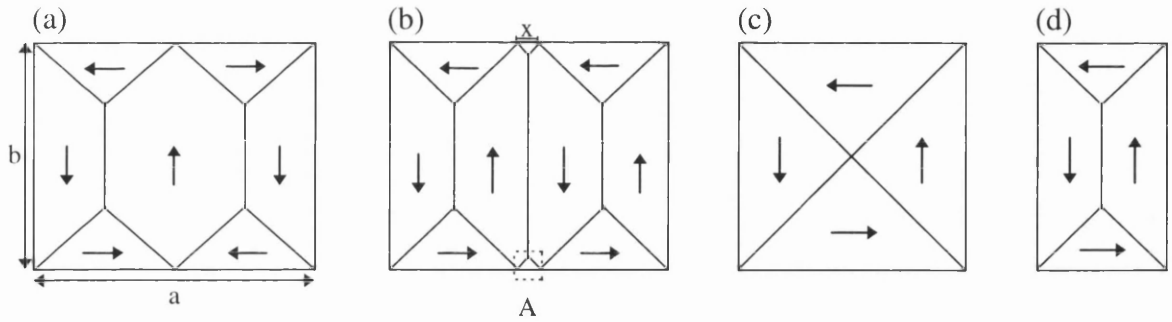


Fig 8.7(a-d): Schematic representation of the different domain structures observed for fluxguides on Si

The four domain closure state appears to be the most energetically stable for the majority of structures deposited on Si with an aspect ratio below unity and was observed in fluxguides down to a height of $\approx 3\text{-}4\mu\text{m}$, Fig 8.8

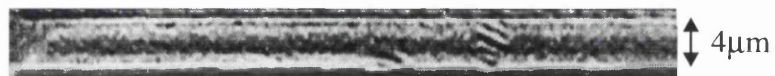


Fig 8.8: Closure structure in a $4\mu\text{m}$ fluxguide

8.5.2 Ceramic substrate

The remanent magnetic structures of fluxguides deposited on AlSiMg are shown in Fig 8.9(a-r). Again these were imaged by subtraction of the + and - Kerr rotations. Although these states are similar to those observed for the fluxguides on Si there are two main differences; (a) the complex domain structure observed for an aspect ratio of 1.21-1.14 on Si is not observed and (b) the seven domain structure is observed even for an aspect ratio of ≈ 0.93 . As expected the four domain solenoidal state which was observed for aspect ratios of ≈ 0.93 or below in Si is also observed for fluxguides on AlSiMg and again this structure was observed down to fluxguide heights of $3\text{-}4\mu\text{m}$, though these are not shown here.

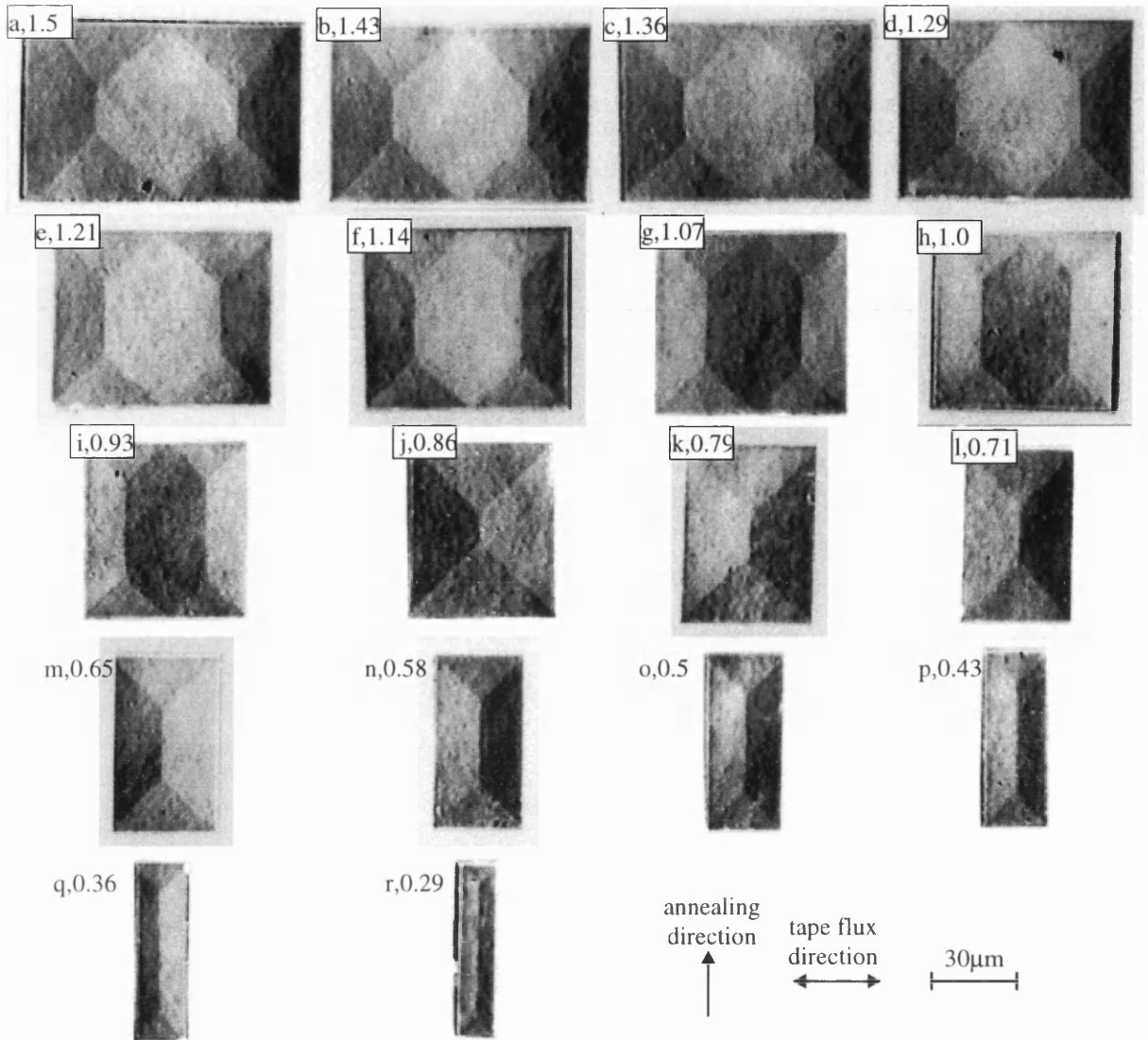


Fig 8.9(a-r): Fluxguides on a AlSiMg substrate

As both the AlSiMg and Si substrates are non-magnetic any differences in domain structure must be due to the roughness of the substrate. It is therefore possible to use the length at which a transition between domain structures occurs in order to deduce information about the anisotropy of the fluxguides on the two substrates.

In the following calculations it is assumed that a perfect flux closure state exists, i.e. $\text{div } \mathbf{M} = 0$, everywhere. In the case of Si the energy of the state depicted in Fig 8.7(b) is given by,

$$E_{\text{tot}} = (3b - a)t\sigma_{180} + 2\sqrt{2}at\sigma_{90} + \frac{K_{\text{Si}}t((a-x)^2 + 2x^2)}{4} \quad (8.1)$$

where a and b are the dimensions of the fluxguide (see Fig 8.7(a)), x is the height of the small closure domain, Fig 8.7(b), t is the fluxguide thickness and σ_{180° and σ_{90° are the wall energies of 180° and 90° walls respectively.

The energy of the state in Fig 8.7(c) is given by,

$$E_{\text{tot}} = 2\sqrt{2}at\sigma_{90} + \frac{K_{\text{Si}}a^2t}{2} \quad (8.2)$$

At the fluxguide height where the transition between these two states occurs the energies of the two states are equal. Therefore equating eqns. 8.1 and 8.2 at the transition height a_{Si} gives,

$$\sigma_{180} = \frac{K_{\text{Si}}(a_{\text{Si}} - x)(a_{\text{Si}} + 3x)}{4(3b_{\text{Si}} - a_{\text{Si}})} \quad (8.3)$$

In the case of the ceramic substrate the transition is between the states shown schematically in Figs 8.7(a) and (d). For the state of Fig 8.7(a) the energy is given by,

$$E_{\text{tot}} = (2b - a)t\sigma_{180} + 2\sqrt{2}at\sigma_{90} + \frac{K_{\text{cer}}a^2t}{4} \quad (8.4)$$

whereas the energy for the state shown in 8.7(d) is given by,

$$E_{\text{tot}} = (b - a)t\sigma_{180} + 2\sqrt{2}at\sigma_{90} + \frac{K_{\text{cer}}a^2t}{2} \quad (8.5)$$

Again equating these at the transition height of a_{cer} gives the 180° wall energy as,

$$\sigma_{180} = \frac{K_{\text{cer}}a_{\text{cer}}^2}{4b_{\text{cer}}} \quad (8.6)$$

Taking σ_{180} as $A^{1/2}K^{1/2}$ and assuming A is equal for FeNbSiN on both substrates then equations 8.3 and 8.6 lead to an expression relating the anisotropy constants for FeNbSi deposited on Si and ceramic substrates,

$$K_{\text{Si}}^{\frac{1}{2}} = \frac{a_{\text{cer}}^2(3b_{\text{Si}} - a_{\text{Si}})}{b_{\text{cer}}(a_{\text{Si}} - x)(a_{\text{Si}} + 3x)} K_{\text{cer}}^{\frac{1}{2}} \quad (8.7)$$

Assuming values of a for each transition which are half way between the heights in which the two different states were observed a_{cer} and a_{Si} are estimated as $58 \pm 2 \mu\text{m}$ and $73 \pm 2 \mu\text{m}$ respectively. Values for both b_{cer} and b_{Si} were measured from Figs 8.6 and 8.9 and are taken as $65 \pm 2 \mu\text{m}$ and $62 \pm 2 \mu\text{m}$ respectively. x is estimated as $5 \pm 1 \mu\text{m}$. Upon substituting these values into eqn 8.7 the relationship between the anisotropy constants is,

$$K_{Si} = (0.96 \pm 0.19)K_{cer} \quad (8.8)$$

Thus from the above analysis the use of AlSiMg with a SiO₂ base layer has very little effect, when compared with Si/SiO₂, on the anisotropy of the FeNbSiN which is deposited on top.

8.5.3 Ferrite substrate

Although the influence of induced anisotropy is obvious in the domain structures of fluxguides on a non-magnetic substrate the shape of the fluxguide also played an important role in determining the magnetic structure. This is due to the demagnetising energies which result in closure structures even for fluxguides with heights of $\approx 3\text{-}4 \mu\text{m}$. As previously mentioned the existence of domains in the front fluxguide results in increased noise which reduces the performance of the head and consequently, it would be an advantage if they could be eliminated. As already mentioned one possible way of reducing the probability of forming closure structures is to laminate the fluxguide and so allow a form of flux closure between adjacent layers. Alternatively a form of lamination can be achieved by depositing the fluxguide on a ferrite substrate. These configurations may support a single domain state at aspect ratios where closure structures were observed for non-magnetic substrates. The domain structure of fluxguides of varying height, deposited on ferrite are shown in Figs 8.10(a-r). The most striking difference between these structures and those observed for fluxguides on a non-magnetic substrate is that the wall structures are much more erratic. For an aspect ratio of approximately 1.5 to 1.14 (Figs 8.10 (a-f)) we observe several domains running parallel to the direction of the annealing field. The walls are not

as straight and cusp like domains often exist at the edges (for example see the domains marked B on Fig 8.10 (b)).

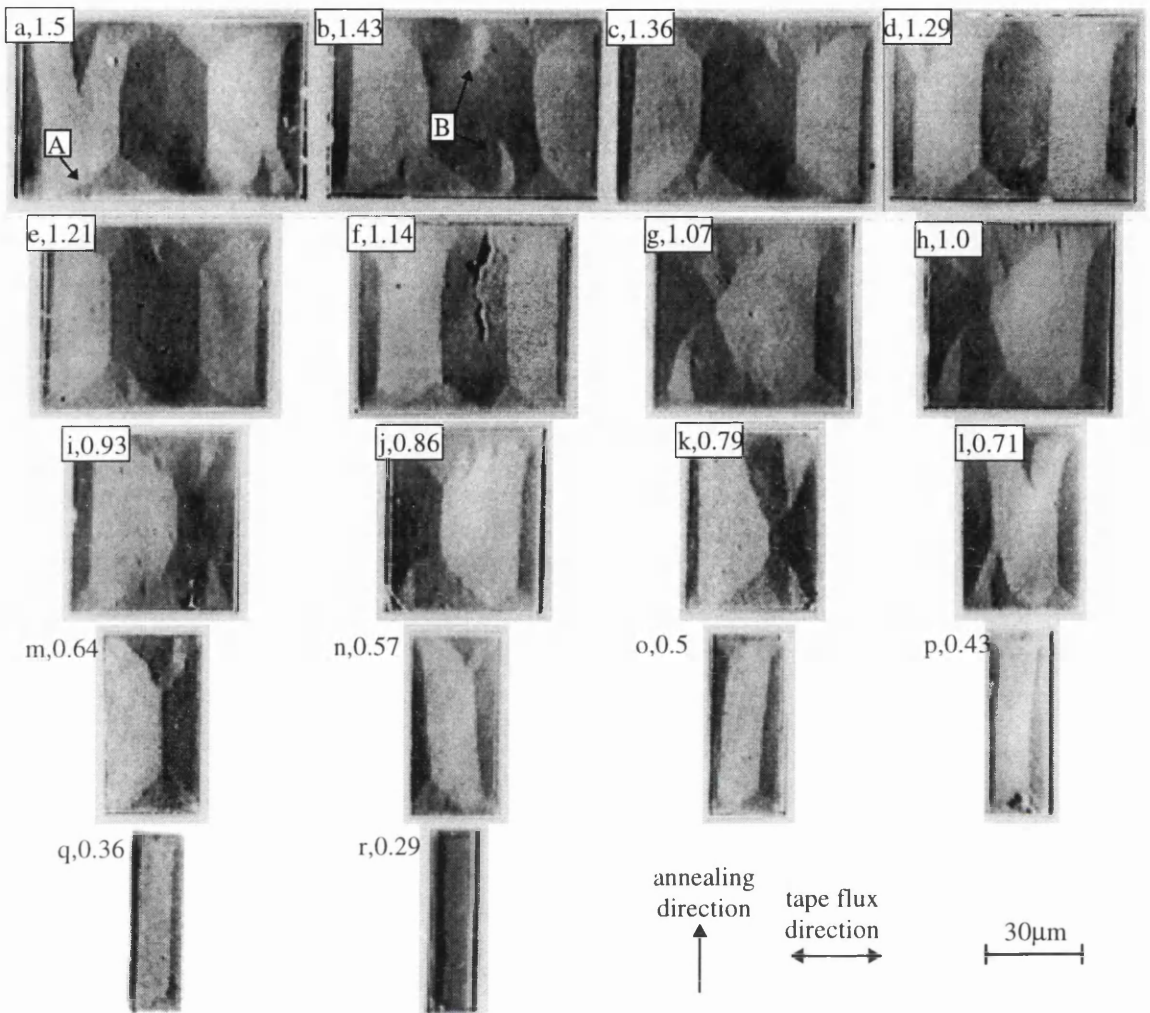


Fig 8.10(a-r): Domain structures in fluxguides on ferrite substrate

The closure domain walls which are observed in fluxguides on a ferrite substrate often appear curved (for example see wall marked A in Fig 8.10(a)). This is perhaps a consequence of the ferrite offering a form of flux closure and so lowering the energy penalty encountered if $\text{div } \mathbf{M} \neq 0$ at a wall. An interesting domain structure can often be observed in fluxguides deposited on ferrite at the junction between three different domain walls. The situation which was observed for structures on a non-magnetic substrate is depicted schematically in Fig 8.11(a). A magnetic singularity is often present at the junction (Hubert, 1988) and this has been indicated on the figure. On a ferrite substrate however a structure similar to that depicted in Fig 8.11(b) is often formed instead, (for

example see Fig 8.10(c) and (e)). Such a structure clearly carries a significant amount of charge and must be stabilised via interactions between the magnetisation in the fluxguide and that of the underlying ferrite.

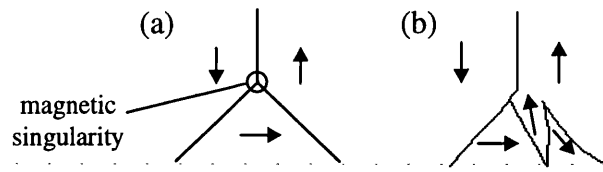


Fig 8.11(a): Closure structure observed in fluxguides on a non-magnetic substrate, **(b)** structure observed in fluxguides on ferrite.

As the aspect ratio of the fluxguides on ferrite is reduced towards unity the domain structure becomes more “confused”, Figs 8.10(g-h). These structures do not appear to be particularly affected by the induced anisotropy and many different directions of the magnetisation vector can be seen within the fluxguide. Such complicated domain structures would certainly lead to noise within any head which utilised fluxguides with such a large dimension. As the aspect ratio is reduced to below unity the domain structures remain rather confused, Figs 8.10(i-m). Unlike the case of fluxguides on a non-magnetic substrate there is no critical fluxguide height for a transition between well defined magnetic states. At an aspect ratio of ≈ 0.5 , however, a more ordered domain structure is observed, Fig 8.10(n). This structure is also found to exist for fluxguides with smaller aspect ratios, Figs 8.10(o-r). At the magnification at which these images were taken it is difficult to distinguish the domain structures in the smaller fluxguides. It is therefore necessary to use a different objective lens, with a higher magnification, in order to image magnetic contrast from within these fluxguides. The resulting images are shown in Fig 8.12(a-f), (the fluxguide height is quoted below each image). The domain structures within these fluxguides are extremely important as any changes with decreasing height may be responsible for the transitions between the stable, metastable and unstable regimes which are indicated on Fig 8.2. For fluxguides with a height below approximately $15\mu\text{m}$ the contrast which arises from the edges of the structure starts to become important. It is therefore crucial that the two images which are used for subtraction are near perfectly aligned.

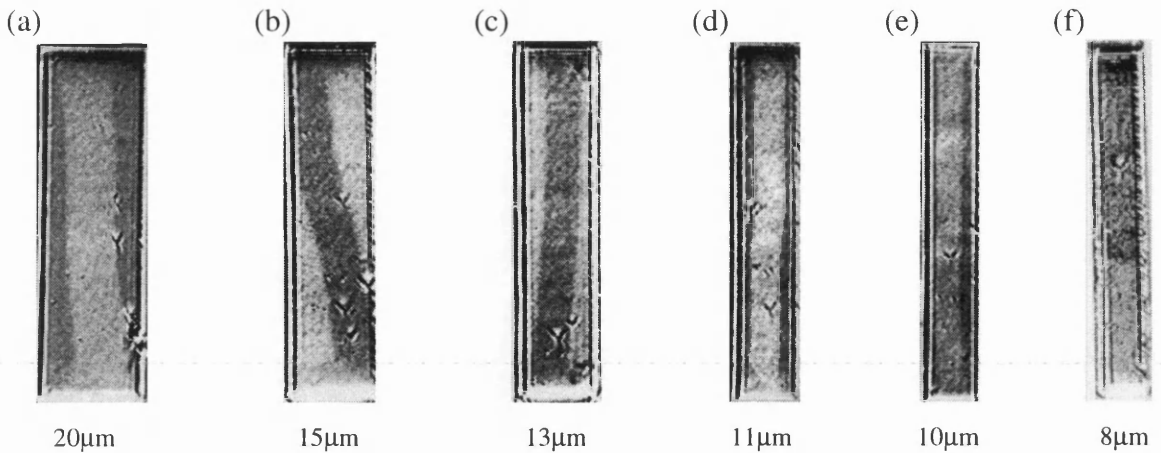


Fig 8.12(a-f): Domain structures in fluxguides with small heights on a ferrite substrate .

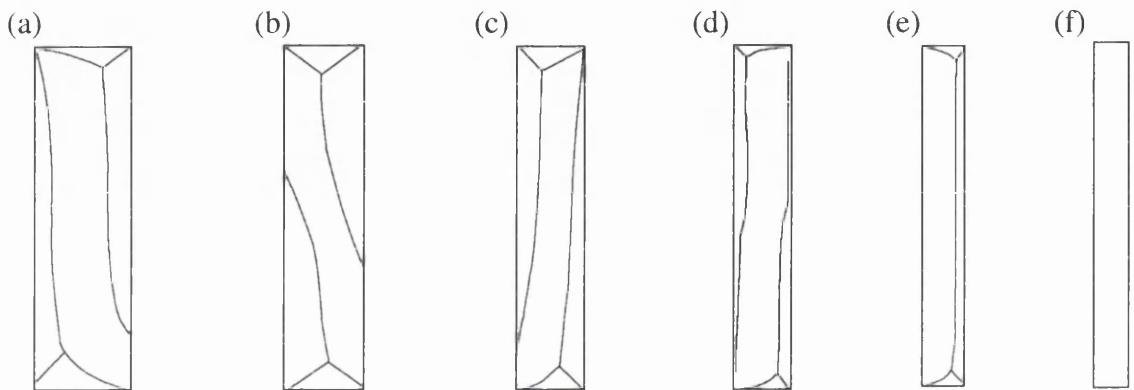


Fig 8.13(a-f): Schematics of probable domain structures shown in Fig 8.12(a-f)

Below approximately $5\mu\text{m}$ the resolution of this particular Kerr microscope becomes the limiting factor. From the Kerr photographs shown in Fig 8.12(a-f) it is possible to draw schematics of the probable domain structures within the fluxguides. These are shown in Fig 8.13(a-f) and from the contrast in Fig 8.12(f) it appears that for FeNbSiN fluxguides, deposited on ferrite, a near single domain state exists for a fluxguide height of $\approx 8\mu\text{m}$. It should however be noted that at this fluxguide height domain structures at the very edge of the structure may be indistinguishable from edge contrast.

8.6 THEORY OF DOMAIN STRUCTURE IN FLUXGUIDES

The energy of a single domain state in a fluxguide is due entirely to the magnetostatic interactions which occur between the free pole densities at either ends of the structure. It is therefore possible, by following the calculations of Rhodes and Rowlands (1954), to calculate the energy of a single domain state simply by summing the magnetostatic energy generated by two sheets of charge. The calculations are shown in Appendix A1 and were performed using the Mathcad5 software package. In the case of a fluxguide on a non-magnetic spacer the magnetostatic energy is determined by both the self energy and the interaction energy of the two charge densities situated at either end of the fluxguide. Fig 8.14 shows a graph of the sum of these energy terms as a function of the fluxguide height, (see Appendix A1).

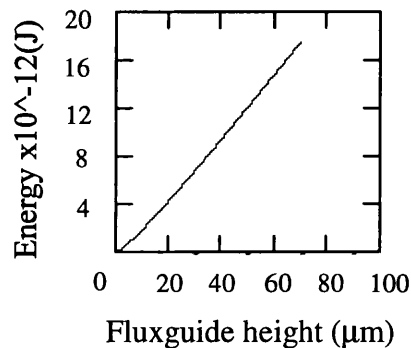


Fig 8.14: Fluxguide energy for a single domain state on a non-magnetic substrate.

The energy of a single domain state for a fluxguide on ferrite can also be calculated using the Rhodes and Rowland formula though it is first necessary to apply the method of image charges to the problem. The case of a ferrite substrate is shown schematically in Fig 8.15.

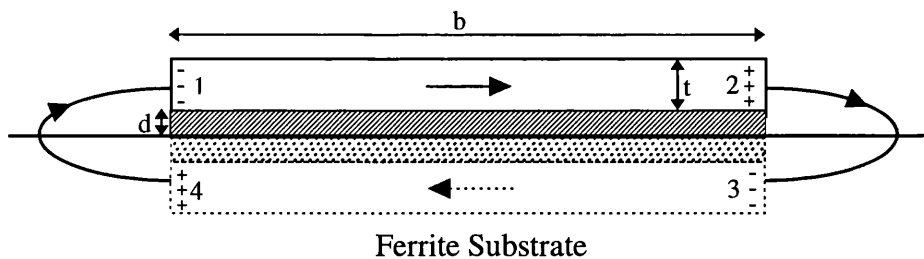


Fig 8.15: Schematic of fluxguide showing the generation of image charges in the ferrite

From electrostatics a charge density σ will give a reflection density of $-\sigma(\mu-1)/(\mu+1)$ in the ferrite at the same distance on the other side of the interface. Thus in the case of a magnetic substrate it is necessary not only to sum all the self energies at points 1-4 on Fig 8.15 but also the interaction energies between all the charge densities, whether they be in the ferrite or the fluxguide. The calculations are again done using Mathcad5 and shown in Appendix A1. As one would expect the fluxguide energy is highly dependent on the separation distance between the fluxguide and the ferrite. This parameter is labelled d on Fig 8.15 and in the experimental images shown earlier was $0.75\mu\text{m}$. The calculation was performed for several different values of d and the resulting graphs, which show the fluxguide energy as a function of height, are plotted together in Fig 8.16.

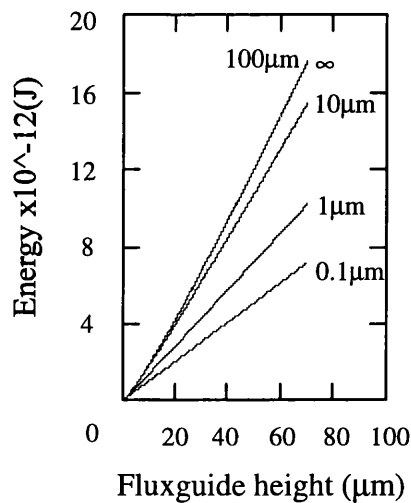


Fig 8.16: Plot of fluxguide energy on ferrite vs height of fluxguide, for different values of d .

For the value of d corresponding to the fluxguides shown previously in Fig 8.10(a-r) the energy of a single domain state is substantially reduced by the presence of the ferrite substrate. When the separation distance is $\approx 100\mu\text{m}$ the energy is equivalent to that of fluxguides deposited on a non-magnetic substrate. The energy of a closure domain structure can also be calculated and compared to that of the single domain state. Details of this calculation are given in Appendix A2 and the graph of the energy of the different closure structures, together with the single domain energy, are given in Fig 8.17(a). The area of interest in the figure, which is the cross-over point to a multiple domain state, is shown in more detail in Fig 8.17(b). From this graph a cross over point of $0.5\text{-}0.6\mu\text{m}$ is

predicted. This is approximately a factor of fifteen times smaller than that observed experimentally, where a transition appeared to occur at approximately $8\mu\text{m}$.

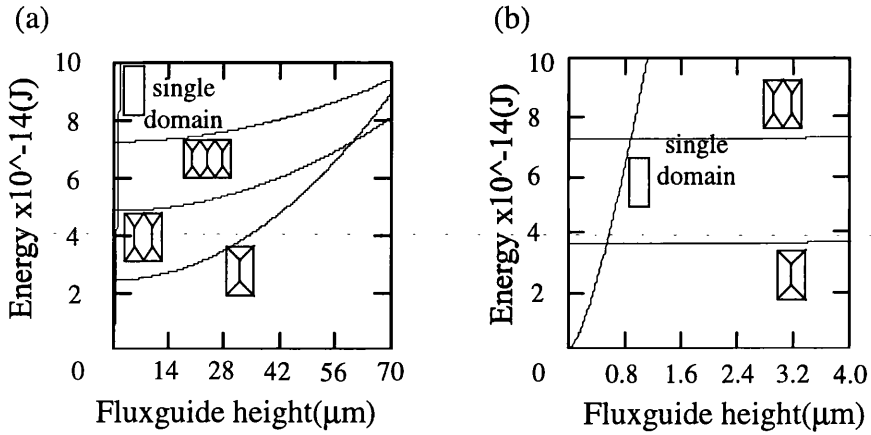


Fig 8.17: Closure domain energies compared to single domain state.

A possible reason for this discrepancy is that the state which was observed for the $8\mu\text{m}$ fluxguide in Fig 8.12(f) is not truly single domain. It is quite possible that small flower, or concertina, domains exist at the ends of the fluxguide. These have been observed by other authors (McVitie, 1988) and a simplified schematic of the structure is shown in Fig 8.18.

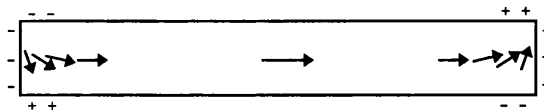


Fig 8.18 Simplified schematic of flower domains

Such a structure would lower the magnetostatic energy and allow a cross-over at a higher fluxguide height. For a cross-over of $8\mu\text{m}$ it is estimated that the magnetic poles at the ends of the structure would have to be reduced by $\approx 80\%$. The flower structure would however incur extra energy contributions from poles generated on the sides of the long axis as well as a contribution from a non-zero divergent component of magnetisation. Further calculations which take into account these other contributions are required to assess if the cross-over point exists at a fluxguide height of $8\mu\text{m}$.

8.7 IN-SITU MAGNETISING EXPERIMENTS

The previous studies have revealed the zero field states of fluxguides on both magnetic and non-magnetic substrates. In this section we move on to investigate the response of these domain structures to an external field.

8.7.1 Remanent States

The domain structure of any fluxguide is dependent on the history of the sample. In the previous sections the zero field states were brought about by the relaxation of a saturating field directed orthogonal to the tape flux direction. This typically resulted in a simple solenoidal domain structure such as that shown in Fig 8.19(a). Similar states are achieved when the fluxguide is ac demagnetised along this direction. When, however, the saturating field is parallel to the tape flux direction the remanent state tends to be more complicated. A typical remanent state for this direction of field is shown in Fig 8.19(b) and involves many more domains running orthogonal to the tape flux direction.

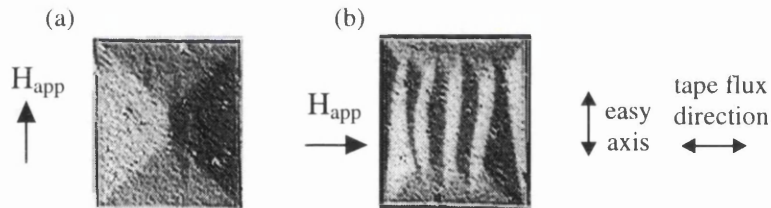


Fig 8.19: Remanent states in two fluxguides for different directions of saturating field (a) orthogonal to tape flux direction (b) parallel to tape flux direction.

These domain structures can be attributed to the induced anisotropy which is directed orthogonal to the tape flux direction. When the applied field is also directed along this direction, Fig 8.19(a), there is effectively no torque exerted on the magnetisation and upon relaxation shape anisotropy dictates the domain structure. If however the applied field is directed parallel to the tape flux direction, Fig 8.19(b), relaxation of the field results in an effective hard axis reversal and many domains form in the remanent state.

8.7.2 Response of Fluxguides on a Non-magnetic Substrate to an External Field.

In this section the subtraction of a near saturated state from the one in the field of interest is used in order to reveal magnetic contrast. An external d.c. field was applied using the coils situated below the specimen and the response of the domain structure of the fluxguides studied. Figs 8.20(a-g) show the response of a fluxguide with an aspect ratio of 1.43 to an external field applied parallel to the tape flux direction. The number quoted with each image is the applied field in Oe.

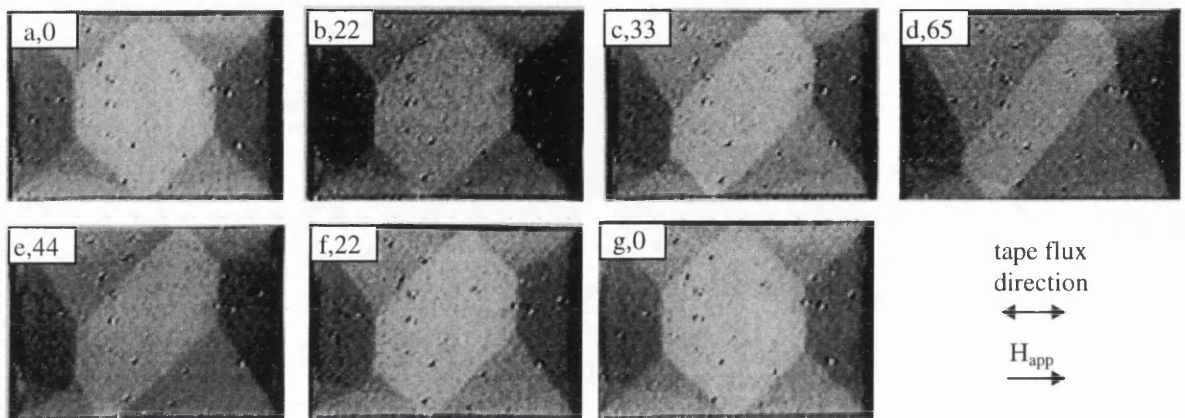


Fig 8.20(a-g): Response of a fluxguide (aspect ratio=1.43) on ceramic substrate to an applied field.

The response of the above domain structure to an applied field is as one would expect. Domains with a direction of magnetisation parallel to the applied field grow at the expense of those directed in the opposite direction, Figs 8.20(b-d). The domain structure becomes severely perturbed under the application of the field but all changes are reversible. Relaxation of the field returns the domain structure to the original solenoidal configuration where the net magnetisation in any direction is zero, Figs 8.20(g). It is also possible that the magnetisation within the domains parallel to the easy axis contribute to the permeability of the fluxguide by rotating towards the applied field direction. It does however appear that domain wall motion makes up a significant part of the hysteresis cycle.

The response of fluxguides with the same domain structure as that in Figs 8.20(a-g), but deposited on a Si, were very similar to those described above. When however an external field is applied to the more complicated state, which was depicted schematically in Fig

8.7(b), an interesting result is observed. An extract from the magnetising sequence is shown in Figs 8.21(a-d) and as the applied field is increased there is again an increase in the domains with a magnetisation lying parallel to the field direction. What is interesting, however, is the growth of the domain marked A on Fig 8.21(c). The fact that this occurs is justification for a structure which was shown in Fig 8.7(b).

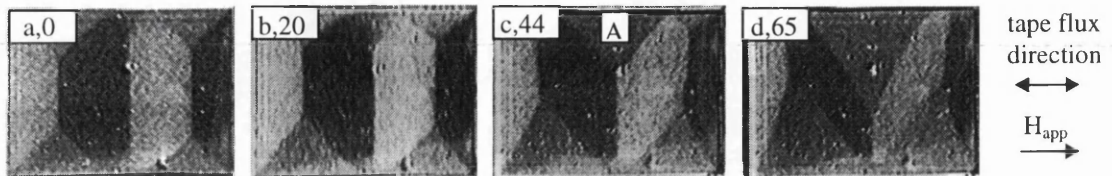


Fig 8.21(a-d): Extract from the magnetising sequence of a fluxguide on Si.

The response of a fluxguide to the application of a field parallel to the tape flux direction is of vital importance from the point of view of a head. It has been shown in Fig 8.20(a-g) that in the case of large fluxguides, which support the 7 domain closure structure, the application of a field in the direction of the tape flux leads to only reversible changes in the magnetisation. This however is not the case when the aspect ratio is less than unity and a four domain state exists. Figs 8.22(a-h) show an extract from a magnetising sequence of such a fluxguide (aspect ratio=0.86).

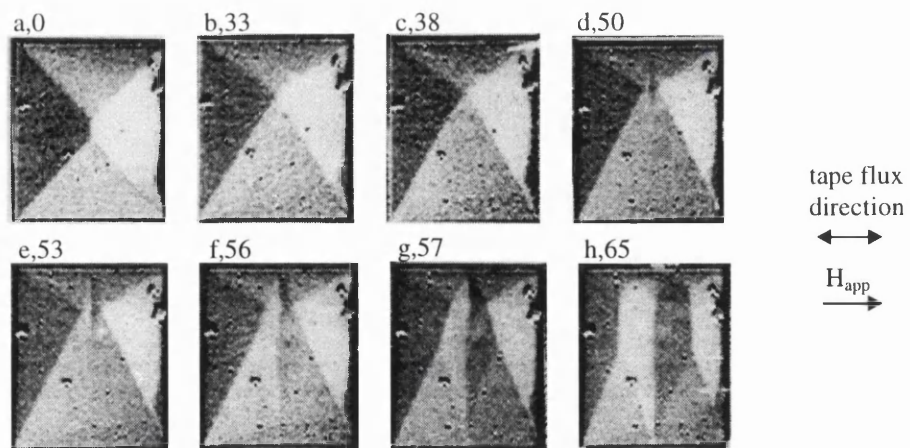


Fig 8.22(a-h): Point of no return for fluxguides on a non-magnetic substrate

As in previous sequences an increase in the applied field leads to an increase in size of the closure domain with a direction of magnetisation parallel to the field direction, Fig 8.22(b). If the field is relaxed from the state shown in Fig 8.22(b) the fluxguide would return to its original state. If, however, the field is further increased the magnetic free pole density near

the junction of the four domains becomes energetically unfavourable. The domain structure therefore alters in order to lower the magnetostatic energy. The structure which is most often formed resembles a Bloch line in a cross-tie wall and is shown schematically in Fig 8.23(a). Alternatively however a 180° wall can be nucleated at the junction and this is shown in Fig 8.23(b). The “cross-tie type” structure which is nucleated in Figs 8.22(d-f) develops upon increasing the applied field and results in the growth of a wall which is approximately orthogonal to the field direction, Figs 8.22(e-g).

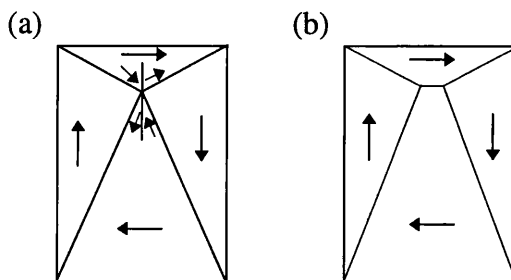


Fig 8.23(a) Schematic depiction of domain structure formed in Fig 8.22(e), **(b)** schematic of alternative domain structure which is occasionally formed.

For the fluxguide shown in Figs 8.22(a-h) minor hysteresis loops which do not exceed field values of 50-55 Oe result in the permeability being made up of entirely reversible processes. For fields above 50-55 Oe the changes in magnetisation become irreversible and relaxation of the field results in states which are far more complicated than the original four domain solenoidal structure. The field required to bring about irreversible changes is defined, in this thesis, as the point of no return. By similar magnetising experiments to that shown in Fig 8.22(a-h) the point of no return was estimated for fluxguides with other heights. A plot of this parameter as a function of aspect ratio is shown in Fig 8.24. It can be seen from this graph that the field required to reach the point of no return increases rapidly with a decreasing aspect ratio. Consequently for aspect ratios below ≈ 0.79 there is insufficient field from the magnetising coils in order to reach the point of no return.

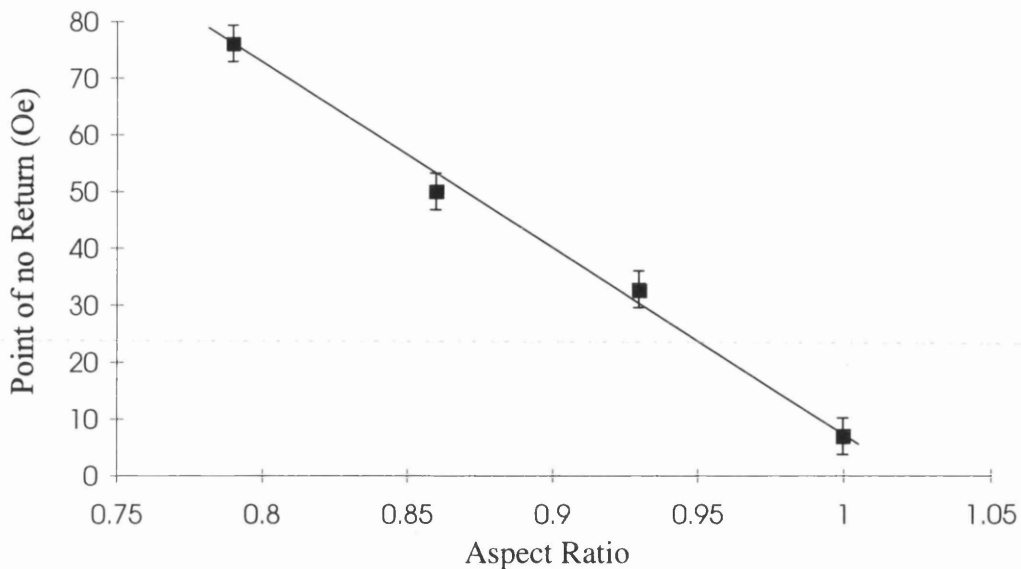


Fig 8.24: Graph of field required for “point of no return” vs aspect ratio.

The stiffening of the domain structure which causes this is due to a decrease in the flexibility of the closure domain walls which occurs as the fluxguide becomes increasingly narrow. This is illustrated well in the following experiment where the “tickling method” of revealing magnetic contrast is used in order to assess domain wall movement. Figs 8.25(a-g) show “tickled images” of a series of fluxguides which decreasing aspect ratio. The field applied to each of these fluxguides in order to perturb the magnetisation is 70 Oe and is directed along the tape flux direction.

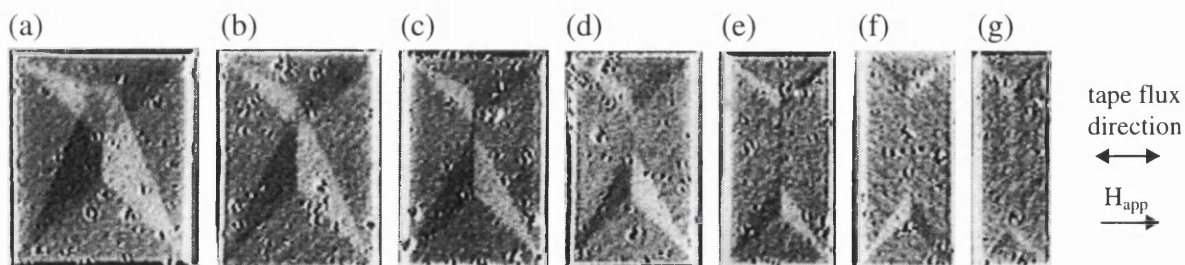


Fig 8.25(a-g): “Tickled states” showing the before and after position of domain walls

The stiffening of the domain structure which occurs for a decreasing aspect is most probably due to the collection of free poles on domain walls. Assuming that the largest

contributing factor to the permeability of a fluxguide is due to wall motion a decrease in aspect ratio therefore results in a decrease in permeability. Since the position of domain walls can be deduced from the subtraction images of Figs 8.25(a-g) it is possible using binary image analysis, similar to that performed in previous chapters, to deduce the normalised net magnetic moment in the direction of the applied field. This has been done for the images in Fig 8.25(a-f) and Fig 8.26 shows a plot of this parameter versus the fluxguide aspect ratio.

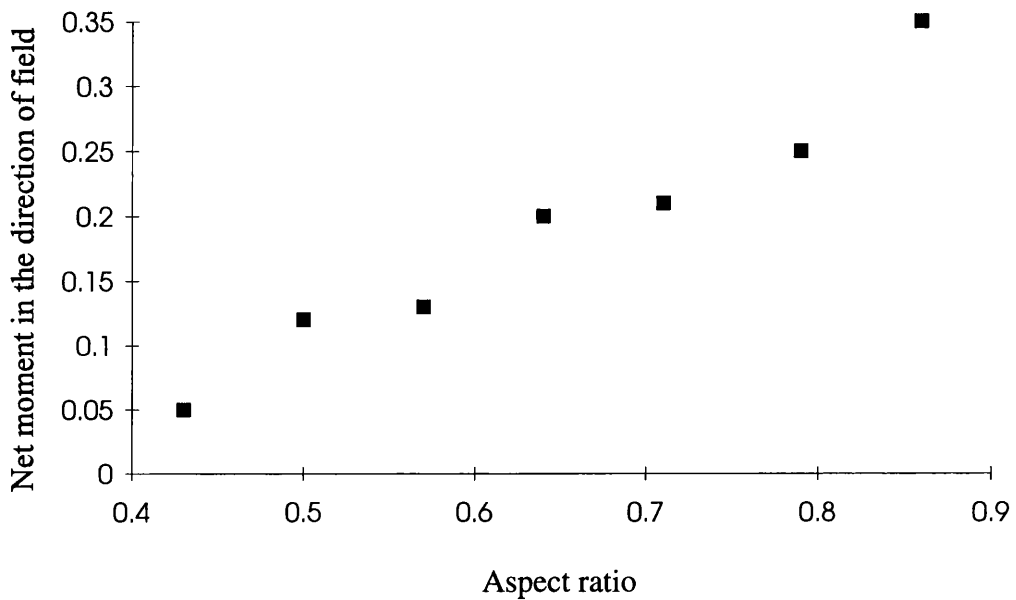


Fig 8.26: Graph of normalised net magnetic moment in the direction of the applied field vs aspect ratio

Although in this section we have shown that a large fraction of the permeability appears to be due to wall motion it is important to realise that while this is true for d.c. fields it is not necessarily true for a.c. fields. It would therefore be interesting to repeat the previous experiments using a scanning Kerr microscope with “lock-in” detection where, if possible, the driving frequency is set to that which is of interest for many recording applications (10-100 kHz).

8.7.3 Response of Fluxguides on a Magnetic Substrate to an External Field.

As already mentioned previously it would be advantageous, from the point of view of distortion in the output of a working head, if it were possible to design a front fluxguide which was single domain. Although in section 8.5.3 it appeared that fluxguides with

heights of approximately $8\mu\text{m}$ or below, deposited on ferrite, gave such a state it is important to study the response of these structures to an applied field. Due to the high permeability of ferrite the maximum field which can be applied to the FeNbSiN fluxguides, by the external coils ($\approx 80\text{ Oe}$), is insufficient to perturb the domain structure within the fluxguides. It is therefore necessary to use an alternative method of applying fields to the sample which involves passing a small current through the wire which is situated below the fluxguides. The wire is orientated in such a way that the induced field, upon passing a current, is parallel to the tape flux direction and is sufficient to saturate the larger fluxguides on the mask. Figs 8.27(a-n) show the response of a fluxguide which was deposited on ferrite and has an aspect ratio=1.0. The magnetic contrast was revealed by the subtraction of the saturated state from each of the images which were acquired under the application of a field. The number quoted is the wire current in mA. As was observed in section 8.5.3 the domain structure in the zero field state, Fig 8.27(a), appears to be rather confused when compared with those on a non-magnetic substrate.

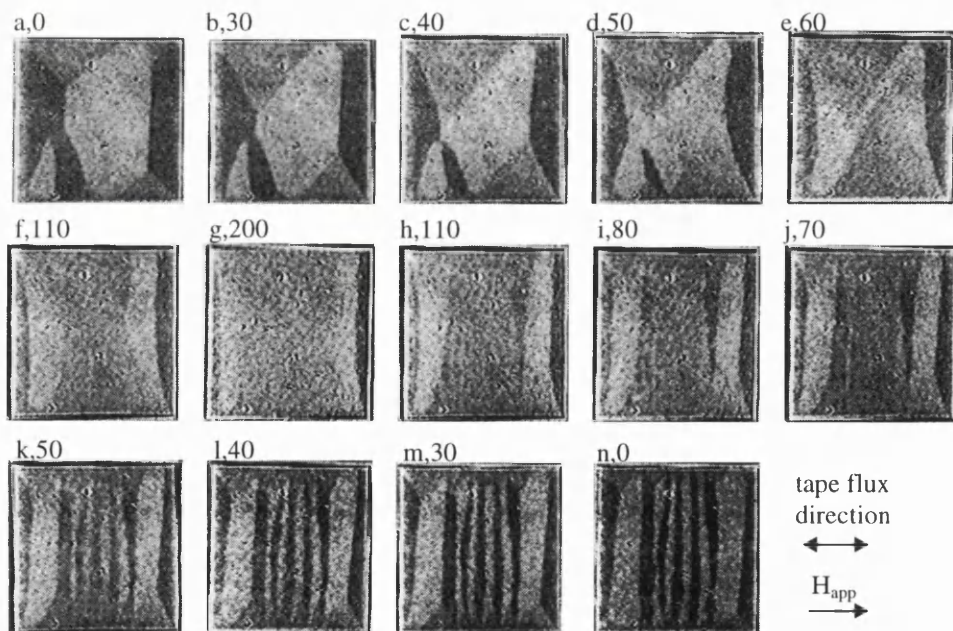


Fig 8.27(a-n): Response of fluxguide on ferrite, with an aspect ratio of 1.0, to a field parallel to tape flux direction

Upon the application of fields produced by a drive current of 30mA domains with a direction of magnetisation parallel to the field grow at the expense of those orientated in the opposite direction, Fig 8.27(b). Further increases in field result in the magnetisation in the central section of the structure rotating towards the field direction, Figs 8.27(d-f). Full

saturation of the fluxguide is not however achieved due to narrow domains which exist at the edges orthogonal to the average direction of magnetisation, Fig 8.27(g). These domains lower the magnetostatic energy by continuing to allow a degree of flux closure within the fluxguide layer. Relaxation of the applied field results in a hard axis type reversal as domains, with magnetisation parallel to the easy axis, nucleate, Fig 8.27(h-j). The wall density in the central region of the fluxguide grows as the field is further relaxed and the contrast between these domains also becomes more pronounced, Figs 8.27(k-m). In the zero field state a structure similar to that observed for fluxguides on a non-magnetic substrate, after the application of a field parallel to the tape flux, is observed, Fig 8.27(n). Again such a complicated structure makes the use of fluxguides with these properties in a head impractical.

When fields are applied to fluxguides of a smaller aspect ratio the complicated domain structure observed in the remanent state of Fig 8.27(n) is not generated. Figs 8.28(a-g) shows the response of a fluxguide with an aspect ratio of 0.36 to fields which are again generated using the underlying bias wire.

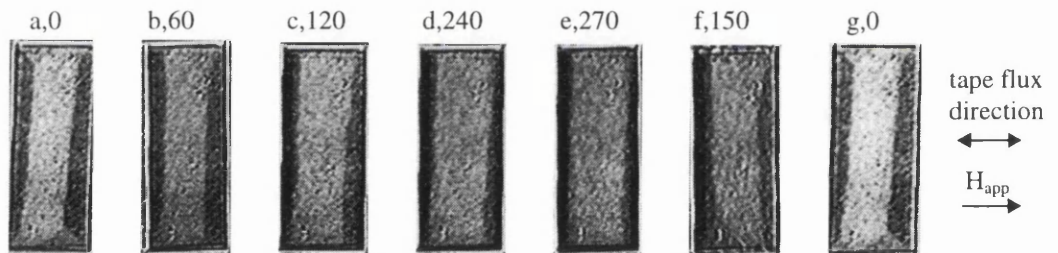


Fig 8.28:(a-g): Response of fluxguide on ferrite, with an aspect ratio of 0.36, to field parallel to tape flux direction

As can be seen from Fig 8.28(a) the familiar zero field state which is observed for fluxguides deposited on ferrite with an aspect ratio below ≈ 0.5 is observed. Again the numbers quoted with each image are the wire current in mA. The application of a field does not appear to generate domain wall motion. The domains which run parallel to the easy axis appear to slowly fade out with increasing field, Fig 8.28(b-d). At the maximum field, which is produced by a current of 270 mA, the contrast within the fluxguide appears to be relatively weak, Fig 8.28(e), but narrow edge domains can still be discerned running orthogonal to the applied field direction. Relaxation of the field results in the return to a domain pattern which appears near identical to that of the original zero field state, Fig

8.28(g) Since this reversal involves few domain walls and domain wall motion does not appear to play an important role it is likely that the noise transferred to the sensor from the fluxguide would be substantially less than that of larger fluxguides.

8.8 SUMMARY

In this chapter the domain structures of FeNbSiN fluxguides have been studied using Kerr microscopy. These studies have shown the different magnetic states which exist for fluxguides of varying aspect ratio deposited on both magnetic and non-magnetic substrates. In the case of non-magnetic substrates the transitions between different closure states were used to investigate possible variations in anisotropy caused by the underlying substrate. It was found that variations in anisotropy between ceramic and Si were minimal. For fluxguides deposited on a ferrite substrate, with an aspect ratio greater than ≈ 0.5 , the magnetic state appeared to be significantly more complicated than those on non-magnetic substrates. This was probably due to a decrease in the influence of shape anisotropy which is caused by partial flux closure with the ferrite. In the case of fluxguides deposited on ferrite a single domain state appeared to exist at a height of $\approx 8\mu\text{m}$.

The response of fluxguides to an external (d.c.) field, directed parallel to the tape flux direction, was also studied during this chapter. In the majority of fluxguides wall motion appeared to play an important role in the hysteresis cycle of the fluxguide. For small aspect ratios shape anisotropy resulted in a stiffening of the domain structure and upon applying a field changes in the magnetic state became fully reversible. For fluxguides on a non-magnetic substrate it was possible to define a field value where changes in the domain structure became irreversible. This field value was define as “the point of no return” and was approximately inversely proportional to the aspect ratio. For fluxguides on a magnetic substrate the application of fields to fluxguides with a small aspect ratio did not appear to cause significant wall motion. This implies that the noise transferred from these fluxguides to a sensor would be significantly less than that of the larger fluxguides.

CHAPTER 9: CONCLUSIONS AND FUTURE WORK

9.1 INTRODUCTION

The work presented in this thesis has shown that the reversal mechanisms of the magnetic layers within a spin-valve can be studied using the Lorentz mode of transmission electron microscopy. Both the free and the biased layer reversal mechanisms show new and interesting physical phenomena which are due to the proximity of other magnetic layers. The reversal of the “free” ferromagnetic layer is substantially altered by the presence of GMR enhancing layers, while the biased layer reversal mechanism is highly dependent on whether FeMn or TbCo is used for biasing.

9.2 CONCLUSIONS

Thin permalloy films were investigated in chapter 3 and typical hard and easy axis reversal mechanisms were observed upon applying an external field. Magnetisation ripple was visible in all films studied and by considering DPC images it was apparent that the ripple structure was dependent on the thickness of the permalloy film. The ripple was partially quantified as a function of film thickness by analysis of the Fourier Transforms of the DPC images. Interactions between domain walls and inclusions were studied in some detail and in particular the mechanism for the creation of 360° walls, via this interaction, was studied. It was noted that in all the isolated permalloy films studied the creation of 360° walls could only be brought about by an inclusion and consequently these wall structures were always associated with at least one pinning point.

In chapter 4 the free layer reversal mechanisms of spin-valves with co-linear easy axes and biasing directions were studied. Magnetisation ripple was observed in both the free and biased layers of the spin-valves, though it did appear substantially less in the latter. The reversal of spin-valves with a permalloy free layer differed markedly from that of an isolated permalloy layer with the most obvious difference being the large number of stable 360° walls formed during the process. Unlike those in an isolated layer, these 360° walls were not necessarily associated with topographical contrast and often changed direction several times along the length of the wall. The idea of charge compensation from the biased

layer was suggested as a reason for the stabilisation of the wall structures. Addition of a thin, GMR enhancing, Co layer at the interface of the free and spacer layers resulted in a modification of the free layer reversal mechanism. The domain walls appeared far more erratic than those observed in spin-valves without Co. Addition of Co to the alloy used for the free layer also affected the switching mechanism by increasing the anisotropy field.

In chapter 5 the free layer reversal mechanisms for spin-valves with an orthogonal alignment of easy axes and biasing directions were considered. The main conclusion from this chapter was the fact that coherent rotation of free layer magnetisation could be achieved by deliberately off-setting the applied field from the biasing direction by only a small angle. Perfect alignment, however, caused the rotation of adjacent areas of the free layer magnetisation towards the field direction in either a clockwise or an anti-clockwise sense, with the nucleation of 360° walls between the boundaries. DPC imaging allowed high resolution profiles to be taken across these walls. The absence of wall structures for fields applied at slight angles to the biasing direction is significant from an applications point of view as this would inevitably lead to an improvement in the noise characteristics of the sensor.

In chapter 6 the reversal mechanisms of biased layers were studied in some detail. In the case of FeMn the reversal proceeded by the nucleation of very erratic domain structures which existed on a fine scale (typically a few microns). In the case of uniaxial TbCo the reversal mechanism was quite different and the phenomenon of magnetisation creep was prominent during the process. The reversal was dominated by domain wall motion and due to there being relatively few nucleation sites the domain wall density was low. The walls which did exist were very erratic and typically changed direction several times over a length scale of few microns. Domain structures were observed in the biased layer after the application of a vertical field. These structures were replicated in the free layer and double domain walls existed at the boundaries. DPC imaging was used to study the domain boundaries in fine detail and allowed the in-plane component of magnetisation in the TbCo layer to be estimated. A model with two easy axes was postulated to account for domain structures in the remanent state. While TbCo offers advantages over FeMn, such as maintaining biasing to higher temperatures and a higher resistivity, the creation of domain structures in the biased layer after the application of a large vertical field may have serious implications for using uniaxial TbCo as a biasing mechanism.

Chapter 7 dealt with the nucleation of a magnetic vortex which was stabilised in a buckled film by the presence of a vertical field. While the structure of the vortex was not fully understood the application of a field with an in-plane component revealed that it was confined to regions with exaggerated bend contours. Other complicated magnetic structures which would generally not be expected for fields of the magnitude applied were also observed in the buckled films.

In chapter 8 the magnetic states of fluxguides, which are intended for thin film heads, were studied. These structures were deposited on both magnetic and non-magnetic substrates and the zero field states were studied as a function of aspect ratio. This revealed what appeared to be a transition from a multiple domain state to a single domain state at a fluxguide height of $\approx 8\mu\text{m}$. This may be responsible for an improvement in the noise characteristics of prototype heads when the front fluxguide height is reduced below $8\mu\text{m}$.

9.3 FUTURE WORK ON CONTINUOUS FILMS

Future work to complement that which has been presented in this thesis can be divided into two distinct categories. The first relates to continuous films while the second concentrates on patterned spin-valve structures.

9.3.1 Reasons for the Existence of Weak Ferromagnetic Coupling Across the Spacer Layer

The existence of weak ferromagnetic coupling between two ferromagnetic layers has been variously ascribed to either Néel or pin hole type coupling. Although recent publications tend to favour the existence of Néel coupling (Kools, 1995) it is possible that pin holes could still exist. If pin holes are indeed the cause of weak ferromagnetic coupling then it has been suggested that these take the form of valleys of Ni which exist at grain boundaries (Egelhoff, 1995). It would therefore be interesting to use either X-ray or PEELS analysis in order to obtain a Ni composition profile across a grain. One would expect a local increase in the percentage Ni at the edge of the grain if pin holes exist.

9.3.2 Further Investigations of Reversal Mechanisms in Spin-valves

From an applications point of view the coherent rotation of free layer magnetisation which was observed in chapter 5 is a very interesting phenomenon. The absence of domain walls would obviously have implications for the noise characteristics of spin-valve sensors. A model has been formulated by Labrune et al (1995) to explain the transition from a free layer reversal which involves walls to one which only displays coherent rotation. This model follows the approach of Stoner and Wohlfarth (1948) and allows a phase diagram to be drawn which predicts different switching mechanisms as the angle between the applied field and the biasing direction varies. Each spin-valve is quantified by the parameter h_j , which is defined as the coupling field divided by the anisotropy field. Fig 9.1 shows the calculated phase diagram for spin-valves with co-linear easy axes and biasing directions.

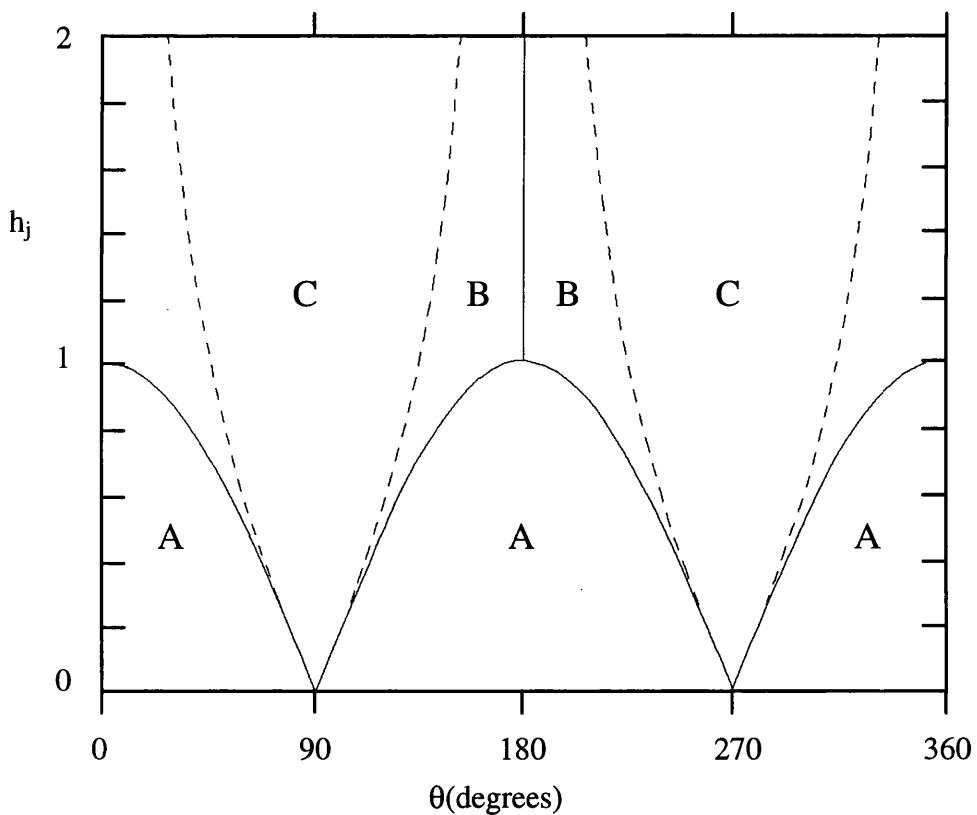


Fig 9.1: Phase diagram for reversal processes in spin-valve with parallel easy axes (Labrune et al, 1995)

The angle θ is defined as that between the applied field and the biasing direction while the different reversal modes are shown schematically in Fig 9.2. Here shaded angles represent angles over which the magnetisation rotates.

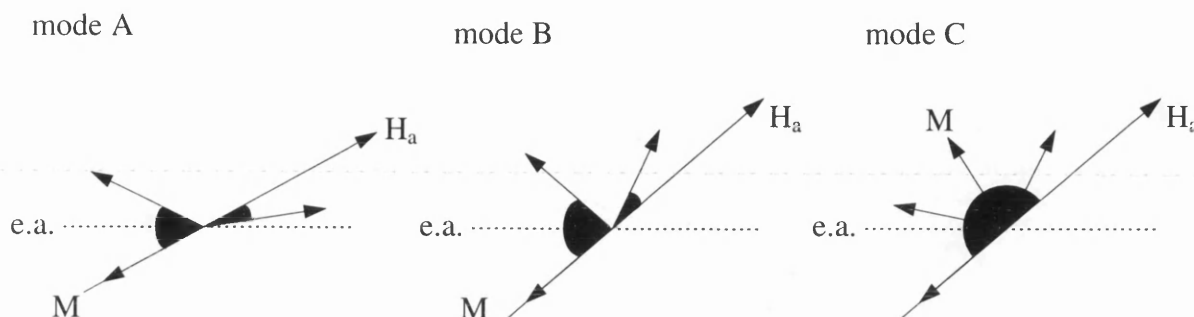


Fig 9.2: Graphical depiction of modes of reversal

The angle at which the onset of mode C occurs is the critical parameter for head applications. Provided the values of anisotropy and coupling fields are known, this model, through the use of Fig 9.1, can be used to predict the reversal of any spin-valve with co-linear easy axes and biasing directions. A phase diagram also exists for orthogonal spin-valves. The different modes which are predicted by Labrune are in agreement with experimental data acquired by J.C.S. Kools, using Kerr microscopy. This however was limited to a sampling area determined by the size of the Kerr spot (typically $\approx 1\mu\text{m}$). It would therefore be interesting to probe the phase diagrams of both parallel and orthogonal spin-valves using Lorentz microscopy where the reversal mechanism can be assessed over an area of $100\mu\text{m}^2$.

In chapter 4 we noted that during the free layer reversal of a permalloy spin-valve reverse domains were nucleated at a characteristic angle. These angles may be dependent on the copper spacer layer thickness and it would be interesting to study them as a function of this parameter.

9.3.3 Further Studies of 360° Wall Structures

Although high resolution images of 360° walls were presented in chapter 5 these were only for sections of wall which were orthogonal to the average direction of magnetisation in the rest of the film. From the Fresnel image, Fig 4.12(a), the structure of a 360° wall

appears to vary when the magnetisation in the rest of the film is not orthogonal to the wall. It would therefore be interesting to compare 360° wall profiles for sections of wall from different parts of a 360° loop. The influence of varying the direction of a 360° wall in the free layer with respect to the biasing direction would also be interesting and it is hoped that future studies on this can be compared with theoretical calculations of M Labruno which are presently under way at the Université Paris-Nord.

9.3.4 Further Studies of Magnetisation Creep

The studies of magnetisation creep which were presented in chapter 6 were an initial investigation into the time dependence of the reversal of a permalloy layer biased by TbCo. As was mentioned in chapter 6 these measurements were flawed in two critical ways. The first was that a pinning point was present at the top of the field of view. This resulted in a nucleation site and therefore perturbed the reversal mechanism. It is therefore necessary to repeat the experiments of section 6.4 on another sample in which there is no artificial nucleation site. The second flaw is that the time dependence of the sample was studied over a restricted area of $120 \times 120 \mu\text{m}^2$. Thus the results of section 6.4 may not be representative of the rest of the sample. It is therefore desirable that the bulk magnetic properties of the permalloy/TbCo layer be quantified using magnetometry while the experiments of section 6.4 are repeated on a new sample grown at the same time.

9.3.5 Other biasing Mechanisms

While FeMn and TbCo biasing mechanisms have been studied extensively during this thesis spin-valves biased by NiO have not been considered. Although such a biasing mechanism has some advantages over both FeMn and TbCo its use is restricted by the poor biasing field which can be obtained (typically 80-100 Oe). It would therefore seem sensible to study the micromagnetics of NiO biasing with the aim of improving the biasing field while maintaining the desirable properties of NiO.

9.3.6 Calculations for Vortex

From the studies of the vortex in chapter 7 it is clear that there is still much to be learnt about the existence of such a structure. Although the conditions for its existence are rather contrived it would be interesting, from a scientific point of view, if the structure could be explained. It would therefore seem worthwhile if some theoretical calculations of the vortex could be attempted in order to explain its existence.

9.4 PATTERNED SPIN-VALVES

While the experiments in this thesis have shed considerable light on the behaviour of continuous spin-valve films it is also necessary to consider the effects of patterning on the magnetic state. These effects will be due to the existence of demagnetising fields and are important as any application of spin-valves will ultimately involve patterned structures.

9.4.1 Picture Frame Structures

As mentioned in chapter 1 the patterning in DCC heads for an AMR sensor is of a picture frame type with a barber pole structure deposited on top. Due to the linearity of sensors which utilise the GMR effect the barber pole structure is no longer required. In prototype DCC heads, however, the picture frame is still used and it would therefore be interesting to study the effects on the magnetic properties of such patterning on a spin-valve. Initial experiments are encouraging though at present only permalloy picture frames have been deposited on Si_3N_4 windows. Since the width of the picture frame is larger than the Si_3N_4 window several samples have been prepared where different areas of the picture frame overlap with the window. These are shown in Fig 9.3(a-c) and as can be seen some of the picture frames have rounded corners. It is hoped that such a shape may reduce the need for domain walls to be present. These structures were fabricated by J.C.S. Kools using standard lift-off technology. A layer of Cu was, however, evaporated over the window prior to sputtering. This increased the thermal conductivity of the window and so tended to improve edge acuity and minimise the probability of tearing.

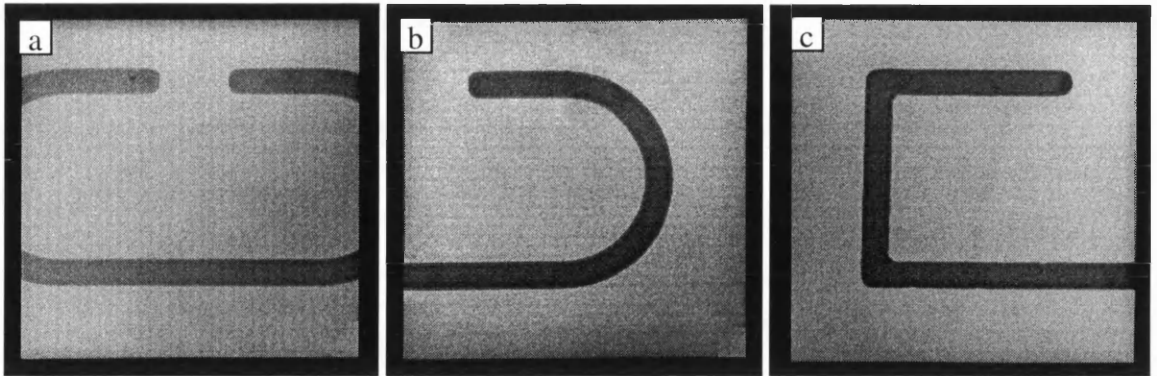


Fig 9.3(a-c): Examples of picture frame structures deposited on Si_3N_4 windows

The edges of the picture frame seem reasonably well defined over a scale of less than a micron and a corner of a structure can be seen in the bright field image of Fig 9.4(a). When the imaging lens is defocused magnetic contrast is revealed and Fig 9.4(b) shows such a Fresnel image, again of a picture frame corner. Fresnel imaging enhances edge contrast and therefore the edges of the picture frame appear more irregular in Fig 9.4(b)

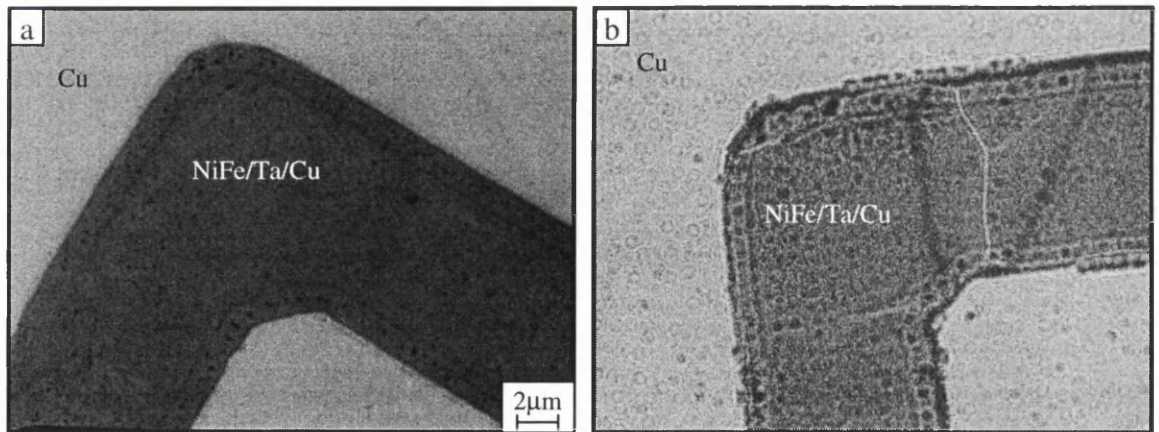


Fig 9.4(a) Bright field image of corner of picture frame **(b)** Fresnel image of picture frame corner

Unfortunately there is a significant amount of scattering by the underlying Cu layer. This results in reasonably strong diffuse contrast which obscures that which arises from the Lorentz deflection. Future samples could possibly use an Al conducting layer rather than Cu. At present the patterning of spin-valves into picture frames has not been particularly successful. This is due to corrosion of the FeMn which is exposed at the sides of the

structure during the lift-off process. This problem has to be overcome before spin-valve picture frames can be fabricated on Si_3N_4 windows.

9.4.2 Small elements

Many designs of magnetoresistive read heads do not utilise the picture frame structure which is used in the Philips DCC head. In other designs a rectangular sensor which is shown schematically in Fig 5.2 is often used. The domain structure within such a sensor is obviously important from the point of view of optimising the output from such a head. It is therefore valuable to be able to study these domain structures using electron microscopy. There are two possible methods of fabricating small elements, with comparable dimensions to that of a sensor, which can be studied in the electron microscope. The first method is standard lift-off technology while the second is via an etching route (see later). After several attempts structures were fabricated using the lift-off method and it was possible to obtain an array of small spin-valve elements on a Si_3N_4 window. These particular samples were made by B. Khamsehpor from a uniaxial biased TbCo spin-valve which was deposited by P.P. Freitas. The remanent states of the particles after a saturating field parallel to the biasing direction were imaged using DPC and one of the mapping directions is shown for an array of particles in Figs 9.5(a-o). When the biasing direction is parallel to the long axis of the element the observed domain structure is similar to those observed in permalloy elements where shape anisotropy is the dominant energy term (McVitie, 1988). That is to say the central section of the element has a direction of magnetisation which is parallel to the long axis while small flower domains exist at the short ends of the structure. When, however, the biasing direction is orthogonal to the long axis of the element the shape anisotropy has only a minor influence on the domain structure. This is illustrated by comparing spin-valves with the same dimensions, but orthogonal biasing directions, i.e. Figs 9.5(d and b) or (c and g). The magnetic states shown in Fig 9.5(a-o) do not allow a complete flux closure within the particle. This results in a leakage of flux and consequently stray fields can be seen emanating from the structures.

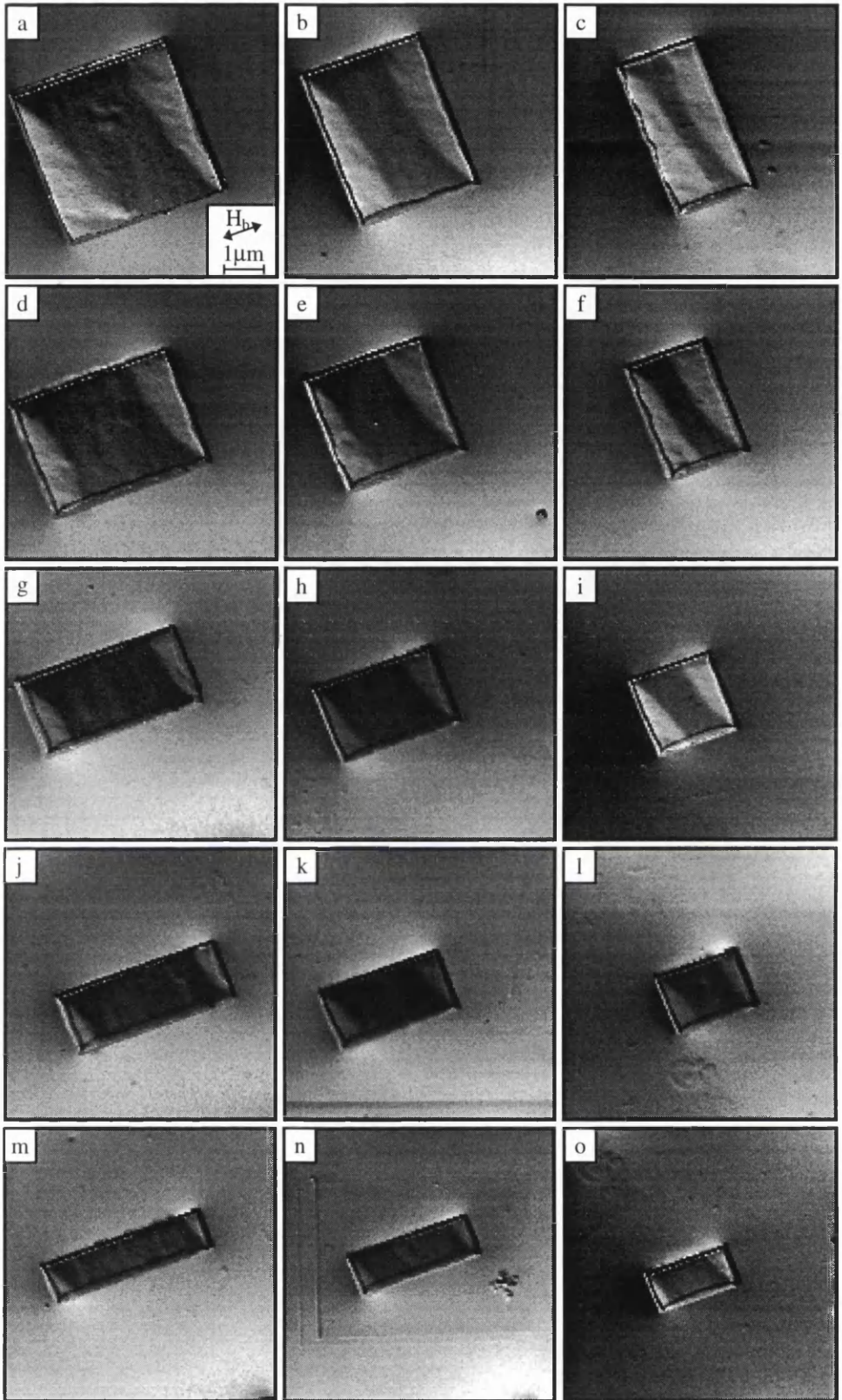


Fig 9.5(a-o): Single DPC images of spin-valve elements

The energy considerations for the free layer magnetisation in a spin-valve element are more complicated than those of a continuous film. The structuring of the spin-valve will result in a shape anisotropy directed along the long axis of the element. On the other hand the biased layer, which is probably near single domain, will result in stray fields which partially flux close through the free layer. This will result in an effective field acting on the free layer magnetisation which tends to align the magnetisation anti-parallel to the biasing direction. There will also be the coupling field which will have the effect of encouraging a parallel alignment of the free layer magnetisation with the biasing direction. A micromagnetic calculation of the magnetisation within a shielded spin-valve structure can be found in a recent publication by Yuan and Bertram (1994).

As such structured spin-valves are similar to those used in many head designs it would be very worthwhile to study the response of the magnetic states to an external field. This can quite simply be achieved by tilting the specimen in the microscope whereby a component of the objective lens field is introduced anti-parallel to the biasing direction. Alternatively the situation within a working head could be closely simulated by using a double tilt rod. By tilting about one axis a d.c. field, representative of electrical biasing, would be generated orthogonal to the biasing direction. Tilting about the other axis would then give field components parallel to those which would arise from a passing tape. An advantage of using the DPC mode for these studies is the fact that the stray fields which emanate from the element would also be imaged simultaneously as the domain structure within the element.

In chapter 6 the response of a continuous TbCo biased spin-valve to a vertical field was investigated. We remarked that the creation of domain structures in the remanent states would have a seriously detrimental effect on the performance of sensors which utilise the TbCo biasing mechanism. It was however pointed out that these structures may be influenced by buckles in the Si_3N_4 membrane. When vertical fields are applied to the small elements complicated structures are also nucleated. The magnetic structure observed in the element of Fig 9.5(b) after the application of a vertical field is shown in the orthogonal DPC maps of Figs 9.6(a-b). As can be seen this structure is severely perturbed from that observed after the application of a saturating field parallel to the biasing direction.

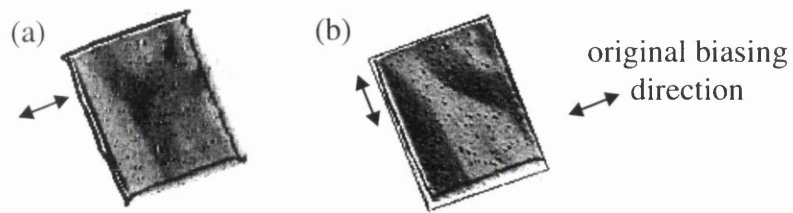


Fig 9.6(a-b) DPC images of TbCo biased spin-valve element after the application of a vertical field.

It is very unlikely that buckling exists in the membrane on a scale which is less than the dimensions of the element shown above. Figs 9.6(a-b) therefore imply that such domain structures are due to the uniaxial nature of TbCo and not any bending of the membrane. This is the main draw-back of using uniaxial TbCo as a biasing mechanism and may outweigh any advantages which exist over FeMn. Further work on the remanent states of elements with different dimensions would be of interest.

An alternative route to patterned spin-valve structures is by etching. This has been successful in defining permalloy elements, (Khamsehpour et al 1995), and has distinct advantages over the lift-off technique. Not only is the edge acuity improved but it also becomes possible to pattern a continuous film without the need for any pre-deposition steps. Unfortunately, however, from initial experiments the etching process appears to affect the biasing mechanism of FeMn. Further work is required to overcome these problems but perhaps TbCo etched elements will not suffer from such problems due to being less sensitive to processing techniques.

Appendix A1:

The following is the annotated calculation sheet for the Mathcad5+ software package which was used to calculate the graphs of section 8.5.

$$a := 0.01 \cdot 10^{-6}, 0.02 \cdot 10^{-6} .. 70 \cdot 10^{-6}$$

$$b := 70 \cdot 10^{-6}$$

$$c := 4 \cdot 10^{-7}$$

$$d := 0.75 \cdot 10^{-6}$$

$$\sigma := \frac{1.45 \cdot 10^4}{4 \cdot \pi}$$

$$\mu := 5000$$

$$\psi(x) := \ln(x + \sqrt{1 + x^2})$$

$$t1(p, q) := (p^2 - q^2) \cdot \psi\left[\left(\frac{p^2 + q^2}{2}\right)^{-\frac{1}{2}}\right]$$

$$t2(p, q) := p \cdot (1 - q^2) \cdot \psi\left(\frac{p}{\sqrt{1 + q^2}}\right)$$

$$t3(p, q) := p \cdot \psi\left(\frac{p}{q}\right) \cdot q^2$$

$$t4(p, q) := \psi\left(\frac{1}{q}\right) \cdot q^2$$

$$t5(p, q) := 2 \cdot p \cdot q \cdot \operatorname{atan}\left(\frac{q \cdot \sqrt{1 + p^2 + q^2}}{p}\right)$$

$$t6(p, q) := \pi \cdot p \cdot q$$

$$t7(p, q) := \frac{(1 + p^2 - 2 \cdot q^2) \cdot \sqrt{1 + p^2 + q^2}}{3}$$

$$t8(p, q) := \frac{(1 - 2 \cdot q^2) \cdot \sqrt{1 + q^2}}{3}$$

$$t9(p, q) := \frac{(p^2 - 2 \cdot q^2) \cdot \sqrt{p^2 + q^2}}{3}$$

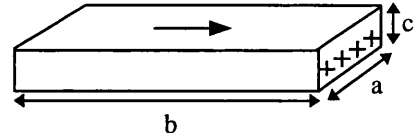
$$t10(p, q) := \frac{2 \cdot q^3}{3}$$

$$F(p, q) := t1(p, q) + t2(p, q) + t3(p, q) + t4(p, q) + t5(p, q) - t6(p, q) - t7(p, q) + t8(p, q) + t9(p, q) + t10(p, q)$$

For a fluxguide on a non-magnetic substrate the total energy is the self energy of the two charge densities plus the mutual interaction energy. Equation 3.11 of R&R thus gives:

$$E(a) := 2 \cdot (a \cdot 100)^3 \cdot \left(F\left(\frac{c}{a}, 0.0000000000\right) - F\left(\frac{c}{a}, \frac{b}{a}\right) \right) \cdot \sigma^2 \cdot 1 \cdot 10^{-7}$$

Note: One has to be careful with cgs units. Value "a" in this formula is in centimetres and the energy is converted from ergs to Joules by multiplying E(a) by $1 \cdot 10^{-7}$

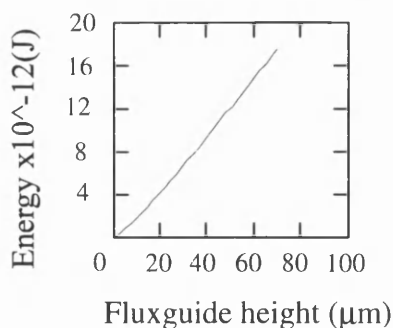


d=the thickness of the spacer layer between the fluxguide and the ferrite

σ =the magnetic pole density. It corresponds to Ms value in cgs units

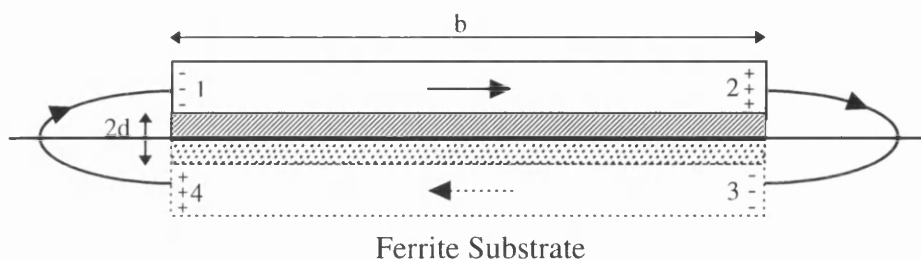
Splitting up the terms of equation 2.18 in Rhodes Rowland (R&R) and calculating the sum of the terms in F(p,q). Note: p and q are reduced parameters; $p=c/a$, $q=b/a$

Graph of single domain fluxguide vs fluxguide height (a)



FLUXGUIDE ON A FERRITE SUBSTRATE

There are many more terms to the energy equation when there is a magnetic substrate



For a fluxguide on a ferrite substrate the method of image charges is used to find the charge distributions within the ferrite. From electrostatics a charge density of σ gives a reflection charge of $\sigma(\mu-1)/(\mu+1)$ in the ferrite at the same distance on the other side of the interface.

The self energy of the individual planes of sheet charge

From eqn. 2.21 of R&R

$$T1(a, d) := 2 \cdot (a \cdot 100)^3 \cdot \sigma^2 \cdot F\left(\frac{c}{a}, 0.0000001\right) \quad \text{Self energy of sheet charges 1 and 2}$$

$$T2(a, d) := 2 \cdot (a \cdot 100)^3 \cdot \sigma^2 \cdot \left(\frac{\mu-1}{\mu+1}\right)^2 \cdot F\left(\frac{c}{a}, 0.0000001\right) \quad \text{Self energy of sheet charges 3 and 4}$$

The interaction energies when sheets are in same medium

$$T3(a, d) := -2 \cdot (a \cdot 100)^3 \cdot \sigma^2 \cdot F\left(\frac{c}{a}, \frac{b}{a}\right) \quad \text{Interaction energy for 1 and 2}$$

$$T4(a, d) := -2 \cdot (a \cdot 100)^3 \cdot \sigma^2 \cdot \left(\frac{\mu-1}{\mu+1}\right)^2 \cdot F\left(\frac{c}{a}, \frac{b}{a}\right) \quad \text{Interaction energy for 3 and 4}$$

The interaction energies when sheets are in different media

Interaction energy between 2 and 3 and between 1 and 4

$$T5(a, d) := -2 \cdot (a \cdot 100)^3 \cdot \sigma^2 \cdot \left(\frac{\mu-1}{\mu+1}\right) \cdot \left[F\left[\frac{2 \cdot c + (2 \cdot d + c)}{a}, 0.0000001\right] + F\left(\frac{2 \cdot d + c}{a}, 0.0000001\right) - 2 \cdot F\left[\frac{c + (2 \cdot d + c)}{a}, 0.0000001\right] \right]$$

Interaction energy between 1 and 3 and between 2 and 4

$$T6(a, d) := 2 \cdot (a \cdot 100)^3 \cdot \sigma^2 \cdot \left(\frac{\mu - 1}{\mu + 1} \right) \cdot \left[F \left[\frac{2 \cdot c + (2 \cdot d + c)}{a}, \frac{b}{a} \right] + F \left(\frac{2 \cdot d + c}{a}, \frac{b}{a} \right) - 2 \cdot F \left[\frac{c + (2 \cdot d + c)}{a}, \frac{b}{a} \right] \right]$$

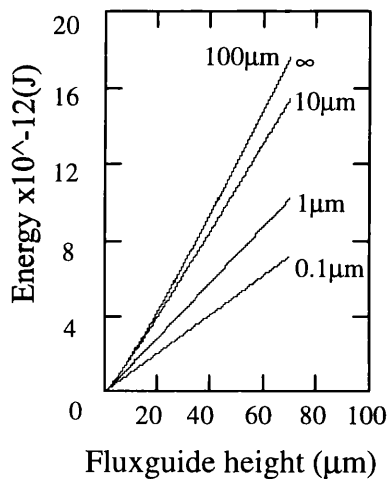
$$T(a, d) := (T1(a, d) + T2(a, d) + T3(a, d) + T4(a, d) + T5(a, d) + T6(a, d)) \cdot 1 \cdot 10^{-7}$$

Note: The vertical distance between sheets of charge in the fluxguide and those in the ferrite is $2d+c$

The total energy of the fluxguide = $T(a, d)$ -(the energy of the image fluxguide)
 -(1/2 the interaction energy between sheets in different mediums)

Nb: Only half the energy of that due to interactions between charges which exist in different mediums is included as this is a virtual energy.

$$TOT(a, d) := T(a, d) - E(a) \cdot \left(\frac{\mu - 1}{\mu + 1} \right)^2 - \frac{1 \cdot 10^{-7}}{2} \cdot (T5(a, d) + T6(a, d))$$



Graph of single domain energy vs fluxguide height for a fluxguide on a ferrite substrate. The calculation has been repeated for different spacer thicknesses and as d tends to ∞ the energy tends to that when a non magnetic substrate is used.

Appendix 1B

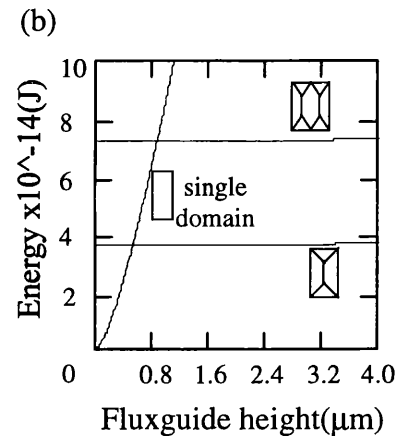
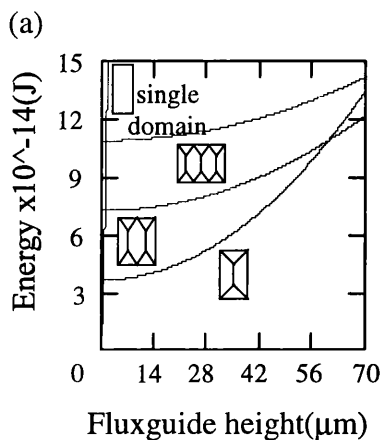
Fluxguide on non magnetic substrate.

$K := 100$ Approximate anisotropic constant for FeNbSiN

$\gamma_{180} := K \cdot \frac{(58 \cdot 10^{-6})^2}{4.65 \cdot 10^{-6}}$ Energy of a 180° wall as deduced from the fluxguide height where a transition from a 4 to a 7 domain structure was observed (see section 8.4)

$\gamma_{90} := \frac{1}{2 \cdot \sqrt{2}} \cdot \gamma_{180}$ Approximation made by Slonczewski et al (1988). This means that 90° wall energy is proportional to 180° wall energy

$$\text{close}(a, n) := \frac{K \cdot a^2 \cdot c}{2 \cdot (n - 1)} + (n - 1) \cdot \left(b - \frac{a}{n - 1} \right) \cdot c \cdot \gamma_{180} + 2 \cdot \sqrt{2} \cdot a \cdot c \cdot \gamma_{90}$$



Graphs showing the cross-over point from single domain to multiple domain structures. This appears to happen at around 0.5-0.6 μm which does not compare well to the 8 μm observed by Kerr microscopy. It is however noted that in the experiment there may well be some rotation of M at the end of the fluxguide in an attempt to reduce the amount of free poles at the edges. For a cross-over at 8 μm the pole density would have to be reduced by 80%.

REFERENCES**Chapter 1**

- M.N. Baibich, J.M. Broto, A. Fert, F. Nguyen Van Dau, F. Petroff, P. Etienne, G. Creuzet, A. Friederich and J. Chazelas, *Phys. Lett.* **61**, 2472 (1988)
- R.Becker, *Z. Physik*, **62**, 253 (1930)
- F.Bitter, *Phys. Rev.*, **38**, 1903 (1931)
- S. Chikazumi, in "Physics of Magnetism" ed. S.H. Charap (J. Wiley & Sons) (1964)
- B. Dieny, V.S. Speriosu, S.Metin, S.S.P. Parkin, B.A. Gurney, P. Baumgart and D.Renard, *J. App. Phys.*, **69**, 4774 (1991)
- B. Dieny, *J.M.M.M.*, **136** 335 (1994)
- A. Fert and P. Bruno, *Ultrathin Magnetic Structures* eds. B. Heinrich and A. Bland Springer-Verlang, Berlin (1992)
- W. Folkerts, J.C.S. Kools, Th.G.S.M. Rijks, R.Coehoorn, M.C. de Nooijer, G.H.J. Somers, J.J.M. Ruigrok and L. Postma *IEEE Trans. Mag.*, **30**(6), 3813 (1994)
- P.P. Freitas, J.L. Leal, L.V. Melo, N.J. Oliveria, L.Rodrigues and A.T. Sousa, *J. Appl. Phys. Lett.*, **65**, 4 (1994)
- H.M. Fuller and M.E. Hale *J. App. Phys.*, **31**, 238 (1960)
- M.A.M. Gijs and M. Okada, *Phys. Rev. B* , **46**, 2908 (1992)
- E. Grochowski and D.A. Thompson, *IEEE Trans. Mag*, Vol. **30**, No. 6, 3797 (1994)
- B.A. Gurney, V.S. Speriosu, J.P. Nozieres, H. Lefakis, D.R. Wilhoit O.U. Need, *Phys. Rev. Lett*, **71**, 4023 (1993)
- W. Heisenberg, *Z.Physik*, **49**, 619 (1928)
- K.E. Kujik, W.J. van Gestel and F.W. Gorter, *IEEE \trans. Mag.*, **11**, 1215 (1975).
- G.C.P. Lokhoff, *IEEE Trans. Cons. Elect.*, **37**, 702 (1991)
- J.L. Leal, L.M. Rodrigues, A.T. Sousa and P.P. Freitas *J. Mag. Mag. Matt.*, **140**, (3) 2215 (1995)
- N.F. Mott *Proc. Roy. Soc.*, **156**, 368 (1936)
- S.S.P. Parkin, N. More and K.P. Roche, *Phys. Rev. Lett.*, **64**, 2304 (1990)
- S.S.P. Parkin, R. Bhadra and K.P. Roche, *Phys. Rev. B*, **66**, 2152 (1991)
- S.S.P. Parkin, *Phys. Rev. Lett.*, **71**, 1641 (1993)
- M.Prutton, *Thin Ferromagnetic Films* (Buterworth) (1964)

- W.Thomson Proc.Roy.Soc., **8**, 546 (1851)
- C. Tsang, R.E. Fontana, T.Lin, D.E. Heim, V.S. Speriosu, B.A. Gurney and M.L. Williams
IEEE Trans. Mag., **30**, No 6, 3801(1994)
- P.Weiss, J.Phys., **6**, 661 (1907)
- V.Zieren, G. Somers, J.Ruigrok, M. de Jongh, A. van Straalen and W.Folkerts, IEEE
Trans. Mag.,**29**, No 6, 3064 (1993)

Chapter 2

- Y.Aharanov and D.Bohm, Phys. Rev., **115**, 485 (1959)
- F. Bitter, Phys. Rev., **38** 1903 (1931)
- J.N. Chapman and G.R. Morrison, J. Magn. Magn. Mater., **35**, 254 (1983)
- J.N. Chapman, J.Phys. D: Appl. Phys., **17** 623 (1984)
- J.N. Chapman, I.R. McFadyen and S.McVitie, IEEE Trans. Mag., **26**, 5 (1990)
- J.N. Chapman, A.B. Johnston, L.J. Hyderman, S. McVitie, W.A.P. Nicholson and B.
Bormans, IEEE Trans. Mag., **30**, No. 6 (1994)
- J.M. Cowley, Appl. Phys. Lett., **15**, 58 (1969)
- J.M. Cowley, Ultramicroscopy, **2**, 3 (1976)
- J.M. Cowley, Ultramicroscopy, **41**, 335 (1992)
- N.H. Dekkers and H. de Lang, optic, **41**, 452 (1974)
- C.E. Hall "Introduction to electron microscopy" McGraw-Hill (1953)
- M.E.Hale, H.W. Fuller and H. Rubenstein, J. Appl. Phys., **30**, 789 (1959)
- P.B. Hirsch, A. Howie, R.B. Nicolson, D.W. Pashley, M.J. Whelan "Electron microscopy
of thin crystals" Butterworths (1965)
- J. Kerr Rep. Brit. Assoc., **5** (1876)
- Jenkins and White, "Fundamentals of Optics" M^cGraw-Hill Book Co. 524 (1981)
- J. Kranz and A. Hubert, Die Möglichkeiten der Kerr-Technik zur Beobachtung
magnetischer Bereiche. Z. Angew. Phys. **15**, 220-232 (1963)
- M.Mansuripur J. App. Phys. **67** 6466 (1990)
- G.R. Morrison, Ph.D. Thesis, University of Glasgow (1981)
- P.M. Mul, B.J.M. Bormans and L. Schapp, published in the proceedings of the xiith
International conference for electron microscopy. (1990)
- A. Tonomura, Rev. Mod. Phys. **59**, No. 3 (1987)

K.Tsuno and T.Taoka, Jap. J. Appl. Phys., **22** 1047 (1983)

W.Voight, "Magnetooptik, in: Handbuch der Elektrizität und des Magnetismus, Vol. IV, ed. Graetz A." A. Barth, Leipzig 667-710 (1920)

Chapter 3

R.M. Bozorth and J.G. Walker, Phys. Rev. **89**(3): 624 (1953)

R.L. Conger and F.S. Essig, J. Appl. Phys. **28**, 855 (1957)

J.N. Chapman, L.J. Heyderman, S. McVitie, W.A.P. Nicholson, Proceedings of the 2nd International Symposium on Advanced Materials (1995)

S. Chikazumi, in "Physics of Magnetism" ed. S.H. Charap (J. Wiley & Sons.), (1964)

R.F. Egerton, Proceedings of the 40th Scottish Universities Summer School in Physics, Dundee (1992)

H.W. Fuller and M.E. Hale, J. Appl. Phys. **31**(2) 238 (1960)

R.F.C. Farrow, Journal of Crystal Growth **104** 556 (1990)

M.F. Gillies, J.N. Chapman and J.C.S. Kools J. Mag. Mag. Mat. **140-144**, 721 (1995)

M.E. Hale, H.W. Fuller and H. Rubenstein, J. Appl. Phys. **30** 789 (1959)

S.J. Hefferman, J.N. Chapman and S. McVitie, J. Mag. Mag. Mat. **95**, 76 (1991)

H. Hoffmann, I.E.E.E. Trans. Mag. ,Vol. Mag-4, 32, 1 (1968)

J.W.M. Jacobs and J.F.C.M. Verhoven, J. of Microscopy, **143**, 103 (1986)

R. Jérôme, T. Valet and P. Galtier **30**(6) 4878 (1994)

C. Kittel and J.K. Galt In Solid State Physics, **3**, 439, New York, Academic Press, (1956)

J.C.S. Kools, T.G.M. Rijks, R.F.O. Reneerkens, M.F. Gillies and J.N. Chapman, to be published in J. Appl. Phys. (1995)

S. McVitie, J.N. Chapman, L. Zhou, L.J. Heyderman and W.A.P. Nicholson J. Mag. Mag. Mat. **148** (1995)

R. Nakatani, K. Hoshino, S. Noguchi and Y. Sugita Jpn. J. Appl. Phys. **33** 133 (1994)

D.G. Neerinck et al, accepted for publication in Thin Solid Films, (1995)

W.A.P. Nicholson Mikrochim. Acta **114-115**, 53(1994)

W.A.P. Nicholson and J.N. Chapman, to be published. (1995)

M. Prutton, Thin Ferromagnetic Films, Butterworth (1964)

Th.G.S.M. Rijks, R.L.H. Sour, J.C.S. Kools, D.G. Neerinck, M.F. Gillies, A.E.M. de Veirman, R. Coehoorn and W.J.M. de Jonge to be published as proceedings of Intermag 1995

- D.O. Smith, J. Appl. Phys. **29**,264 (1958)
 D.O. Smith , J. Appl. Phys. suppl; **32**(3): 70S (1961)
 I.W. Wolf, T.Appl. Phys., **33**, 1152, (1962)

Chapter 4

- P. ten Berge, N.J. Oliveria, T.S. Plaskett, J.L. Leal, H.J. Boeve, G. Albuquerque, J. Ferreira, A.R. Morais, A.T. Sousa, L. Rodrigues and P.P. Freitas, to be published as proceeding of Intermag (1995)
- B. Dieny, et al., J. Appl. Phys., **69**, 1279 (1991)
- W. Folkerts, J.C.S. Kools, Th.G.S.M. Rijks, R. Coehoorn, M.C. de Nooijer, G.H.J. Somers, J.J.M. Ruigrok and L. Postma, IEEE Trans. Mag. **30**, 3813 (1994)
- W. Folkerts, J.C.S. Kools, M.C. de Nooijer, J.J.M. Ruigrok, L. Postma, K. -M.H. Lenssen, G.H.J. Somers and R. Coehoorn- submitted to IEEE Trans. Mag. March 1995
- L. Folks and R. Street, J. Appl. Phys. **76** (10), 6391 (1994)
- P.P. Freitas, J.L. Leal, L.V. Melo, N.J. Oliveria, L.Rodrigues and A.T. Sousa, J. Appl. Phys. Lett., **65**, 4 (1994)
- R.D. Hempstead, S. Krongelb and D.A. Thompson IEEE Trans Mag.,**14** (5), 521 (1978)
- L.J. Heyderman. J.N. Chapman and S.S.P. Parkin, J. Magn. Magn. Mat. **138**, 344 (1994)
- L.J. Heyderman, H. Niedoba H.O. Gupta and I.B. Puchalska, J. Magn. Magn. Mat. **96**, 125 (1991)
- E.J. Hsieh and R.F. Soohoo, AIP Conference Proceedings **5**, 727 (1971)
- R. Kergoat et al, presented at ICMFS '94 or Université Paris Sud Ph.D. thesis (1995)
- J.C.S. Kools^A, J. Appl. Phys., **77**, (7) 2993 (1995)
- J.C.S. Kools^B, J.J.M. Ruigrok, L. Postma, M.C. de Nooijer and W. Folkerts, submitted to J. Appl. Phys. Nov. 1995
- J.C.S. Kools^C private communication (1995)
- L. Neel, Comptes Rendus **255**, 1676 (1962)
- S.S.P. Parkin, R. Bhadra and K.P. Roche, Phys. Rev. B, **66**, 2152 (1991)
- Th.G.S. Rijks, R. Coehoorn, J.T.F. Daemen and W.J.M. de Jonge J. Appl. Phys., **76** (2) 1092 (1994)
- D.O. Smith and K.J. Harte, J. Appl. Phys. **33**, 1399 (1962)
- R. Schäfer, A. Hubert and S.S.P. Parkin, IEEE Trans. Mag. **29**, 2738 (1993)

- R. Street and S.D. Brown, *J. Appl. Phys.* **76**, (10) 6386 (1994)
- C. Tsang, R.E. Fontana, T.Lin, D.E. Heim, V.S. Speriosu, B.A. Gurney and M.L. Williams
IEEE Trans. Mag., **30**, No 6, 3801 (1994)
- C.H. Wilts and F.B. Humphrey, *J. Appl. Phys.*, **39**, 1191 (1968)
- I.W. Wolf, *J. Appl. Phys.*, **33**, 1152S (1962)

Chapter 5

- W. Folkerts, J.C.S. Kools, Th.G.S.M. Rijks, R. Coehoorn, M.C. de Nooijer, G.H.J. Somers, J.J.M. Ruigrok and L. Postma, *IEEE Trans. Mag.* **30**, 3813 (1994)
- P.P. Freitas, J.L. Leal, L.V. Melo, N.J. Oliveria, L.Rodrigues and A.T. Sousa, *J. Appl. Phys. Lett.*, **65**, 4 (1994)
- A. Hubert *phys. stat. sol.* **38**, 699 (1969)
- D.E. Heim, R.E. Fontana Jr., C. Tsang, V.S. Speriosu, B.A. Gurney and M.L. Williams
IEEE Trans. Mag., **30**, 316 (1994)
- J.C.S. Kools private communication (1995)
- S. McVitie, J.N. Chapman, S.J. Hefferman and W.A.P. Nicholson, *Journal de Physique*, **49**, 1817 (1988).
- Th.G.S.M Rijks, W.J.M. Dejonge, W. Folkerts, J.C.S. Kools and R. Coehoorn *App. Phys. Lett.*, **65**(7), 916 (1994)
- C. Tsang, R.E. Fontana, T.Lin, D.E. Heim, V.S. Speriosu, B.A. Gurney and M.L. Williams
IEEE Trans. Mag., **30**, No 6, 3801 (1994)

Chapter 6

- T. C. Anthony, J.A. Brug and S. Zhang *IEEE Trans Mag* **30** (6) 3819(1994)
- P. ten Berge, N.J. Oliveria, T.S. Plaskett, J.L. Leal, H.J. Boeve, G. Albuquerque, J. Ferreira, A.R. Morais, A.T. Sousa, L. Rodrigues and P.P. Freitas, to be published in the proceedings of Intermag (1995)
- W.C. Cain, J.W. Lee, P.V. Koeppe and M.Kryder, *IEEE Trans. Magn. MAG-24*, 2609 (1988)
- W.C. Cain, M.H. Kryder *J. App. Phys.* **67** (9) 5722 (1990)
- M.J. Carey and A.E. Berkowitz *Appl. Phys. Lett.* **60** (24) 1992
- B. Dieny, V.S. Speriosu, B.A. Gurney, S.S.P. Parkin, D.R. Wilhoit, K.P. Roche, S. Metin, D.T. Peterson and S. Nadimi, *J. Mag. Mag. Matt.* **93** 101 (1991)

- W.F. Egelhoff et al J.App. Phys. **78** (1) (1995)
- W. Folkerts, J.C.S. Kools, M.C. de Nooijer, J.J.M. Ruigrok, L. Postma, K. -M.H. Lenssen, G.H.J. Somers and R. Coehoorn- submitted to IEEE Trans. Mag. March 1995
- L. Folks and R. Street, J. Appl. Phys. **76** (10) 6391 (1994)
- P.P. Freitas^A, J.L. Leal, T.S. Plaskett, L.V. Melo and J.C. Soares J. Appl. Phys. **75** 6385 (1994)
- P.P. Freitas^B, J.L. Leal, L.V. Melo, N.J. Oliveira, L. Rodrigues and A.T. Sousa, Appl. Phys. Lett. **65** (4) 1 (1994)
- P.P. Freitas, private communication (1995)
- R.D. Hempstead, S. Krongelb and D.A. Thompson IEEE Trans. Mag. **MAG-14**(5) 521 (1978)
- L.J. Heyderman Ph.D. thesis University of Bristol(1991)
- R. Junglut et al, J. Mag. Mag. Mat. **148** 300 (1995)
- R. Kergoat, Ph.D. thesis, Univ. Paris Sud (1995)
- M. Labrune, S. Andrieu, F. Rio and P. Bernstein, J.Magn.Magn Mater. **80**, 211 (1989)
- A.P. Malozemoff, J. App. Phys. **63** 3874 (1988)
- H. Niedoba, A. Hubert, B. Mirecki and I.B. Puchalska, J.Magn.Magn Mater. **80**, 379 (1989)
- R. Ploessl, J.N. Chapman A.M. Thompson J. Zweck and H. Hoffmann, J. Appl. Phys. **73**, 2447 (1993)
- T.S. Plaskett. G. Albuquerque and P.P. Freitas presented at Intermag 1995
- N. Smith and W.C. Smith, J. App. Phys. **69** (4) 2471(1991)

Chapter 7

- A. Bogdanov and A. Hubert, J. Mag. Mag. Mater. **138** 255 (1994)
- A. Bogdanov and A. Hubert, Phys. Stat. Sol. B-Basic Research **186**(2) 527 (1994)
- A. Hubert, Journal De Physique **49** C8-1859 (1988)
- R. Ploessl, J.N. Chapman A.M. Thompson J. Zweck and H. Hoffmann, J. Appl. Phys. **73**, 2447 (1993)
- M.E. Schabes and H.N. Bertram, J. Appl. Phys., **64**(3), 1347 (1988)

Chapter 8

- G. Somers et al private communication (1994)
- A. Hubert Journal De Physique C8-1859 (1988)
- G.S. Krinchik and V.A. Artem'ev, Zh. Eksp. Teor. Fiz. **53**, 1901 (1967)[Sov. Phys. JETP **26**, 1080 (1968)]
- J-P. Lazarri and I. Melnick, IEEE Trans. Magn. MAG-7, 146 (1971)
- Y. Litake and Y. Shimada IEEE J. on Mag. in Japan Vol 7 (2),113 (1992)
- S. McVitie, Ph.D Thesis, University of Glasgow (1988)
- K. Nago, H. Sakakima and K. Ihara IEEE J. on Mag. in Japan Vol 7 (2),119 (1992)
- J.A.C. van Ooyen, J. Magn. Magn. Mat. **26**, 223 (1982)
- P. Rhodes and G. Rowlands, Leeds Phil. and Lit. Soc., 191, (1954)
- O.J. Wimmers, M.T. Johnson and P. Lasinski, J.Mag. Magn. Mat. **89**, 61 (1990)
- V.Zieren, G. Somers, J.Ruigrok, M. de Jongh, A. van Straalen and W.Folkerts, IEEE Trans. Mag.,**29**, No 6, 3064 (1993)

Chapter 9

- W.F. Egelhoff et al, presented at MML'95 (1995)
- B. Khamsehpour, C.D.W. Wilkinson, J.N. Chapman and A.B. Johnston submitted to J. Appl. Phys (1995)
- J.C.S. Kools J. Appl. Phys., **77**, (7) 2993 (1995)
- J.C.S. Kools J. App. Phys., presented at MML'95 (no publication) (1995)
- M. Labrune, J.C.S. Kools, A. Thiaville and D. Tomas, presented at MML'95 and to be published in J. App. Phys. (1995)
- E.C. Stoner and E.P. Wohlfarth, Phil. Trans. Roy. Soc., **A240**, 599 (1948)
- S.W. Yuan and H.N. Bertram, J. Appl. Phys., **75**, 6385 (1994)

Appendix

- J.C. Slonczewski, B. Petek, B.E. Argyle, IEEE Trans. Magn., **24**(3), 2045 (1988)